



University of Liège
Montefiore Institute of Electricity
Department of Electrical Engineering and Computer Science
Research Unit "Power Transmission and Distribution (TDEE)"

Wake-Induced Oscillations in Cable Structures: Finite Element Approach

PhD Thesis by Dmitry Snegovskiy
Under Promotion and Supervision of Dr. Pr. Jean-Louis Lilien

Liège-Toulouse-Moscow
2001-2010

To Tatiana, Our Children Dasha and Vladimir

Table of Contents

1	Introduction	1
1.1	Cable structures.....	3
1.1.1	Overhead transmission line.....	3
1.2	Bundle conductors.....	4
1.2.1	Spacers.....	5
1.2.2	Yoke plate.....	7
1.3	Bundle cable dynamics.....	8
1.3.1	Linear theory.....	8
1.3.2	Torsional motion.....	10
1.3.3	Torsional stiffness.....	12
1.3.4	Limitations and solutions.....	13
1.4	Wind effects on cables in bundle.....	13
1.4.1	Cable aerodynamics.....	13
1.4.2	Notions of wake.....	15
1.5	Overview of wake-induced oscillation.....	21
1.5.1	Conditions of occurrence[18], [19].....	22
1.5.2	Damages due to wake-induced oscillations.....	25
2	Model of wake-induced oscillation.....	27
2.1	Introduction.....	27
2.1.1	Application of quasi-steady hypothesis.....	27
2.2	Wake-induced flutter model.....	30
2.2.1	Solving the eigenvalue problem.....	34
2.2.2	Aerodynamic data.....	36
2.2.3	Stiffness properties of suspension.....	40
2.2.4	Comparison to previous studies.....	40
2.2.5	Critical flutter velocity.....	42
2.2.6	Effect of structural damping.....	44
2.2.7	Domain of application of the flutter model.....	47
3	Finite element model.....	49
3.1	Overview of existing models.....	49
3.2	SAMCEF Mecano model of wake interaction.....	49
3.3	Spacer model.....	51
3.3.1	Spacer basic properties.....	51
3.3.2	Finite element model of spacer.....	54
3.4	Time integration scheme.....	56
3.5	Numerical examples.....	58
3.5.1	Single 45 m – long span twin bundle model.....	58
3.5.2	Single span 80 m long: twin bundle.....	60
3.5.3	Three equal 80 m subspans, twin bundle.....	62
3.6	Synthesis.....	68
4	Parametric study.....	69
4.1	Effect of conductor torsion.....	70
4.1.1	Model description.....	70
4.1.2	Results.....	71
4.1.3	Synthesis.....	78
4.2	Effect of spacer articulation.....	78
4.2.1	Model description.....	79

4.2.2	Results	80
4.2.3	Synthesis	86
4.3	Effect of staggered spacers placement	86
4.3.1	Model description.....	86
4.3.2	Results	88
4.3.3	Synthesis	93
4.4	Combined staggering + spacer damper	94
4.4.1	Model description.....	94
4.4.2	Results	96
4.4.3	Synthesis – comparison by Global Instability Index.....	102
4.5	Overall parametric study synthesis	103
5	Overview of protection methods against wake-induced oscillation.....	104
5.1	Overview of existing methods.....	104
5.1.1	Increase of subconductor separation	104
5.1.2	Reduction of proportion of conductors in the wake.....	104
5.1.3	Tilt of bundle.....	105
5.1.4	Short subspan lengths	105
5.1.5	Uneven placement of spacers.....	105
5.1.6	Spacer dampers	107
5.1.7	Combined method for protection of line against vibrations and subspan oscillations.....	107
5.2	Suggestions to methodology for definition of optimal placement of spacers	108
6	Experimental validation	110
6.1	Input data.....	111
6.1.1	Span properties.....	111
6.1.2	Conductor properties	111
6.1.3	Bundle properties	111
6.1.4	Spacer damper data	111
6.2	Assessment of spacer damper dynamic properties	112
6.2.1	Sine sweep model.....	113
6.2.2	Model of spacer damper integrated with two subspans.....	116
6.2.3	Synthesis	118
6.3	Benchmarking calculations results	119
6.3.1	Reference field test results.....	119
6.3.2	Model of span.....	121
6.3.3	Calculation results: Wind 8 m/s, subspan 4.....	121
6.3.4	Calculation results: wind 11 m/s, subspan 7.....	125
6.3.5	Calculation results: wind 17 m/s, subspan 5.....	129
6.4	Summary. Comparison to field test data and other studies	134
7	Conclusions	135
8	List of references	137
	Acknowledgments	142
	Annex A. Aerodynamic coefficients of a leeward cylinder	143
	Annex B. On numerical resolution of wake loads on a leeward cylinder.....	154
	Annex C. Close-wake interference	159
	Annex D. Summary of bundle oscillation theory by Transfer Matrix Method	162
	Annex E. Short glossary.....	165

1 Introduction

In this work we consider the overhead power transmission lines (OHL). Their specifics are related to the presence of cables (conductors) whose length between supporting towers may extend to dozens of thousand meters. The OHL components are exposed to a combination of natural actions – wind, rain, ice / snow / frost deposits. Compared to other structural parts, conductors have the highest flexibility and very low structural self-damping (of the order of 0.1 % of critical damping or lower, depending on frequencies [77]). They are among structural elements the most sensitive to these actions.



Credit to, "Cheeky Monkey Foto"

Figure 1-1. Overhead transmission lines: left – two-circuit, equipped with single conductors per phase, right – single-circuit, equipped with bundled conductors (here, twin bundle) per phase

Since early fifties the increased energy demand gave a rise to large construction of high-voltage and extra-high-voltage overhead lines [20] equipped with bundled electrical conductors (Figure 1-1). For such arrangements there was noticed a kind of wind-induced oscillations originated by a zone of disturbed and retarded air flow (wake), that the cables located upwind (windward) cast onto the downwind (leeward) ones. The effect of this phenomenon called Wake-Induced Oscillations (WIO) resulted in fatigue damages of conductors, failures of insulator strings and cable suspension hardware and fatigue failures of spacers.

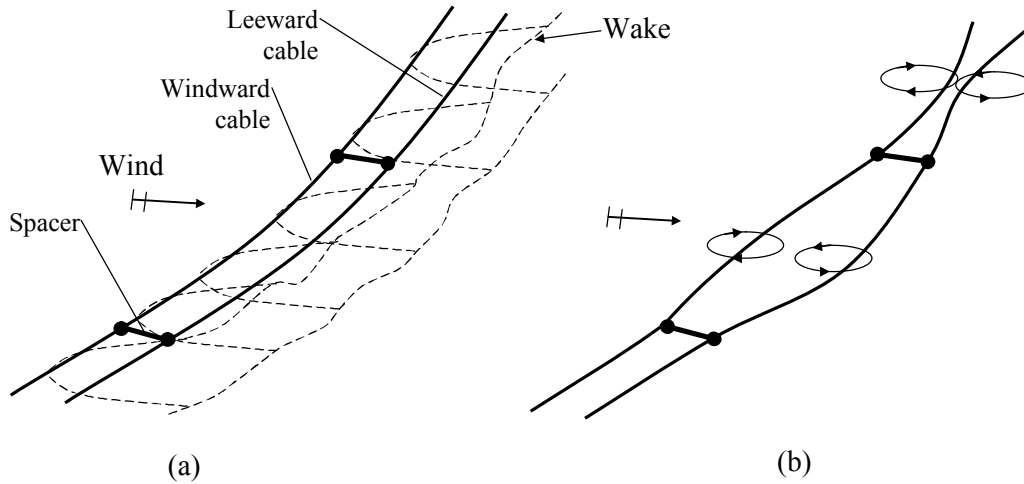


Figure 1-2. (a) Bundle conductors under wind: shielding of leeward conductor by the windward one caused by the wake. (b) Subspan oscillations – a typical case of wake-induced oscillations

There have been identified analogues to transmission lines' WIO in other regular structures subject to the cross-flow of viscous fluids (air, gas, water etc.): heat exchanger tubes, clusters of fuel rods of nuclear reactors [7], groups of chimneys, buildings [46]. Early works in this field relate to the aerodynamics of tandem and staggered twin struts to support the wings of biplanes and published by Pannell, Griffiths and Coales in 1915 [90]. Other cable structures like suspenders in suspension bridges [34] or stays in cable-stayed bridges [12] may be also subject to wake-induced oscillations. In each of these cases, conditions of oscillations' occurrence and structural response depend on cable's specific mass and stiffness, kind of fixation, dimension scale versus fluid viscosity and velocity (Reynolds number) etc. The cables' separation plays important role, as there are different kinds of wake interference especially when the cables are closely spaced.

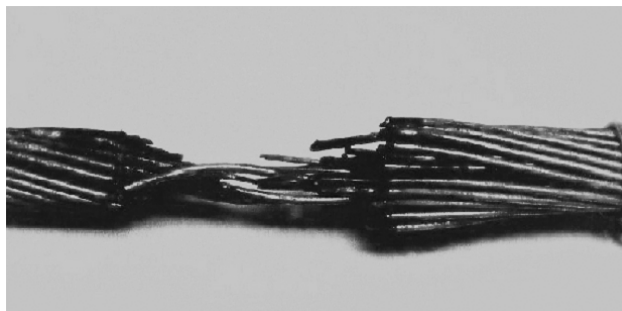


Figure 1-3. Severely damaged conductor under spacer clamp due to subspan oscillation [EPRI, 2006]

A number of research projects were entertained to study the wake-induced oscillations of different structures, which brought to development of analytical and experimental models and methods of protection against this phenomenon. A particular solution to overhead lines was found by unevenly distributing the spacers along the line span. To achieve that, no unique approach exists; virtually each

grid company, or manufacturer of spacers proceeds with its own method. It may rely on different basis, either field experience or analytical study or a mixture of them. And, despite advances in numerical modelling of latest decades, few publications uncover phenomenological side of WIO.

The issues of modelling WIO in a view of helping to develop methods for protection of line against WIO are a main subject of this work.

Original Advances of Thesis

Original advances studied in this thesis include:

- Current state-of-the art for analytical calculation of WIO, including the loads in the wake
- Overview of classic theory of wake-induced flutter and its evaluation from the standpoint of modern numerical tools for analytical applications (e.g., Matlab)
- Nonlinear Finite-Element Modelling of WIO using classic theory of wake-induced flutter, study of its domains of application, advantages and limitations, including validation upon field experiments
- Foundation of basic methodology for optimal placement of spacers over the bundle conductor span

1.1 Cable structures

1.1.1 Overhead transmission line

The overhead transmission line (OHL) consists of towers, conductors, insulators, and the line hardware for joining the conductors and for properly supporting the high-voltage line to the transmission line tower.

OHL is made of a sequence of several line sections. A schematic representation of one line section is depicted in Figure 1-4. Each section begins and ends with an anchoring tower on which different cables are attached with the anchoring insulator chains. The intermediate (suspension) towers in-between enable to hang the cables from the suspension insulator chains.

The span is a part of a section between two towers. We distinguish the anchor span (tensioned between two anchor towers), suspension span (between suspension towers) and semi-anchor span.

Depending on the line voltage, either one or several conductors per each of three phases may be installed in the OHL section. The bundle configuration is used to increase the current carrying capacity and to reduce corona discharge. Conductor bundles are always used at line voltage 330 kV and beyond. The bundle arrangement of the line will be studied throughout this work.

To avoid contacts between the subconductors in the bundle, the spacers are installed along the span length. The part of a span between two spacers is called a subspan.

The bundle subconductors have equalised tension due to the yoke plates at the anchoring points. In the suspension span the bundle may have the supports that, depending on their type, may allow for longitudinal motion.

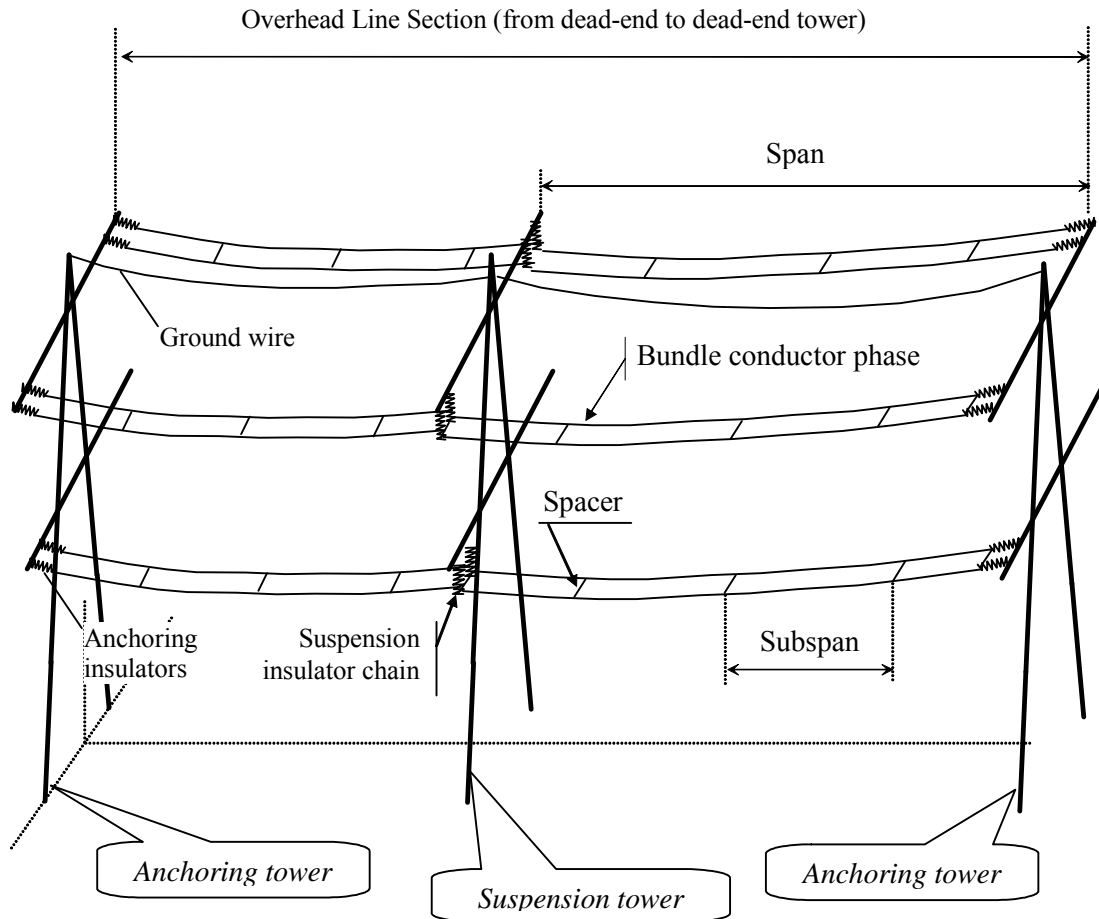


Figure 1-4. Schematic representation of a transmission line section

Tensions in the subconductors are selected in the range of 15...25% UTS¹. In these conditions 20...30 kN tensions per subconductor are common.

In transmission lines different span lengths are encountered. We shall consider the spans about 240...500 m, however, span lengths may be 1500 m or longer (e.g., on river crossings).

1.2 Bundle conductors

The bundle may consist of two, three and up to 12 subconductors. We focus ourselves on the most commonly employed two, three and four-subconductor (twin, triple and quadruple) bundles used to transmit currents having voltage 330 kV, 500 kV and 750 kV² respectively.

¹ Ultimate Tensile Stress

The typical bundle cross-sections are inscribed in a circle making equilateral triangle, square etc. (see some examples in Figure 1-5). The subconductor separation distance, or spacing, d , depends on electrical characteristics of a line and is normally standardized. The spacing is normally within the ranges from 300 to 600 mm. Typical separations are 400 mm (in Russia and Europe), 457 mm (United States). The spacing 600 mm is employed on the long spans in the crossings.

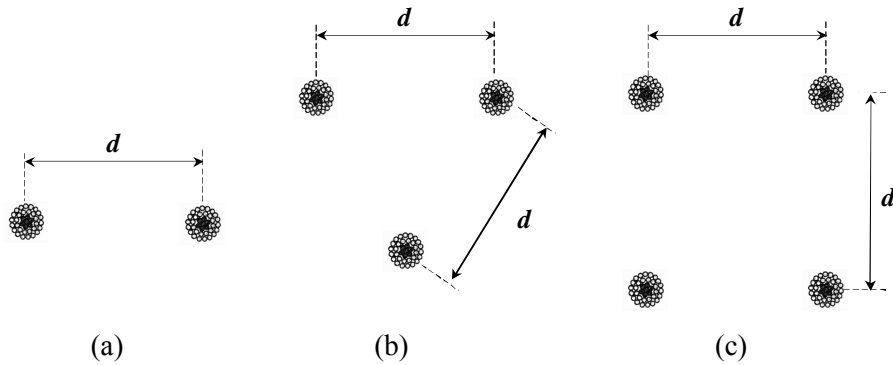


Figure 1-5. Cross-sections of twin (a), triple (b) and quadruple (c) bundles

Some of subconductor cross-sections are shown in Figure 1-6. The stranded conductors (a) are the most common, however, smooth conductors (b) and (c) are increasingly employed. Different outer stranding makes different surface roughness and, consequently, causes differences in aerodynamic properties.

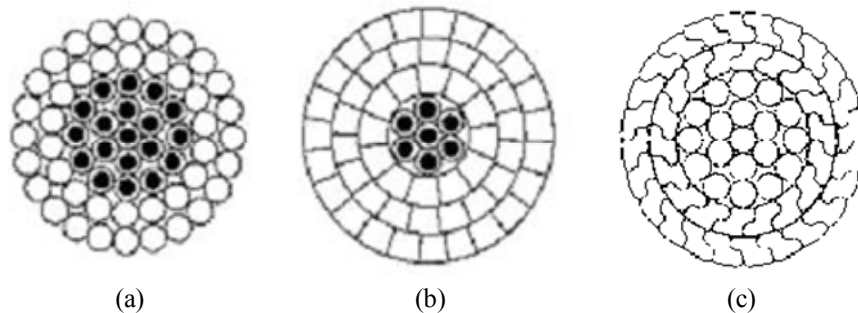


Figure 1-6. Examples of stranded (a) and smooth (b), (c) subconductors' cross-sections

1.2.1 Spacers

The spacers maintain the distance between the subconductors in the bundle under all normal conditions of line service. Main designs of spacers are referred to in [74] and [20]. We list here rigid, articulated and damping spacers:

² Russian voltage levels

1.2.1.1 Rigid spacer

Spacers of this type are mainly installed in twin bundle (like the one shown in Figure 1-7), however, array spacers for multiple bundles also exist [63]. Rigid spacer with bolted fixation to the conductor includes a central frame and clamps. Mass of a twin bundle rigid spacer is about 2...3 kg.

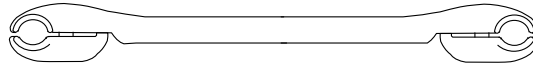


Figure 1-7. Rigid spacer [74]

1.2.1.2 Articulated spacers

Unlike the rigid spacers, in articulated ones the frame is connected to the clamp via pins (Figure 1-8). In particular, this allows for large longitudinal movements of subconductors without damaging the spacers. Articulated spacers are still offered by line fittings manufacturers.

As well as for rigid spacers, there are twin and multiple bundle articulated spacers [32].

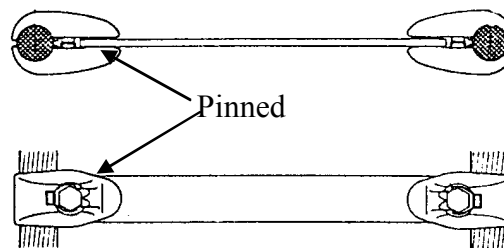


Figure 1-8. Articulated spacer [74]

1.2.1.3 Spacer dampers

One example among large variety of spacer dampers is shown in Figure 1-9. Spacer dampers generally include the following components:

- frame
- clamps
- arms, connected to the frame via articulations, and
- damping elements in the arm articulations.

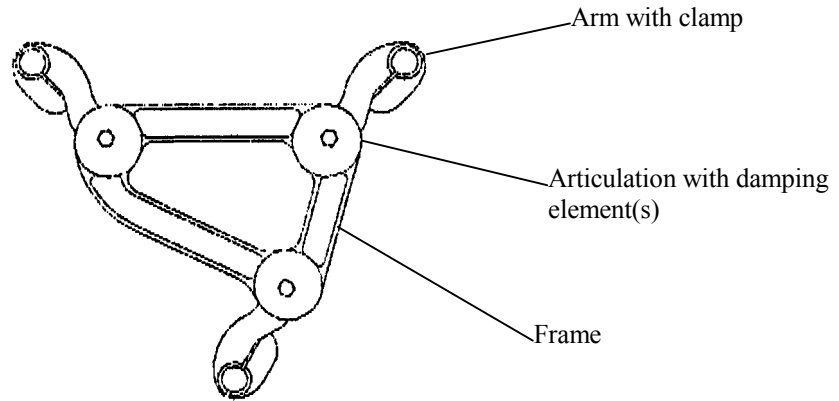


Figure 1-9. Spacer damper [74]

For the future study, a prototype spacer damper can be considered having characteristics as follows: rotation of spacer damper arms is of the order $\pm 12...15^\circ$. The attachment of arms allows for longitudinal movement (along the conductor) about $\pm 6...8^\circ$. The central frame has the mass of the order of 2...2.5 kg. Damping elements allow for stiffness of the arm rotation with respect to the frame about 10...15 N/deg. Combined effect of damping and articulated motion allows for decay of aeolian vibrations and WIO.

1.2.2 Yoke plate

Yoke serves to equalize tensions in each of subconductors in a bundle. As the bundle is deflected under wind pressure, the windward and leeward subconductors obtain different tensions. Note, that some tension difference may be introduced at line installation in order to detune the subspan oscillation, as well as aeolian vibration of the subconductors (no subconductors' lock-in at the same time). This combination of tensions may be either insufficient or changed upon the ageing of the line, as long as it becomes favourable to the WIO.

The difference between tensions may arise due to the gust effects plus the wake (windward subconductor has drag only; leeward one has not only the drag but also the lift force). Eigenfrequencies of both subconductors arise, but leeward subconductor will be tensioned slightly more. Since the wind pressure is still different, the sag of cables will differ. However, this difference is still slight.

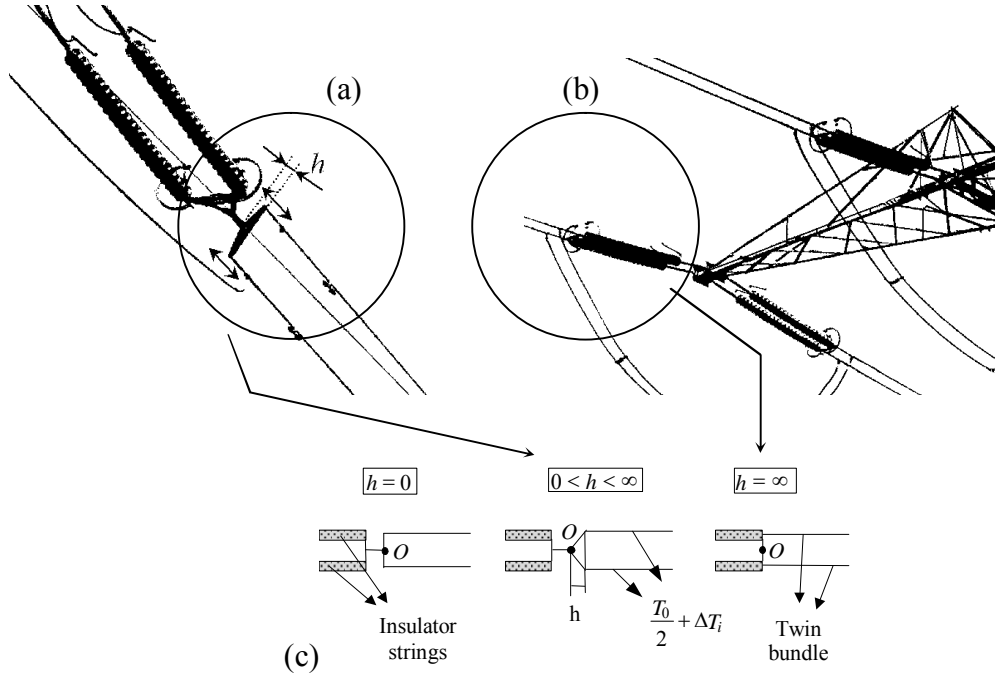


Figure 1-10. Different anchoring arrangements of a twin bundle conductors.
a) Yoke plate b) Subconductors directly connected to the insulator chains
c) Schematic view in the plane of the subconductors

For more than two subconductors in the bundle, the anchoring arrangement is a more complex assembly of yoke plates.

Despite the use of yoke plate, imperfections in line design (support hardware, running angle insulator posture), inaccurate sagging, differential creep of conductors, catenary blowout or sloping terrain may lead to the tilt of bundle with respect to the incident flow [20]. As will be shown in Section 1.5.1.4, the tilt favours, at certain angles, to the onset of the wake-induced oscillation.

1.3 Bundle cable dynamics

In this chapter some baseline notions of cable dynamics are discussed in their application to the bundle of cables. The evaluations presented here are for general information.

1.3.1 Linear theory

As a first approximation of bundle cable dynamics in the transmission line conductors, we can apply the linear theory developed by Irvine [33] for a cable with sag-to-span ratio about 1:8 or less.

First consider a single cable suspended between supports, having its own weight expressed by mass per unit length, m [kg/m], subject to tension T [N]. The cable profile is defined from the equilibrium of an elementary volume, and is described by a parabola shape,

$$w(x) = \frac{mgl^2}{2T} \left(\frac{x}{l} - \left(\frac{x}{l} \right)^2 \right) \quad (1.1)$$

where l is the span of cable.

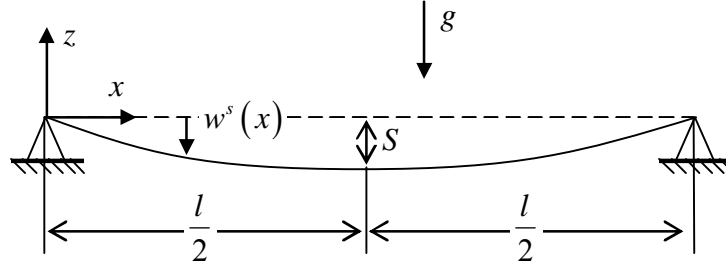


Figure 1-11. Cable under static equilibrium

Cable eigenmodes consist of in-plane and out-of-plane modes. When there is no wind, these modes correspondingly deploy in vertical and horizontal directions.

Out-of-plane modes of cable are defined by equation

$$\phi_n(x) = A_n \sin\left(\frac{n\pi x}{l}\right) \quad (1.2)$$

associated with the natural frequency,

$$f_k = \frac{k}{2l} \sqrt{\frac{T}{m}} \quad (1.3)$$

For the bundle cables with n subspans separated by rigid spacers, additionally to global modes, the subspan modes exist, involving the length of subspans l_i . The natural frequency of the subspan out-of-plane mode is then

$$f_{ki} = \frac{k}{2l_i} \sqrt{\frac{T}{m}}, \quad i = 1 \dots n \quad (1.4)$$

The in-plane modes separate into anti-symmetric (which do not involve the tension variation) and symmetric ones (at which the tension varies). The in-plane frequency (symmetric modes) for the whole span is given by transcendental equation:

$$\tan\left(\frac{\beta_j l}{2}\right) = \frac{\beta_j l}{2} - \frac{4}{\lambda^2} \left(\frac{\beta_j l}{2}\right)^3 \quad (1.5)$$

where

$$\beta_j = \sqrt{\frac{m}{T}} \omega_{z2j-1},$$

$$\lambda^2 = \left(\frac{8d}{l}\right)^2 \frac{EF}{T} - \text{Irvine parameter}$$

The anti-symmetric natural frequencies are given by relationship

$$f_j = \frac{j}{2l} \sqrt{\frac{T}{m}} \quad (1.6)$$

and the mode shape is defined as

$$\psi_{2j-1}(x) = A_{2j-1} \left[1 - \tan\left(\frac{\beta_j l}{2}\right) \sin(\beta_j x) - \cos(\beta_j x) \right] \quad (1.7)$$

In bundle cable in typical horizontal arrangement, the in-plane modes shall be virtually the same, because the spacers do not basically introduce the coupling in these modes.

1.3.2 Torsional motion

The torsional dynamic equilibrium condition for free vibration reads [18],

$$I \frac{\partial^2 \vartheta}{\partial t^2} - \frac{\partial C}{\partial z} = 0 \quad (1.8)$$

Here, ϑ is the angle of rotation of bundle, C is the torque.

Assuming for a bundle $I = mr^2$ (m is the total mass of the bundle per unit length) we have, for small variations,

$$\frac{\partial^2 \Delta \vartheta}{\partial t^2} - \frac{1}{m} \left[\left(\frac{\tau}{r^2} + T_0 \right) \frac{\partial^2 \Delta \vartheta}{\partial z^2} + a \Delta H \right] = 0 \quad (1.9)$$

$$\Delta H = -aK_9 \int_0^L \Delta \vartheta dz$$

Here,

$\tau = \pi \pi_c$ - total intrinsic torsional stiffness of the phase,

$$K_9 = S^T \left[\frac{nL}{EA} \mathbf{U} + 2\mathbf{F} \right]^{-1} \quad S - \text{equivalent stiffness for torsional motion,}$$

$$U = \text{diag}(1, \dots)$$

$$\mathbf{F} = \begin{bmatrix} F_{1,1} & F_{1,2} & \dots & F_{1,n} \\ F_{2,1} & F_{2,2} & \dots & F_{2,n} \\ \dots & \dots & \dots & \dots \\ F_{n,1} & F_{n,2} & \dots & F_{n,n} \end{bmatrix} \quad - \text{flexibility matrix associated to the device by which the}$$

subconductors are fixed to the dead-end towers,

$$S = \{\cos \sigma_1, \cos \sigma_2, \dots, \cos \sigma_n\}^T \quad - \text{vector-matrix of angular positions of the subconductors}$$

$$a = \frac{mg}{T} \quad - \text{inverse of the catenary parameter}$$

$$T_0 \quad - \text{initial tension in the bundle.}$$

Analytical solution for this equation may be found by the following decomposition:

$$\Delta \vartheta_s = \sum_k \Delta \vartheta_{s,k} \sin \frac{k\pi z}{L_s} \quad (1.10)$$

where:

s - span index

k - mode number

Substituting the expression (1.10) into (1.9), multiplying by $\sin(k\pi \vartheta / L_s)$ and integrating between 0 and L_s the partial differential equation splits into a set of ordinary differential equations:

$$\begin{aligned} & \frac{d^2 \Delta \vartheta_{k,s}}{dt^2} + \left(\frac{k\pi}{L_s} \right)^2 \frac{1}{m} \left(T_0 + \frac{\tau}{r^2} \right) \Delta \vartheta_{k,s} + b \frac{1}{k} \left\{ \frac{L_1}{L} \sum_{j \text{ odd}} \frac{\Delta \vartheta_{1j}}{j} + \right. \\ & \left. + \frac{L_2}{L} \sum_{j \text{ odd}} \frac{\Delta \vartheta_{2j}}{j} + \dots + \frac{L_{Ns}}{L} \sum_{j \text{ odd}} \frac{\Delta \vartheta_{Nj}}{j} \right\} = 0 \end{aligned} \quad (1.11)$$

with

$$b = \frac{8a^2 K_9 L}{\pi^2 m}$$

The same system (1.11) can be applied to the vertical motion, replacing ϑ by z , K_9 by K_v and

$$\left(T_0 + \frac{\tau}{r^2} \right) \text{ by } T_0.$$

Computation of modal shape and corresponding frequencies implies the computation of the eigenvalues and the eigenvectors of the matrix associated to those coupled equations.

1.3.3 Torsional stiffness

The bundle torsional modes are different from those of a single cable, and the main reason lies in the nature of a torsional stiffness. While the torsional stiffness of a single cable is a constant depending only on size, construction and age of cable, the bundle torsional stiffness is mainly non-linear and depends on many design parameters like the sag/span ratio, disposition of spacers, geometry of bundle and attachment conditions to the anchoring tower as discussed in [86].

The analytic theory for a bundle conductor phase developed by Nigol [36] proposes the following expression for equivalent torsional stiffness of the bundle:

$$GJ_{Nigol} = n(T_{0i}r^2 + \tau_c),$$

where

n - number of subconductors,

$\tau_c = 0.00028\phi^4$ - torsional stiffness of the subconductors (ϕ being the diameter of the conductor, mm),

T_{0i} - initial tension in each subconductor, N

r - the bundle radius, m

The resulting torsional stiffness dimension is $N \cdot m^2 / Rad$.

The disadvantage of this expression is that it treats the bundle as a whole without taking into account the spacers' arrangement. In the same time, the lengths of subspans (especially near extremities) directly influence the torsional stability of the bundle.

Wang [86] developed a new theory for bundle torsional stiffness which takes into account the sag/span ratio of the bundle phase and the variations of the bundle radius during the torsion. The expressions obtained in this work are rather complicated. However, for a bundle conductor for which the subconductors are directly connected to the insulator chains ($h = \infty$), Wang obtained a simple expression for the initial bundle torsional stiffness of the first torsional mode:

$$GJ_{h=\infty} = n(\tau + r^2 T_{0i}) + \frac{16r^2 K_{h \rightarrow \infty}}{3L} D^2, \quad (1.12)$$

where

$$K_{h \rightarrow \infty} = \frac{EA_{ph}}{nL_s} \sum_{i=1}^n (\cos \sigma_i)^2,$$

σ_i - the angles of subconductors with respect to horizontal axis.

Assessment of torsional stiffness is important for assessment of spacers' placement since the distribution of spacers may influence this parameter.

1.3.4 Limitations and solutions

Above statements are valid for rigid spacers in the span. If the spacers are not rigid, the motions in adjacent subspans are coupled through motions of the spacer clamps. In this case, instead of a series of modes for each subspan, corresponding to its harmonics, with the modes for each subspan independent of those to the others, there is a series of modes of the span as a whole, each generally involving motions in all subspans. The modes in this series are represented by different ratios of amplitudes among the various subspans, and each mode has, in general, a different frequency. The node points do not fall precisely at spacers.

The solutions to this case may be different. Claren et al. [10] and later Rawlins [60], [61] proposed a method for taking into account the flexibility of spacers and travelling waves in the bundle. Their results indicate, that both eigenfrequencies and mode shapes for flexible or damping spacers are not similar with the same span, were the spacers rigid. Nowadays, this problem is successfully solved with numerical methods (in present work see, for example, the single-spacer damper, two-subspan modal analysis of quad bundle presented in Section 6.2.2).

1.4 Wind effects on cables in bundle

Wake-induced oscillation encompasses several types of motion, observed in conductor bundles that are caused by aerodynamic shielding of leeward-lying conductors by windward ones. The leeward conductors that lie in the wakes of windward conductors are subject to forces not experienced by single conductors, and these forces permit wind-induced motions to occur that are peculiar to bundles.

Prior to discuss the subject of the wake-induced oscillation, we present here a brief description of cable aerodynamics. Special accent is made on the wake and the inherent loads on a conductor submerged in it.

1.4.1 Cable aerodynamics

A cable exposed to the wind is subject to air pressure, whose resultant is expressed via three components: drag and lift forces and the moment. When approximating the portion of conductor as circular cylinder of unitary length, these forces read:

$$\begin{aligned}
F_D &= \frac{\rho V^2}{2} D C_D \\
F_L &= \frac{\rho V^2}{2} D C_L \\
F_M &= \frac{\rho V^2}{2} \left(\frac{\pi D^2}{4} \right) C_M
\end{aligned} \tag{1.13}$$

Here,

- ρ density of the air, kg/m^3 ;
 V velocity of incident flow, m/s ;
 C_D dimensionless drag coefficient
 C_L dimensionless lift coefficient
 C_M dimensionless moment coefficient
 D conductor diameter, m

Dimensions of resulting forces are: $F_D, F_L : \text{N/m}$, $F_M : \text{N}\cdot\text{m/m}$

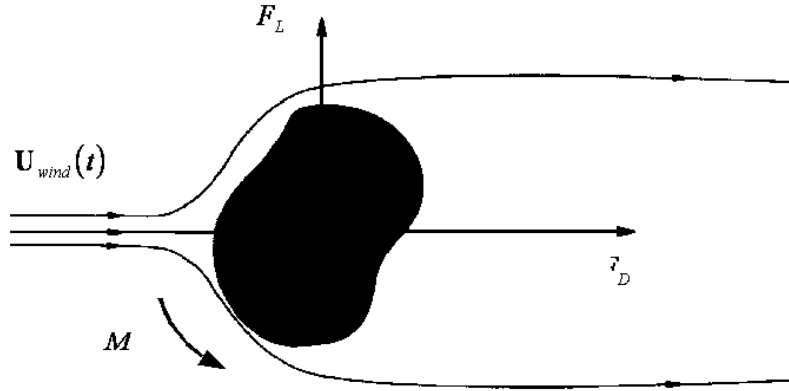


Figure 1-12. Aerodynamic forces acting onto a bluff body

Aerodynamic moment acts on a conductor in case of ice deposit, making its cross-section noncircular. For bare circular conductors (see Figure 1-6), which are susceptible to wake-induced oscillations [19], $F_M = C_M = 0$.

The following subsection presents some aspects of the wake genesis. We mostly refer to the cylinder as the aerodynamic model of the cable in the wind tunnel tests.

1.4.2 Notions of wake

In the disturbed flow of the wind blowing onto the cable one distinguishes several zones (Figure 1-13). The wake is the largest zone, consisting of succession of eddies, elongated downstream. There are different states of wake as function of the Reynolds number:

$$Re = \frac{VD}{\mu} \quad (1.14)$$

where D is cylinder's diameter, m ; V the wind velocity, m/s , and μ the cinematic viscosity, m^2/s ($\mu_{AIR} = 1.5 \cdot 10^{-5} m^2/s$).

The wake starts forming from $Re \approx 40$ as the *free shear layers* between accelerated flow (2) and retarded flow (1) start rolling up into alternating vortices. Their pattern known as Von Kármán (or Kármán-Bénard) trail exists only at very low Re (up to 100...140). Further Re rises, the flow fluctuations disturb the wake stronger, making it turbulent. At $Re \approx 200$ turbulence involves the *far wake* at 40...50 cylinder diameters, and at $Re \approx 300...400$ the *near-wake* becomes also turbulent.

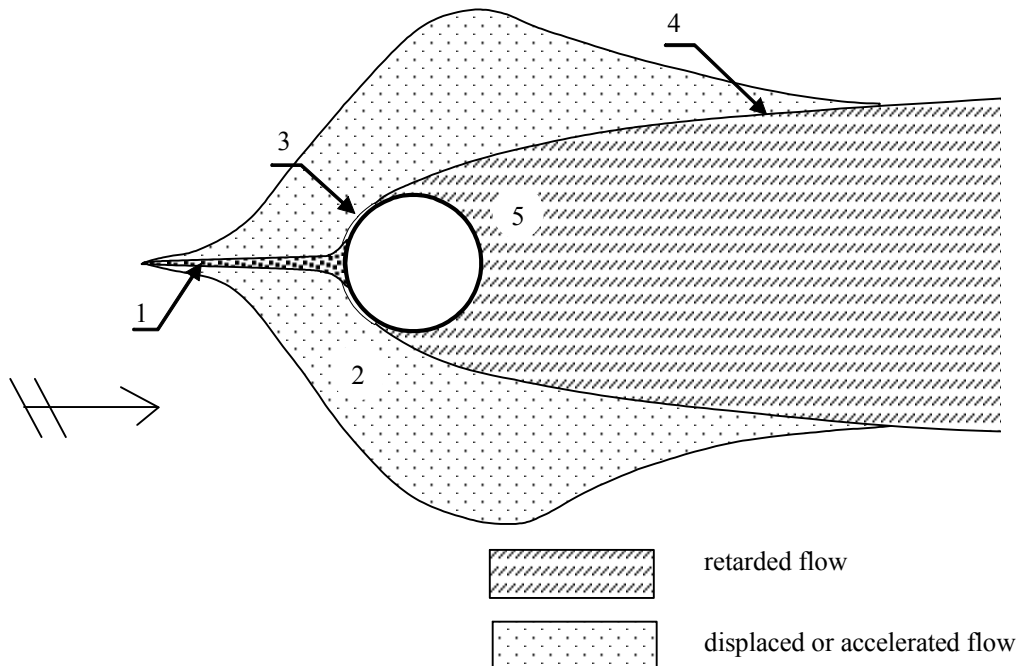


Figure 1-13. Regions of disturbed flow around cylinder (Zdravkovich, 1997): (1) Narrow region of retarded flow; (2) Displaced and accelerated flow; (3) Boundary layer near the surface of cylinder; (4) Free shear layer separating the accelerated flow and the wake; (5) Wake

The state of the flow corresponding to low and normal wind velocities is denoted, after Zdravkovich, TrSL for “Transition in the Shear Layer”. At this state, eddies result from rolling up of a

shear-layer across the near-wake. When one growing eddy is strong enough to draw the other shear layer across the wake, the subsequent eddy is cut-off from a further supply of circulation. Hence the latter being shed from the cylinder at this stage, giving rise to a trail of alternate turbulent eddies [93].

Above classification treats the flow mostly from the standpoint of layers' transitions into different states upon the Reynolds number change. But, as soon as we consider the vibrations of conductor as an elastic cylinder, another classification, referred for instance by Brika and Laneville [38], is worth to be noticed. This classification treats different states of vortices forming the wake. Without going into depth of this subject worth of separate study, note here, that depending on the conductor frequency synchronization with the vortex detachment frequency, two general shapes of vortices are distinguished: 2S (no synchronization) and 2P (frequencies synchronized, lock-in occurs; general condition for the aeolian vibration). Actually, there is a broad variety of vortex patterns, which are also dependent on whether conductor is windward or leeward, and there is a large amount of studies done on this subject by Williamson, Roshko, Laneville, Brika and other researchers.

In what follows, we remain within the averaged wake consideration (no split into separate vortices), staying within classification described by Zdravkovich.

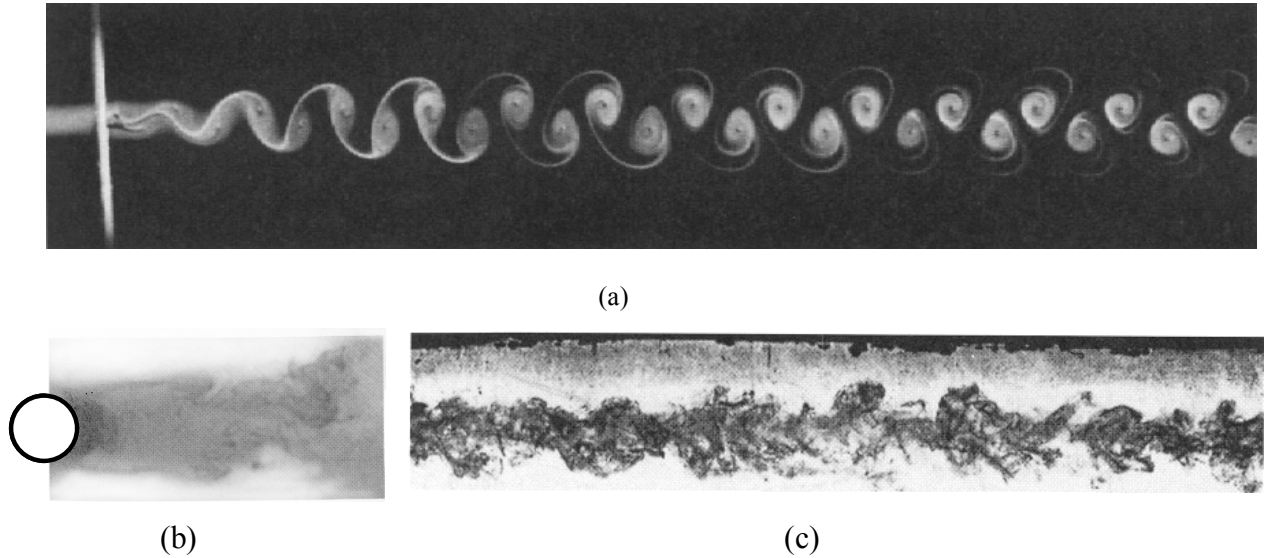


Figure 1-14 (a) Wake at $Re = 100$. Near-wake (b) and far-wake (c) at TrSL state [93]

So, in terms of TrSL state, the wake is the characteristic one to stranded electrical conductors at wind velocities $U \sim 0.1$ m/s to $\sim 15 - 20$ m/s.

Regarding the forces in the wake, we distinguish the high-frequency components of drag and lift, and quasi-stationary forces. The former ones are bound by the Strouhal number,

$$St = \frac{f_s D}{U}, \quad (1.15)$$

where f_s is the frequency of periodic vortex shedding from a structure (cylinder) of diameter D in a steady flow of velocity U . The latter ones are time-averaged and we pay to them most of

attention, since for wake-induced oscillation of bundle conductors the quasi-steady hypothesis applies (see Section 2.1.1).

Quasi-stationary, or static force field in the wake has boundaries depicted in Figure 1-15.

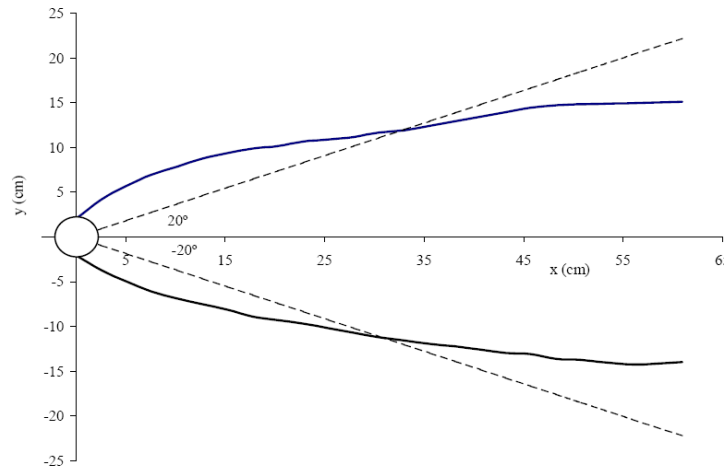


Figure 1-15. Wake boundaries (wind tunnel test data)

As mentioned above, further Re grows, the flow transitions to the turbulent state closer to the cylinder. Next to the free-shear layer, it is a boundary layer, circumscribing the surface of cylinder that is set to turbulent state. Simultaneously, the boundary layer becomes more ‘sticky’, so that the point of detachment into free shear layer moves behind along the surface of cylinder. The wake is getting narrower and the drag coefficient falling sharply. The resulting drag force stagnates in a region of drag coefficient fall; it is a phenomenon of drag crisis.

For the smooth cylinder this state, known as “transition into turbulence in boundary layer” (TrBL), occurs at $Re \sim 2 \times 10^5$. Any surface roughness of cylinder reduces the critical level of Re . Conventional stranded conductors like ACSR Aster (diameter 30.5 mm) have transition state at $U \sim 15$ m/s and smooth conductors with their flattened surface of outer strands (like Compact or with Z-shaped strands – see [43] for the latter) have critical Re value in-between the purely smooth cylinder and stranded conductors.

Prior to the drag crisis, there is short “single-bubble” state associated with random appearance of bubble on the upper or lower surface of the cylinder and accompanied with sharp and short appearance of positive or negative lift. This growth exists in a very narrow range of Reynolds number and disappears in TrBL state.

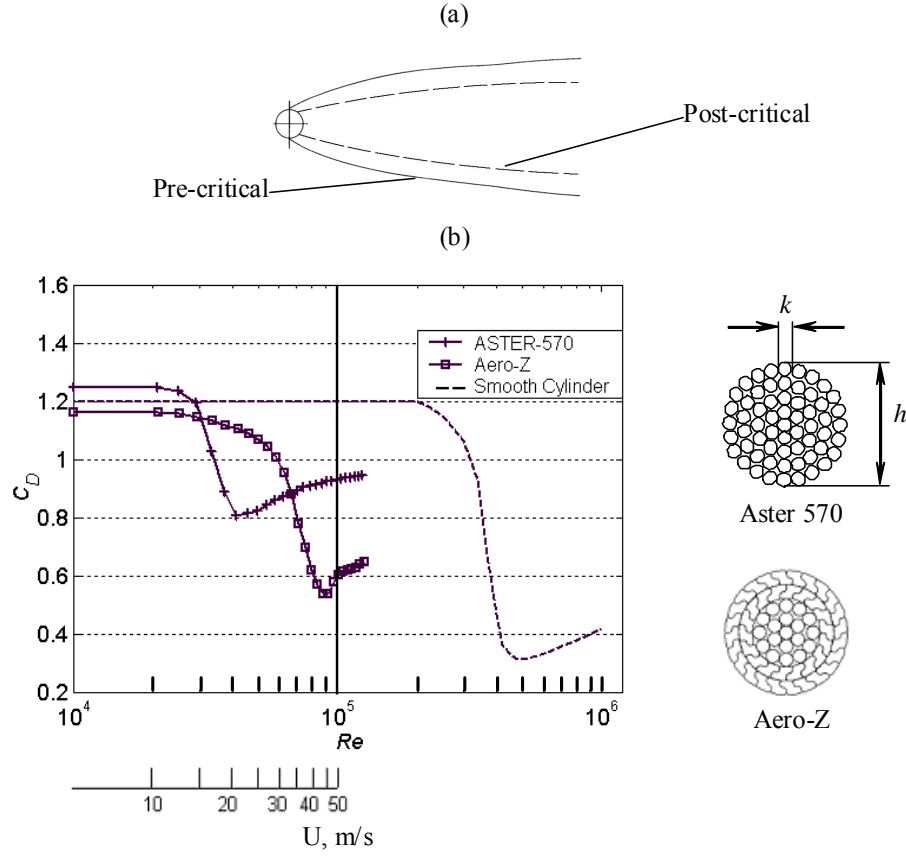


Figure 1-16. Drag crisis. (a) Narrowing of the wake in post-critical state. (b) Variation of drag coefficient for disturbance-free flow, influenced by surface roughness of cable, on single cylinder [Courtesy Nexans-Benelux].

1.4.2.1 Local velocity in the wake

As it is mentioned in Section 1.4.2, in the wake the mean velocity is retarded with respect to the free stream (see Figure 1-13). This reduction in the far-wake can be approximately described by an empirical function [3]. If we denote dimensionless horizontal and vertical spacing correspondingly

$\xi = \frac{Y}{D}$, $\eta = \frac{Z}{D}$, and the free-stream drag coefficient C_{DMax} (for a smooth cylinder $C_{DMax} \cong 1.2$),

then the ratio between the free-stream velocity, V , and the local velocity in the wake, $V_l(\xi, \eta)$ reads

$$b(\xi, \eta) = \frac{V_l(\xi, \eta)}{V} = 1 - C_{DMax} \cdot \sqrt{\frac{C_{DMax}}{(\xi + 6.0)}} \exp(-0.69 \cdot (\eta / B)^2); \quad (1.16)$$

where

$$B = 0.23 \sqrt{C_{DMax} \cdot (\xi + 6.0)};$$

Selective profiles of the flow velocity retardation in the wake are shown in the Figure 1-17.

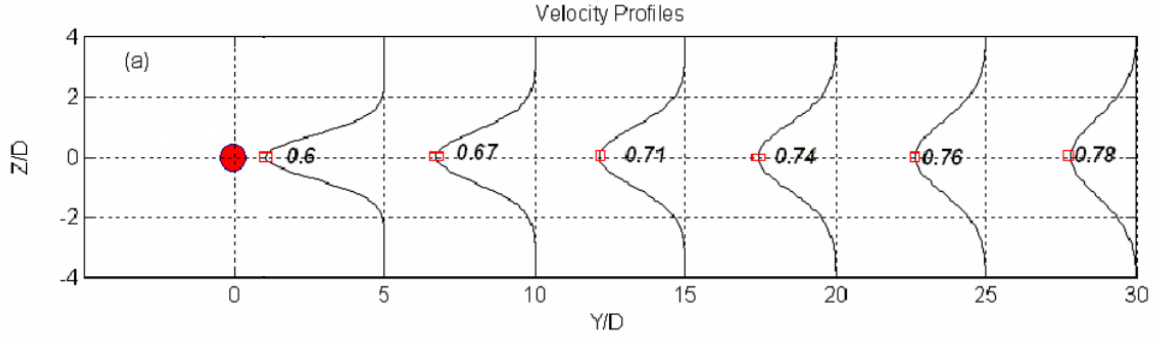


Figure 1-17. Selective profiles of velocity deficit $b(\xi, \eta)$ along the wake direction. Abscissa: horizontal dimensionless spacing (in cylinder diameters), ordinate: vertical dimensionless spacing.

Another representation of local wind velocity profile via the mean drag coefficient is suggested by Diana [16]:

$$b(y, z) = \frac{C_D(y, z)}{C_{DMax}} \quad (1.17)$$

Here, $C_D(y, z)$ is the drag coefficient of leeward cylinder. It gives a qualitatively close distribution.

In Section 2.2 we will see, that account of local velocity is needed for appropriate notation of lift and drag forces acting on the leeward cylinder.

1.4.2.2 Loads on the leeward cylinder in the wake

Now consider the downstream cylinder submerged in the wake of the same upstream cylinder. The time-averaged flow in the wake is directed towards the wake centreline. Effect of the flow retardation on the aerodynamics of the downstream cylinder may be compared to the one created by the airplane wing. The wing is specially profiled in order to form the retarded flow on its upper surface in order to create the lift force in the incident flow. In the wake, the flow distribution is such that the cylinder, originally neutral, is exposed to unevenly retarded flow. As result, the downstream cylinder obtains the reduced drag and nonzero lift, the latter being oriented towards the centreline of the wake.

A draft image of lift and drag distributions in the wake is presented in Figure 1-18. The drag coefficient reflects the velocity retardation profile as shown in Figure 1-17. The image of lift coefficient corresponds to the derivative of drag coefficient by vertical coordinate, $C_{Dz}(y, z)$.

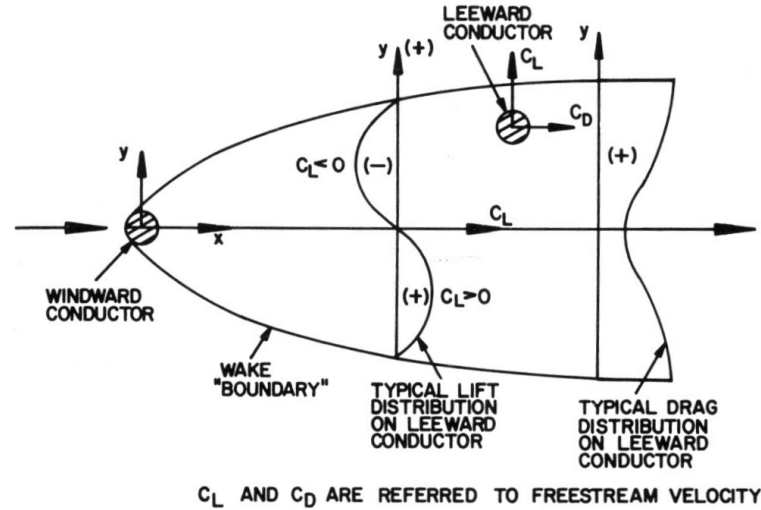


Figure 1-18. Aerodynamic forces on leeward conductor [19]

Collection of aerodynamic coefficients on the leeward cylinders is presented in Annex A. Simpson [70], Price [56], Wardlaw et al. [88], Diana [15], [16] and others contributed to the measures of loads imparted on smooth cylinders, smooth and stranded conductors in the wake.

Until nowadays wind-tunnel tests are the only credible source of information about wake-induced loads. An attempt of numerically obtaining the wake-induced lift and drag coefficients was done at the beginning of this work (see Annex B). An industrial CFD tool [21] was tested on a pair of smooth cylinders subject to the flow at Re 20k. Analysis has demonstrated, that such computation allows for obtaining the results approaching to the experimental data up to certain degree. Above conclusion, after some investigations, may be attributed not only to some specific CFD package, but it may be extended to the most of “industrial” CFD tools. It is known after many cases discussed, that achieving some resemblance of CFD result to the reality is mostly brought via tuning up of a lot of purely mathematical parameters with as much conditions out of real sense that such analysis becomes far away from relationship to its practical application. Certainly, modern CFD packages allow for estimation of quite complex structures and high velocity flows, providing credible results. But, as it happens often in numerical sciences, a simply shaped problem (like a cylinder in the non-viscous flow) reveals to be a nice benchmarking task.

An exemplary distribution of lift and drag coefficients, obtained from wind-tunnel test by Price [56] for a smooth cylinder is given in Figure 1-19. Notice that, as the separation between cylinders rises, the enlargement of the wake transmits into profiles of the aerodynamic coefficients.

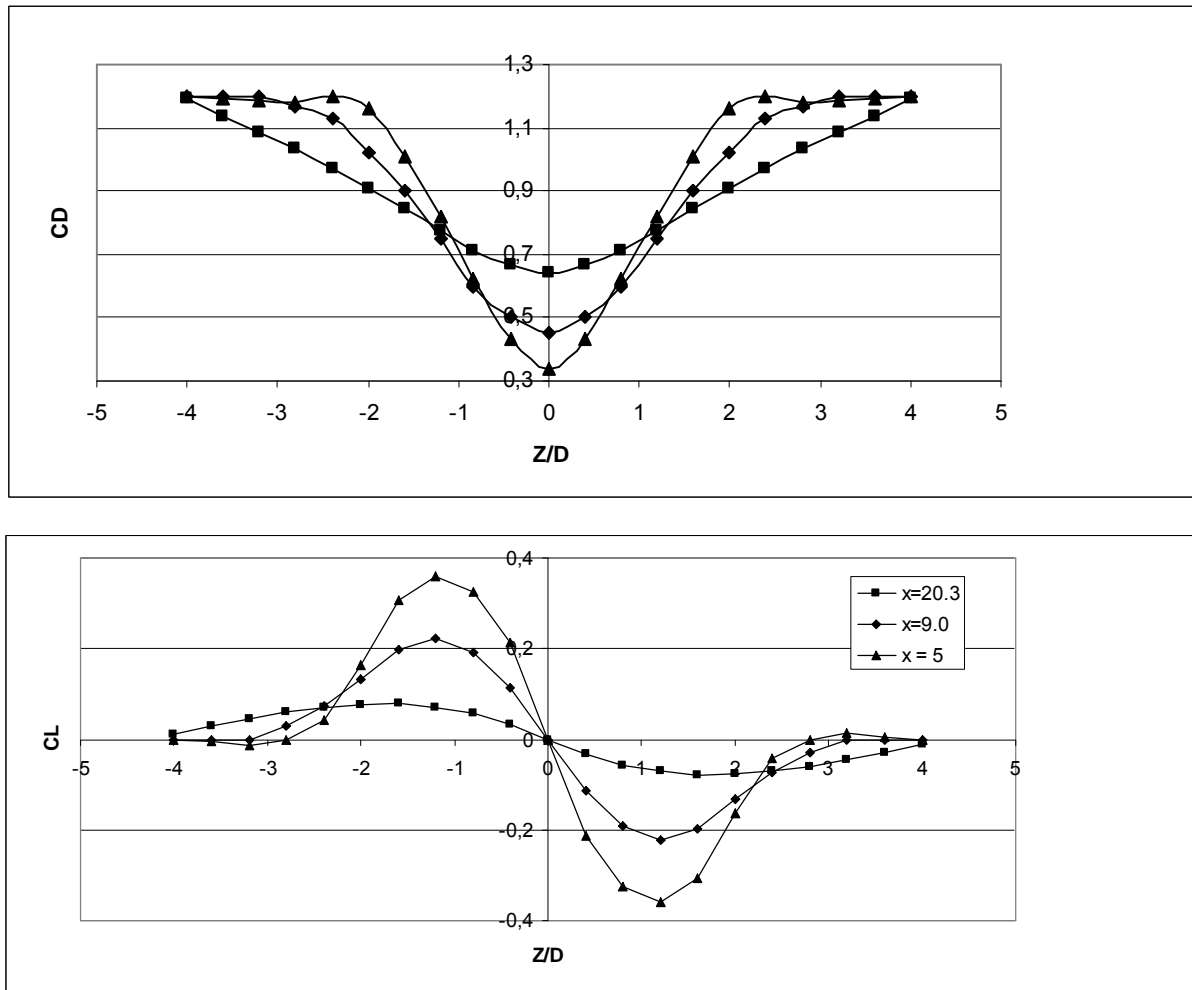


Figure 1-19. Force coefficients for a smooth circular cylinder with a free stream
 $Re = 3.58 \times 10^4$ and turbulence intensity 1.5 %. Markers denote cylinders' spacing, y/d : $\circ - 5.0$, $\bullet - 9.0$,
 $\Delta - 20.3$. Data after [Price, 1975]

The wake narrowing in critical state (drag crisis) is obviously transferred into the loads on the leeward cylinder (e.g., compare in Figure A - 3, the pre-critical curves for stranded conductor, Re 26k and post-critical for Re 54k).

Since during oscillations the subconductors may approach up to clashing, consider the near-wake (within $0 \leq |Y/D| < 5$). At such distance, the time-averaged coefficients acting on the leeward cylinder vary strongly across-wake. At distances less than $Y/D = 3$ the drag coefficient takes negative values (see Annex C).

As the leeward cylinder is at distance less than $1.5D$, the windward cylinder's lift and drag coefficients are also affected [92], [58], see Figure A - 6.

1.5 Overview of wake-induced oscillation

The four principal types of wake-induced motion are illustrated in Figure 1-20. Three of these types, B, C and D, are termed "rigid-body modes" since little distortion of the bundle cross-section

occurs. They are similar to the fluttering motions of the ribbon. In each of these modes generally one of three degrees of freedom (vertical, horizontal or rotational) is dominant, however, other two are present.

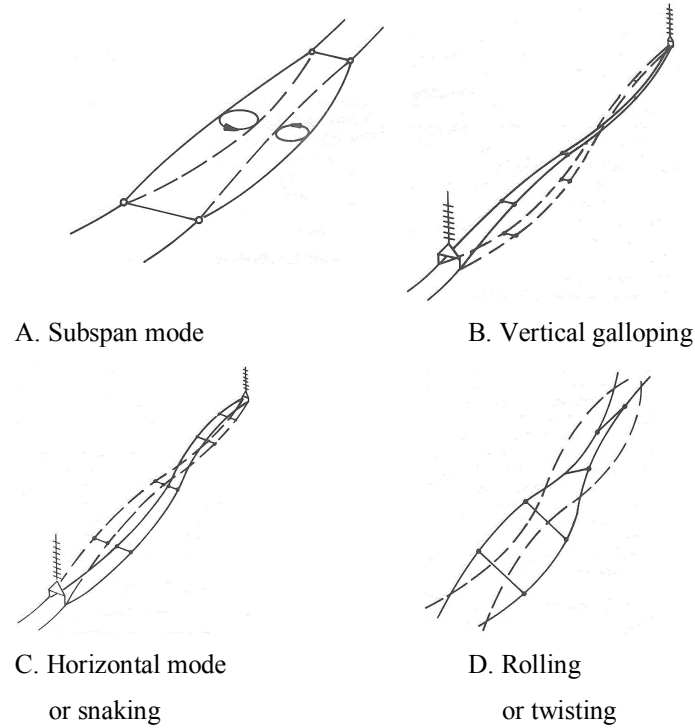


Figure 1-20. Classification of wake-induced motions [EPRI, 1979]

The subspan mode (Figure 1-20, A) takes the form of one or several loops between spacers in a span, with nodes at or near the spacers³. The trajectories of individual subconductors are elliptical, and windward-leeward pairs of subconductors often move approximately in phase opposition. Motions in adjacent subspan are usually synchronized but are not necessarily in phase or exactly out-of phase. The one-loop-per-subspan form is the most common. More than two loops per subspan are rarely observed, except when the conductors are wet.

Detailed analysis of wake-induced oscillations over a whole span reveals that several modes participate in the motion at the same time [19].

1.5.1 Conditions of occurrence[19], [20]

A number of conditions must be satisfied simultaneously in order the wake-induced oscillations may appear. The tilt of bundle with respect to the wind must be right, the subconductor separation expressed as a/d , the ratio of spacing a to the diameter d must not be too large, the spacing system

³ Note, that in case of spacer dampers, the nodes of certain modes are displaced from the spacer attachment points. Pure stable subspan mode is mostly encountered in the span with uniform placement of rigid spacers.

and support arrangements must be amenable, and the wind must be of sufficient smoothness. The latter appears to be particularly restrictive.

1.5.1.1 Wind

Wake-induced oscillations occur in moderate to strong winds, usually in the range of 7 to 18 m/s. The observations over different terrains show that most severe oscillations occur under smooth winds, i.e. blowing over flat terrain. Earlier observations showed that wind direction should be close to 90 degrees (perpendicular to the line) [19]. However, later studies indicate that maximum instability corresponds to the yaw angle 20...30° [20]⁴.

1.5.1.2 Sag/Tension

It is considered that the lower tension (greater sag) of conductors favours the incidence of wake-induced oscillations. The sag being greater, so does the ratio between the in-plane and out-of-plane eigenfrequencies of cable subspan.

More details on OHL conductor installation rules are presented in [24]. For a single span, the typical installation parameter is defined as 4 x span length at 45 C. When expressed in conductor's mass per kilometre, M (kg/m) and span length L (m), it allows calculating the initial tension T_0 (N) as follows:

$$T_0 = 4L \frac{M g}{1000} \quad (1.18)$$

The corresponding sag for the single span with zero inclination may be calculated on basis of (1.1). For mid-span point ($x = 0.5l$) it reads

$$w(0.5l) = \frac{mgl^2}{8T} \quad (1.19)$$

This results in the following sag/tension dependency (see Figure 1-21):

⁴ Noteworthy is that aeolian vibration intensity and character also depends on the yaw angle, and actually on the wind alignment vs. stranding of the conductor. Maximum aeolian vibrations are observed as the wind blows along the strands[45]

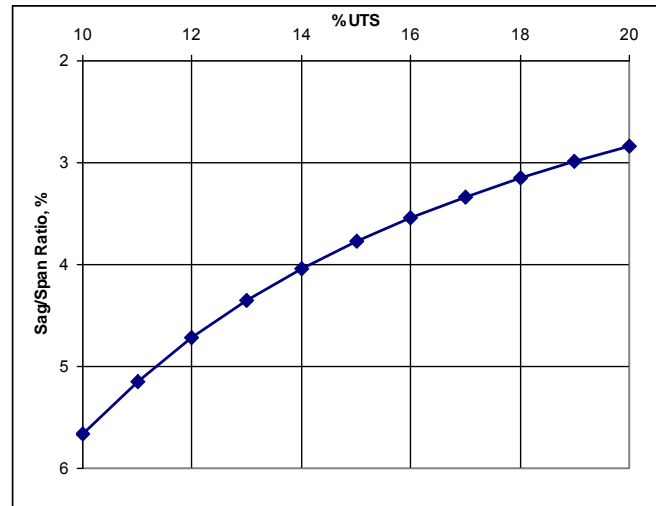


Figure 1-21. Sag to tension ratio for the 525 span, conductor ASTER 570

With increased current transmission via OHL, under high solar radiation, the conductor elongates leading to undertension and increase of sag. Consequently, the relationship between sag and tension drops, leading to increase of separation between the higher in-plane and out-of-plane eigenmodes, which approach to the subspan eigenmodes. More exact relationship of eigenvalues for the subspans is, however, not obtainable by means of linear theory described in Section 1.3.1, especially when uneven subspan scheme is considered. The approaches to calculation of subspan eigenmodes can be found in [11], [18].

This separation is less affected, however, when we consider the subspans, due to relatively short length. The shorter subspans are, less they are subject to the seasonal or transmission effects. A simple estimate of such dependency is presented in Figure 1-22. Here, the subspan is considered a “short span” with in-plane eigenfrequency calculated after (1.5) and out-of-plane frequency after (1.3).

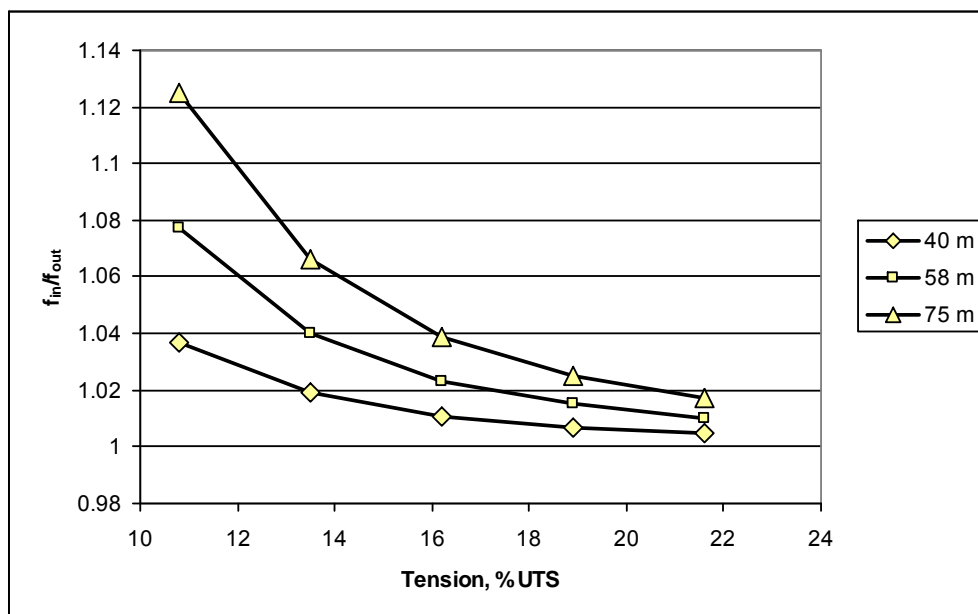


Figure 1-22. Influence of subspan length on relationship between in-plane/out-of-plane eigenfrequencies

1.5.1.3 Conductors' condition

Although the wake-induced oscillations may occur with ice on the conductors, or when there is rain, the motions are most often observed when the conductors are bare and dry.

1.5.1.4 Tilt

In horizontal arrangement of the bundle, the leeward conductor is found in tandem behind the windward conductor, and is not susceptible to the wake-induced oscillation. The situation changes when the bundle is tilted due to factors described in Section 1.2.2. One distinguishes positive and negative tilt, depending on location of leeward conductor in the upper or lower half of the wake correspondingly. Most observations of wake-induced oscillations in twin and quad bundles corresponded to the positive tilt. In triple bundles the wake-induced oscillations are mostly observed at negative tilts.

There is no explanation found to justify why such difference occurs between twin/quad and triple bundles' behaviour (see, for example, [20] Section 5.2.2.2.4). In wind-tunnel tests for suspended twin cylinders at properties, similar to conductor bundles, the oscillations were observed at negative tilts, which have been supported by Simpson's theory [70] and his successors [56], [79]. A linear model which predicts twin bundle instability at positive tilt has been developed by Rawlins [60], the summary of his theory is presented in Annex D. Another explanation, originally following from Simpson's theory, is suggested by Price, explaining it with the fact that out-of-plane subspan frequency may be greater than in-plane frequency (case of excessive tension).

This work is mainly based upon Simpson's theory which provides necessary conditions for the wake-induced interaction at the level of cable finite elements. The discussion regarding the conditions for bundle oscillation at positive tilt is presented in Section 2.2.7.

1.5.2 Damages due to wake-induced oscillations

Damages from the wake-induced oscillations include:

- failures of insulator strings

In the suspension span

- wear of the suspension hardware, particularly of links supporting the clamps
- wear of the subconductors. Two kinds of wear are observed. In the middle of subspan outer strands are affected by subconductor clashing in the subspan mode.
- fatigue of spacers and spacer dampers leading to clamp loosening

Time required for severe damage to develop is assessed about 1 month to 8 years or more. Wake-induced phenomena are not as dramatic as galloping [36], however, when uncontrolled they also contribute into reduction of OHL service life.

In the following chapter, effect of main structural parameters is discussed in the context of modelling the wake-induced interaction, namely, with application of the flutter theory.

2 Model of wake-induced oscillation

2.1 Introduction

In this chapter we talk mainly about flutter model of wake-induced oscillations. According to Rawlins, in real OHL the flutter occurs only in particular spans and this is only one kind among several wake-induced phenomena in electrical conductors. Nevertheless, the model has been largely investigated.

Its basis was founded by Simpson [70] who considered a pair of cylinders on elastic suspensions. Further the properties of flutter model were investigated by Price [56] who introduced some updates and studied a difference between damped and undamped flutter theory. Among other works Tsui [79] can be mentioned who made a detailed case study.

A summary of wake-induced flutter studies was done by Chen in his large review of flow-induced oscillations of groups of cylinders [7].

Above models were realized upon linear approach. Nonlinear models were also developed for pair of cylinders. Diana and Gasparetto [14] suggested the method for predicting amplitudes of wake-induced oscillation based on the balance of energy introduced to the oscillating cylinder on the ascending part of elliptical path, and energy removed on the descending part of path. Price and Maciel [57] presented a solution for limit cycle by Krylov and Bogoljubov method of averaging, showing that nonlinear flutter boundaries are more extended with respect to the linearized approach. Kern and Maitz [35] presented a method for calculating the limit cycle using multiple time scales, however, obtained very low amplitudes that are far from developed nonlinear oscillations.

2.1.1 Application of quasi-steady hypothesis

Wake-induced oscillations are traditionally considered within quasi-steady theory [70], [9], which in particular allows the use of time-averaged aerodynamic data. The assessment relies upon the estimate of reduced frequency of oscillations, $f_R = \frac{f d}{V}$, which should be sufficiently small. Indeed, in case of electrical conductors, as seen in Figure 2-1, the highest f_r is almost of the order smaller than the Strouhal number.

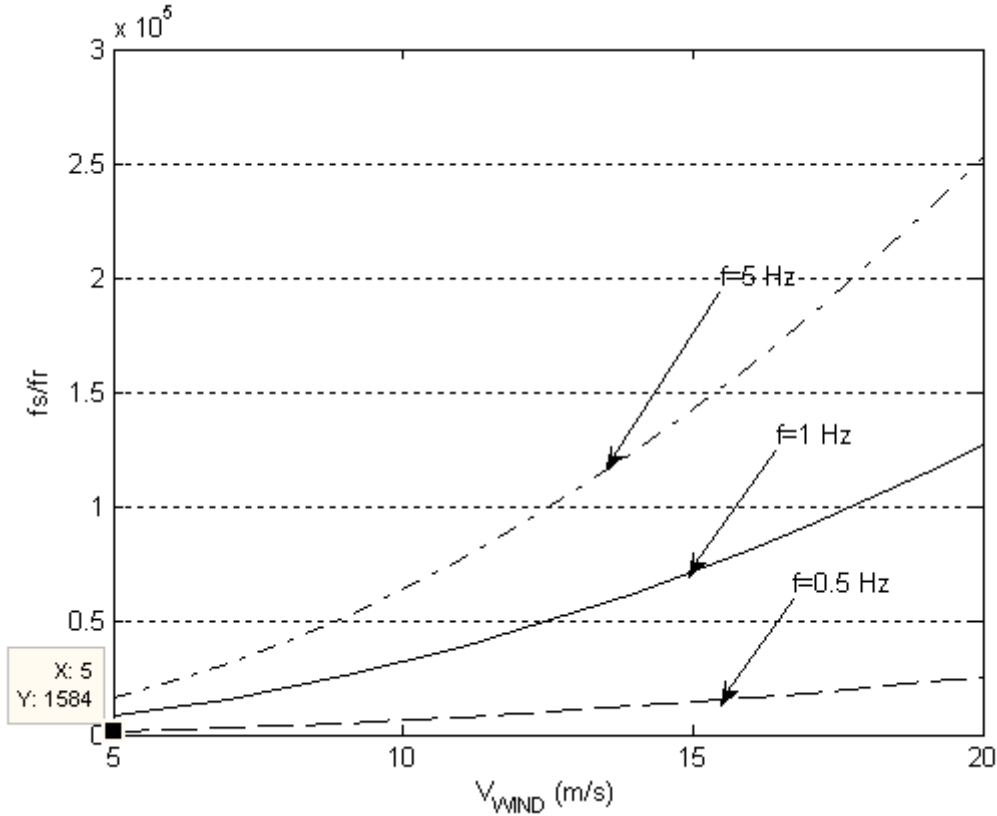


Figure 2-1. Ratio of Strouhal frequency vs. reduced frequency within the range of winds causing wake-induced oscillations.

There is another estimate for applicability of the quasi-steady theory [67]: nonstationary effect of the flow can be neglected if the time needed for the flow particle to run some characteristic length (e.g., separation between subconductors b) is considerably less than the quarter of the subconductor oscillation period, T (inverse the subspan oscillation frequency, f_s). Overall condition reads,

$$\frac{b}{V} \gg \frac{T}{4} = \frac{1}{4f_s}, \text{ or } U_r \gg 4 \quad \left(U_r = \frac{V_l}{b \cdot f_s} \right)$$

Here, b is subconductor separation, V flow velocity, T - subconductor oscillation period, V_l local fluid velocity.

The advantage of this estimate is that it establishes direct relationship between the fluid nonstationary effects like the time delay for the flow particles to travel from the windward to the leeward conductor, and the structural response.

If we take the characteristic incident wind velocity, $V = 7...18$ m/s, and approximate the corresponding local velocity in the wake $V_l = 0.7V$, subconductor separation $b = 0.4m$, and

investigate the full range of wake-induced oscillation frequencies, 0.15 to 10 Hz, then the reduced velocity levels are as shown in Figure 2-2 below.

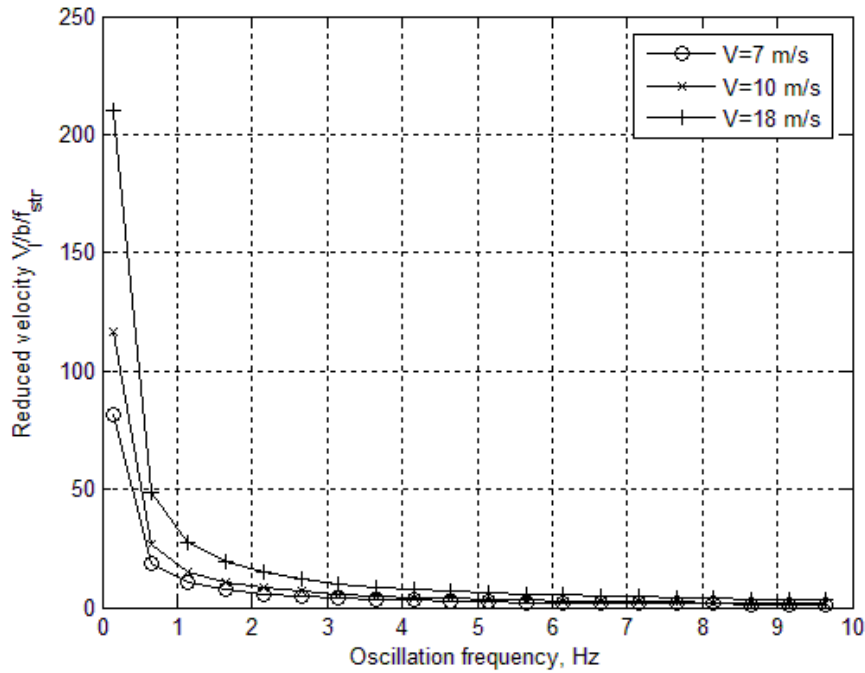


Figure 2-2. On verification of condition $V_R \gg 4$ (Levels of reduced velocity for three different incident wind velocities, V)

The immediate conclusion from above distribution is that only for lowest oscillation frequencies and higher wind velocities, V , the quasi-steady hypothesis may be applicable. For example, for typical subspan oscillation frequency, 1 Hz, and wind velocity, 10 m/s, the reduced velocity $U_r = 15$: this is at the limit of application of quasi-steady hypothesis.

Another conclusion is that at lower wind velocities, probably, not only quasi-steady effects bring to wake-induced oscillations. Remind that at these velocities, the vortex shedding frequency is of the order of 25 Hz, i.e. only 2.5 times higher than the higher frequency of wake-induced oscillations. We may suppose, that at these frequencies the phenomenon of wake-induced oscillations is coalescent with the vortex-shedding resonant effects which cause aeolian vibrations.

However, we leave the above idea to the future studies, while in this work we still rely upon the quasi-steady hypothesis. The reason is that here we study the low-frequency oscillations, i.e. of the order of 1 Hz. In this range, the traditional quasi-steady hypothesis applies according to both approaches.

2.2 Wake-induced flutter model

In this model the conductors' twin bundle is reduced to a rigidly fixed windward and elastically suspended leeward one. Such reduction is possible basically for two cases: that of telegraph wire, and of nearly equal subspans. The motion of leeward cylinder only is considered, as this is the motion that inhibits the subspan oscillation. The action of windward cylinder is considered only via space-dependent local velocity and lift and drag coefficients.

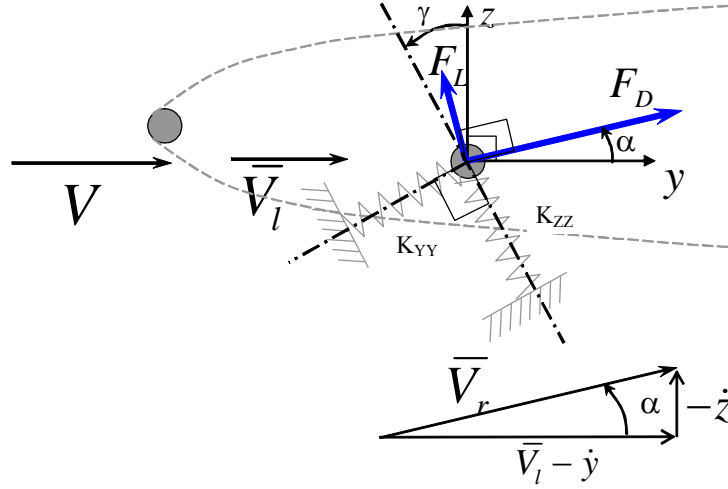


Figure 2-3. Wake-induced action on elastically suspended leeward cylinder

The state of leeward cylinder is described by a system of two equations of motion along two axes y and z :

$$\begin{cases} m\ddot{y} + 2m\zeta_Y\omega_Y\dot{y} + k_{YY}y + k_{YZ}z = F_Y \\ m\ddot{z} + 2m\zeta_Z\omega_Z\dot{z} + k_{ZZ}z + k_{YZ}y = F_Z \end{cases} \quad (2.1)$$

Here,

m [kg/m] mass per unit length of cylinder,

ζ_Y, ζ_Z critical damping ratio,

F_Y and F_Z [N/m] force components which result from the drag and lift forces acting on the leeward cylinder.

k_{YY}, k_{ZZ} and k_{YZ} [N/m] axial and coupled stiffnesses per unit length, N/m, resulting from inclination of the suspension and modelling the blowback of the bundle under the wind (see Section 2.2.3 for more details).

Forces F_Y and F_Z are axial components of the drag and lift forces which read

$$\begin{cases} F_L = \frac{1}{2} \rho V_r^2 d \tilde{C}_L \\ F_D = \frac{1}{2} \rho V_r^2 d \tilde{C}_D \end{cases} \quad (2.2)$$

Here, \tilde{C}_D and \tilde{C}_L are aerodynamic coefficients defined with respect to the local velocity, V_l ; \bar{V}_r is a vector resulting from subtraction of the local wind velocity and the speed of the leeward cylinder (see Figure 2-3).

$$\bar{V}_r = (\bar{V}_l - \dot{y}) + (-\dot{z}) \quad (2.3)$$

Axial components of forces, F_Y and F_Z , relate to the drag and lift forces via relationships

$$\begin{cases} F_Y = F_D \cos \alpha - F_L \sin \alpha \\ F_Z = F_D \sin \alpha + F_L \cos \alpha \end{cases} \quad (2.4)$$

\bar{V}_r is inclined to the axis y with an induced angle of attack, α

$$\begin{aligned} \cos \alpha &= \frac{V_l - \dot{y}}{V_r} \\ \sin \alpha &= \frac{-\dot{z}}{V_r} \end{aligned} \quad (2.5)$$

The aerodynamic coefficients, obtained experimentally, refer to the free-stream velocity, V . To make use of them, introduce the relationship between the « local » and « free-stream » coefficients as

$$\begin{Bmatrix} C_D \\ C_L \end{Bmatrix} = b^2 \cdot \begin{Bmatrix} \tilde{C}_D \\ \tilde{C}_L \end{Bmatrix}, \quad b^2 = \left(\frac{V_l}{V} \right)^2 \quad (2.6)$$

The coefficient b is found from the relationship (1.16).

By substitution of (2.2) - (2.6) into (2.1), we obtain the full equations of leeward cylinder motion,

$$\begin{cases} m\ddot{y} + 2m\zeta_Y\omega_Y\dot{y} + k_{YY}y + k_{YZ}z = qV_r \frac{1}{b^2} (C_D(V_l - \dot{y}) + C_L\dot{z}) \\ m\ddot{z} + 2m\zeta_Z\omega_Z\dot{z} + k_{YZ}y + k_{ZZ}z = qV_r \frac{1}{b^2} (-C_D\dot{z} + C_L(V_l - \dot{y})) \end{cases} \quad (2.7)$$

Here, $q = \frac{1}{2}\rho d$ is the air pressure with ρ air density (1.22 kg/m^3), and d cylinder's diameter.

By solving this system numerically in time domain we can calculate the motion of leeward cylinder in order to obtain the limit cycle. However, this system does not tell anything about stability of leeward cylinder at the given wake location. To analyse this we suppose that leeward cylinder has been driven at the equilibrium position in the wake and consider the small motions around this position. So we linearize the equations of motion by passing from nonlinear lift and drag coefficients to their linear analogs by expanding them in Taylor series:

$$\begin{aligned} C_D(y, z) &= C_D(y_0, z_0) + \frac{\partial C_D}{\partial y}y + \frac{\partial C_D}{\partial z}z + O(y^2, z^2) \\ C_L(y, z) &= C_L(y_0, z_0) + \frac{\partial C_L}{\partial y}y + \frac{\partial C_L}{\partial z}z + O(y^2, z^2) \end{aligned} \quad (2.8)$$

(Here, $C_D(x_0, y_0)$ and $C_L(x_0, y_0)$ are the coefficients in the equilibrium position.)

We define the square norm of the relative fluid velocity V_r , after (2.3)

$$V_r^2 = V_l^2 - 2V_l\dot{y} + O(\dot{z}^2) \quad (2.9)$$

and, since the quantities y and z being small, therefore, the angle α is small as well:
 $\cos\alpha \approx 1$

$$\sin\alpha \approx \alpha = \frac{-\dot{z}}{V_l} + O\left(\frac{\dot{y}\dot{z}}{V}\right) \quad (2.10)$$

Next, we:

- take the basic equations of motion (2.1) and substitute (2.10) into (2.4) (small-order values being omitted hereinafter),
- express force components, F_D and F_L as in (2.2) given (2.6) and (2.9); and substituting the expanded C_D and C_L as in (2.8), and

- introduce the dimensionless coordinates $\tilde{y} = \frac{y}{d}$ and $\tilde{z} = \frac{z}{d}$, passing to dimensionless

derivatives $C_{Dy} = \frac{\partial C_D}{\partial \tilde{y}} \frac{1}{d} = \frac{1}{d} \tilde{C}_{Dy}$, and identically for C_{Dz} , C_{Ly} and C_{Lz} .

We finally obtain, putting beyond the parentheses the common terms,

$$\begin{cases} m\ddot{\tilde{y}} + 2\zeta_y \dot{\tilde{y}} + k_{yy} \tilde{y} + k_{yz} \tilde{z} = \frac{1}{2} \rho V^2 \left(C_D + \tilde{C}_{Dy} \tilde{y} + \tilde{C}_{Dz} \tilde{z} - 2C_D \frac{\dot{\tilde{y}}}{V_l} d + C_L \frac{\dot{\tilde{z}}}{V_l} d \right) \\ m\ddot{\tilde{z}} + 2\zeta_z \dot{\tilde{z}} + k_{zz} \tilde{z} + k_{yz} \tilde{y} = \frac{1}{2} \rho V^2 \left(C_L + \tilde{C}_{Ly} \tilde{y} + \tilde{C}_{Lz} \tilde{z} - 2C_L \frac{\dot{\tilde{y}}}{V_l} d - C_D \frac{\dot{\tilde{z}}}{V_l} d \right) \end{cases}, \quad (2.11)$$

Next we regroup the terms at \tilde{y} , \tilde{z} and their derivatives and obtain the system

$$M_{STR} \ddot{r} + [C_{AER} + C_{STR}] \dot{r} + [K_{AER} + K_{STR}] r = F_{AER} \quad (2.12)$$

Here,

$$r = \begin{bmatrix} \tilde{y} \\ \tilde{z} \end{bmatrix} \quad \text{- column vector of displacement components;}$$

$$M_{STR} = \begin{bmatrix} m & 0 \\ 0 & m \end{bmatrix} \quad \text{- structural mass matrix;}$$

$$K_{STR} = \begin{bmatrix} k_{yy} & k_{yz} \\ k_{yz} & k_{zz} \end{bmatrix} \quad \text{- structural stiffness matrix (remind that suspension stiffnesses, } K_{yy} \text{ and } K_{zz} \text{)}$$

are expressed in terms of axial and coupled components, k_{yy} , k_{zz} and k_{yz});

$$C_{AER} = q \frac{d}{V_l} \begin{bmatrix} 2C_D & -C_L \\ 2C_L & C_D \end{bmatrix} \quad \text{- aerodynamic damping matrix } (q = \frac{\rho V^2}{2});$$

$$C_{STR} = 2 \begin{bmatrix} \zeta & 0 \\ 0 & \zeta \end{bmatrix} \quad \text{structural damping matrix;}$$

$$K_{AER} = -q \begin{bmatrix} \tilde{C}_{Dy} & \tilde{C}_{Dz} \\ \tilde{C}_{Ly} & \tilde{C}_{Lz} \end{bmatrix} \quad \text{- aerodynamic stiffness matrix;}$$

$$F_{AER} = q \begin{bmatrix} C_D \\ C_L \end{bmatrix} \quad \text{column vector of aerodynamic forces at the equilibrium position.}$$

We then study this system by bringing it to homogeneous form and investigating the stability of its complex eigenvalues.

2.2.1 Solving the eigenvalue problem

By analogy with the approach of Bolotin [5], we seek the solution of (2.12) as

$$\tilde{y} = \tilde{y}_0 \exp(\lambda \frac{V}{l} t), \quad \tilde{z} = \tilde{z}_0 \exp(\lambda \frac{V}{l} t), \quad l = \sqrt{y^2 + z^2} \quad (2.13)$$

After substitution of (2.13) into (2.12) and division by m we obtain the following homogeneous linear system

$$\begin{bmatrix} m_{11}\lambda^2 + d_{11}\lambda + k_{11} + b_{11} & m_{12}\lambda^2 + d_{12}\lambda + k_{12} + b_{12} \\ m_{21}\lambda^2 + d_{21}\lambda + k_{21} + b_{21} & m_{22}\lambda^2 + d_{22}\lambda + k_{22} + b_{22} \end{bmatrix} \times \begin{bmatrix} \tilde{x}_0 \\ \tilde{z}_0 \end{bmatrix} = 0, \quad (2.14)$$

Here,

$$\begin{aligned} m_{11} &= m_{22} = 1; & m_{12} &= m_{21} = 0; \\ d_{11} &= 2aC_D + 2\zeta\chi; & d_{12} &= -aC_L; \\ k_{11} &= \chi^2; & k_{12} &= k_{21} = \varphi\chi^2; \\ b_{11} &= -\frac{al}{db}\tilde{C}_{Dx}; & b_{12} &= -\frac{al}{db}\tilde{C}_{Dz}; \\ d_{21} &= 2aC_L; & d_{22} &= aC_D + 2\zeta\varepsilon\chi \\ b_{21} &= -\frac{al}{db}\tilde{C}_{Lx}; & k_{22} &= \varepsilon^2\chi^2 \\ & & b_{22} &= -\frac{al}{db}\tilde{C}_{Lz} \end{aligned}$$

$$a = \frac{1}{2} \frac{\rho dl b}{m} \quad \text{density ratio}$$

$$\chi = \frac{\omega_{yy} d}{V} \quad \text{reduced velocity } (\omega_{yy}^2 = \frac{k_{yy}}{m} \text{ and idem for } \omega_{zz} \text{ and } \omega_{yz})$$

$$\varepsilon = \frac{\omega_{zz}}{\omega_{yy}} \quad \text{frequency ratio}$$

$$\varphi = \left(\frac{\omega_{zy}}{\omega_{yy}} \right)^2 = \left(\frac{\omega_{yz}}{\omega_{yy}} \right)^2 \quad \text{coupling frequency ratio}$$

Equating to zero the determinant on the left side, one obtains the quartic polynomial of λ :

$$a_4 \lambda^4 + a_3 \lambda^3 + a_2 \lambda^2 + a_1 \lambda + a_0 = 0 \quad (2.15)$$

The coefficients $a_i, i = 0 \dots 4$, read

$$\begin{aligned}
 a_4 &= m_{11}m_{22} - m_{12}m_{21} = 1 \\
 a_3 &= m_{11}d_{22} + m_{22}d_{11} - m_{12}d_{21} - m_{21}d_{12} = 3aC_D + 2\zeta(\varepsilon + 1)\chi \\
 a_2 &= m_{11}(k_{22} + b_{22}) + m_{22}(k_{11} + b_{11}) + d_{11}d_{22} - d_{12}d_{21} = \\
 &= (\varepsilon^2 + 4\zeta^2 + 1)\chi^2 + 2aC_D\zeta(2\varepsilon + 1)\chi + 2a^2(C_D^2 + C_L^2) - \frac{al}{db}(\tilde{C}_{Dx} + \tilde{C}_{Lz}) \quad (2.16) \\
 a_1 &= d_{11}(k_{22} + b_{22}) + d_{22}(k_{11} + b_{11}) - d_{12}(k_{21} + b_{21}) - d_{21}(k_{12} + b_{12}) = \\
 &= (4\zeta\varepsilon^2)\chi^3 + aC_D[(2\varepsilon^2 + 1) - \varphi r]\chi^2 - 2\zeta\frac{al}{db}(\tilde{C}_{Dx} + \tilde{C}_{Lz})\chi \\
 &\quad - \frac{a^2l}{db}C_D(2\tilde{C}_{Lz} + \tilde{C}_{Dx}) + \frac{a^2l}{db}C_L(2\tilde{C}_{Dz} - \tilde{C}_{Lx}) \\
 a_0 &= k_{11}k_{22} + b_{11}b_{22} + k_{22}b_{11} + b_{22}k_{11} - k_{12}k_{21} - b_{12}b_{21} - k_{12}b_{21} - b_{21}k_{21} = \\
 &= (\varepsilon^2 - \varphi^4)\chi^4 + \frac{al}{db}[\varphi^2(\tilde{C}_{Dz} + \tilde{C}_{Lx}) - \varepsilon^2\tilde{C}_{Dx} - \tilde{C}_{Lz}]\chi^2 + \left(\frac{al}{db}\right)^2(\tilde{C}_{Dx}\tilde{C}_{Lz} - \tilde{C}_{Dz}\tilde{C}_{Lx})
 \end{aligned}$$

These coefficients are essentially the same as those obtained by Tsui [79] for coupled system, except that in our expressions the terms containing structural damping, ζ , are present.

The roots of (2.15) are two pairs of the complex conjugate numbers, $\lambda = \delta \pm i\omega$, $i = \sqrt{-1}$. The system becomes dynamically unstable if $\text{Re}(\lambda) = \delta > 0$ in one of the roots at least. On the flutter boundary, the damping term vanishes to zero, thus giving $\lambda = \pm i\omega$. By substituting the latter into (2.15) and equating to zero the real and imaginary parts of resulting equation, one obtains the system

$$\begin{cases} a_4\omega^4 - a_2\omega^2 + a_0 = 0 \\ \omega(\omega^2 a_3 - a_1) = 0 \end{cases} \quad (2.17)$$

There are three ways of resolving this system. By substituting the nontrivial solution, $\omega^2 = \frac{a_1}{a_3}$, from the second equation (2.17) into the first one, we obtain third Routh's penultimate test function, T_3 . One may show, that the general condition for instability leads to an inequality:

$$T_3 = a_1a_2a_3 - a_1^2a_4 - a_0a_3^2 \leq 0. \quad (2.18)$$

This is the way the stability was studied by Simpson [70], and later by Tsui [79] and Price [56].

On another hand, we see from the first equation (2.17) that the only condition which could bring to the positive real roots,

$$\omega_{1,2}^2 = a_2 \pm \sqrt{a_2^2 - 4a_4a_0} \geq 0$$

is that radicand being nonnegative. One thus obtains the second Routh's penultimate test function,

$$T_2 = a_2^2 - 4a_4a_0 \geq 0 \quad (2.19)$$

Use of this function is proposed, for instance, by Kern and Maitz [35].

Finally, we can directly investigate the roots of the quadric polynomial (2.15).

All three approaches are possible to apply in different parametric spaces, in sake of those regions where the maximum real part of roots grows to zero.

The polynomial (2.15) was solved in Matlab package.

2.2.2 Aerodynamic data

In study of wake-induced oscillations it is very important to rely upon good aerodynamic data. Among the data available (see Annex A) for smooth cylinder two sources provide coefficients in the large range of spacings: that published by Diana [15] and by Price [56]. For stranded conductor, the EPRI first edition of “Orange Book” [19] provides a semi-empirical fit for Chukar conductor, distinctive by that it is dependent not only on space, but also on Reynolds number.

In our work we used the smooth cylinder data, keeping in mind that the conductor data can be used instead. Use of analytical expressions for C_D and C_L greatly simplifies the way to obtain the derivatives and, in finite-element analysis, it has accelerated the computation. Diana curves provide simple polynomials, however, they cannot be used for stability study since the derivative C_{Lz} tends to zero at $z = 0$ while there should be minimum. So it was of interest to apply other aerodynamic data, e.g., obtained by Price. Advantage of these data is that they snapshot the enlargement of wake along the longitudinal spacing (see Figure A - 8). Furthermore, in certain regions of wake their derivatives meet the condition of dynamic instability established by Simpson,

$$C_{Ly}C_{Dz} < 0 \quad (2.20)$$

The Price’s data have been approximated by polynomial fitting similar to Boeing one used in EPRI “Orange Book” 1st ed. [19]. The fitting was done in Matlab package by following method:

2.2.2.1 Lift coefficient

- First the test data available, $C_L(y, z)$ $y = [5 \ 9 \ 20.3]$, $z = [-4...4]$ were approximated, for each y , by 10th order polynomials providing sufficient correspondence (see Figure 2-4). Full scale by z should be taken to ensure good shape of derivatives $C_{Lz}(z)$. The expressions were obtained,

$$C_L(y_j, z) = \sum_{i=0}^{10} a_{i,j} z^{10-i}, \quad j = 1, 3 \quad (2.21)$$

- Now, for each i (power of z) the coefficients $a_{i,j}$, $j = 1...3$, were approximated along coordinate y by quadratic polynomials:

$$a_{i,j} \Rightarrow a_{i,j}(z) = \sum_{j=1}^2 b_{i,j} y^{(2-j)}, i = 0 \dots 6 \quad (2.22)$$

Example of fitting for higher power coefficient is shown in Figure 2-5. Note that deep sink of quadratic approximation curve does not directly transfer into lift coefficient dependency on y (see Figure 2-6), and reflects only a behaviour of numerical function.

Full expression for an arbitrary point of wake reads,

$$C_L(y, z) = \sum_{i=1,3,\dots}^9 \left(\sum_{j=0}^2 b_{i,j} y^{(2-j)} \right) z^{(10-i)} \quad (2.23)$$

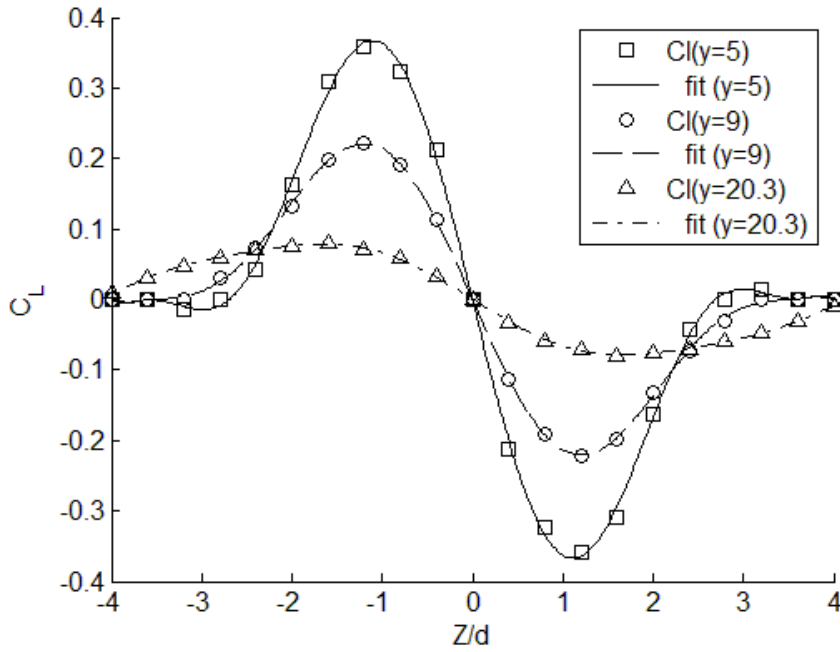


Figure 2-4. Fitting lift coefficient by z coordinate

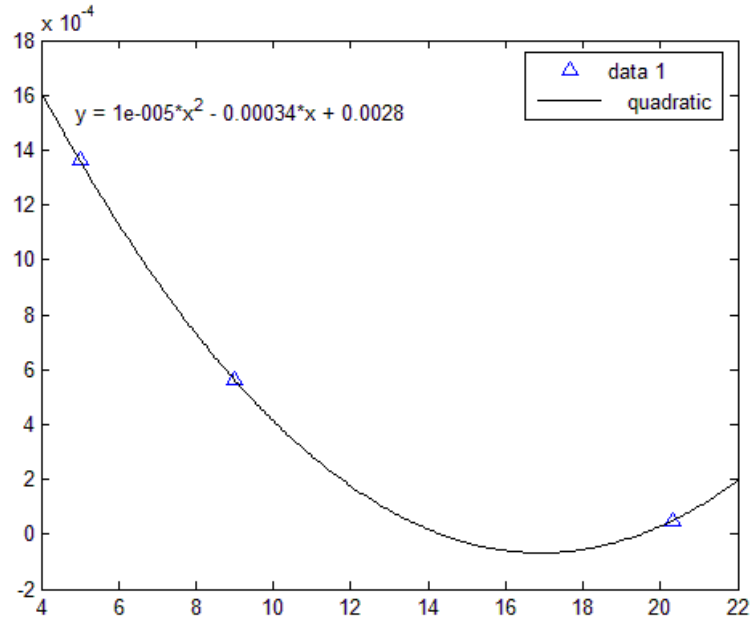
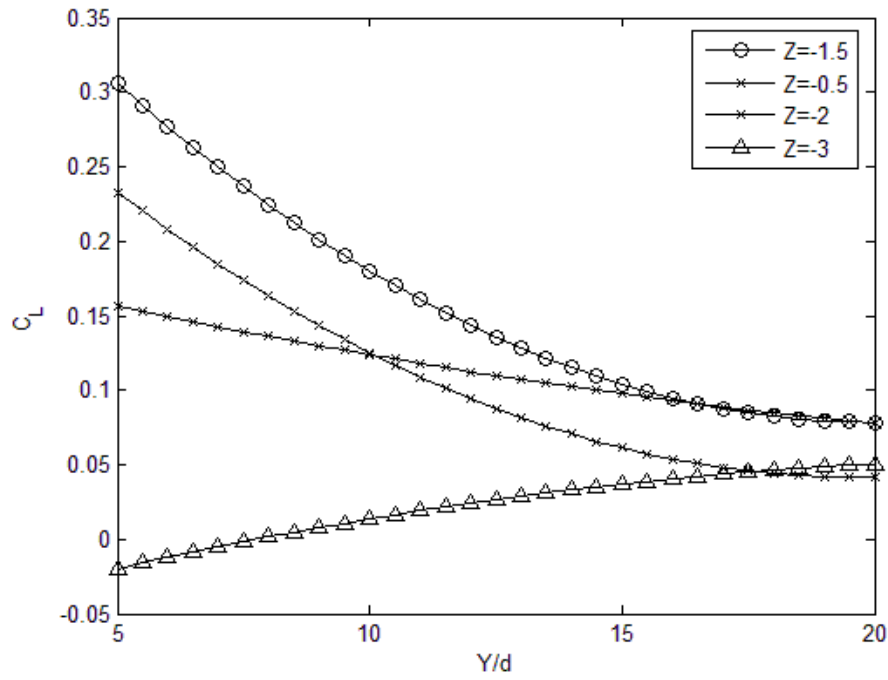


Figure 2-5. Fitting polynomial coefficient by x coordinate


 Figure 2-6. Lift coefficient fitted data as function of Y (all coordinates are dimensionless)

The boundary of data was defined after approach of C_{Lz} to zero levels. It was accounted that at $y=20.3$ the zero level is outside of $z = 4$. The linear boundary was finally defined,

$$O(\tilde{y}, \tilde{z}) = 0.0684\tilde{y} + 3.215$$

It was possible to reduce the number of terms in the polynomial by omitting those of them who are of little order ($e-17 \dots e-20$). Maximum absolute error due to this reduction is $\Delta|C_L| \leq 2 \cdot 10^{-15}$.

Full surfaces of drag and lift coefficient are shown in Annex A, Figure A - 8 - Figure A - 9.

2.2.2.2 Drag coefficient

Approximation of drag coefficient seems to be a more simple process since the data is symmetric. However, test data show that drag derivative $C_{D_z}|_{z=0} = 0$. When approximating one-half of data, e.g. $0 < Z/d < 4$ with lower-order polynomial, the fitting curve has always an inclination to the abscissa (Z axis). For that reason it has been decided to take a full scale of function z/d . In that case, approximation with different order of polynomials shows that 10th order polynomial has the best fitting to the data (see Figure 2-7).

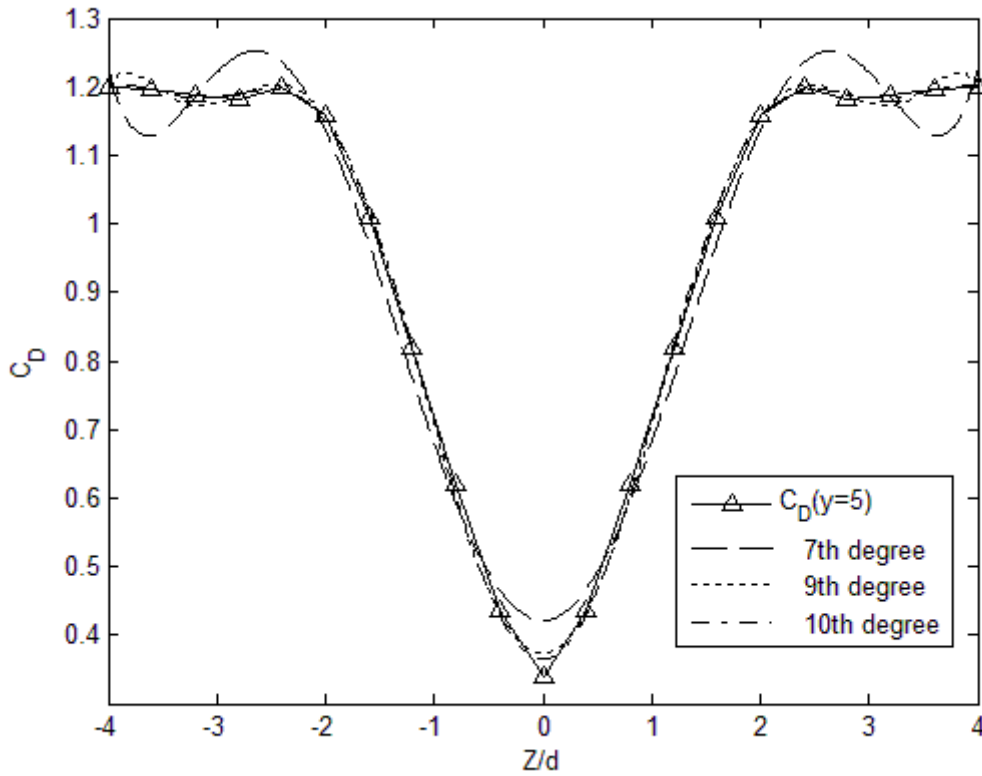


Figure 2-7. Fitting the drag coefficient with different polynomials

Besides a higher order of polynomial, the fitting procedure was the same as for lift coefficient. The expression for fitting polynomial of $C_D(y, z)$, $y = [5 \quad 9 \quad 20]$ reads

$$C_D(y_j, z) = \sum_{i=0}^{10} q_{i,j} z^{10-i}, \quad j = 1, 3 \quad (2.24)$$

Compensatory to the higher order of polynomial, the coefficients $q_{i,j}$ at odd powers of z take the values of the order e-16...e-17 as compared to the other coefficients (e-3...-6) and can be omitted. The maximum error imparted in the absolute values of C_D does not exceed 1.1e-14.

The final expression for C_D reads

$$C_D(y, z) = \sum_{i=0,2,\dots}^{10} \left(\sum_{j=0}^2 p_{2i,j} y^{(2-j)} \right) z^{(10-i)} \quad (2.25)$$

Finally, in the analysis both polynomial and numerical derivatives were used, the latter approximated after test data.

2.2.3 Stiffness properties of suspension

In relationship (2.1) the axial and coupled stiffnesses, k_{YY} , k_{ZZ} and k_{YZ} , are derived from suspension spring stiffnesses, K_Y and K_Z by basis transform [79], accounting for inclination angle, ψ :

$$\begin{bmatrix} k_{YY} & k_{YZ} \\ k_{YZ} & k_{ZZ} \end{bmatrix} = R \begin{bmatrix} K_{YY} & 0 \\ 0 & K_{ZZ} \end{bmatrix} R^T, \quad (2.26)$$

where

$$R = \begin{bmatrix} \cos\psi & -\sin\psi \\ \sin\psi & \cos\psi \end{bmatrix}$$

Positive direction for ψ is counter-clockwise.

2.2.4 Comparison to previous studies

First consider a case referred by Price [56].

Cylinder suspension has following parameters:

Mass per unit length: $m = 2.5$ kg/m (provisory; no information in the article is contained)

Suspension out-of-plane frequency, $f_Y = 4.196$ Hz; in-plane frequency, $f_Z = 4.029$ Hz

Cylinders' diameter $d = 29.4$ mm

Incident flow velocity: $V = 20$ m/s (Re 39.2k)

Suspension inclination: $\psi = 15.5^\circ$ ($g = \tan\psi = 0.2678$)

Structural damping ratio: $\zeta = 0$.

Comparison to the results obtained by Price shows that flutter boundaries obtained by test function T2 (2.19) has very good convergence. The contours of test function T3 (2.18) and global maximal real

part of roots encompass greater horizontal spacings, and are very slightly larger. Both functions include T2 contour.

It shall be noticed, that Price used opposite axes orientation, hence the difference in vertical scale signs.

Another comparison was done for the same model with velocity increased to 25 m/s ($Re\ 48.9k$). As previously, we use the wind tunnel test data for $Re\ 35.8k$. Results are shown in Figure 2-9.

Like in previous case, T2 contours are close to the Price's solution, and T3 and maximum real part of roots are more elongated. General conclusion can be done that despite wind tunnel data for lower Reynolds were used, they are still applicable to higher velocities, as long as critical regime is not achieved.

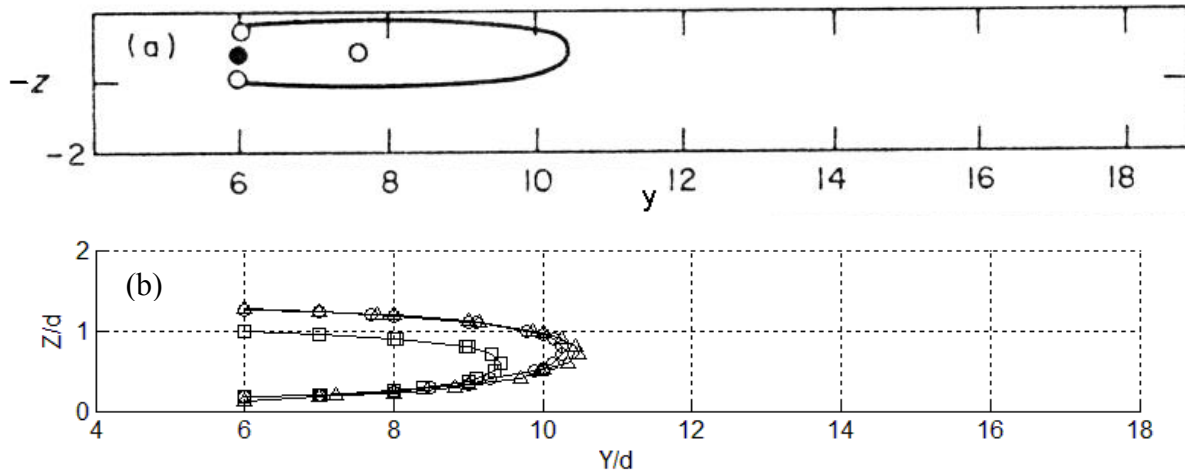


Figure 2-8. Flutter boundaries for a smooth circular cylinder, $V = 20$ m/s, $Re\ 39.2k$ (a) Price results, \circ – experimental, ____-theoretical. (b) Present results – polynomial fit of aerodynamic data and analytical derivatives. Contours obtained by: -□- : second Routh test function, T2; -○-: third Routh test function, T3; -Δ-: maximum real part of polynomial roots.

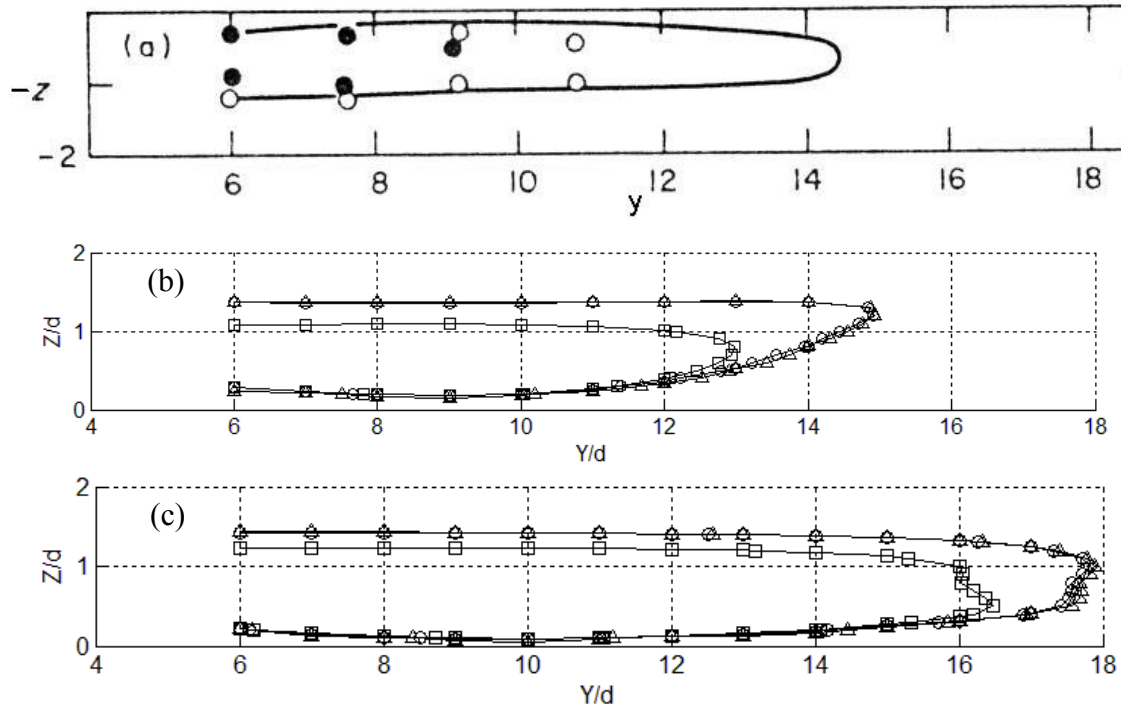


Figure 2-9. Flutter boundaries for a smooth circular cylinder, $V = 25$ m/s, $Re\ 48.9k$ (a) Price results, (b) Present results – polynomial fit of aerodynamic data and analytical derivatives, (c) Present results –. Contours obtained by spline aerodynamic functions and numerically obtained derivatives: \square - : second Routh test function, T2; \circ - : third Routh test function, T3; Δ - : maximum real part of polynomial roots.

The calculations were also done with spline interpolated coefficients and numerically obtained derivatives. Although there was a small difference in their values, the stability boundaries were affected dramatically (see Figure 2-9(c)). Thus, stability study is very sensitive to minor changes in aerodynamic data both affecting aerodynamic stiffness and damping terms in the system of flutter equations (2.12).

2.2.5 Critical flutter velocity

Let us find the critical flutter velocities for a leeward cylinder.

The incipience of critical velocity is well seen on the plot of solution real part versus incident flow velocity Figure 2-10. Two real parts, $\varepsilon_1, \varepsilon_2$ corresponding to four complex conjugate eigenvalues, $\lambda_{1...4} = \varepsilon_{1,2} \pm i\omega_{1,2}$, when solved for increasing incident velocity, provide two branches. If unstable solution exists, one of branches rises to positive values.

This branch initially corresponds to the higher eigenfrequency of in-plane mode. As the solution approaches to instability, the eigenfrequencies become closer in order to coincide. Upon further growth of velocity, the eigenfrequencies remain close to each other, however, they cross-over. This image is similar to the flutter of aircraft wing.

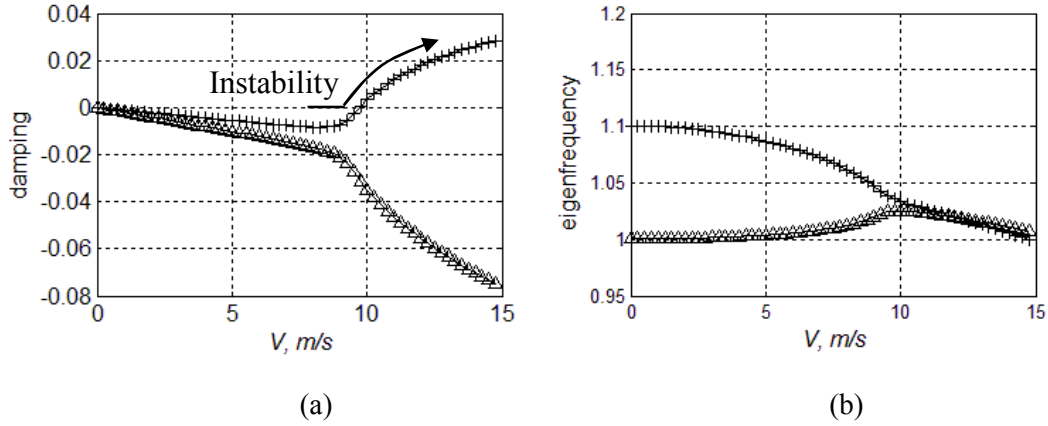


Figure 2-10. Onset of flutter velocity. cylinder diameter: 30 mm, mass 1.6 kg/m, horizontal spacing $y/d = 10$, vertical spacing $z/d = -2.5$, blowback angle $\psi = 15.5^\circ$. -+ -: in-plane mode, -Δ -: out-of-plane mode

It is interesting that in the system with inverse relationship of in-plane and out-of-plane frequencies, the in-plane mode is still the one which brings instability. Such case is shown in Figure 2-11. In this case, where leeward cylinder is located in the upper half-wake, the eigenfrequencies approach, however, they do not fully synchronize. This probably indicates, that although the system is unstable, no steady oscillation would occur.

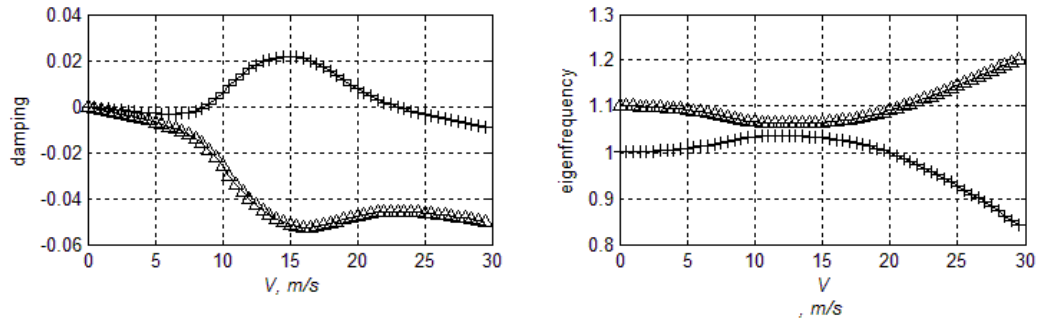


Figure 2-11. Onset of flutter velocity. cylinder diameter: 30 mm, mass 1.6 kg/m, horizontal spacing $y/d = 14$, vertical spacing $z/d = 1.5$, blowback angle $\psi = 15.5^\circ$. -+ -: in-plane mode, -Δ -: out-of-plane mode

Now trace the boundaries of critical velocity versus frequencies relationship. It has been derived analytically by Simpson and later confirmed by Tsui and Price the flutter condition: $f_z/f_y \neq 1$. As seen in Figure 2-12, this condition is met both in case of Price and in present results. However, full solution of system (max. real part of roots) excludes virtually the very point and provides finite critical velocities outside of it. Another point of discussion follows from comparison of solution by test function T2 and general roots of polynomial: the upper boundary is quite larger in the latter case. This fact makes reference to more recent results [57] where very close distribution was obtained by nonlinear solution of system (2.1) (excl. structural damping) by Krylov and Bogoljubov method of averaging. However, this similarity of solutions is rather exceptional. In fact, the function T2 gives more rigorous result from the standpoint of the order of value of solution as here we are looking for zero boundaries obtained analytically. In case of polynomial roots we are tracing the values close to

numerical zeros, and since the order of real part of eigenvalues is small, we risk to be trapped by a numerical error. Hence we may conclude that solution by seeking boundaries from test function T2 provides a more correct image of system stability.

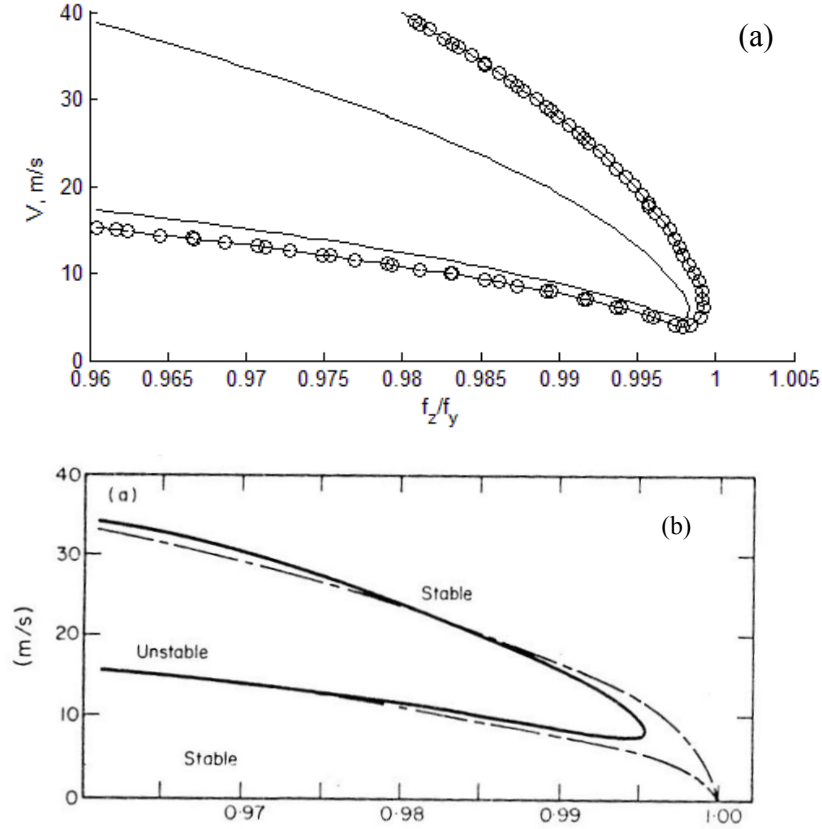


Figure 2-12. Variation of critical velocity with frequency ratio: $y/d = 6$, $z/d = 0.8$; $f_y = 4.196 \rightarrow 4.123$; $f_z = 4.030 \rightarrow 4.123$. Cylinder mass: 2.5 kg/m, blowback 15.5° . (a) Present results: ____ test function T2, -○- - max. real part of roots. (b) results by Price [57] – solid line to compare

2.2.6 Effect of structural damping

After benchmarking upon reference cases let us turn to a more practical case of suspension with the following parameters:

Structural mass: 1.313 kg/m

Cylinder diameter: 24.5 mm

Target spacing: $Y/d = 16.32$ (400 mm)

First let us look at the flutter boundaries variation vs. wind velocity given frequency relationship which virtually guarantees instability: $f_y = 1$ Hz, $f_z = 1.1$ Hz. The blowback angle is variable in order to simulate the effective blowback of the bundle under the wind: $\psi = 0.5V$.

The surface of instability is presented in Figure 2-13. Note, that in this simple 2-DOF analysis the system eigenfrequencies change with respect to the wind velocity. In real conductor spans, the eigenfrequencies will also change upon the wind velocity due to effect of aerodynamic force. This effect is expressed here in terms of aerodynamic stiffness, see (2.12); in the real span the wind velocity increase results in the rise of tension thus stiffening the whole system too.

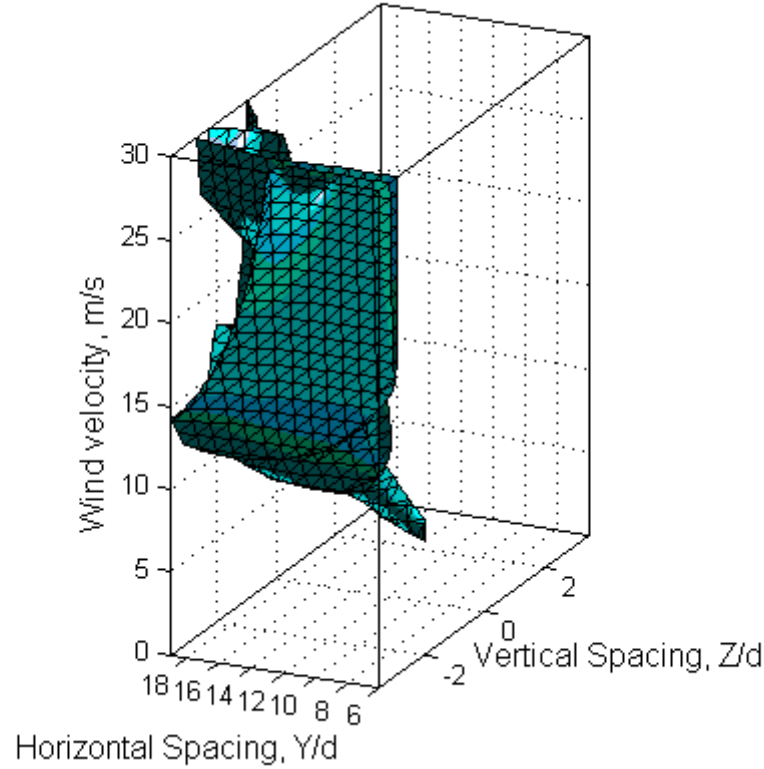


Figure 2-13. Stability boundaries as function of wind velocity. Suspension with the following parameters: Structural mass: 1.313 kg/m; Cylinder diameter: 24.5 mm; Target spacing: $Y/d = 16.32$ (400 mm); Initial frequency relationship $f_y = 1$ Hz, $f_z = 1.1$ Hz; Variable blowback angle: $\psi = 0.5V$.

From this distribution we obtain the most probable vertical spacing for onset of flutter at given horizontal spacing: $Z/d \sim -2.5$.

Having obtained the coordinates of possible flutter, let us turn to definition of critical flutter velocities vs. frequency ratio. The results are shown in Figure 2-14. The conclusion is that only high frequency ratio brings to the flutter, and this is possible for rather high wind velocities.

Now consider the influence of structural damping ζ on the flutter boundaries and critical velocity. The self-damping in the conductors is normally low and it depends on the considered frequency, but also on the tension (dependent, in its turn, on the wind velocity). Within this assessment, we present here the stability boundaries for different values of critical damping.

Up to 0.1% of critical damping the flutter boundary is virtually insensitive to the damping at all. Only the augmentation by an order of value, to 1%, brings some shift to the greater frequency ratios. A considerable effect is possible with the damping 5%, but this level is not practically achievable.

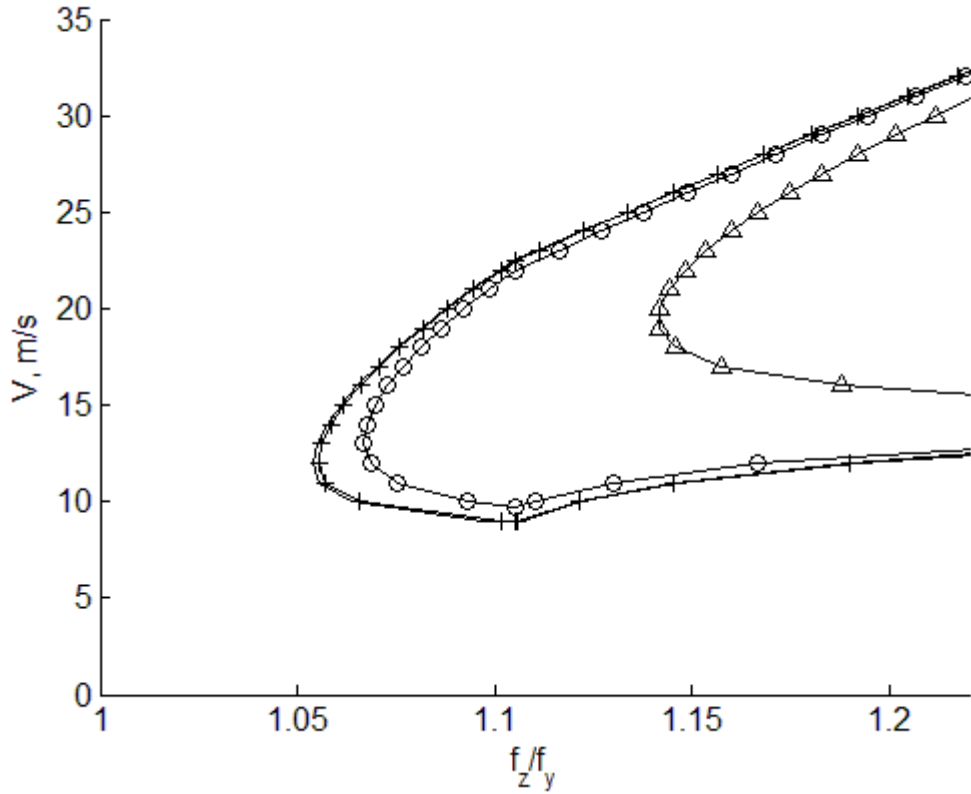


Figure 2-14. Variation of critical velocity with frequency ratio: $y/d = 16.32$, $z/d = -2.5$; $f_y = 0.9 \rightarrow 1$; $f_z = 1.1 \rightarrow 1$; cylinder mass: 1.313 kg/m, diameter 24.5 mm, blowback 10° . — no damping; +- damping 0.1%; -o- damping 1%; -Δ- damping 5%

The above conclusion is confirmed when comparing these results to the surface of flutter boundaries for an unstable cylinder's position and wind velocity. Flutter boundaries are virtually insensible to the damping increase up to the level $\sim 0.1\%$. Starting from this level, some attenuation of boundaries is observed. From $\zeta \sim 1\%$ the flutter region attenuates rapidly.

Normally, the damping is frequency-dependent. Above hypothesis is valid for the damping within the frequency range around 1 Hz. Recall that frequencies of wake-induced oscillation are around 0.15 to 10 Hz (see Section 2.1.1) depending on the oscillation mode, span properties and wind conditions.

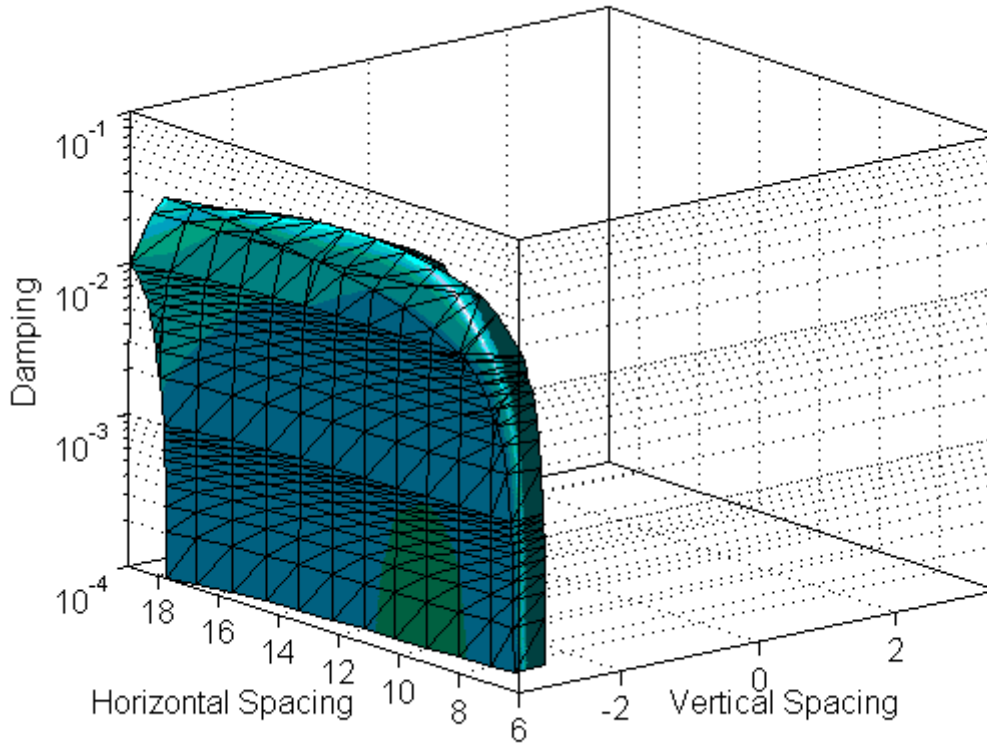


Figure 2-15. Stability boundaries as function of structural damping. Structural mass: 1.313 kg/m; cylinder diameter: 24.5 mm; wind velocity: 15 m/s; blowback angle $\psi = 7.5^\circ$; out-of-plane frequency: $f_y = 1$ Hz, in-plane frequency: $f_z = 1.1$ Hz.

2.2.7 Domain of application of the flutter model

This model permits understanding mechanisms guiding to instability of leeward cylinder. How can it be transmitted to the case of wake-induced oscillation? To clarify this question, we must revert from the model of Figure 2-3 to the practical cases it may correspond.

In [19] two cases are listed, where the flutter model is directly applicable: if there is a span without spacers like in telegraph wires (Figure 2-16 (a)) or a span of nearly equal subspans suspended on the V-strings of insulators (Figure 2-16 (b)). In both cases wake-induced oscillations relate to the leeward conductor only. It may be noticed, however, that in former case the flutter model does not exclude the full subspan oscillations involving the windward subconductor; it treats just the very initial stage of oscillation.

However, as modal analysis of the coupled mode demonstrates, the pure subspan mode may still exist even in case of uneven subspans (see Section 6.2.2). In this case, the eigenfrequencies' pattern, being quite dense, may include (at lower frequencies) the coupled modes where one loop subspan modes co-exists together with a kind of “rigid-body” modes in the adjacent subspan (see Figure 2-17). Thus, in such a case, the flutter theory reveals to be another way for assessment of subspan instability.

3 Finite element model

3.1 Overview of existing models

In the second edition of Orange Book [20] an overview of nonlinear finite element models extends to 1977. In the analysis by Curami et al., the subconductors have been represented with rigid elements. Each subspan included three elements. Simulations have been done for twin and triple bundle.

In a more recent article dated 1986 by Tsui [80], a model of wake interaction is coupled via the external force field with the cable finite elements which initially include up to 16 Degrees-of-Freedom, including bending and torsion. A single element per subconductor per subspan was used in the model. Tsui reported of having obtained the oscillation in subspan mode with a model of span including three 48m subspans. The proof is done by showing synchronized in-plane and out-of-plane modes. Neither amplitudes, nor orbits of oscillations are available.

In 1999, Diana et al. [16] reported of results with a nonlinear model of OHL span with the wake model which has evolved from his works presented in [14] and [15]. Moreover to original wake model (see Annex A, Figure A - 4 and Figure A - 5) the wake aerodynamic coefficients covered near-wake zone similar to that presented in Annex C, Figure C - 3 and Figure C - 5. The simulations allowed observing the different amplitudes in oscillations of windward and leeward conductor under turbulent wind.

It is worthwhile to make a note about some finite difference techniques. Such works were performed in USSR then Belorussia and Russia, by I. Sergey, A. Vinogradov et al. [84]. The more recent studies are referred to Oliveira [55] who included the wake effects in simulations of OHL response under hurricane winds.

3.2 SAMCEF Mecano model of wake interaction

The model described below summarizes the approach described in Section 2 to model the wake-induced interaction in twin conductor bundle. All implementations are done in the FE simulation package SAMCEF v12 [65].

General flow chart of wake interaction model is presented in Figure 3-1.

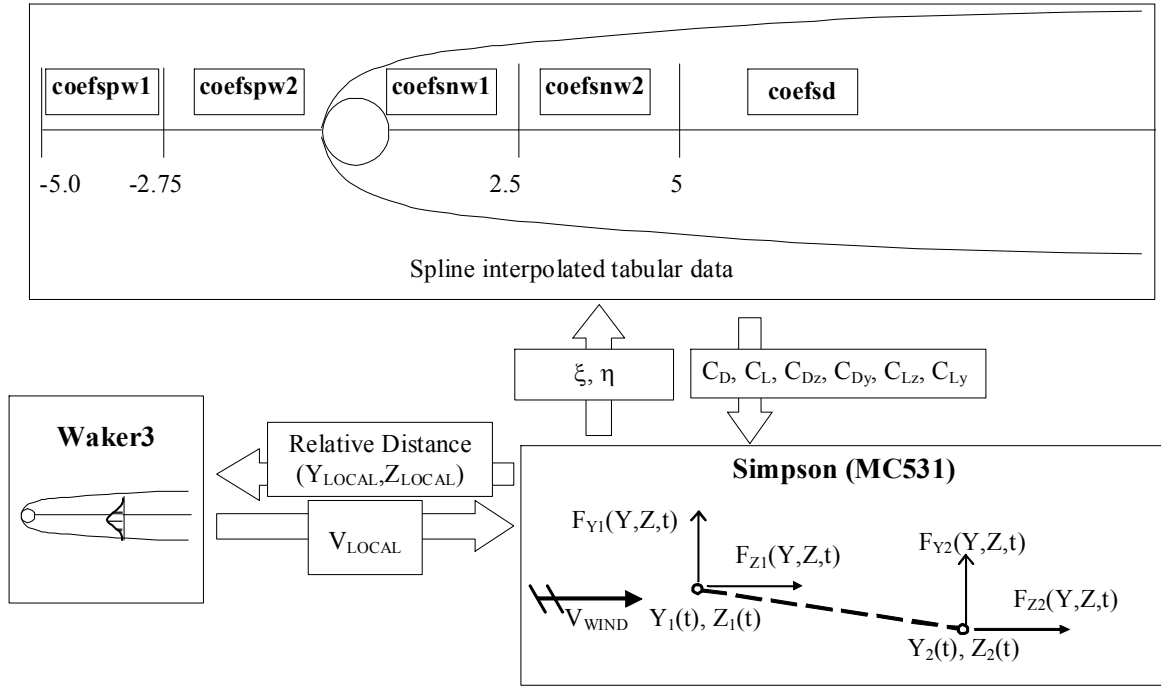


Figure 3-1. Flow chart of wake loads model in the twin bundle

The model is based on user-defined element type MC531 which allows application of external forces to the nodes of cable. The forces are space- and time-dependent and are calculated on basis of lift and drag coefficients' distribution in the wake.

The routine *Simpson.f* obtains, at each time instance, the data on wind velocity and nodal locations for windward and leeward conductor. Based on these data it calculates the dimensionless components of spacing between cable nodes and transfers these data to *Waker3.f* for calculation of local velocity and, depending on location of leeward node in the wake, to the block of wake aerodynamic coefficients routines:

- $\text{coefswn1.f} (\xi = 1 \text{ to } 2.5)$
- $\text{coefswn2.f} (\xi = 2.5 \text{ to } 5)$
- $\text{coebsd.f} (\xi = 5 \text{ to } \infty)$
- coefspw1.f and coefspw2.f - two special routines, based on Price & Païdoussis aerodynamic data (see Annex A), to calculate the case when the windward and leeward subconductors are twisted

The aerodynamic data are stored in tabular form. To obtain a value in any location of cable node at any time instance, two approaches can be used:

- spline interpolation with the use of software package developed by Science & Research Computational Centre at Moscow State University [54]
- polynomial surface fit using the approach described in Section 2.2.2 with the formulas presented in Annex A.

In the final calculations shown here, the far-wake coefficients are calculated with polynomial fit which allows time gain about 2 times as compared to spline-fitted strategy.

3.3 Spacer model

The spacer model is definitive in good representation of WIO. While cable element does not differ as much from formulations done by Granville [65] and Keutgen [36], the spacer shall adequately represent the motion and loads transfer between the subspans.

This point has been specially considered in most of known analytic studies on multi-span models. When calculating the eigenmodes of bundle span, the spacer is represented with the transfer matrix which ensures for interaction between subconductors in the adjacent subspans [1], [11]. Not only the same subconductor at both sides of spacer shall be adequately interacted via the spacer. The opposite subconductors also interact across the spacer, and all that depending on its stiffness and (in case of spacer damper) its damping properties.

The spacer in the FE model can be represented in various ways. If one is based upon the modal analysis models, the spacer might be built with a customized element identically based upon the transfer matrix approach. However, this approach has its limitations when the analysis is done in nonlinear formulation such as in Samcef Mecano. Then, it is preferable building a model of spacer with adequate elements allowing for large displacements and especially rotations.

3.3.1 Spacer basic properties

Consider a rigid twin spacer as a basic example. As is mentioned above, the spacer is a kind of gateway to transfer the efforts and motions along and across the cables in the adjacent subspans. The way it is done can be easily illustrated as shown in Figure 3-2. In fact, the width of the spacer clamp \mathbf{h} is not a point, it is about 50-80 mm. As the subconductor \mathbf{n} and $\mathbf{n+1}$ before and after the spacer move at different amplitudes, they create different efforts, \mathbf{V}_n and \mathbf{V}_{n+1} . As result, due to these efforts differential $\mathbf{dV} = \mathbf{V}_{n+1} - \mathbf{V}_n$ a moment $\mathbf{M} = \mathbf{dV} \times \mathbf{h}$ is generated. This moment is transmitted to the opposing subconductor quasi-totally with a rigid spacer, and in the opposing clamp having the same width \mathbf{h} this moment will be converted again as a pair of forces at the neighbouring subspans. The motion transferred by the spacer, however, will depend mainly upon its stiffness. While an example in the Figure shows the spacer reactions in Y-direction, such behaviour occurs in Z-direction as well.

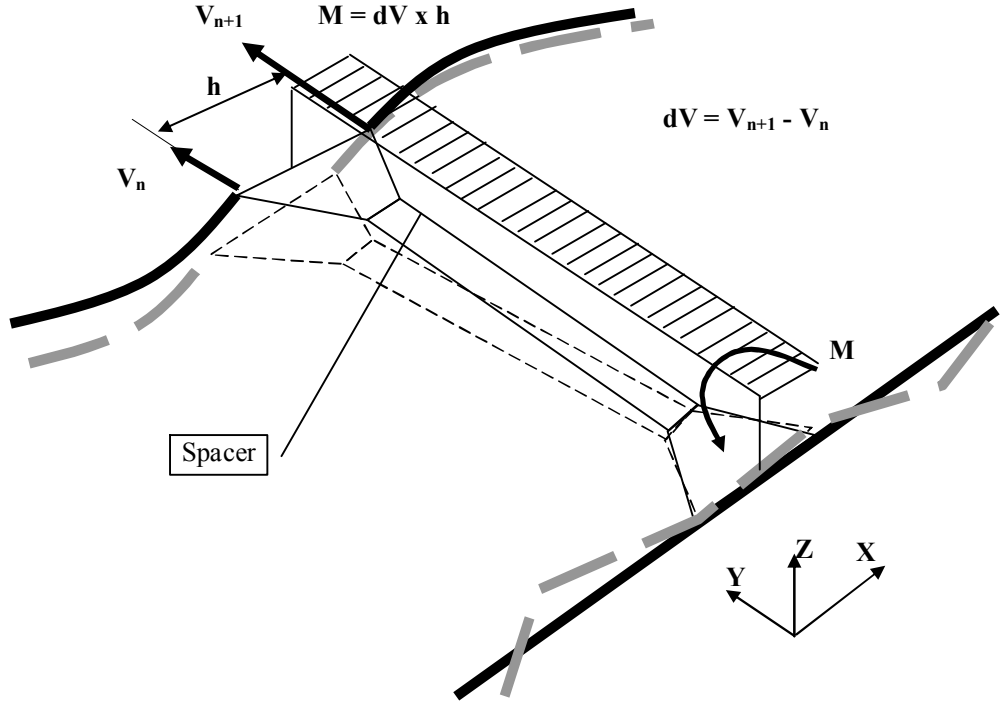


Figure 3-2. Spacer differential behavior at motion transmission

Considering the finite-element modelling, an adequate representation of the clamp width is quite helpful to get the realistic, fast-growing oscillation. In fact, neither cable element (3 translational DOF per node) nor nonlinear beam (3 translational + 3 rotational DOF per node) will transmit the correct differential moment, would the clamp be represented by a single node. The forces and (in case of beam) moments in the single-node clamp are reduced to an interpolation within one node, leading the effect of finite clamp width to be lost.

Until now the rigid spacer has been discussed. Different spacer designs, however, bring other effects in spacer mechanics. For example, a hinged twin spacer will no longer transmit the Y-moment as shown above. However, the torsional X-moment will remain.

It may be noticed that, in reality, each spacer has limitations in rotation of the clamps, especially spacer damper. It means that would the motion amplitude be high, the respective reaction moment should appear again with the spacer arm bounced off by the stopper. In literature, this effect is sometimes considered as an impact which adds to transmission the subspan oscillation motions into the higher harmonics having no excitation and, therefore, playing a damping effect.

One might object that some centimetres clamp width is a negligible distance even considering a normal cable element length (1m) or a subspan length (40-80 m). However, as the FE simulations of wake-induced oscillations demonstrate it in the next chapters, this is quite not the case. In fact, the finite clamp width inherits a more effective transmission of motion between different displacement components. For example (see Figure 3-3), given a spacer clamp width 80 mm and the distance between subconductors 450 mm, a displacement of a clamp end $dV = 10\text{mm}$ would result in longitudinal displacement $dU = 10/80 \times 450 = 56.3\text{ mm}$. This way, with the minor transversal

displacements the spacer serves as a converter between displacements by various motion components. Note, that the transversal displacement dV , due to the final width, will also generate a transversal displacement in the other subconductor.

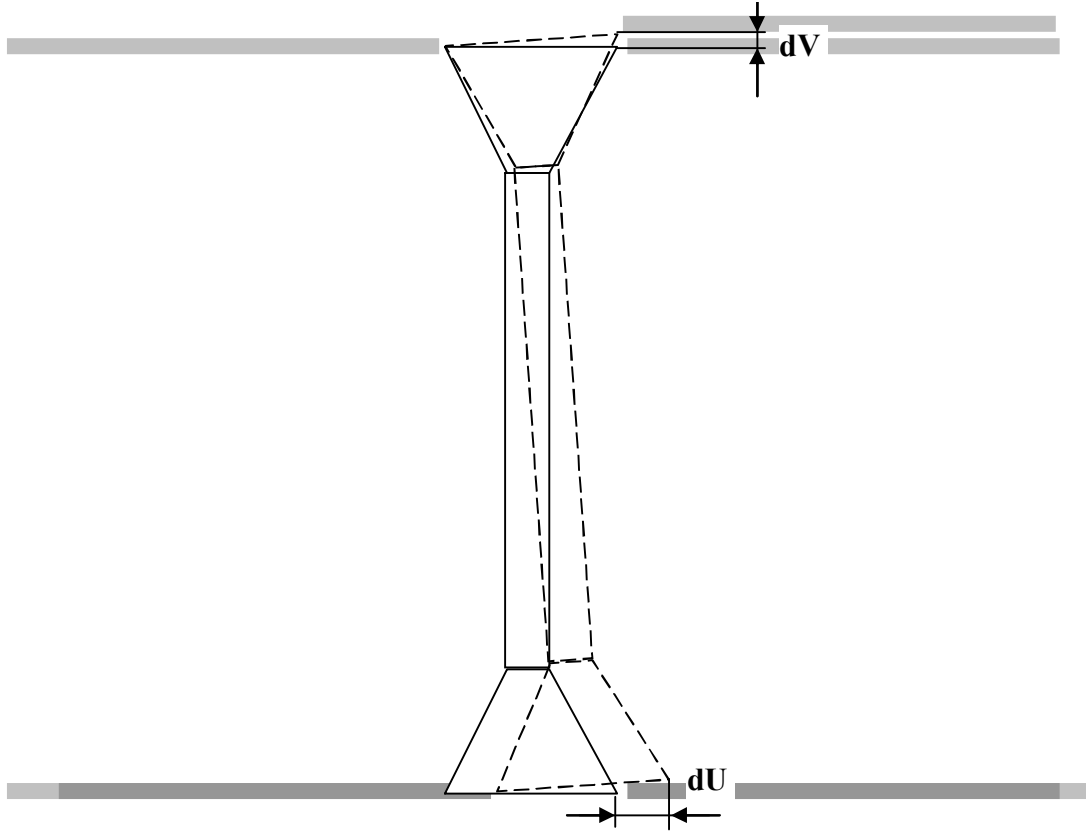


Figure 3-3. Illustration of transmission between different components of motions via spacer

Talking in dynamic sense, the finite clamp width adds not only to locking the subspan mode within a subspan. The oscillation at subspan frequency is transmitted to the opposite subconductor and excites it more effectively than if a single node clamp would be used in the model. A clamp with physical dimensions plays like a barrier in transmission of adjacent waves, and in the same time, it allows for transport of oscillations between different motion components, especially their differences at different sides of each clamp.

Thus, the above-described way to modelling approaches the finite element formulation of spacer (in geometrically nonlinear formulation) to the analytical models built with a transfer matrix method.

3.3.2 Finite element model of spacer

To better illustrate the principle of the spacer loads transmission and modelling approach, in Figure 3-4 the prototype model of spacer is shown. As seen from this model, such a truss structure of elements would perfectly transmit all the loads and motions along and across the subconductors.

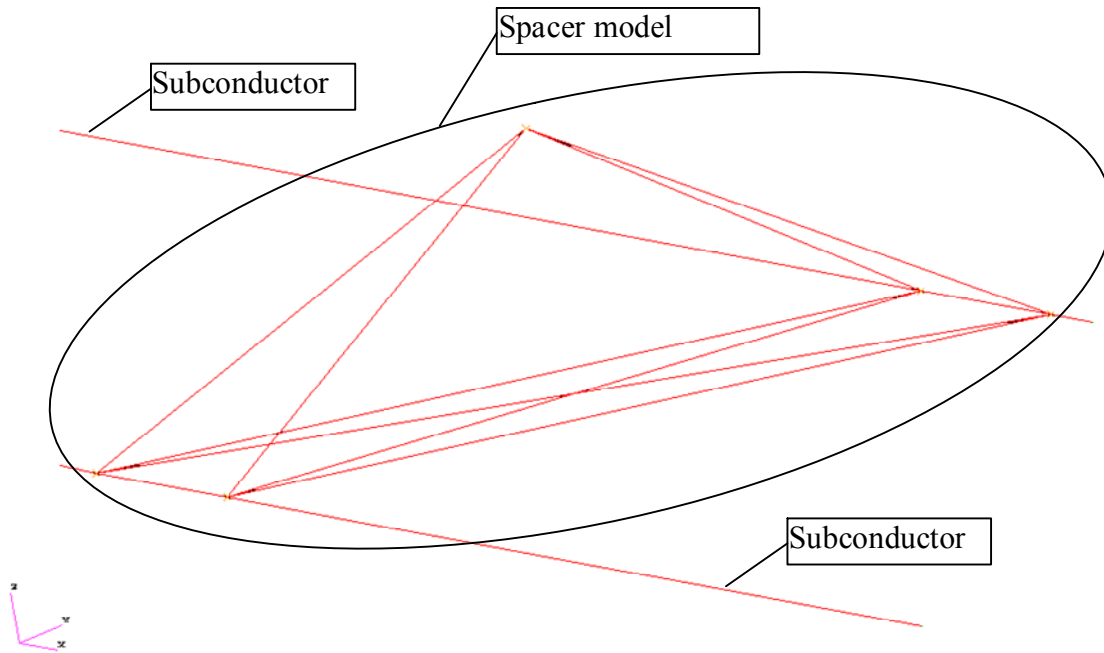


Figure 3-4. Prototype finite-element model of spacer

Upon the further development of the model, the spacer and spacer damper shapes became more representative, in modelling sense. The main problem of good modelling related to a specifics of Samcef Mecano cable elements (which were the best solution from the standpoint of line modelling): they have three translational DOF per node, and connecting it to the other structural elements like bushing or rigid-body element (RBE) inevitably led to computational problems at rotational DOFs at the nodes connecting the spacer structure to the cable. The workaround (perhaps specific only to Samcef) has been finally found in constraining the cable rotational DOFs (which had no any effect onto the cable motions, these DOFs are not used when integrating the cable time response) and then connecting the spacer clamps to the cable via a system of cylindrical Bush elements with the following properties:

- At one side of each clamp, the Bush has high translational stiffness (in order to keep the consistency in motion transmission between the cable and spacer) and zero torsional stiffness

- At the other side of each clamp, the Bush has high transversal translation stiffness but low longitudinal translation stiffness in order to fully allow the cable tension transmission. Torsional stiffnesses are also low.

So, since the conventional cable element has no torsional stiffness, this component is not represented in cable-to-clamp connections. It must be stressed out, that current formulation of Samcef does not allow for correct use of cable element with torsional stiffness developed by Keutgen. As this stiffness is introduced exclusively via seventh DOF, the Samcef structural connections do not adequately integrate this DOF. Probably, future developments of this element will allow for transfer of torsion via a conventional 6-DOF finite element formulation.

As simulations show it below, representation of several subspan modes does not necessarily need for accounting of conductor torsion. However, inclusion of conductor torsional stiffness, in some cases, leads to redistribution of amplitudes between different WIO modes, namely the subspan and snaking. See Chapter 4.1 as example.

The final model of twin spacer looks as shown in Figure 3-5. Note, that bush elements are introduced in the Local Cylindrical Coordinate System formulation; the respective local coordinate frames are oriented with a local Z (longitudinal) axis aligned between the aft and fore nodes on each clamp.

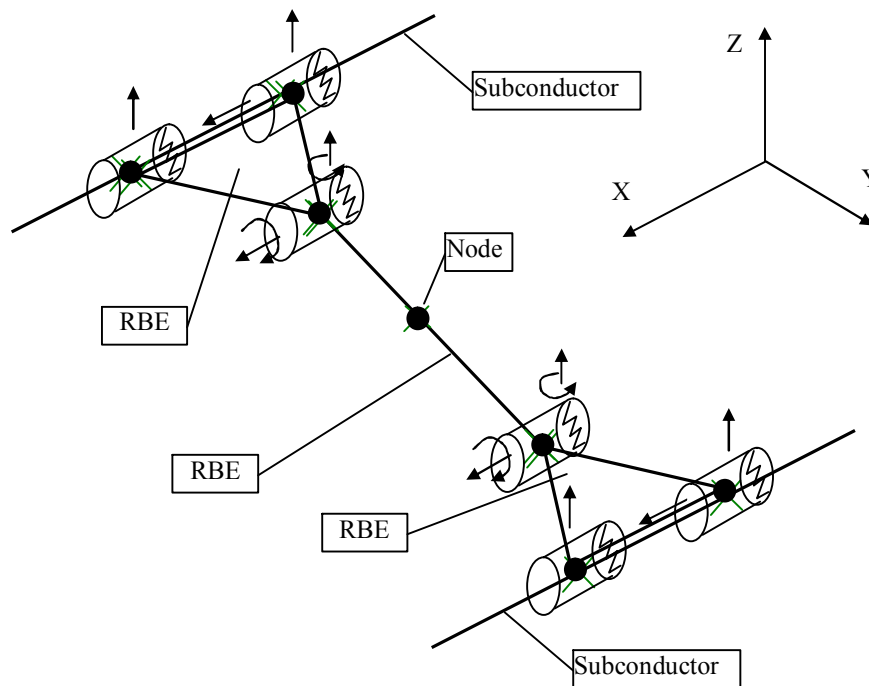


Figure 3-5. Finite Element model of the twin rigid spacer

As it can be seen easily, with introduction of bush elements the spacer model has all necessary components to build a spacer damper. Below an image of spacer damper model is presented, used in benchmarking study (see Section 6).

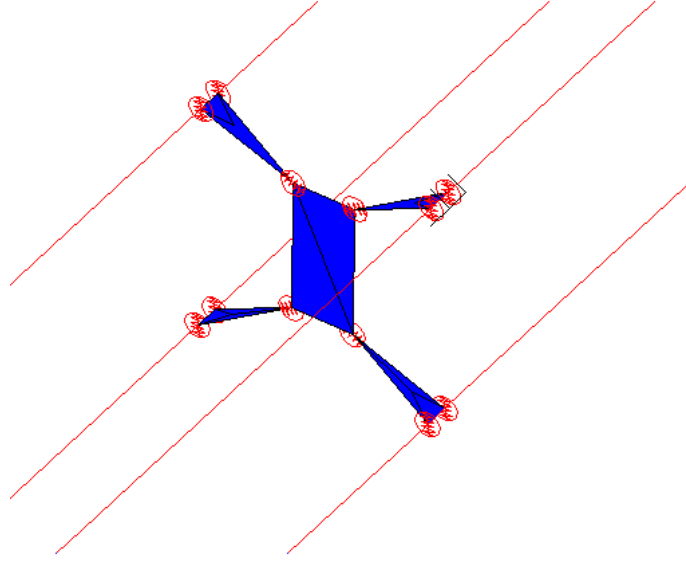


Figure 3-6. Finite element model of quad spacer damper

3.4 Time integration scheme

Another important component for successful simulation of WIO is an appropriate time integration strategy. SAMCEF Mecano implements a Hilbert-Hughes-Taylor implicit integration algorithm (HHT). With this algorithm, the elastic forces and the external forces are weighed over the considered time interval and the equilibrium equations take the general form

$$\mathbf{M}\ddot{\mathbf{q}}_{n+1} + \mathbf{F}_{n+1}^{\text{e.cine}} + (1-\alpha)\mathbf{K}^{\text{e}}\mathbf{q}_{n+1} + \alpha\mathbf{K}^{\text{e}}\mathbf{q}_n = (1-\alpha)(\mathbf{F}_{n+1}^{\text{e.aero}} + \mathbf{F}_{n+1}^{\text{e.g}}) + \alpha(\mathbf{F}_n^{\text{e.aero}} + \mathbf{F}_n^{\text{e.g}}) \quad (3.1)$$

Here,

\mathbf{M} is the mass matrix

$\mathbf{F}^{\text{e.cine}}$ is the coupled inertial force matrix

$\mathbf{F}^{\text{e.aero}}$ is the coupled aerodynamic force matrix

$\mathbf{F}^{\text{e.g}}$ is the gravity force

\mathbf{K}^{e} is the stiffness matrix including structural and aerodynamic components

\mathbf{q} is the nodal displacements (nodal unknowns) vector

α is the numerical damping parameter

$n + 1$ denotes the next time step

n is the current time step

The nodal unknowns at the time step $n+1$ are predicted from the previous time step with

$$\begin{aligned}
 \ddot{\mathbf{q}}_{n+1}^0 &= 0 \\
 \dot{\mathbf{q}}_{n+1}^0 &= \dot{\mathbf{q}}_n + (1-\gamma)h\ddot{\mathbf{q}}_n \\
 \mathbf{q}_{n+1}^0 &= \mathbf{q}_n + h\dot{\mathbf{q}}_n + \left(\frac{1}{2}-\beta\right)h^2\ddot{\mathbf{q}}_n
 \end{aligned} \tag{3.2}$$

where h is the length of time step, $\gamma = \frac{1}{2} + \alpha$, $\beta = \frac{1}{4}(1+\alpha)^2$ and $\alpha \in \left[0; \frac{1}{3}\right]$

If we insert these predictions into relations of the time integration scheme, namely

$$\begin{aligned}
 \ddot{q}_{n+1} &= \frac{1}{\beta h^2}(\mathbf{q}_{n+1} - \mathbf{q}_{n+1}^0) \\
 \dot{q}_{n+1} &= \dot{\mathbf{q}}_{n+1}^0 + \frac{\gamma}{\beta h}(\mathbf{q}_{n+1} - \mathbf{q}_{n+1}^0)
 \end{aligned} \tag{3.3}$$

And then use these relations in the equation (3.1), we obtain a system of residual equations which depends only on \mathbf{q}_{n+1}

$$r(\mathbf{q}^{n+1}) = 0 \tag{3.4}$$

This non-linear system is solved via a Newton-Raphson iteration process: at each iteration, we have to calculate the iteration matrix of a type

$$\mathbf{S} = \left[\frac{\partial r(\mathbf{q}_{n+1})}{\partial q} \right] \tag{3.5}$$

Here, q denotes a specific component nodal unknown.

Within above integration strategy, SAMCEF offers a number of parameters allowing the tune up of solution algorithm at the time step and the step-internal iteration levels. In case of WIO, one has to tune up the algorithm such as the self-excitation of the system due to the wake effects shall not be damped numerically. This has been achieved namely by setting the key integration parameters to the following values:

- At initial time step (when system is assembled and put to the equilibrium),

Parameter	Description	Value
<i>Newton-Raphson Iteration Parameters</i>		
PRCR	Precision threshold for the residual norm of an implicit iteration	1.0E-1
PRCK	Precision threshold (TESF) under which the updating of the iteration stiffness matrix is skipped in an implicit iteration	1.0E-3
<i>HHT Integration Parameters</i>		
ALFA	Numerical damping parameter	5.0E-2

- At transient response time step,

Parameter	Description	Value
<i>Newton-Raphson Iteration Parameters</i>		
PRCR	Precision threshold for the residual norm of an implicit iteration	1.0E-3
PRCK	Precision threshold (TESF) under which the updating of the iteration stiffness matrix is skipped in an implicit iteration	1.0E-5
<i>HHT Integration Parameters</i>		
ALFA	Numerical damping parameter	5.0E-2

The time step is selected to be small enough to detail oscillations at the level of frequencies 1...2 Hz. In all analyses presented here it was equal to 0.025 s.

3.5 Numerical examples

A series of computations has been done to check possibilities of implemented wake interaction model to represent the cable oscillations. Below main results are presented.

3.5.1 Single 45 m – long span twin bundle model

3.5.1.1 Input data

A single subspan model aims at validating the typical example of WIO correspondent to the suspended cylinders. In such configuration it is expected to obtain the elliptical orbit on the leeward conductor. The cable tension is taken such as to represent the in-plane and out-of-plane frequencies relationship close to 1.1. Heavy conductor properties are used.

Parameters of model

Span length:	Conductor diameter	Conductors horizontal spacing	Conductors vertical spacing
45 m	3 cm	10 conductor diameters	-2.5 conductor diameters (leeward conductor lower)

Conductor tension	Conductor mass per unit length	In-plane frequency	Out-of-plane frequency	Frequency relationship
15800 N	1.25 kg/m	1.37 Hz	1.25 Hz	1.096

Parameters of aerodynamic loading

Wind velocity	Aerodynamic data
15 m/s	Price

3.5.1.2 Results

Calculation results are illustrated in Figure 3-7. The leeward conductor oscillates with the elliptical orbit in the middle of span reaching approx. 15 conductor diameters in the major axis and 4.7 conductor diameters in the minor axis. In this case, the ellipse is oriented along the tilt direction of the sagged conductor. Note, that as the orbit develops, during several loops it remains oriented towards the windward conductor. However, as the in-plane and out-of-plane frequencies become coalescent, the out-of plane mode becomes determinant in the oscillation.

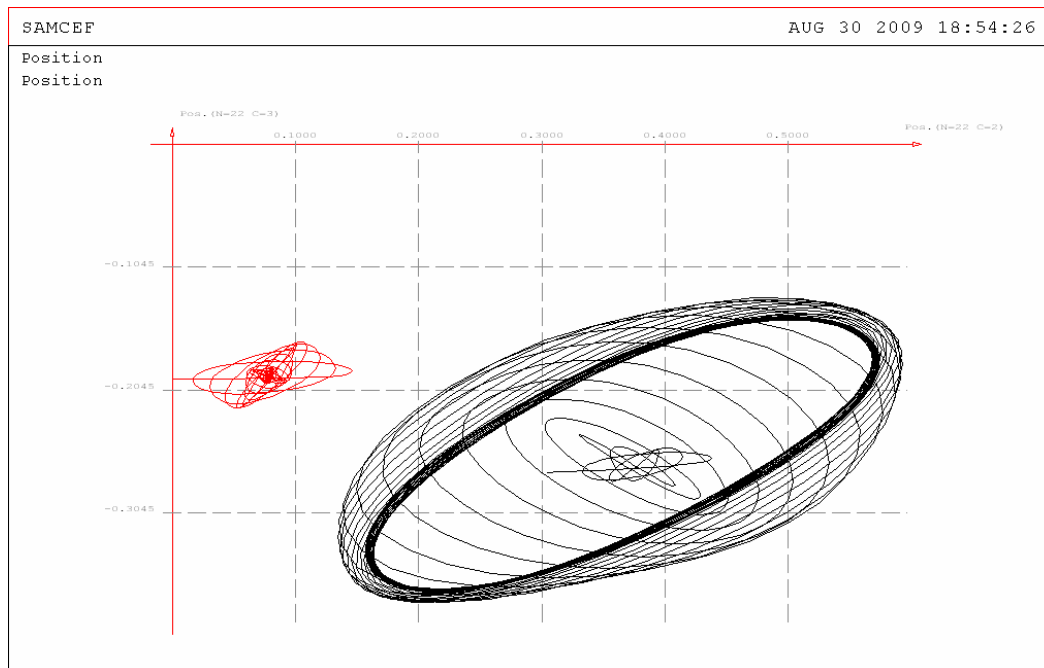


Figure 3-7. WIO in the 45 m long single twin span. Left orbit: windward conductor, right orbit: leeward conductor

This result gives reference to the image of WIO obtained for suspended cylinder in wind tunnel test, see Figure 3-8.

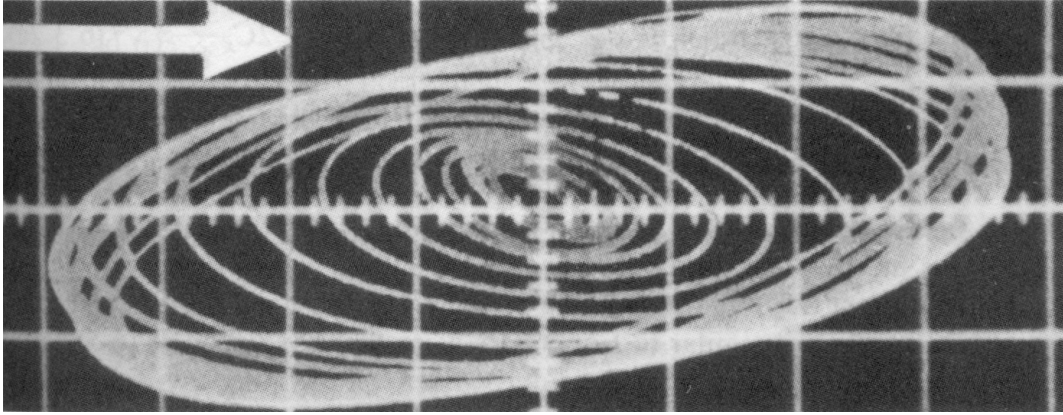


Figure 3-8. WIO orbit obtained in wind tunnel test [68]

3.5.2 Single span 80 m long: twin bundle

In another model of the single span, the span length has been increased to 80 m to see the impact of the closer conditions to the subspan oscillations which in fact are observed in the long subspans. Other conditions like conductor spacing and initial tension are also close to the real span.

3.5.2.1 Input data

Parameters of model:

Span length:	Conductor diameter	Conductors horizontal spacing	Conductors vertical spacing
80 m	3 cm	16 conductor diameters	-2.5 conductor diameters (leeward conductor lower)

Conductor tension	Conductor mass per unit length	In-plane frequency	Out-of-plane frequency	Frequency relationship
30000 N	1.25 kg/m	1.01 Hz	0.96 Hz	1.052

Parameters of aerodynamic loading

Wind velocity	Aerodynamic data
15 m/s	Price

3.5.2.2 Results

Calculation results are illustrated in Figure 3-9. The elliptical orbit of leeward conductor in the middle of span has approx. 16.7 conductor diameters in the major axis and 3.3 conductor diameters in the minor axis. Compared to the first case of Section 3.5.1, the orbit is more elongated and is oriented towards the leeward conductor – as is often observed in real subspan oscillations. Note that, compared to the first case, the sag is not much greater (0.3 m compared to 0.25 m). However, this and also the less frequency ratio indicate, that such subspan model differently absorbs the energy transferred from the wake.

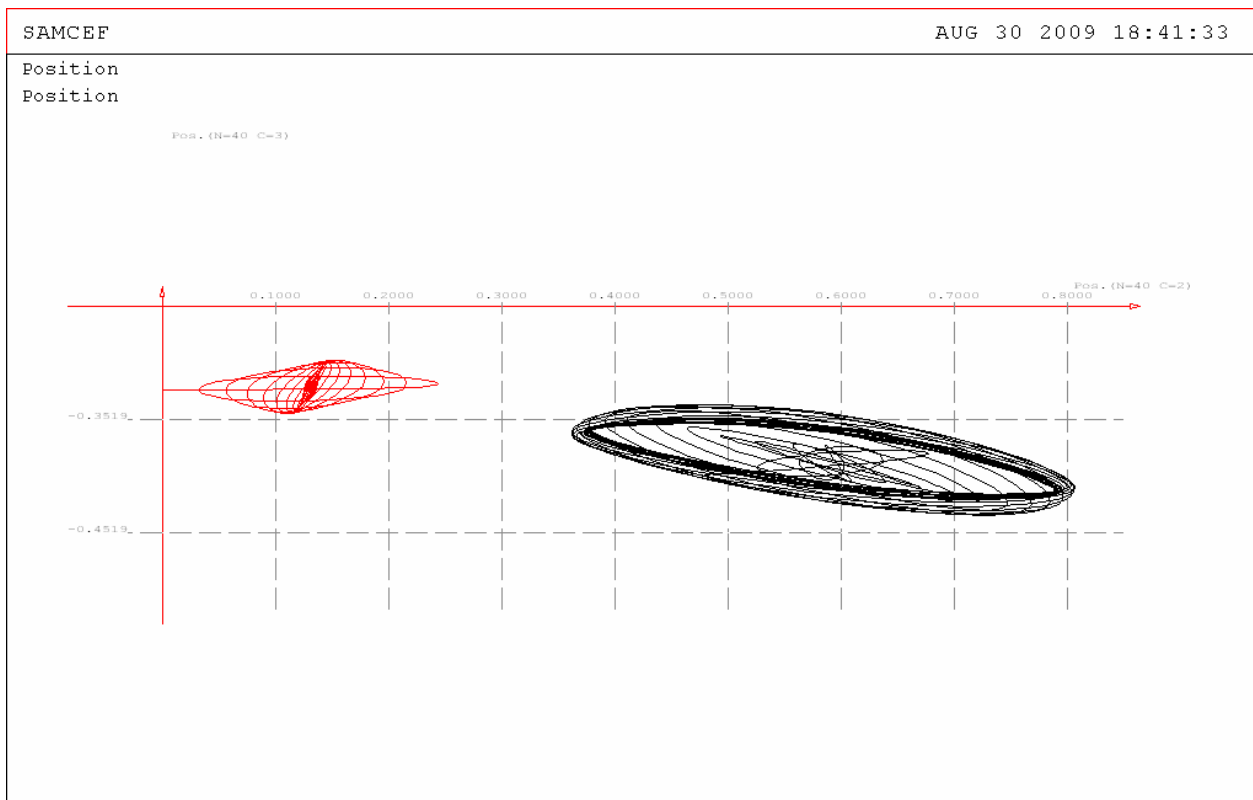


Figure 3-9. WIO in the 80 m long single twin span. Left orbit: windward conductor, right orbit: leeward conductor

Note, that windward conductor makes typical free-decaying oscillations after being excited by initial wind impact (in this and other case studies, the wind grows from zero to the constant within the period of around 1 second).

3.5.3 Three equal 80 m subspans, twin bundle

This case aims at emphasizing the oscillation as it could occur in a very bad case, when the line shall be absolutely prone to WIO. The subspans are long, they are equal and the bundle is tilted.

The model is illustrated in Figure 3-10.

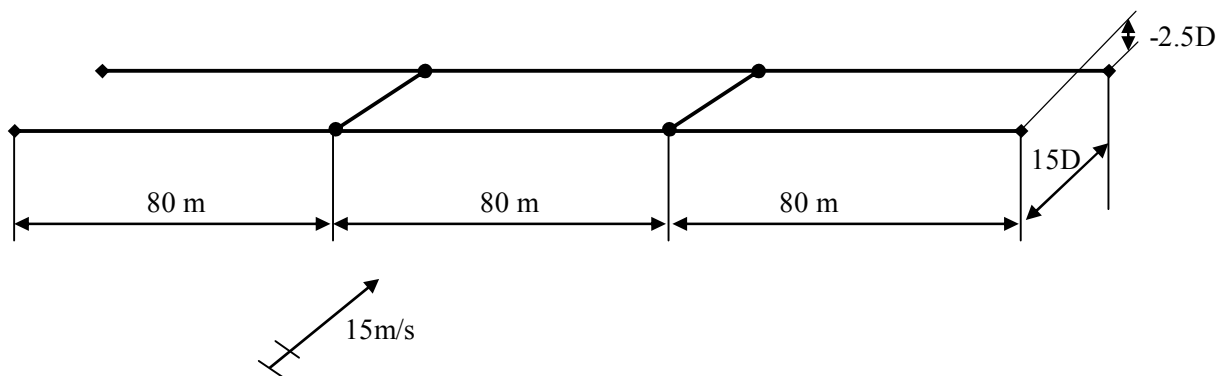


Figure 3-10. Model of two equal 80 m subspans

3.5.3.1 Input data

Parameters of model:

Span length:	Subspans	Conductor diameter	Conductors horizontal spacing	Conductors vertical spacing
240 m	3 x 80m	2.54 cm	15 conductor diameters	2.5 conductor diameters (leeward conductor below)

Conductor tension	Conductor mass per unit length
19 kN (windward), 19.1 kN (leeward)	1.25 kg/m

Parameters of aerodynamic loading

Case no.	Wind velocity, m/s	Aerodynamic data
1	10	Price
2	15	

3.5.3.2 Results – wind 10 m/s

Orbits of oscillations are shown in the figure below. The snaking mode, which was not observed from the known publications of wake-induced oscillation models, here is perfectly represented.

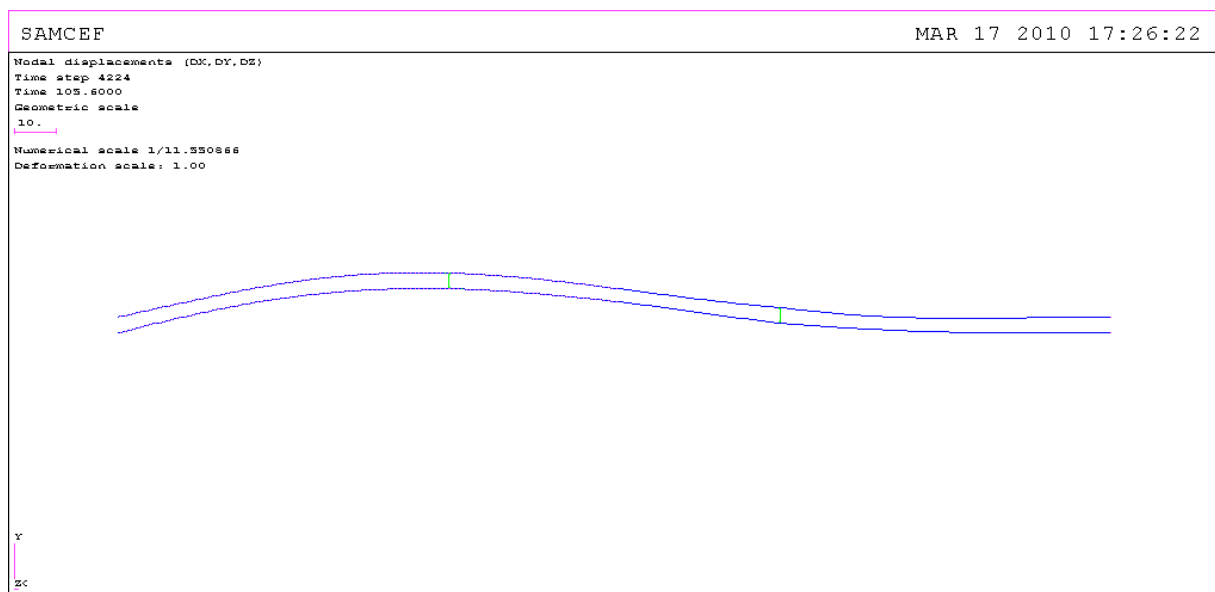


Figure 3-11. Snaking mode after simulation of 3x80m twin bundle

. It is clearly seen from the zoom of Figure 3-12 (see Figure 3-13) that two subspans are moving in the opposite phase. The pure subspan mode is quickly degenerated to the vertical motion (see Figure 3-14).

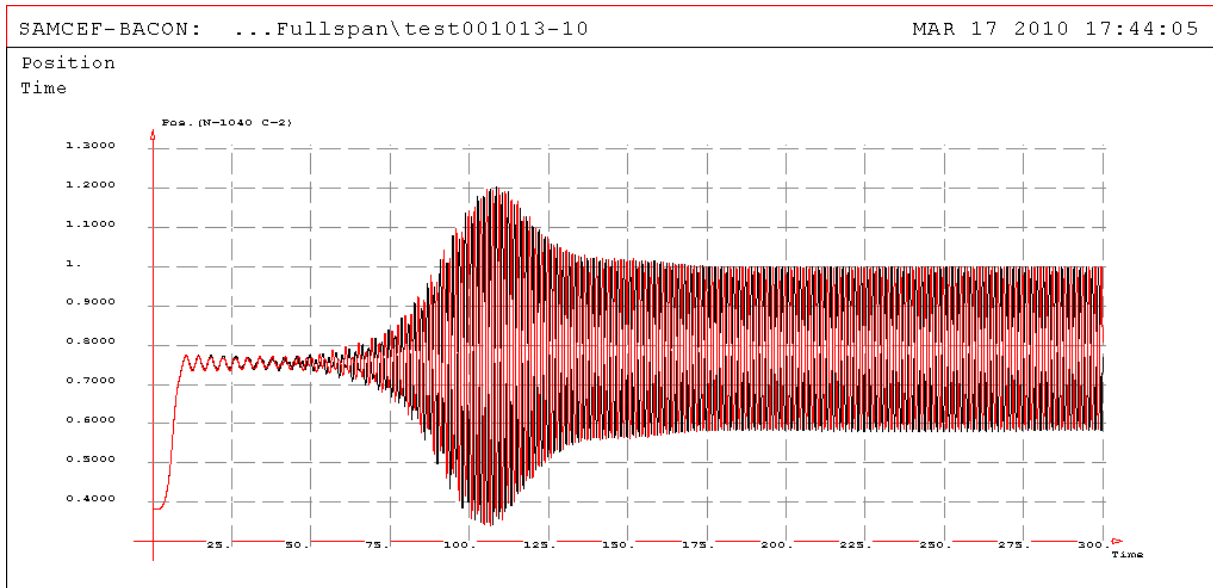


Figure 3-12. Y-component motions in the leeward subconductors, middle of subspan 1 (red) and subspan 3 (black): full simulation curves

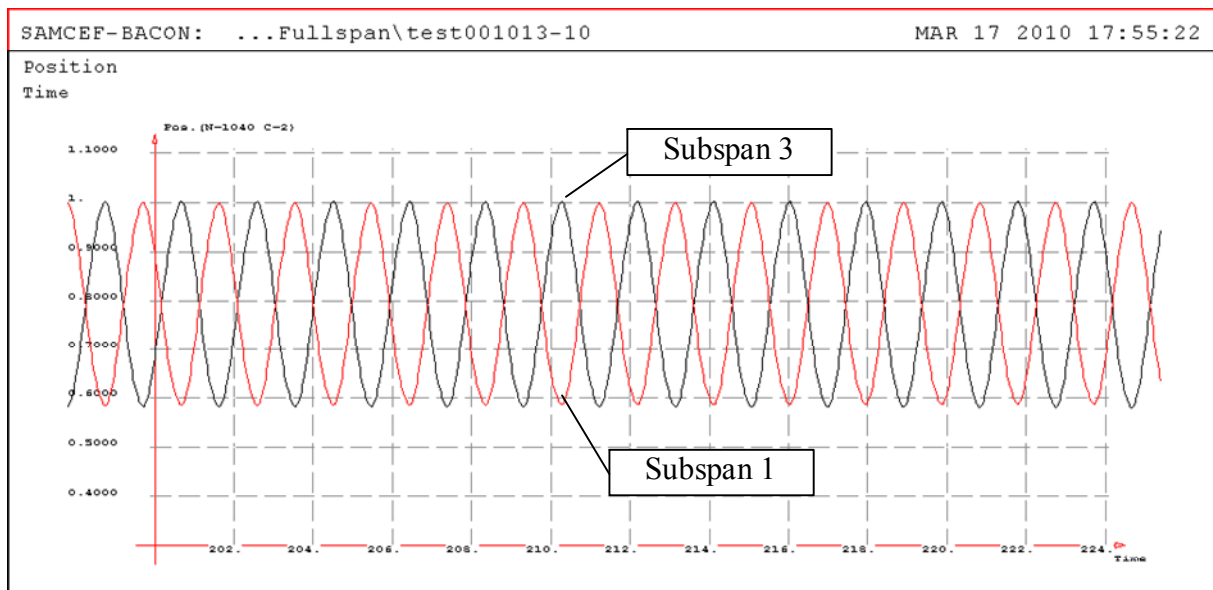


Figure 3-13. Zoom of Y-component motions in the leeward subconductors, middle of subspan 1 (red) and subspan 3 (black): full simulation curves

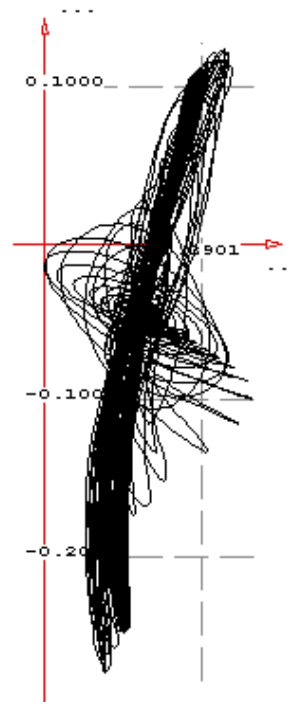


Figure 3-14. Leeward subconductor orbit relative to windward: middle of subspan 1 – identical axes scales

3.5.3.3 Results – wind 15 m/s

Orbits of oscillations are shown in the figure below. The subspan oscillations here are also pronounced, however, they become disturbed by the motion transfers between adjacent subspans

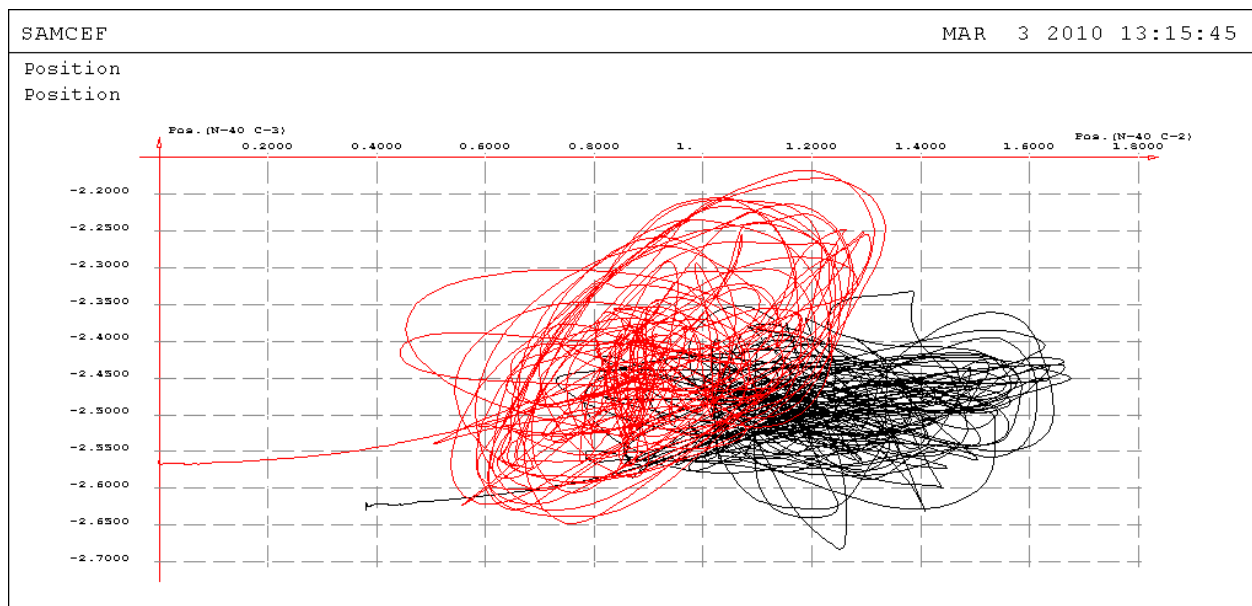


Figure 3-15. Orbits in the middle of end span (no.1): left orbit – windward subconductor, right orbit – leeward

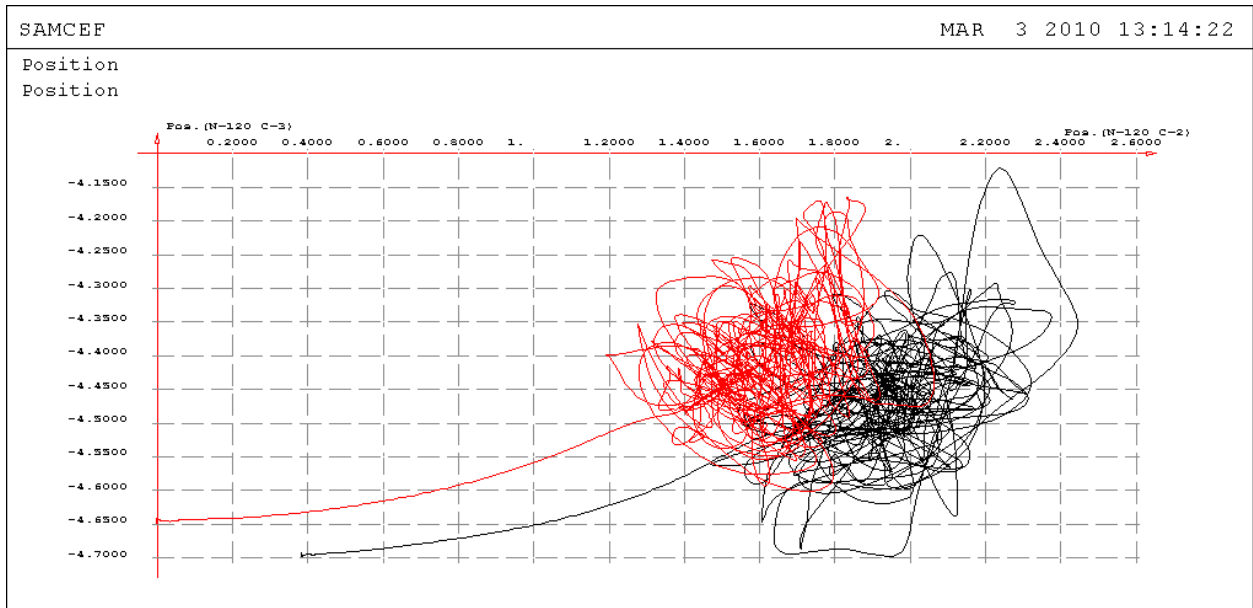


Figure 3-16. Orbits in the middle of middle subspan: left orbit – windward subconductor, right orbit – leeward

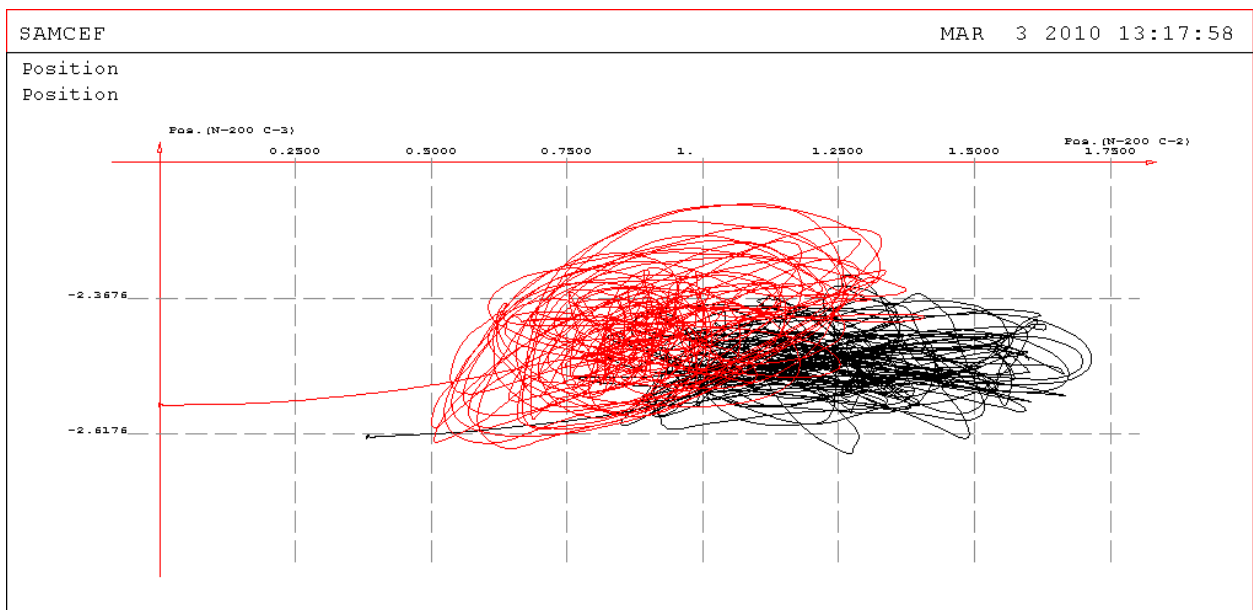


Figure 3-17. Orbits in the middle of end subspan (no.3): left orbit – windward subconductor, right orbit – leeward

It is interesting to see the Y-component motion between the subspan 1 and 3. As shown in Figure 3-18 and Figure 3-19, the pure subspan mode finally transforms into the snaking mode: the motions of two end subspans are opposite at the frequency close to 0.5 Hz – the two loop global mode for this span.

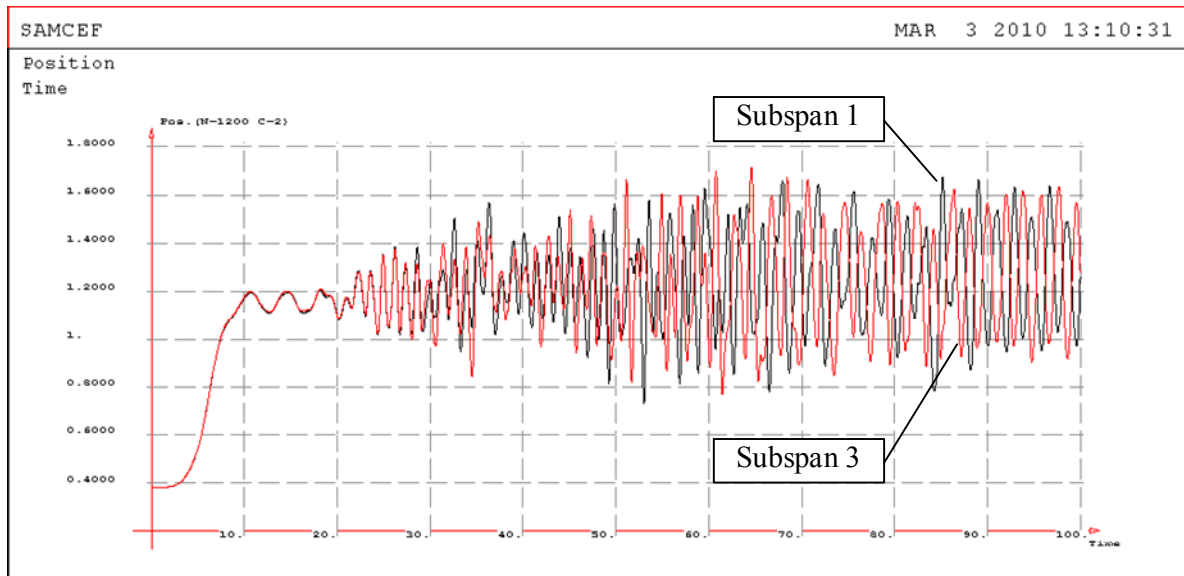


Figure 3-18. Y-component motions in the leeward subconductors, middle of subspan 1 (black) and subspan 3 (red)

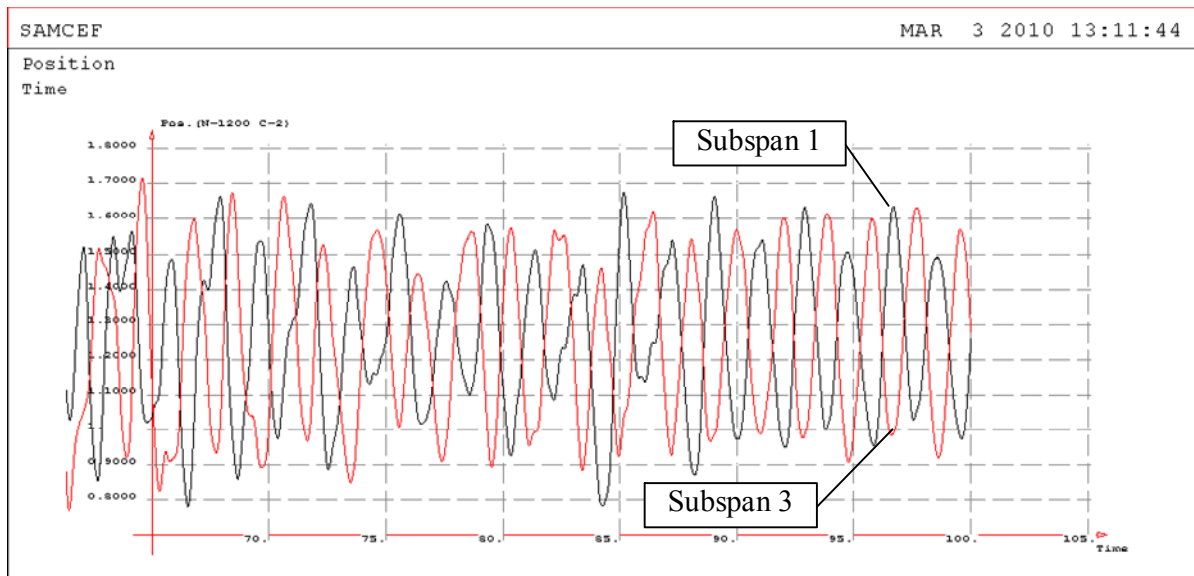


Figure 3-19. Y-component motions (zoomed at 60-100 s interval) in the leeward subconductors, middle of subspan 1 (black) and subspan 3 (red): end of simulation

3.6 Synthesis

Some preliminary conclusions may be done on basis of above examples:

1. Within one span, the WIO is clearly observed in conditions similar to wind tunnel test.
2. With the number of subspans increased, additional effects influence the set-up of WIO. Power transfer between subspans is among the most important issues, at the extent that upper or lower position may lead to self-excited oscillation.
3. The Simpson-type model of wake interaction, by clearly establishing an interaction between cable elements, allows for making realistic simulations of wake-induced phenomena. It is cornerstone, however, to adequately represent structure in the model: the model of spacer appears to be critical in this approach. Account of the finite width of the spacer clamp is necessary to approach the actual loads and motions transfer in the bundle. It might seem that a point clamp would open the road to eliminate the WIO; however, this is nothing but a hypothesis when considering important constraints imposed by spacers design (corona effects, static strength etc.).
4. Bringing together the above mentioned fluid and structural aspects and paying attention to even to some tiny details, the fluid – structure interaction modelling becomes more realistic.

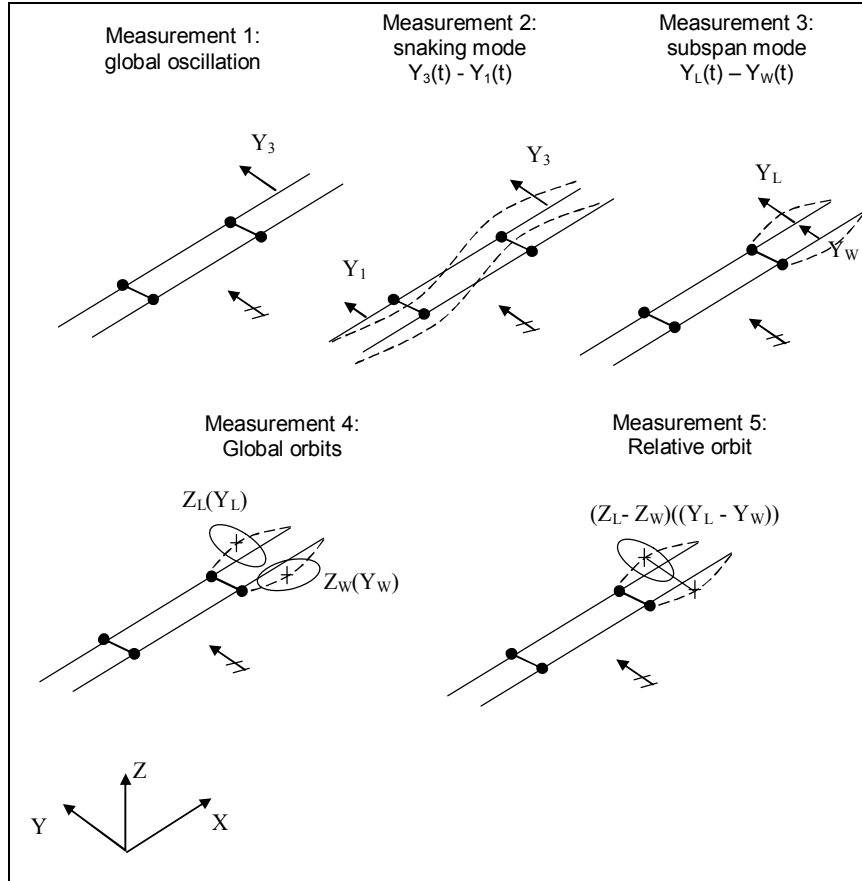
4 Parametric study

As will be shown in subsequent sections, the wake-induced oscillation reveals to be a phenomenon quite sensitive to any of structural effects. Moreover to those of them having been covered here below, other aspects may also influence the onset, grow up, amplitude and the mode of oscillations.

In all comparative studies shown below, the following diagrams are used to illustrate the variations of WIO in the line:

- 1) Y oscillations in the middle of subspan (usually, the end one)
- 2) Subtraction of Y-displacements in two opposite end subspans giving an image of the snaking mode presence in the span
- 3) Subtraction of Y-displacements in the windward from the leeward subconductors giving an image of the subspan mode
- 4) Orbits of oscillations for leeward and windward subconductors to give the global image about oscillation severity
- 5) Relative orbit of leeward subconductor with respect to the windward one, which allows for estimating the subspan oscillation limit cycle, and in particular it allows for seeing if the clashing would occur between subconductors.

These measurements are illustrated in the figure below.



4.1 Effect of conductor torsion

The reason for this study belongs to specifics of SAMCEF conventional cable element (used throughout this work): this element is defined as having just three translational degrees-of-freedom per node. It might be interesting to see how the oscillations described in Section 3.5.3 may be affected by accounting the torsional stiffness of the conductor.

4.1.1 Model description

The torsion has been introduced into the conductor span model by coupling the conventional cable element and nonlinear bush. The latter has been defined as cylindrical bush with respect to the local cylindrical coordinate system (Z axis oriented between the cable element nodes). The couple of elements are illustrated in Figure 4-1. This way of modelling has allowed, moreover to adding torsional stiffness, for seamless integration of spacer into the cable element, since such element couple satisfies conductor description in all six DOF. The computation time for such model increases insignificantly.

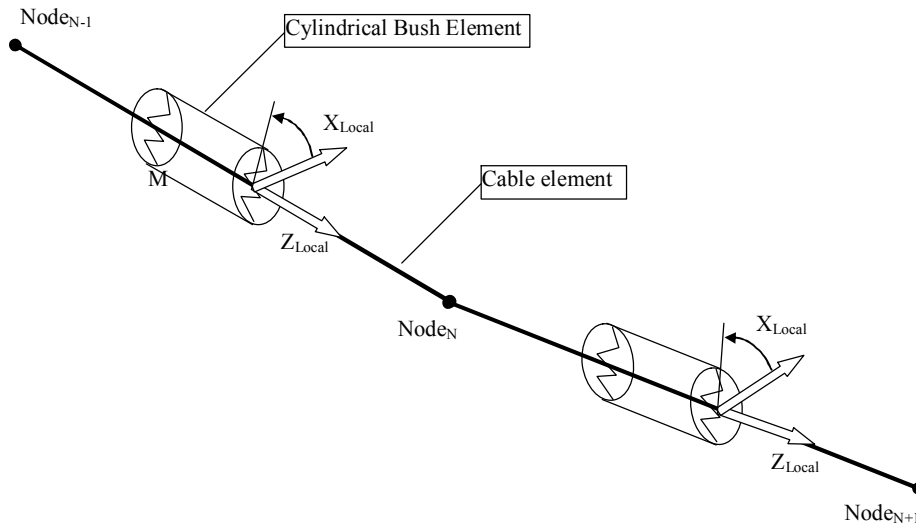


Figure 4-1. Cable+Bush element couples to model conductor torsion

The line span used in the comparison has the following parameters:

Parameter	Reference model	Model 1
Torsional stiffness	No	160 Nm/rad
No. of subconductors	2	
Span length	240	
Subspan composition	80/80/80	
Initial Tension, kN (windward/leeward)	19 / 19.1	
Conductor diameter, mm	25.4	
Conductor mass per unit length, kg/m	1.25	
Subconductors spacing, Y/D Z/D	15 -2.5	
Spacer type	Rigid	
Wind speed, m/s	12	

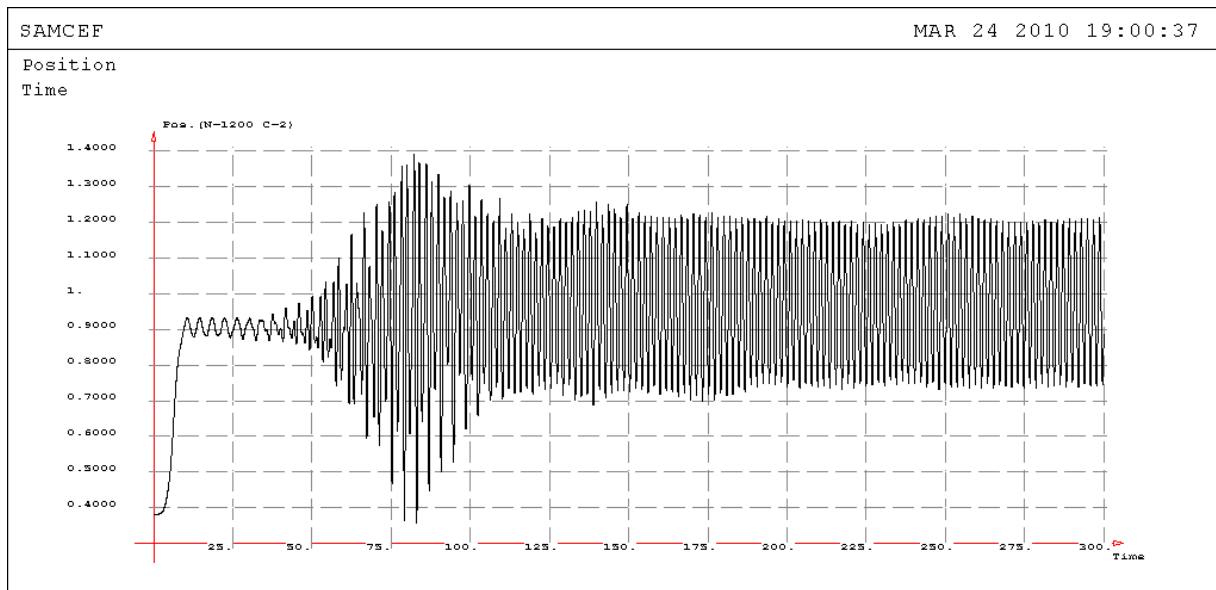
4.1.2 Results

4.1.2.1 Global oscillation

The reference model exhibits mainly the snaking mode, as can be seen from the figure below. The frequency of oscillation is about 2 times less than the subspan frequency (which is ~ 1 Hz) – see Figure 4-2.

Model 1 (conductor torsional stiffness 160 Nm/rad) – already on global oscillation we may see, that a subspan mode I clearly excited and it dominates in the oscillation – see Figure 4-3.

(a)



(b)

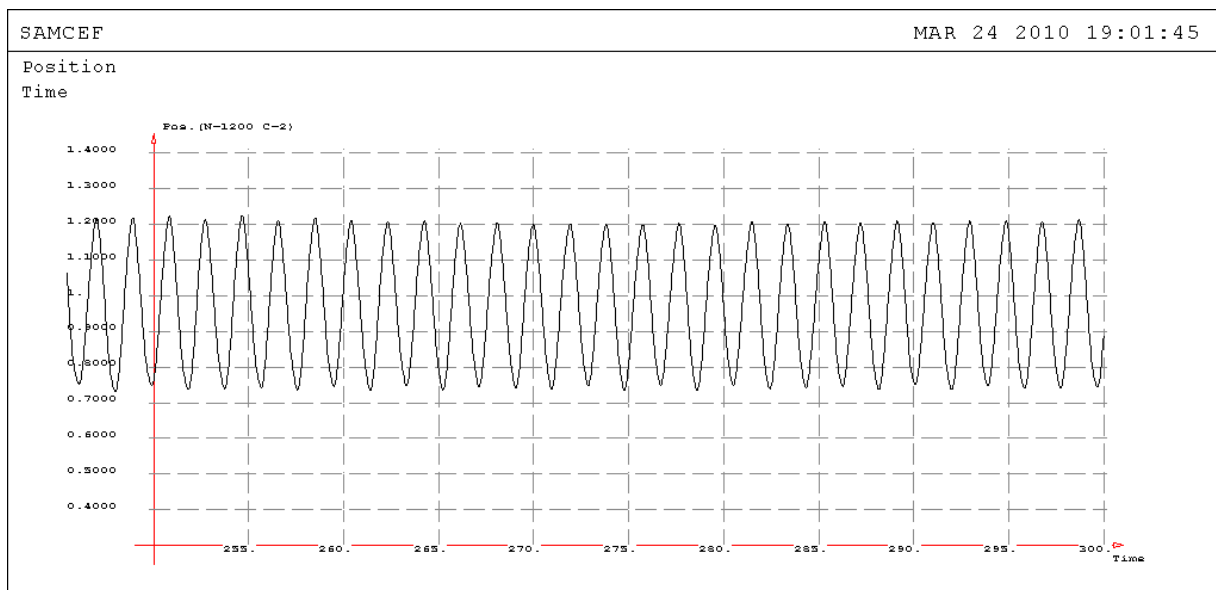
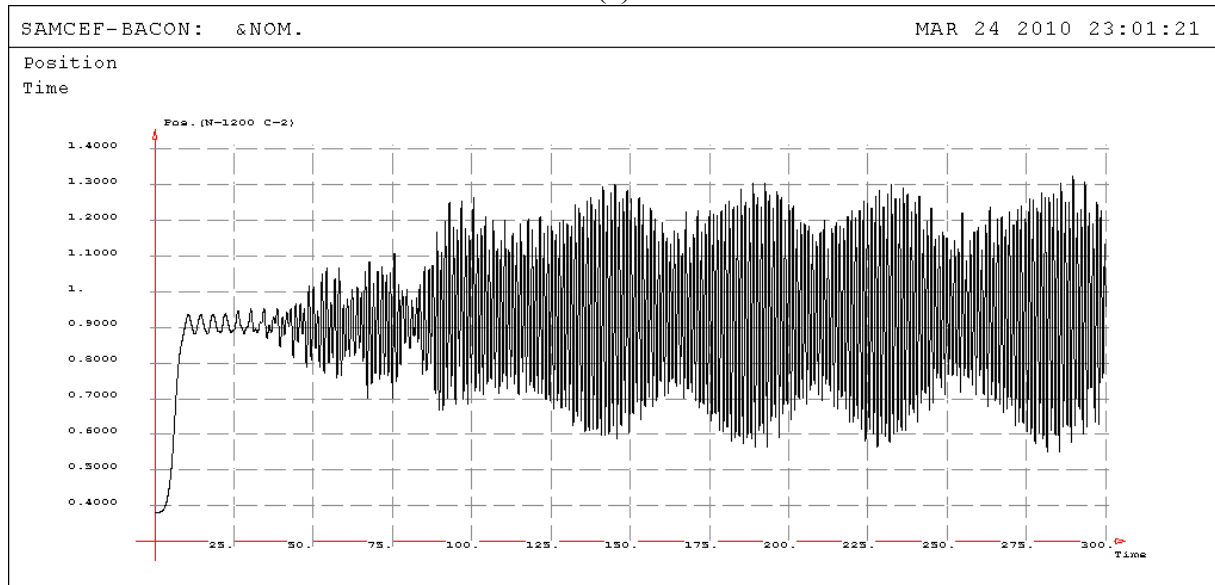


Figure 4-2. Reference model: Y oscillations in the middle of end subspan: (a) overall exposure, (b) zoom to 50 s

(a)



(b)

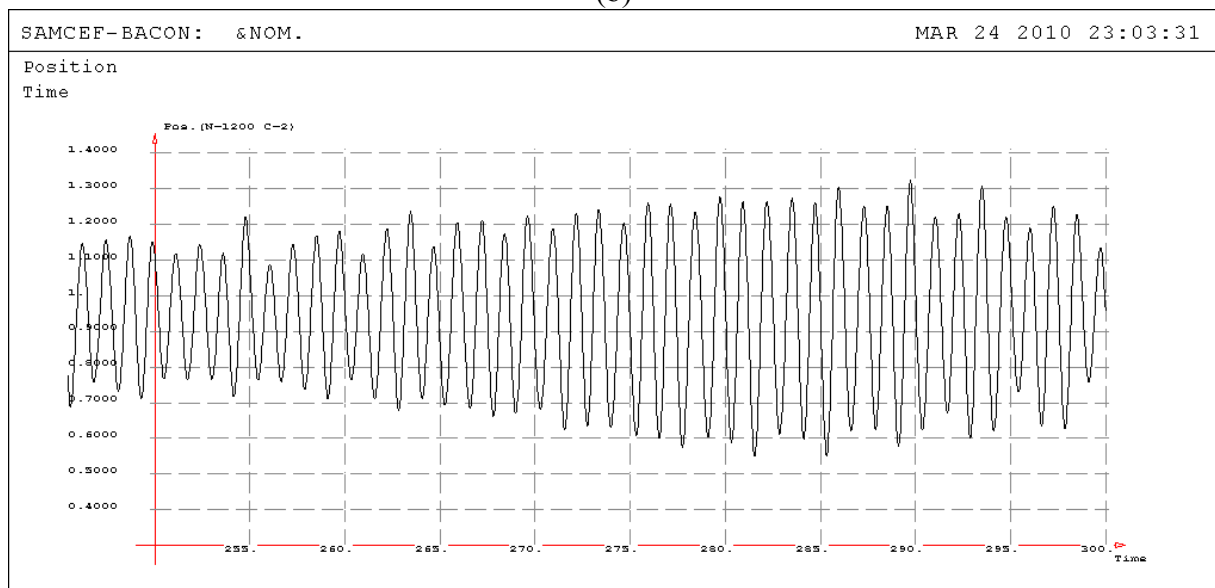


Figure 4-3. Model 1: Y oscillations in the middle of end subspan: (a) overall exposure, (b) zoom to 50 s

4.1.2.2 Snaking mode

Above is specifically clear for **Reference Model** if we take Y-displacements in two opposite subspans and subtract one from another, obtaining relative variation of Y-positions along the line, characteristic for the snaking mode – see Figure 4-4. On the contrary, the **Model 1** shows that snaking does exist; however, it is of considerably less amplitude – about 5 times less.

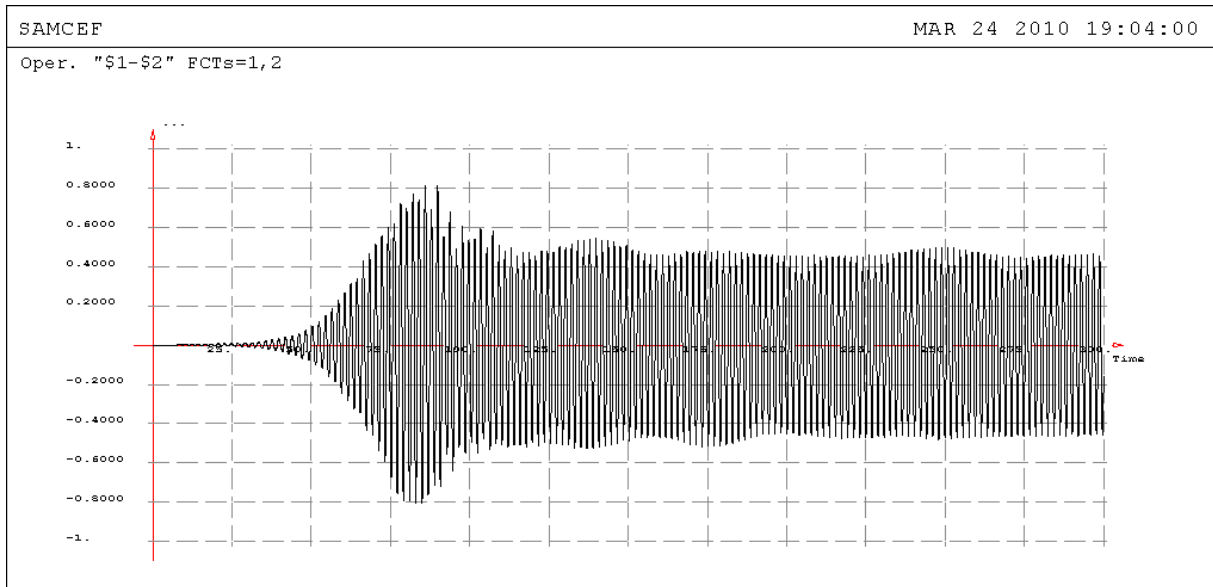


Figure 4-4. Reference model: snaking mode between opposite end subspans.

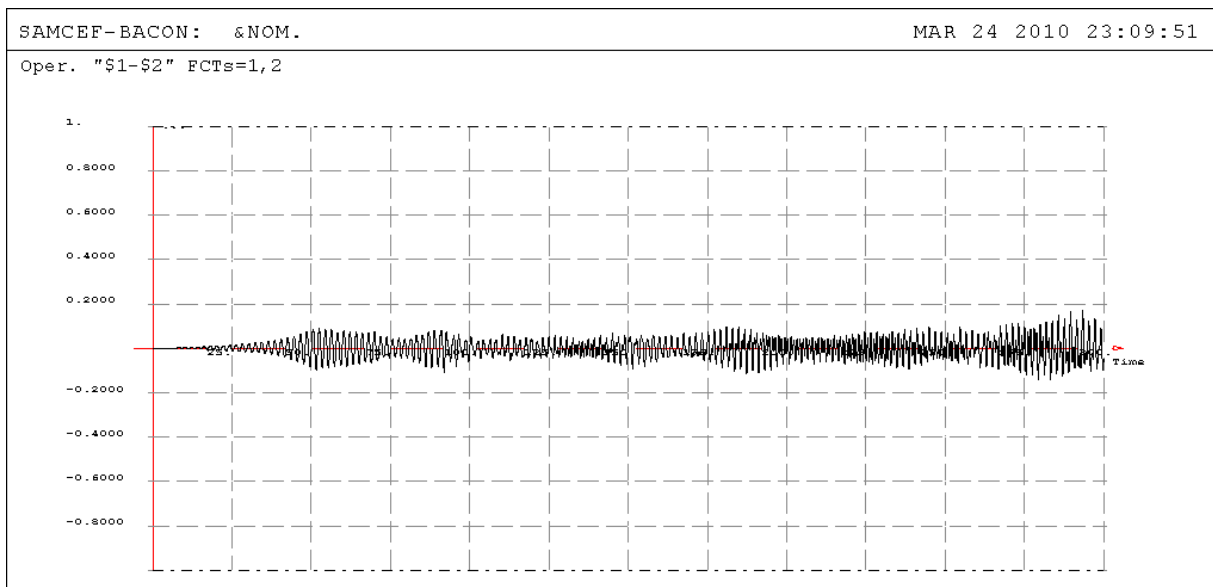


Figure 4-5. Model 1: snaking mode between opposite end subspans.

4.1.2.3 Subspan mode

In the **Reference Model**, the subspan mode is rapidly decaying becoming degenerated. On the contrary, in the **Model 1**, the subspan model is very pronounced; its amplitude is about 7 times greater.

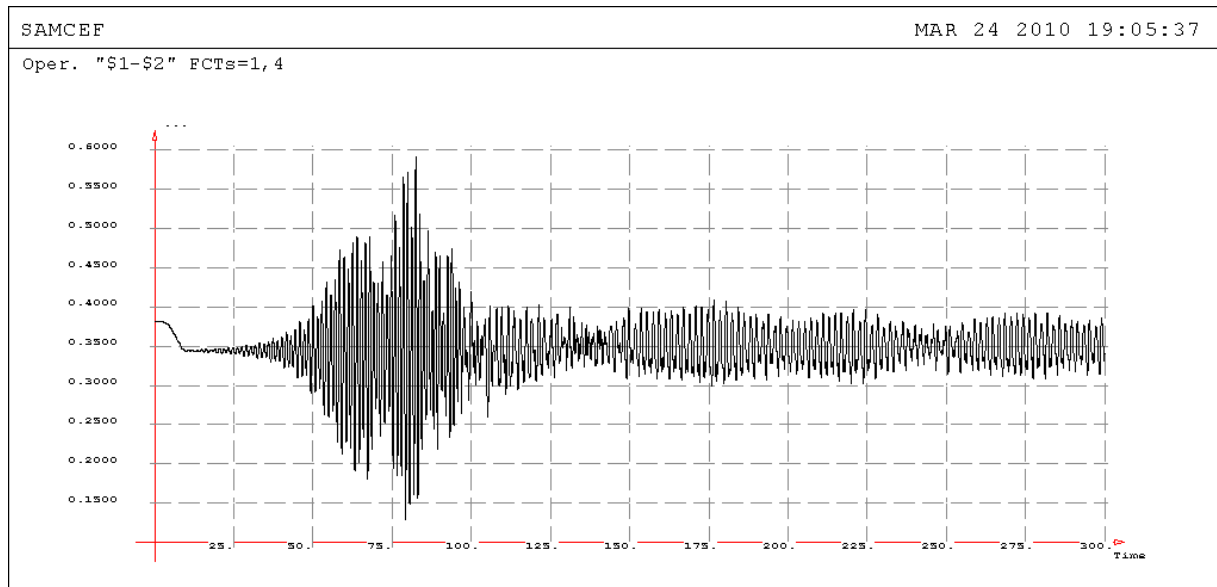


Figure 4-6. Reference model: subspan mode oscillations in the end subspan

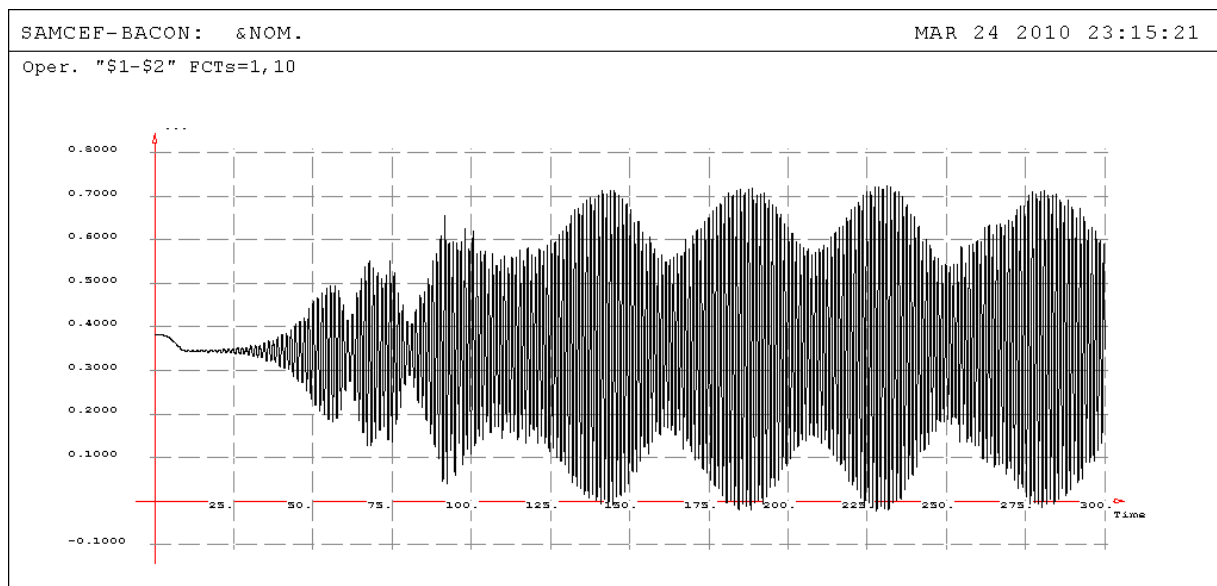


Figure 4-7. Model 1: subspan mode oscillations in the end subspan

4.1.2.4 Global subconductor orbits

The global orbits of subconductors give an image of a quite developed oscillation. However, in the Reference Model (no torsion), the leeward conductor ellipse is clearly degenerated. Instead, in **Model 1** (torsion 160 Nm/rad), the orbits are classical: ellipses made by the leeward conductor, and a damped orbit by the windward one.

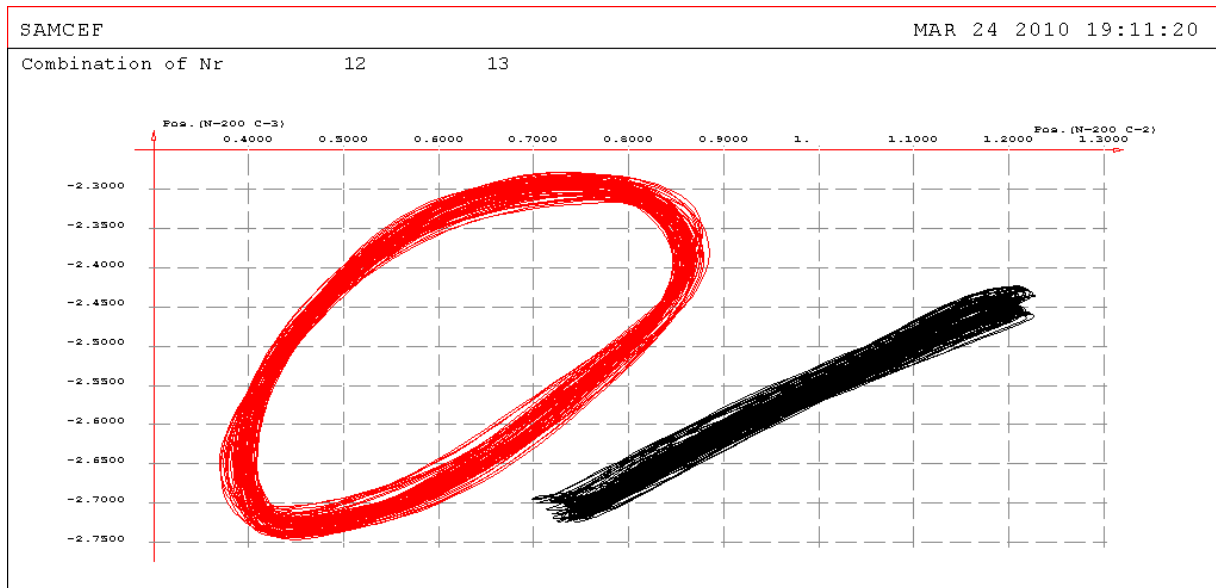


Figure 4-8 Reference model: global orbits. Left orbit – windward subconductor, right orbit – leeward

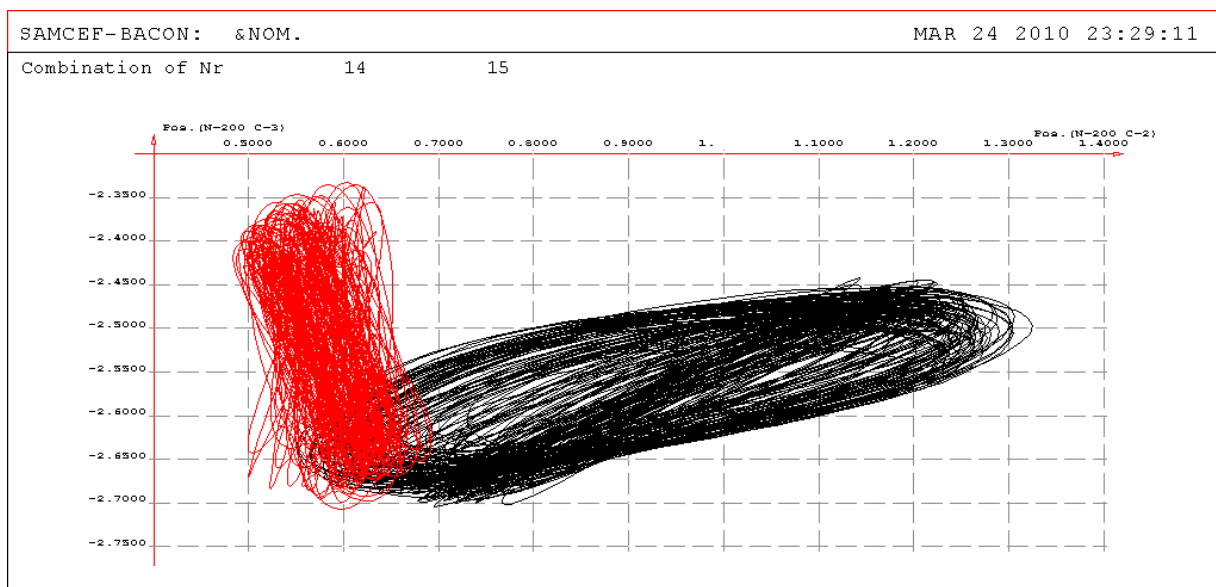


Figure 4-9. Model 1: global orbits. Left orbit – windward subconductor, right orbit – leeward

4.1.2.5 Relative orbits

In the Reference Model, the relative orbit of leeward conductor oscillation is clearly disturbed by the snaking mode giving more global oscillation. In the **Model 1**, the ellipse is perfectly representing the oscillation in the subspan mode. Note, that it reaches sometimes even negative Y distance, which means that subconductors may become crossed over.

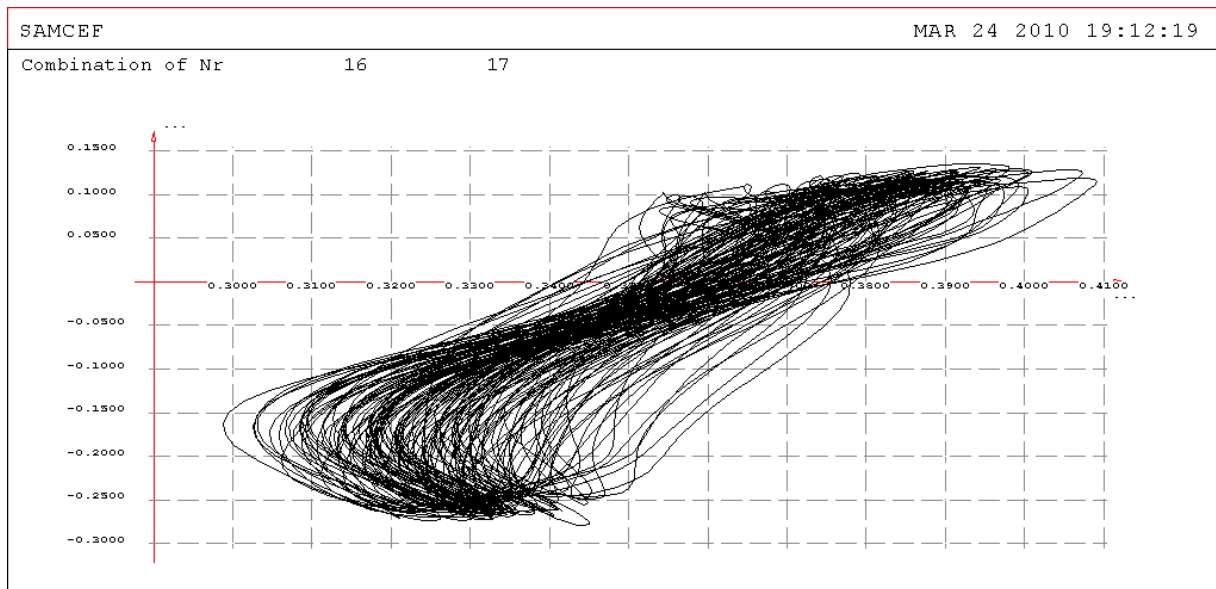


Figure 4-10. Reference model: relative orbit in the end subspan

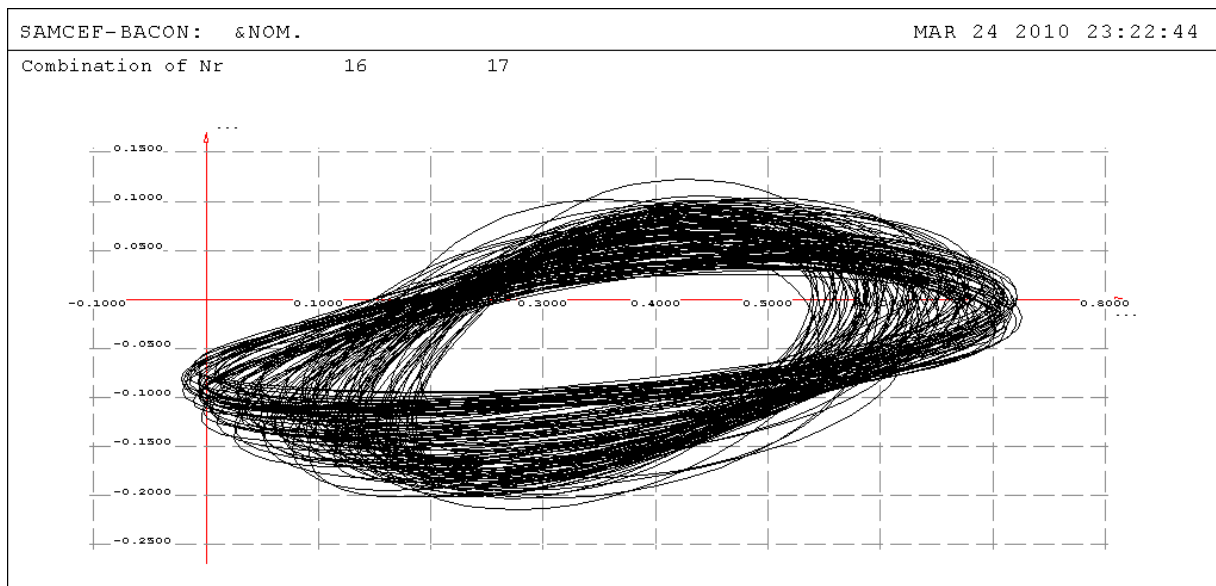


Figure 4-11. Model 1: relative orbit in the end subspan

4.1.3 Synthesis

Out of framework of above demonstration it may be noticed, that further increase of torsional stiffness (gone, in this study, up to 400 Nm/rad) leads to complete synchronization of the subspan modes in the end subspans (1 and 3).

From the standpoint of subspan oscillation, the torsional stiffness therefore plays a stabilizing effect as it is not, within this model, affected by energy input due to the wake. Taking some part of motion energy, the torsion is also locked by the spacers within the subspan, thus making the subspan mode more pronounced. However, depending on its value, it may still allow for some motion desynchronization leading to a snaking of limited amplitude.

4.2 Effect of spacer articulation

This comparative study, still within a model of a twin bundle, aims at validating one of numerous spacer concepts – an articulated twin spacer. An example of such structure is presented in the figure below.

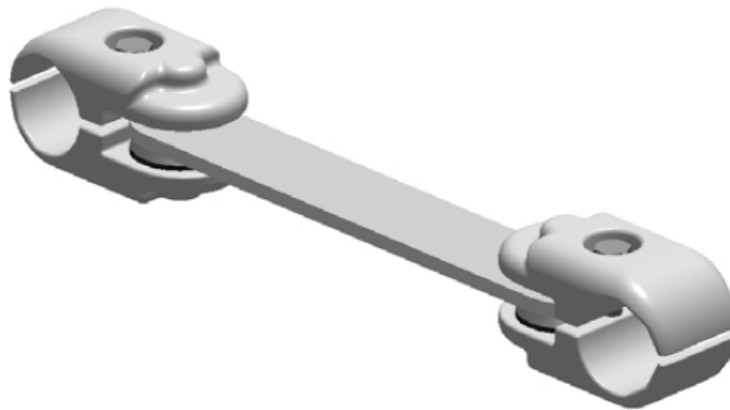


Figure 4-12. Articulated spacer damper

Unlikely the above concept, it was only the articulation modelled but not the damping bush insert, since its properties are not known.

4.2.1 Model description

The model of spacer as shown in Figure 3-5 has been slightly modified for this study. The clamp connections with the spacer arm were modelled by the cylindrical bush elements having free rotation around vertical axes (in local spacer coordinate frames).

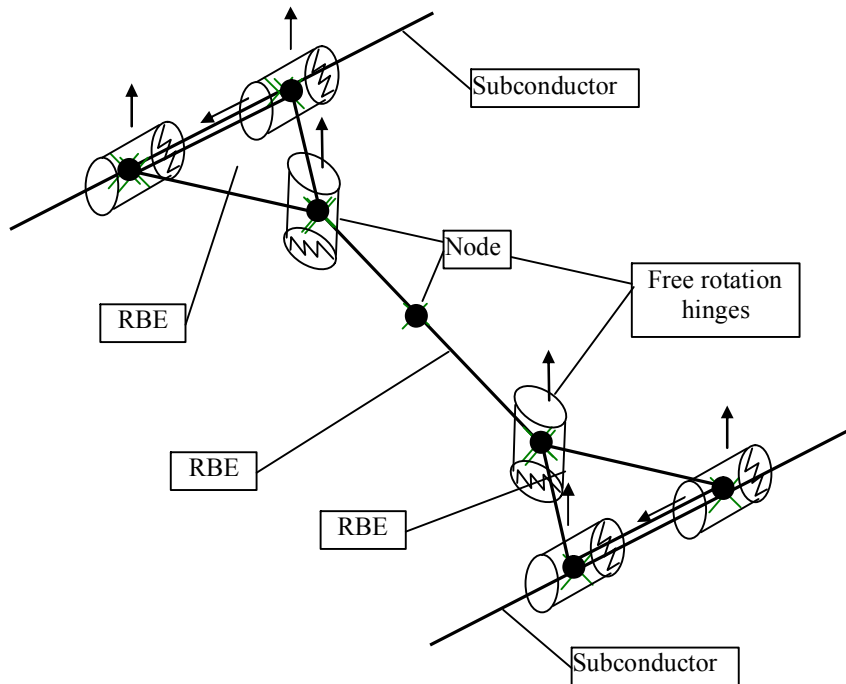


Figure 4-13. Model of articulated twin spacer

The line span used in the comparison has the following parameters:

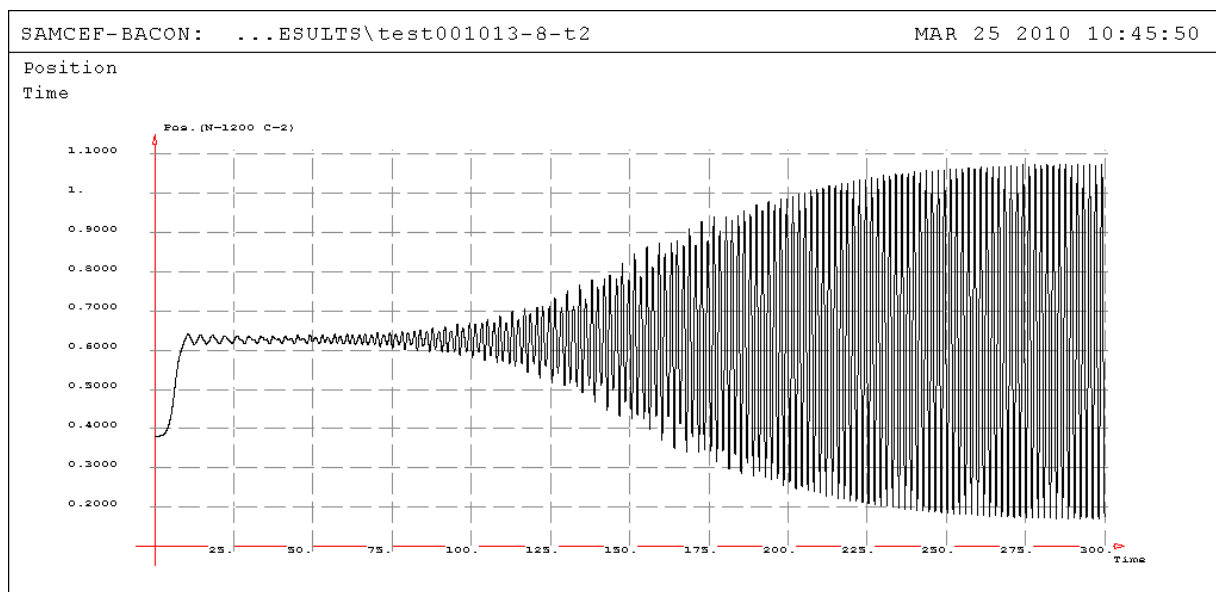
Parameter	Reference model	Model 1
Torsional stiffness	160 Nm/rad	
No. of subconductors	2	
Span length	240	
Subspan composition	80/80/80	
Initial Tension, kN (windward/leeward)	19 / 19.1	
Conductor diameter, mm	25.4	
Conductor mass per unit length, kg/m	1.25	
Subconductors spacing, Y/D Z/D	15 -2.5	
Spacer type	Rigid	Articulated
Wind speed, m/s	8	

4.2.2 Results

4.2.2.1 Global oscillation

As seen from comparison of Reference Model (rigid spacer) and Model 1 (articulated spacer), the global oscillation in the latter case is clearly less: it did not go completely due to the whole system tuned up to the worst case of WIO, however, the oscillation amplitude is more than 2 times less (~ 1 m for Reference Model, and 0.45 m for Model 1).

(a)



(b)

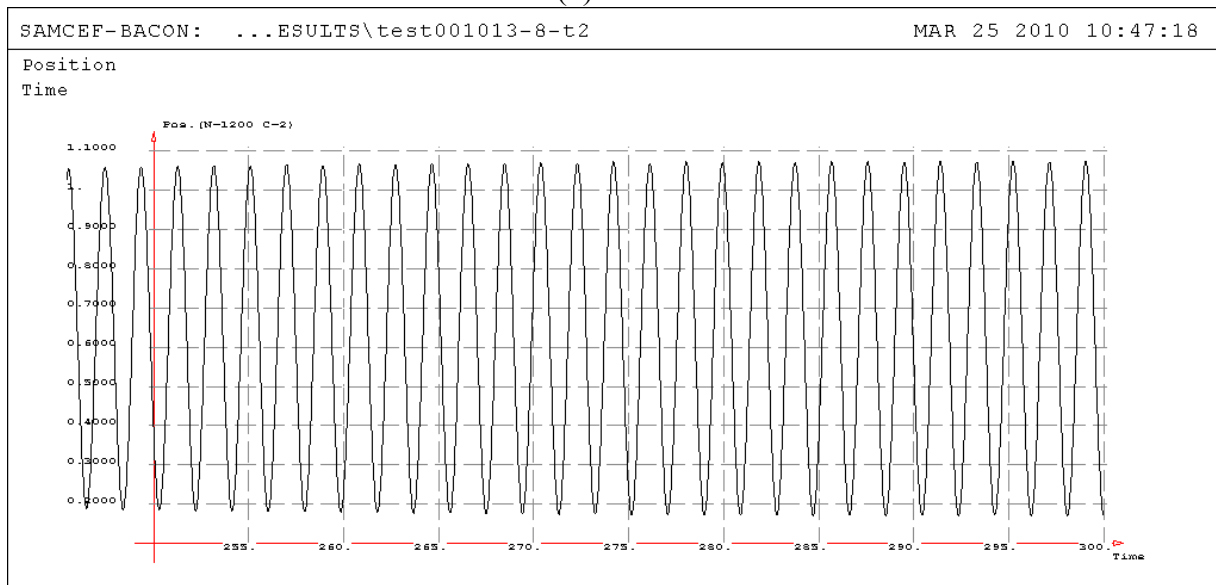
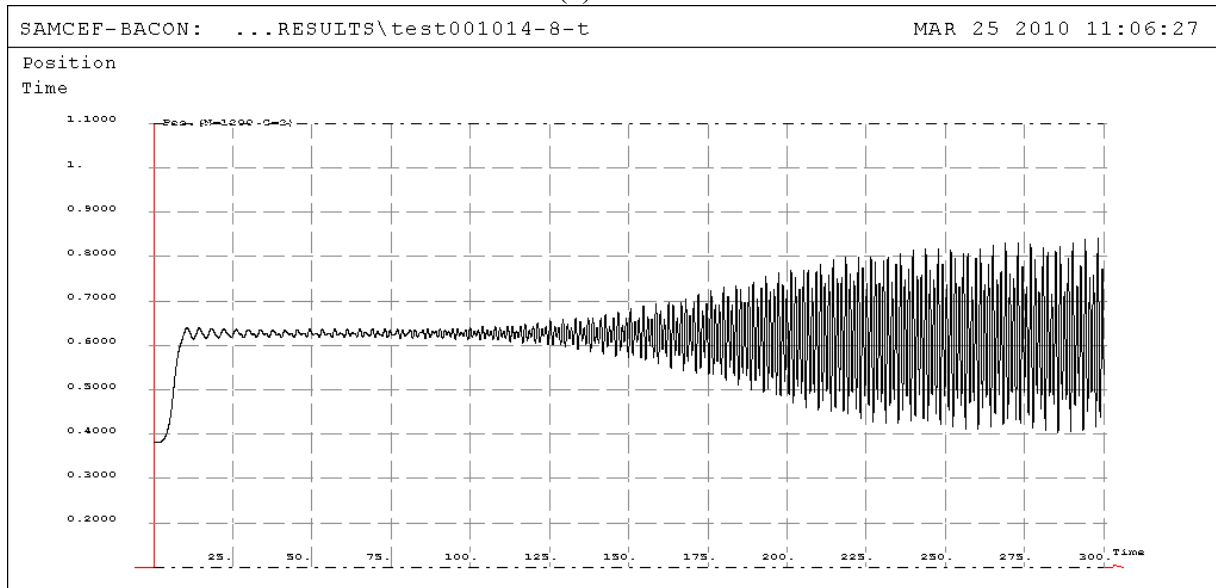


**Figure 4-14. Reference model: Y oscillations in the middle of end subspan:
(a) overall exposure, (b) zoom to 50 s**

(a)



(b)

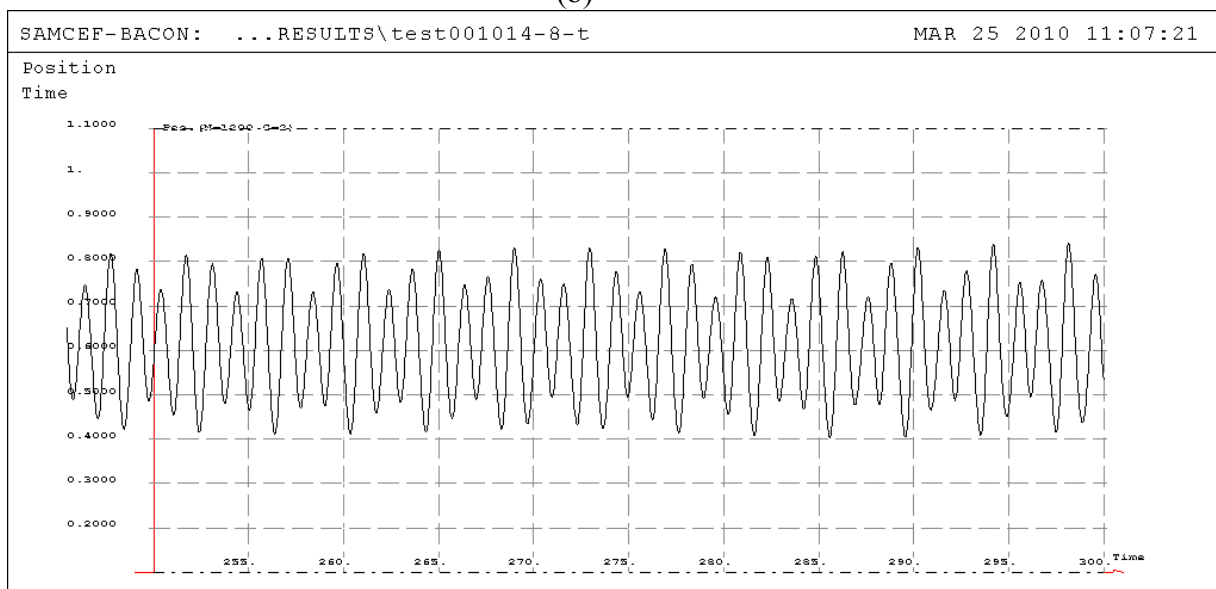


Figure 4-15. Model 1: Y oscillations in the middle of end subspan: (a) overall exposure, (b) zoom to 50 s

4.2.2.2 Snaking mode

With articulated spacer, the snaking mode is clearly not dominant: desynchronization of oscillations in the opposite subspans reaches about 1.8 m with rigid spacers, while with articulated ones it makes about 0.2 m, i.e. about 9 times less.

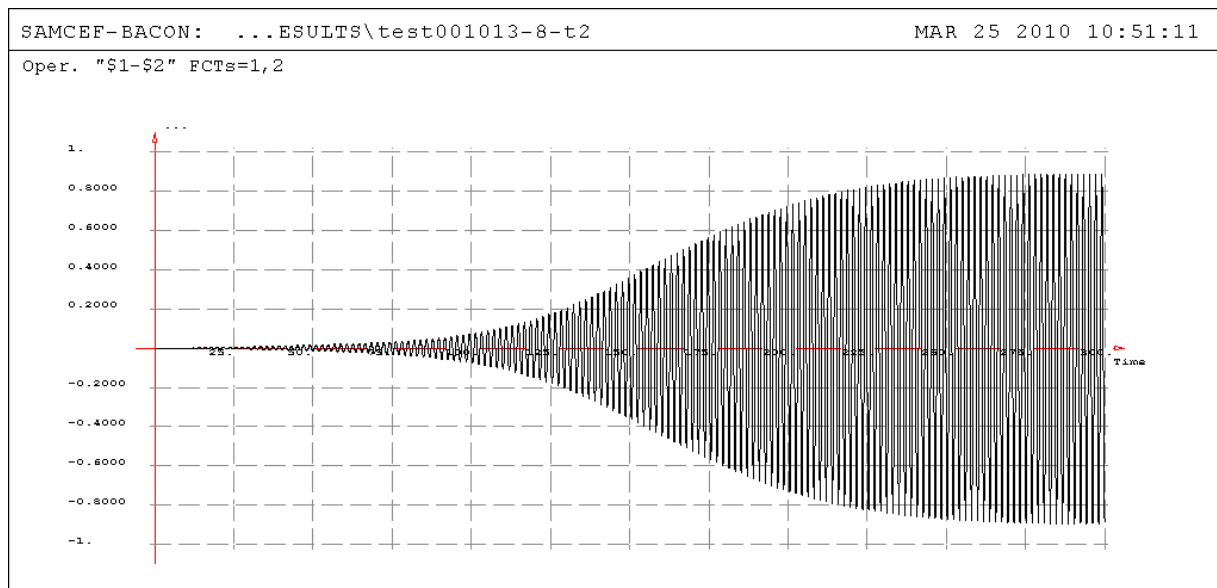


Figure 4-16. Reference model: snaking mode between opposite end subspans.

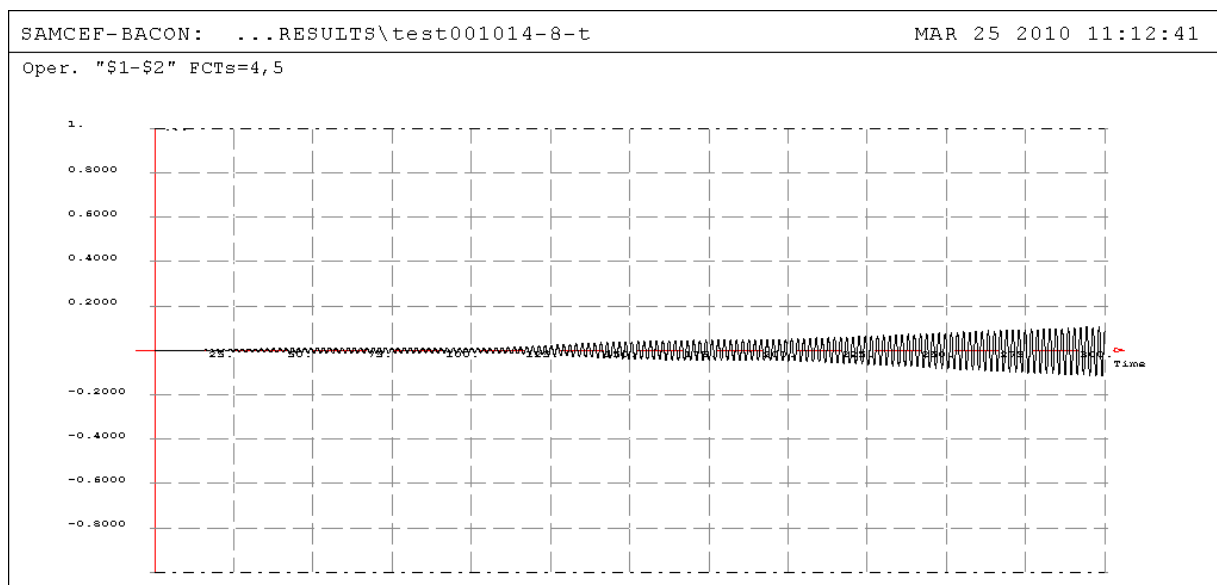


Figure 4-17. Model 1: snaking mode between opposite end subspans.

4.2.2.3 Subspan mode

Contrary to above, the subspan mode is more pronounced with articulated spacer: its Y amplitude is about 0.35 m against just 0.03 m for the rigid spacer. As it will be seen, however, the subspan oscillation in the latter case is more oriented vertically. Anyway, the amplitude remains rather low.

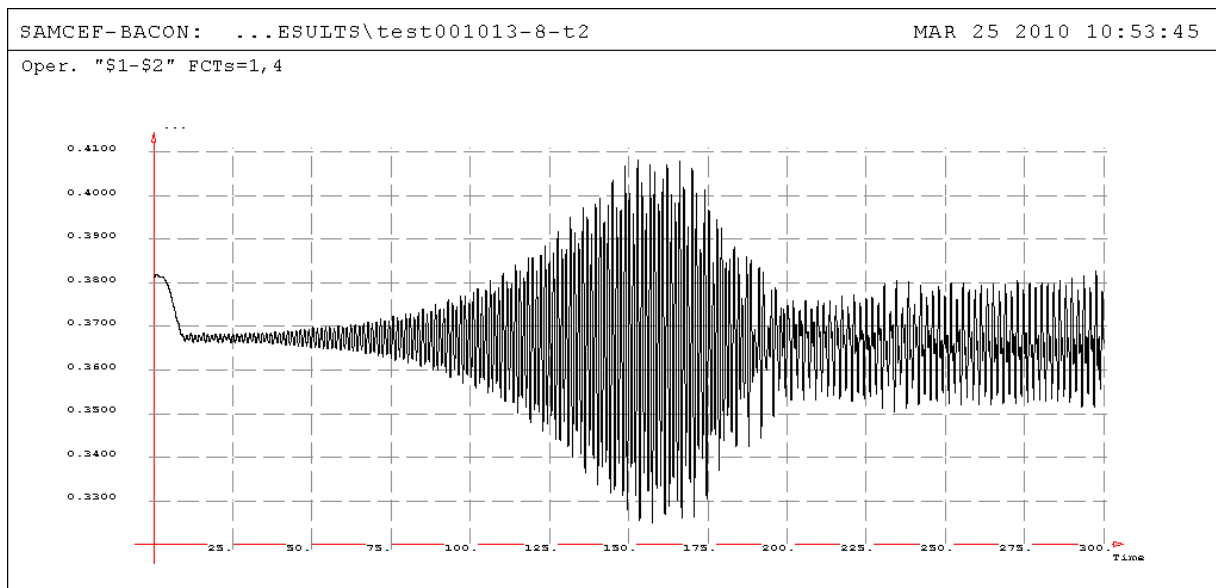


Figure 4-18. Reference model: subspan mode oscillations in the end subspan

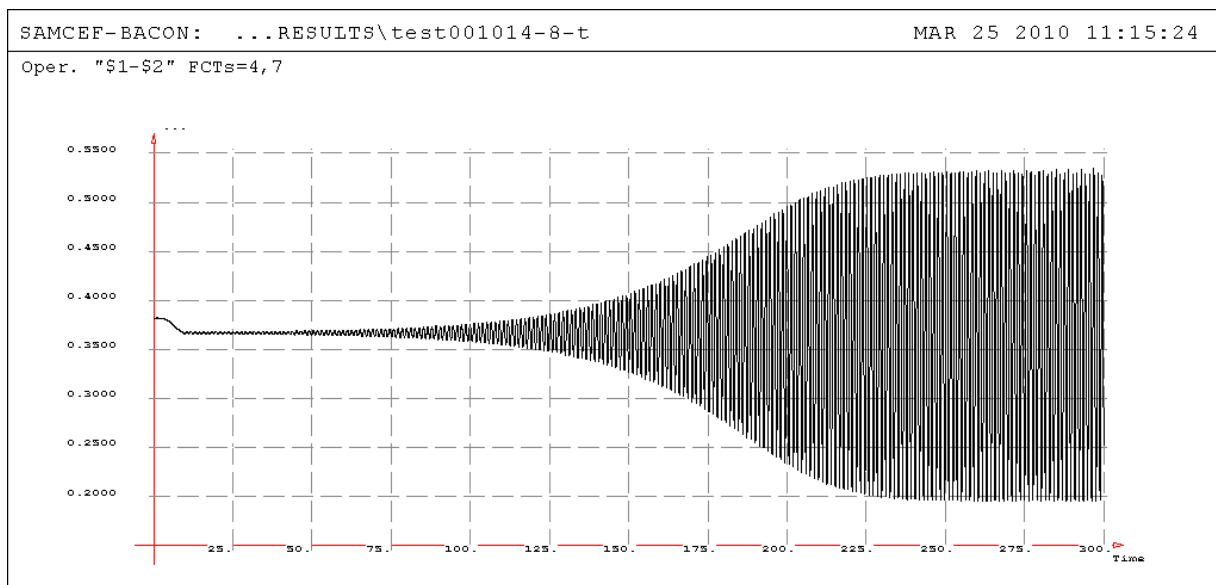


Figure 4-19. Model 1: subspan mode oscillations in the end subspan

4.2.2.4 Global subconductor orbits

Same as in Section 4.2.2.1, the global oscillation image is quite more severe for the rigid spacers; although the articulated one exhibits a clear subspan mode, the amplitude remains moderate.

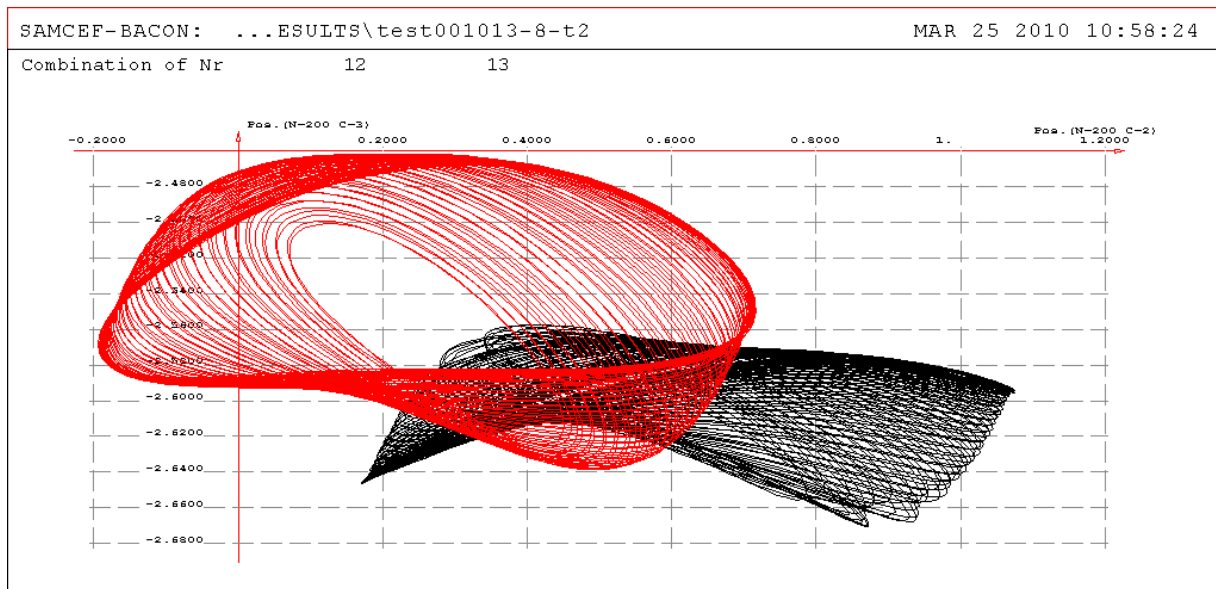


Figure 4-20. Reference model: global orbits. Left orbit – windward subconductor, right orbit – leeward

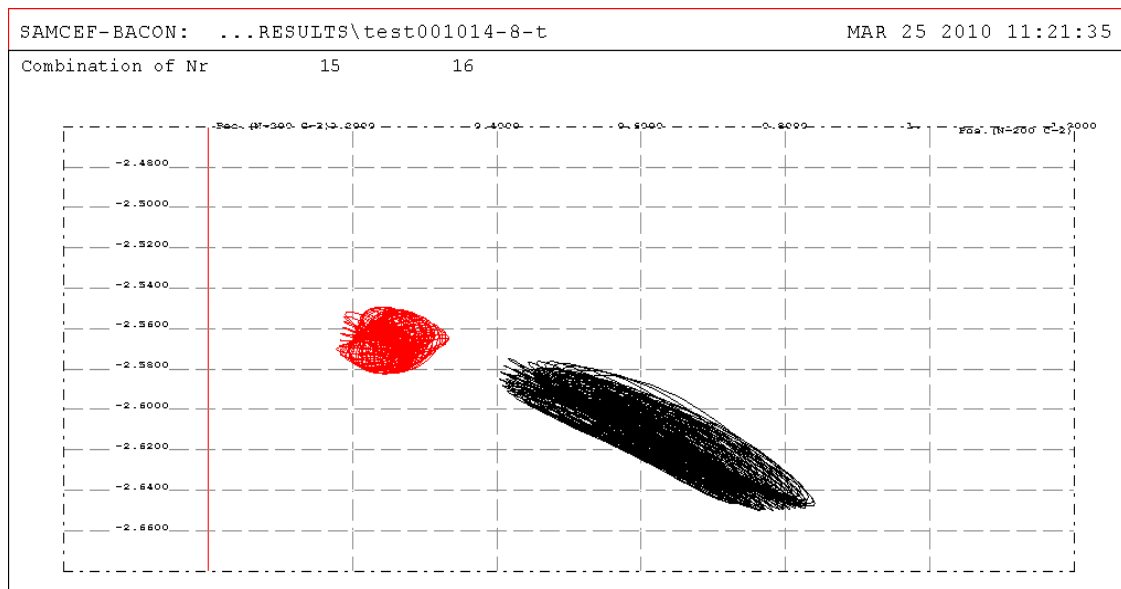


Figure 4-21. Model 1: global orbits. Left orbit – windward subconductor, right orbit – leeward

4.2.2.5 Relative orbits

The motions of leeward subconductor with respect to the windward one show well developed subspan cycle in case of the articulated spacer. Its position remains far enough from the windward one.

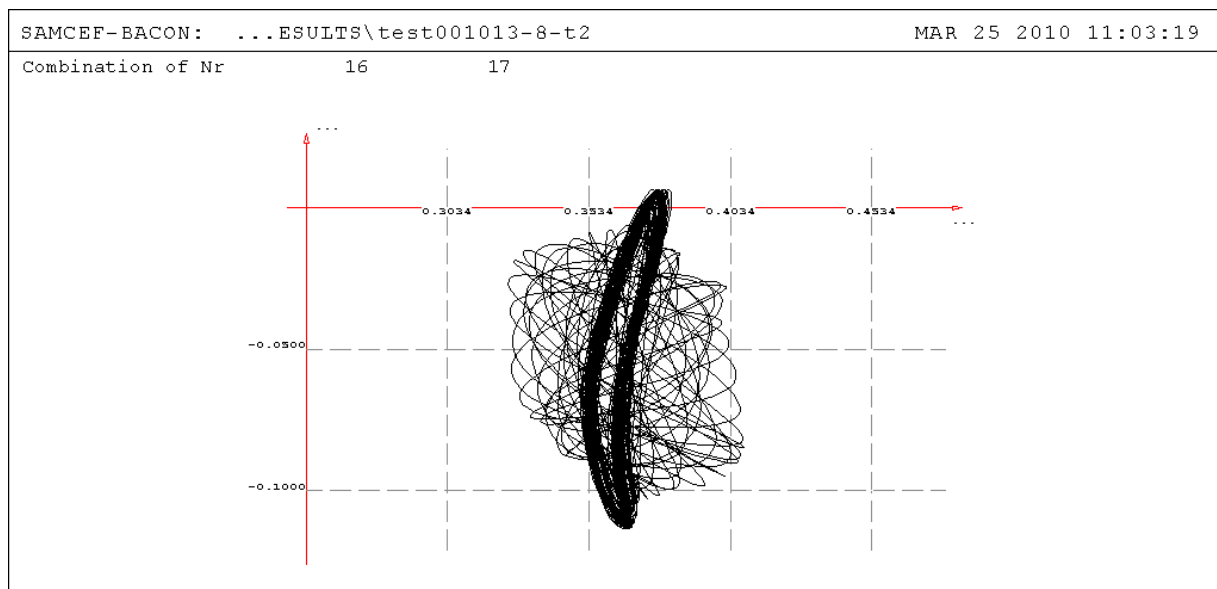


Figure 4-22. Reference model: relative orbit in the end subspan (identical axes)

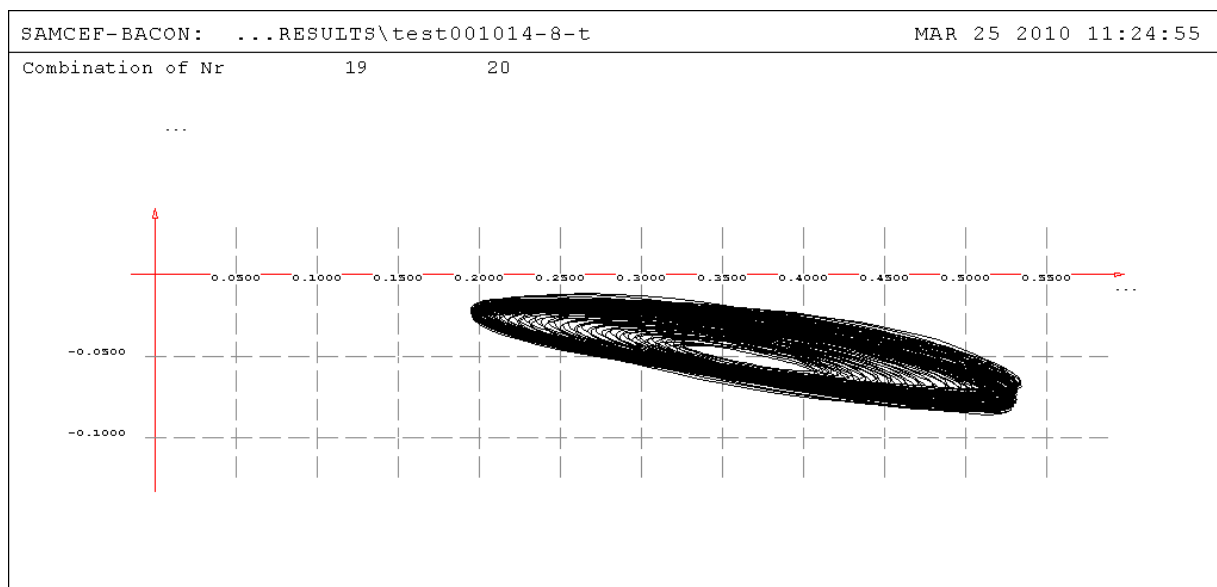


Figure 4-23. Model 1: relative orbit in the end subspan (identical axes)

4.2.3 Synthesis

Above results demonstrate a clear positive effect of the articulated spacer. Within this context, the amplitudes are decreased, as a whole, by about two times. Articulation does not remove the subspan mode, which is the main bearer for the energy imparted by the wake. However, it is partially damped by the windward conductor and remains moderate.

Another consequence of this comparison concerns the wind velocity. Note, that in this example it is 8 m/s – a value quite low, which nevertheless allows effective set up of WIO, thus proving the whole effectiveness of the developed wake interaction model.

4.3 Effect of staggered spacers placement

Until here, the model used in comparisons was a 240 m span equipped with two spacers. Intentionally this was a scheme ineffective against WIO in order to output their most pronounced values. In this comparison, the more realistic case will be dealt with: number of spacers reaches three, a number rather recommended for the 200-250 m spans. Furthermore, a general strategy to reduce the WIO is investigated here with uneven spacers' placement.

4.3.1 Model description

The uneven spacers placement scheme was selected out from CIGRE source (see Section 5.1.5) as follows:

Span length (m)	Nr of spacers	Relative subspan length / span length
180 - 250	3	0.167; 0.334; 0.333; 0.166

The subspan schemes are investigated are illustrated in Figure 4-24:

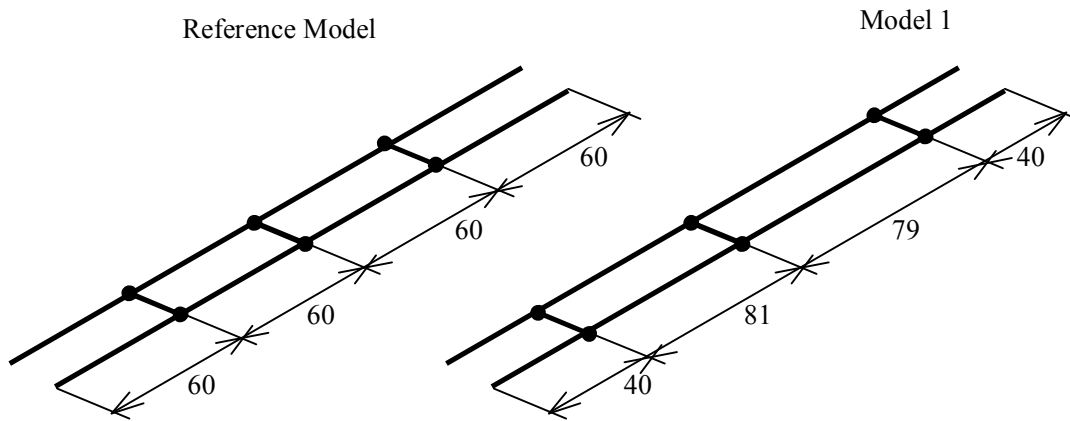


Figure 4-24. Models used in different subspan length comparison

The model parameters are as follows:

Parameter	Reference model	Model 1
Torsional stiffness	No	
No. of subconductors	2	
Span length	240	
Subspan composition	60/60/60/60	40/81/79/40
Initial Tension, kN (windward/leeward)	19 / 19.1	
Conductor diameter, mm	25.4	
Conductor mass per unit length, kg/m	1.25	
Subconductors spacing, Y/D Z/D	15 -2.5	
Spacer type	Rigid	
Wind speed, m/s	12	

4.3.2 Results

4.3.2.1 Global oscillation

Global oscillation in case of staggered placement of spacers brings to overall oscillations reduction about 2 times.

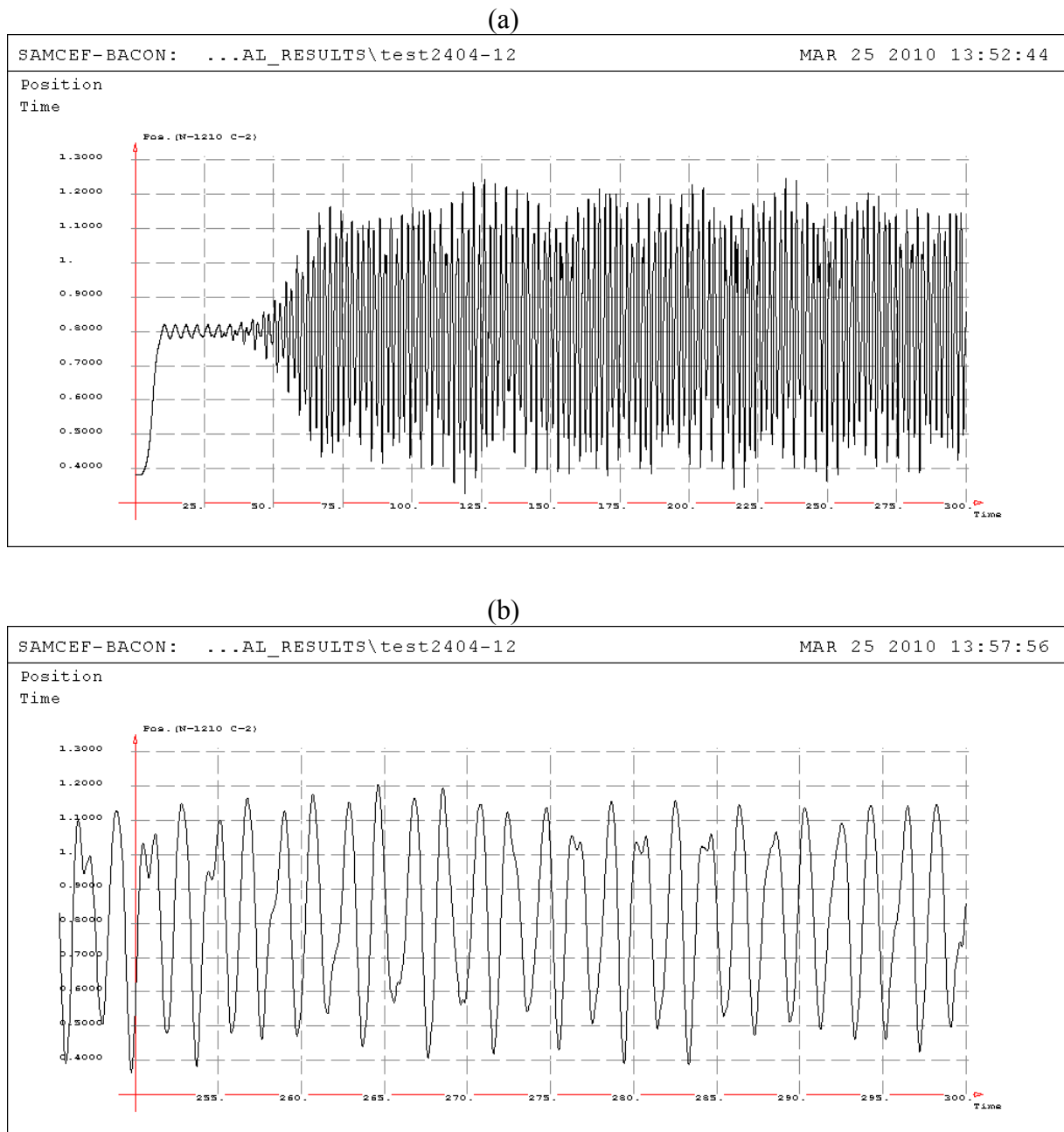
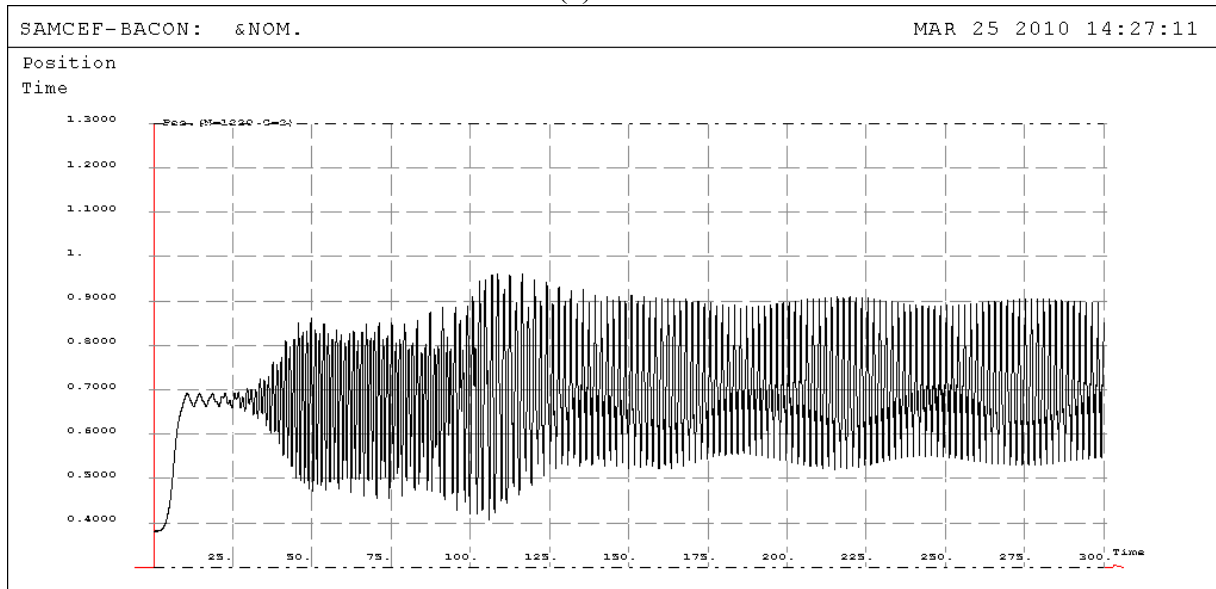


**Figure 4-25. Reference model: Y oscillations in the middle of end subspan:
(a) overall exposure, (b) zoom to 50 s**

(a)



(b)

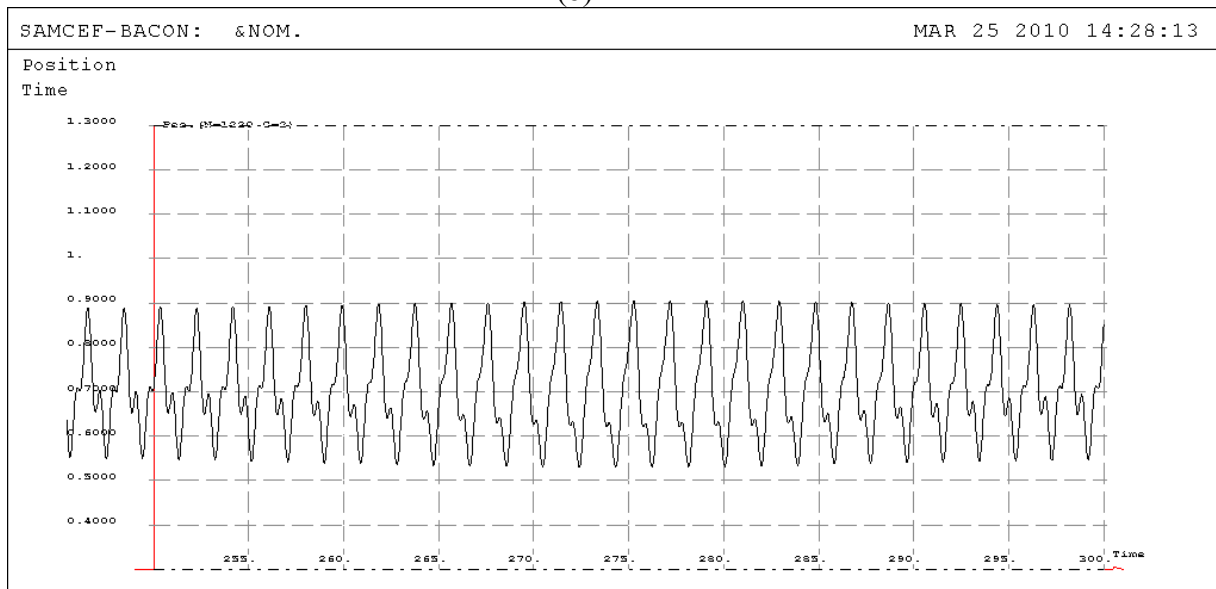


**Figure 4-26. Model 1: Y oscillations in the middle of end subspan:
(a) overall exposure, (b) zoom to 50 s**

4.3.2.2 Snaking mode

The snaking amplitude is also decreased in case of staggered placement by about 1.5 times. However, it reveals to be more stabilized (compare Figure 4-28 to Figure 4-27).

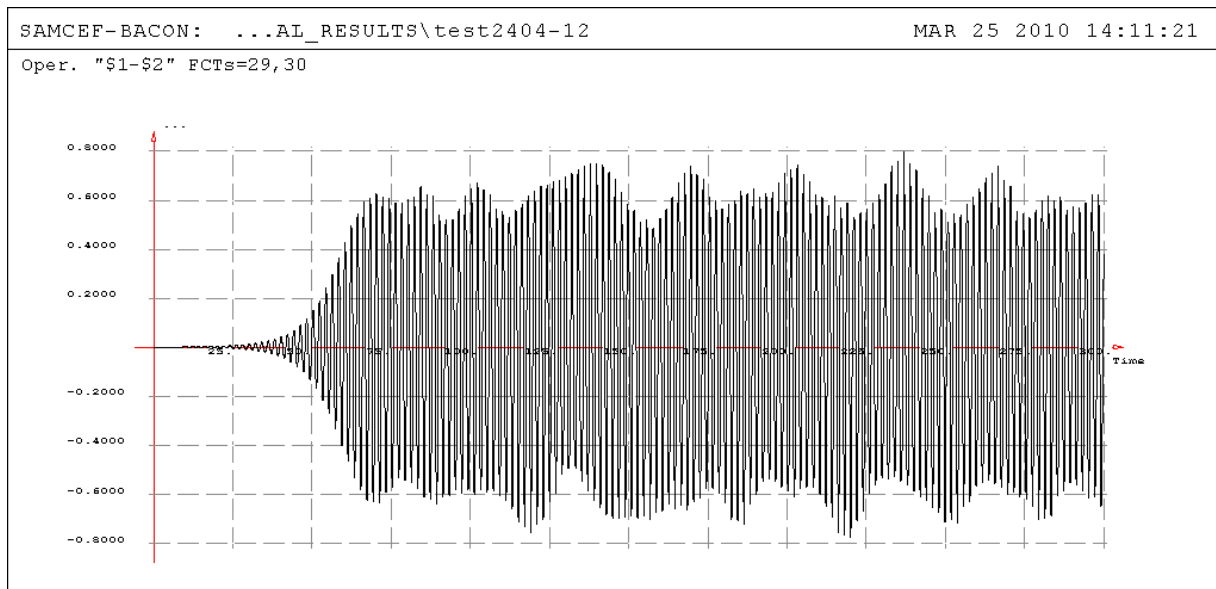


Figure 4-27. Reference model: snaking mode between opposite end subspans.

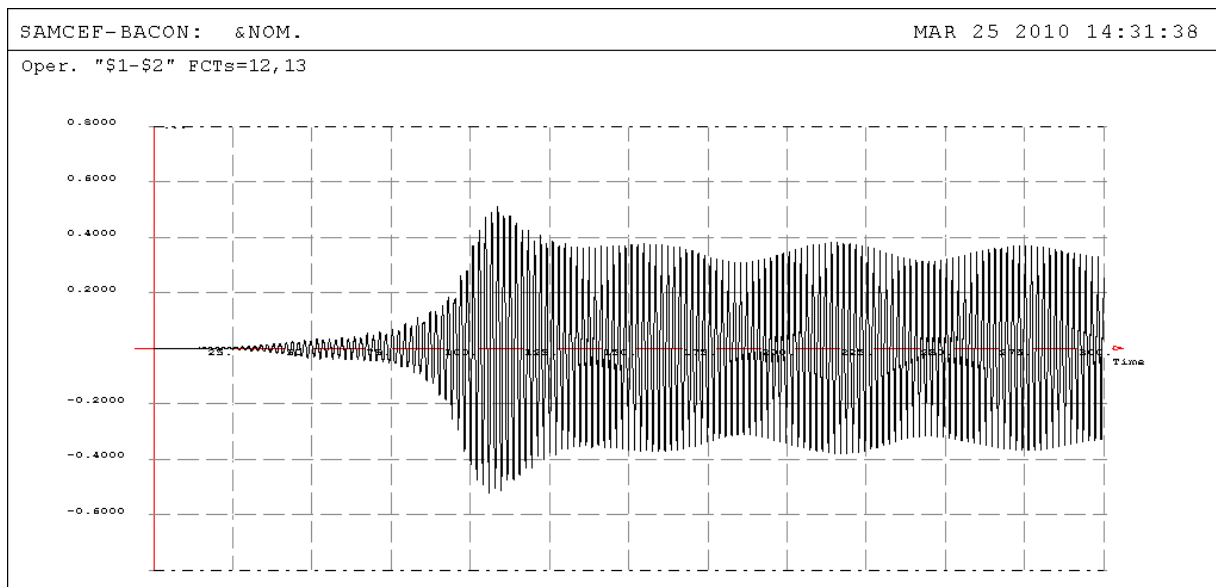


Figure 4-28. Model 1: snaking mode between opposite end subspans.

4.3.2.3 Subspan mode

There is no considerable reduction in subspan mode amplitudes, except that maximum values are reduced in Model 1. The oscillation becomes more stable in this case.

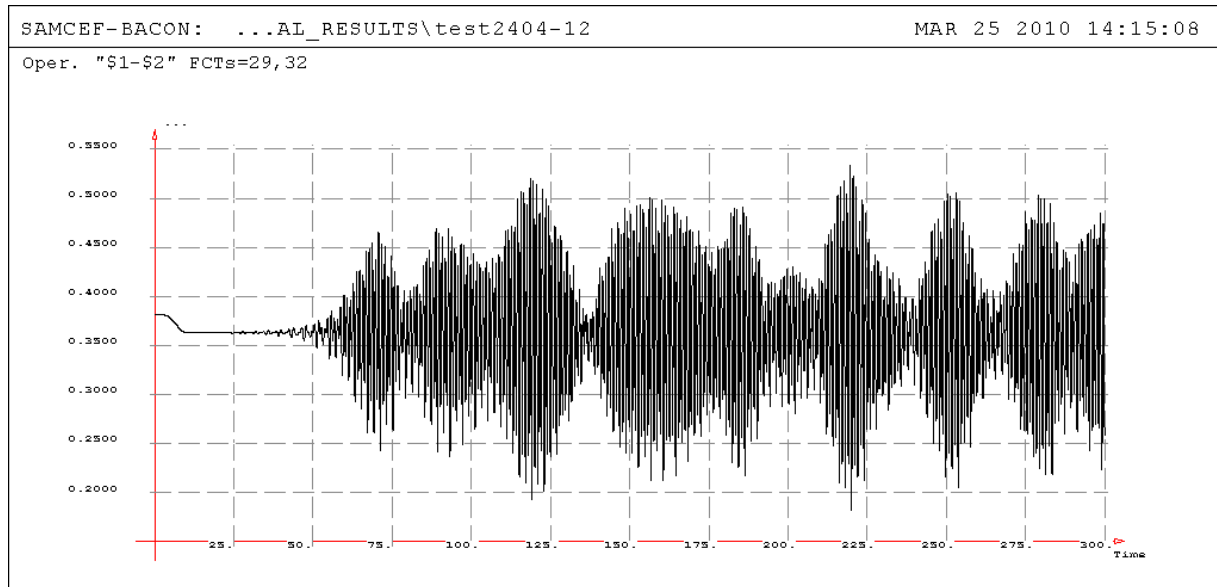


Figure 4-29. Reference model: subspan mode oscillations in the end subspan

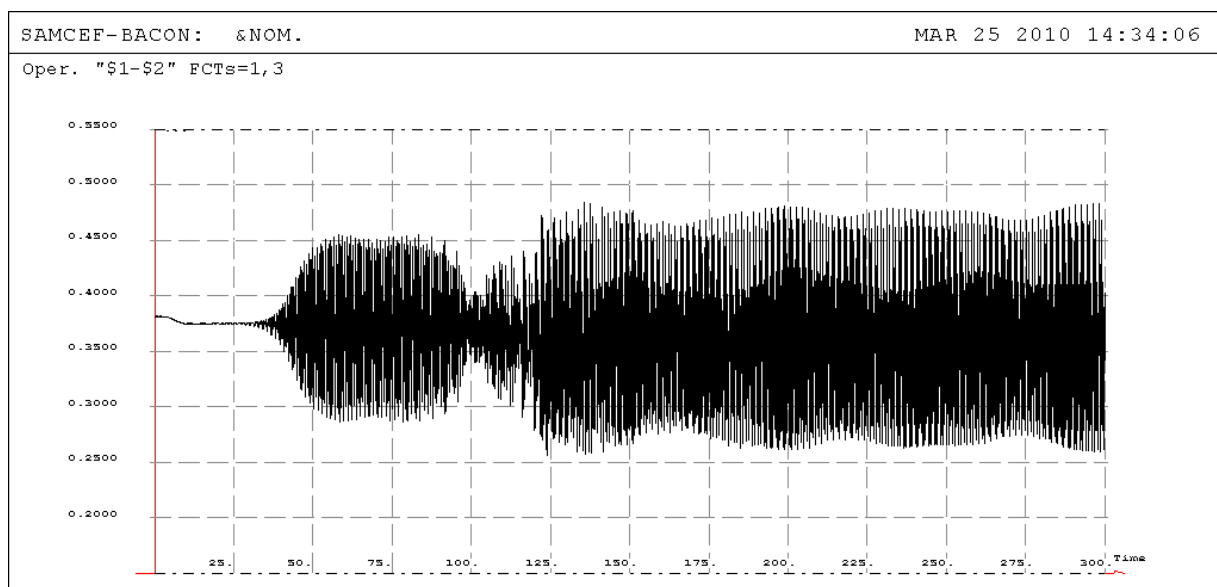


Figure 4-30. Model 1: subspan mode oscillations in the end subspan

4.3.2.4 Global subconductor orbits

Global oscillation orbits show clearly less amplitude of oscillation in staggered placement. However, this is not a reason to conclude that overall oscillation has reduced, as below the end subspan is compared whose length is 1.5 times less.

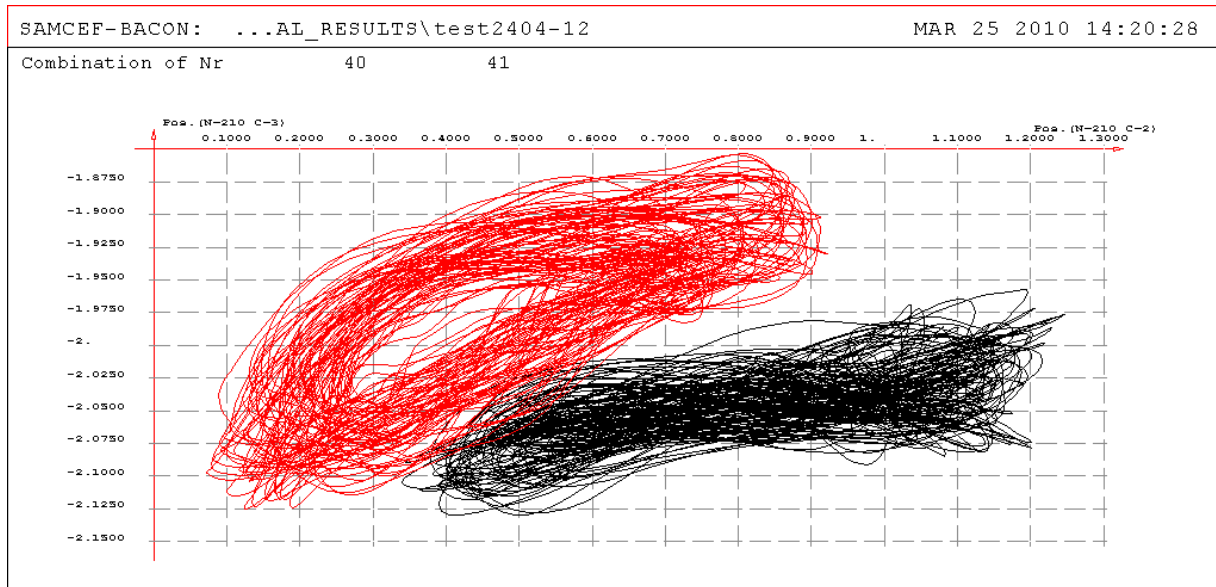


Figure 4-31. Reference model: global orbits. Left orbit – windward subconductor, right orbit – leeward

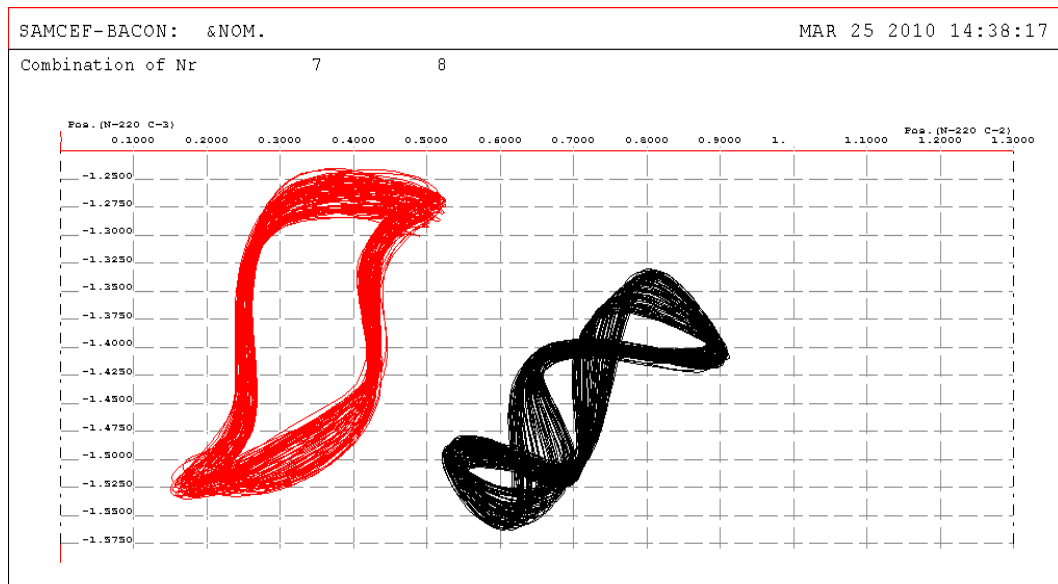


Figure 4-32. Model 1: global orbits. Left orbit – windward subconductor, right orbit – leeward

4.3.2.5 Relative orbits

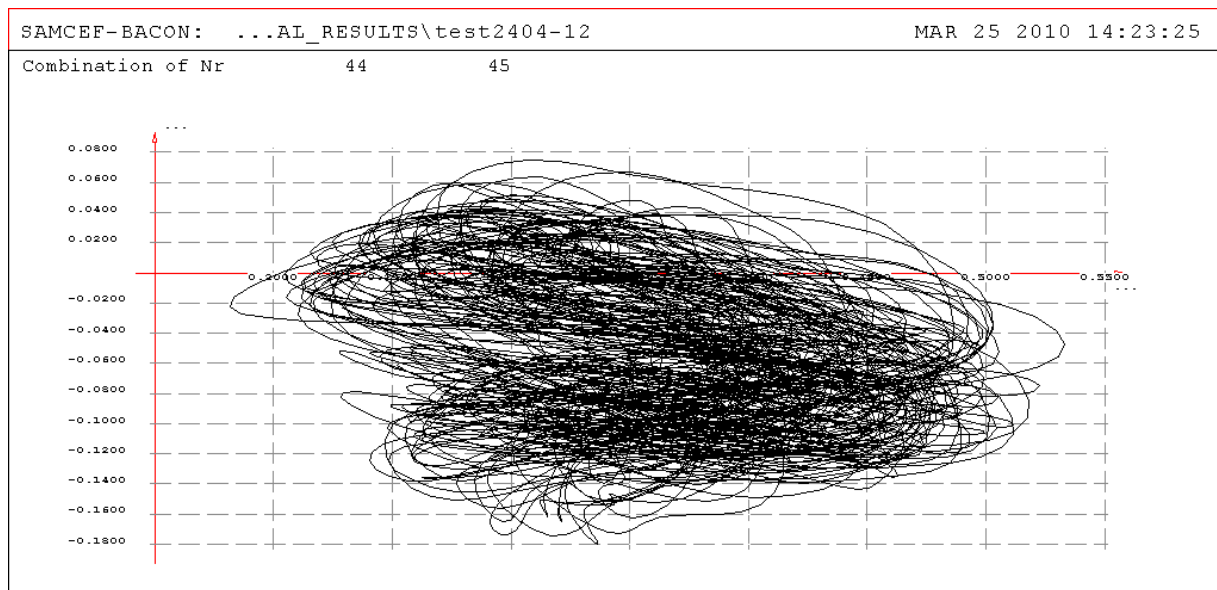


Figure 4-33. Reference model: relative orbit in the end subspan (identical axes)

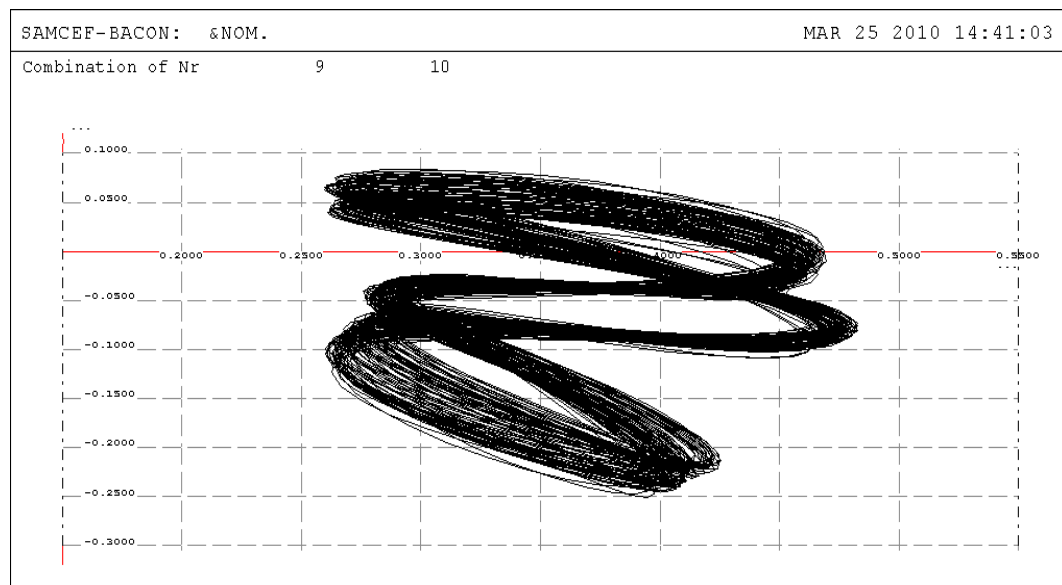


Figure 4-34. Model 1: relative orbit in the end subspan (identical axes)

4.3.3 Synthesis

The staggered spacer placement reveals to be a quite effective means to attenuate the WIO. Clearly, the oscillation modes become coupled and higher subspan modes become involved into response, as seen in global orbits (Figure 4-32) but also the relative subspan orbit (Figure 4-34). The resulting oscillation amplitudes with staggered placement are reduced.

4.4 Combined staggering + spacer damper

This comparison involves a prototype model of twin spacer damper and it aims at verifying whether its use does impart any effect onto the WIO when used together with the staggered placement scheme.

4.4.1 Model description

The model for comparison is based on the same twin bundle 240 m, and staggering scheme is the same as in previous example. The difference with respect to the latter is in the formulation of cable element which is, like in Section 4.2, enables torsional stiffness by coupling with nonlinear bushes. Furthermore, the bending stiffness is also added with the bush element, its exemplary value is taken from the data of ACAR-1300 conductor.

The finite element model of the spacer damper is shown below in Figure 4-35. Its main properties are:

Arm mass	0.25 kg
Central body mass	1 kg
Tensional hinge stiffness	0.82e6 N/m
Rotational hinge stiffness	294.3 Nm/rad
Torsional damping factor	0.32
Torsional damping value	1.32 N m s/rad

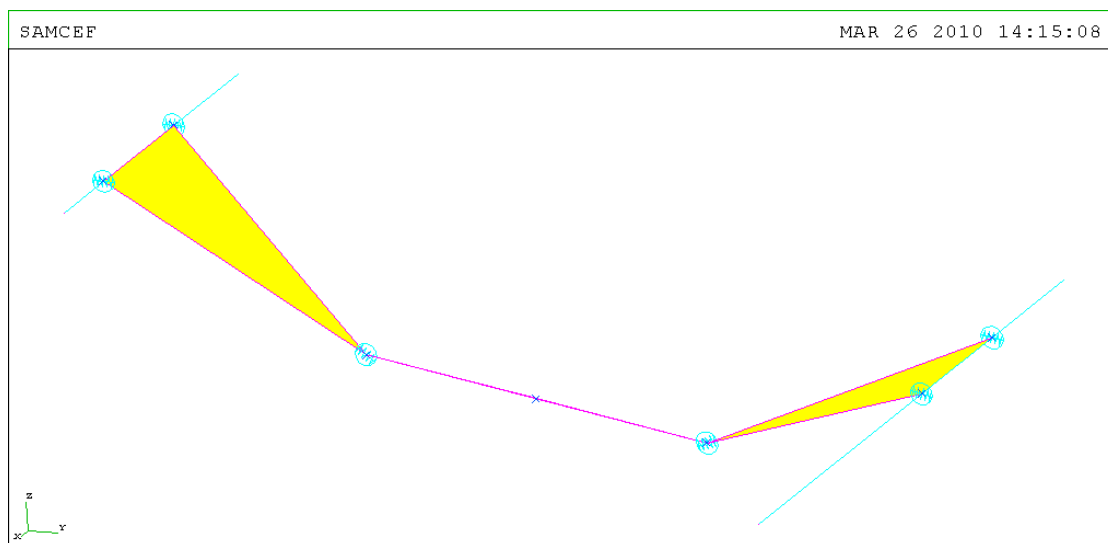


Figure 4-35. SAMCEF model of twin spacer damper

Span model parameters are as follows:

Parameter	Reference model	Model 1 (staggering)	Model 2 (staggering + spacer damper)
Conductor torsional stiffness	160 Nm/rad		
Conductor bending stiffness	64.3 N/m		
No. of subconductors	2		
Span length	240		
Subspan composition	60/60/60/60	40/81/79/40	40/81/79/40
Initial Tension, kN (windward/leeward)	19 / 19.1		
Conductor diameter, mm	25.4		
Conductor mass per unit length, kg/m	1.25		
Subconductors spacing, Y/D Z/D	15 -2.5		
Spacer type	Rigid	Rigid	Spacer Damper
Wind speed, m/s	12		

4.4.1.1 Note about instability index

Results' processing, moreover to the motion diagrams, is added with the study of response spectra and calculation of Global Instability Index. This Index, devised by Hydro-Quebec engineers Houle et al., has been used in numerous study of WIO done by Hardy, Van Dyke and other researchers [25], [26] and [20], and is defined as

$$I.I. = \sum_j \frac{l_j}{60} \sum_i \left(\frac{A_{ij} f_{ij}}{80} \right)^2$$

Where l_j (m) is the length of the j-th subspan, A_{ij} (mm) is the root mean square (R.M.S.) value of the i-th component of the subconductor horizontal displacement at midsubspan in the spectrum of oscillations and f_{ij} (Hz) is the associated frequency. The quantities 60 (m) and 80 (mm/s) are used to normalize the index with respect to subspan length l_j and product $A_{ij} f_{ij}$ respectively. It is to be noted that 80 mm/s corresponds approximately to the R.M.S. value of the fatigue endurance limit of ACSR conductors expressed in terms of $f y_{\max}$. In basic formulation, the inner summation extends to all admissible components within the spectrum $0.6 \text{ Hz} < f_{ij} < 2.75 \text{ Hz}$ while the outer summation extends to all subspans over the test span. Here a modified frequency range is used, $0.5 \text{ Hz} < f_{ij} < 2.75 \text{ Hz}$, in order to cover the snaking mode obtained in these simulations.

4.4.2 Results

4.4.2.1 Global oscillation

The oscillation is sensibly damped with staggered placement (Figure 4-37); effect of spacer damper is not clearly pronounced (Figure 4-38).

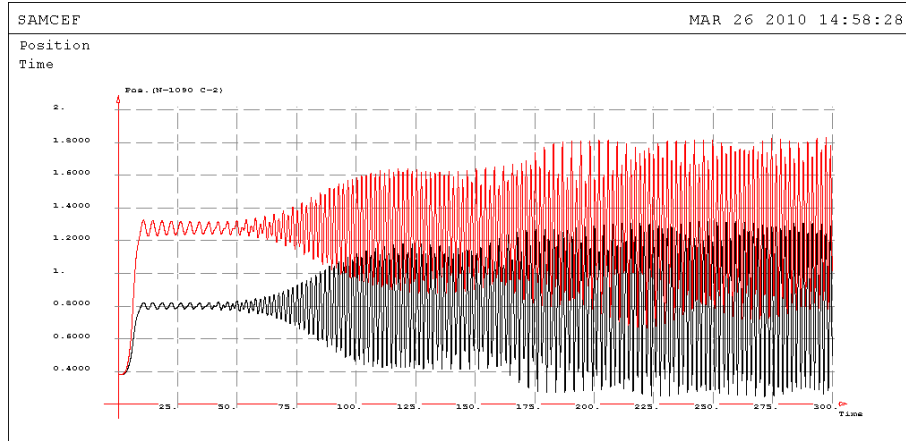


Figure 4-36. Reference model: global Y motion – subspan 1 (curve below), subspan 2 (curve above). Global exposure

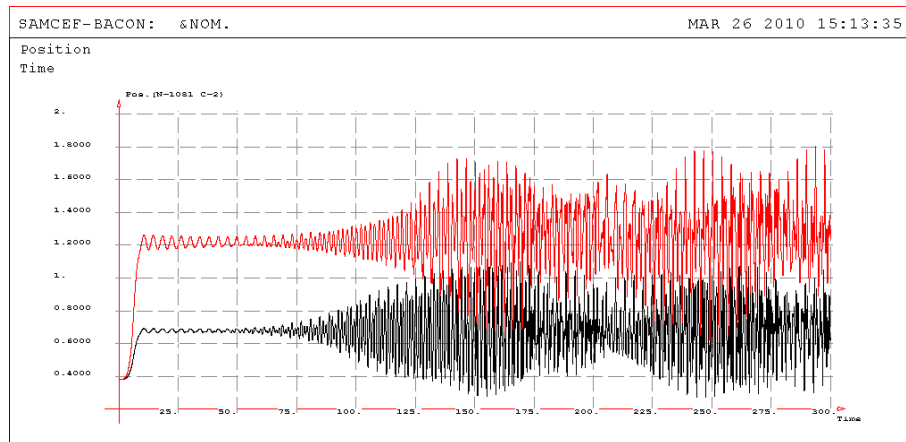


Figure 4-37. Model 1 (staggering): global Y motion – subspan 1 (curve below), subspan 2 (curve above). Global exposure

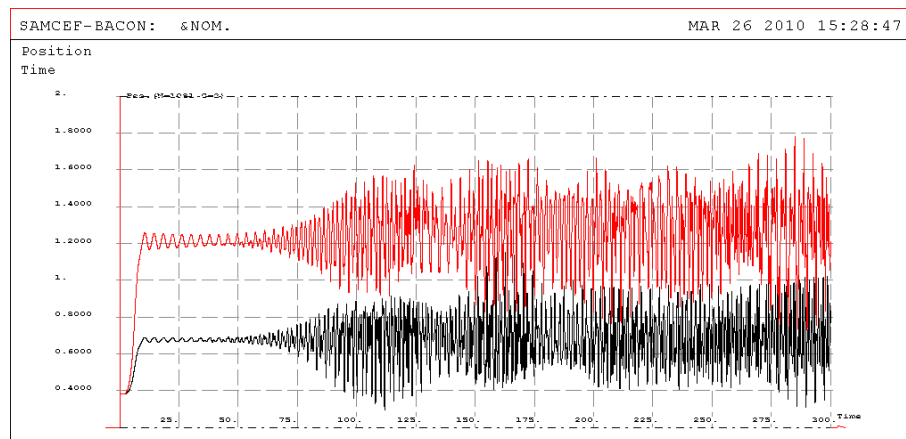


Figure 4-38. Model 2 (staggering + spacer damper): global Y motion – subspan 1 (curve below), subspan 2 (curve above). Global exposure

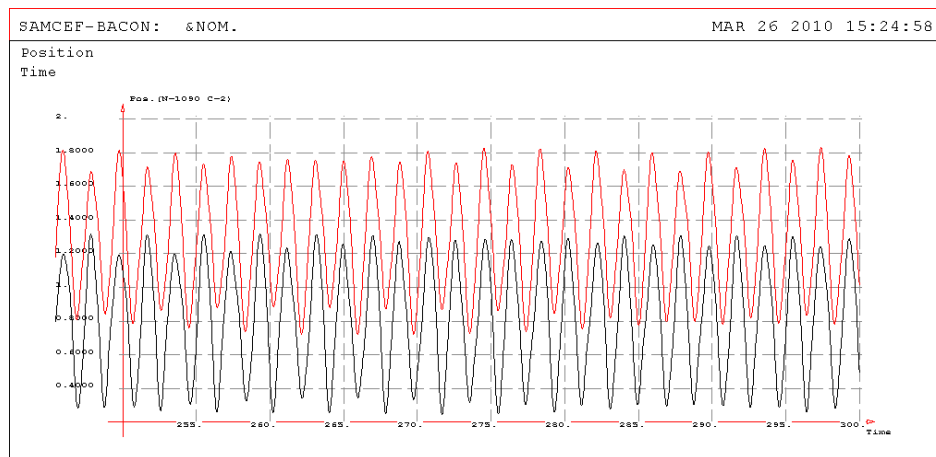


Figure 4-39. Reference Model: global Y motion – subspan 1 (curve below), subspan 2 (curve above). Zoom to 50 s

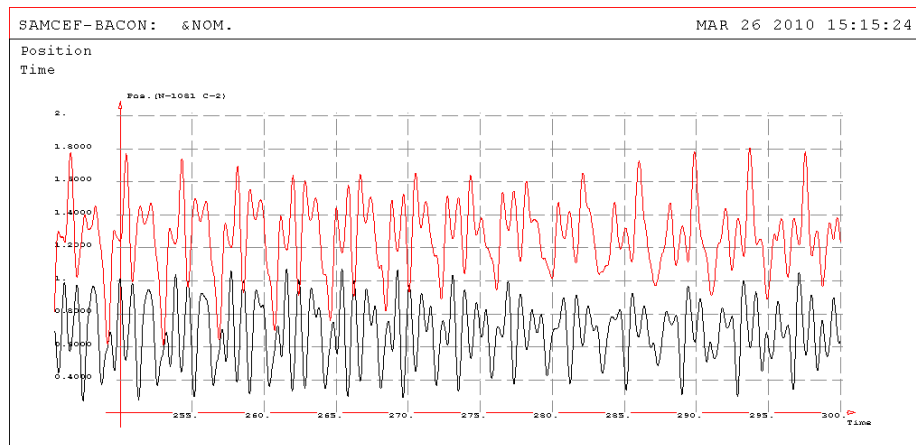


Figure 4-40. Model 1 (staggering): global Y motion – subspan 1 (curve below), subspan 2 (curve above). Zoom to 50 s

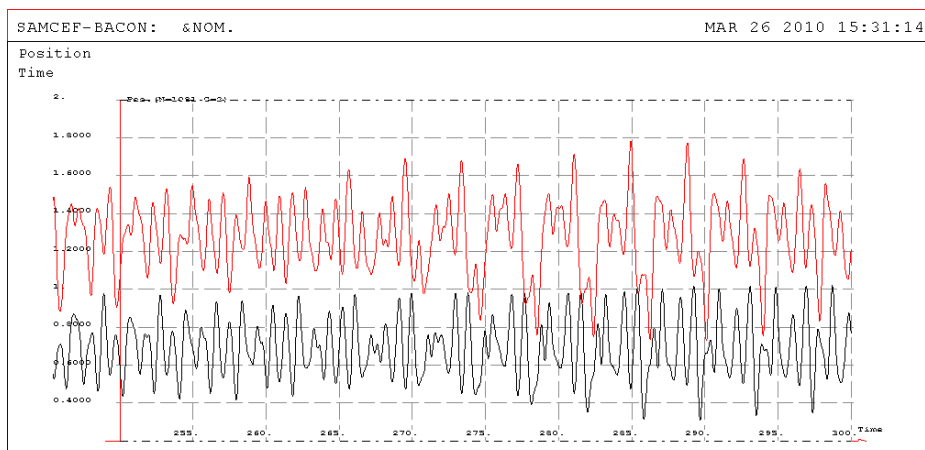


Figure 4-41. Model 2 (staggering + spacer damper): global Y motion – subspan 1 (curve below), subspan 2 (curve above). Zoom to 50 s

4.4.2.2 Global subconductor orbits

Comparing Figure 4-44 to Figure 4-42 and Figure 4-43, the orbits are slightly less in case of staggered + spacer damper scheme.

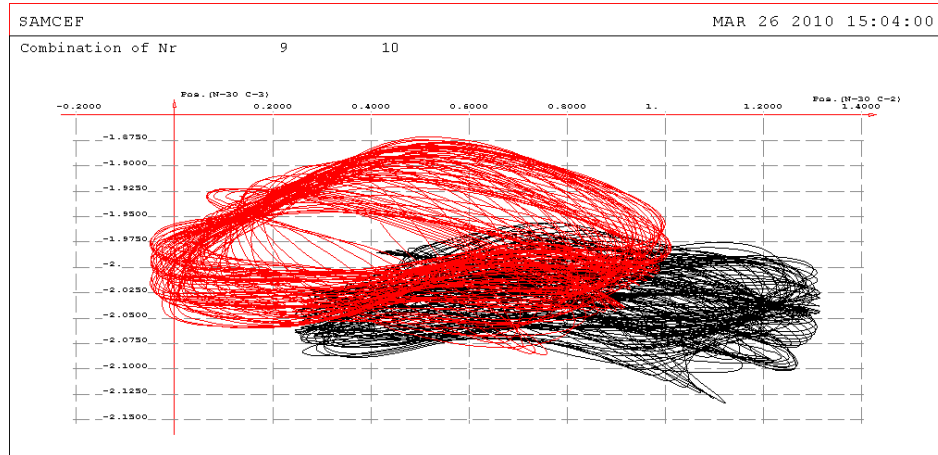


Figure 4-42. Reference model – global subconductor orbits – Subspan 1. Left orbit – windward subconductor, right orbit – leeward

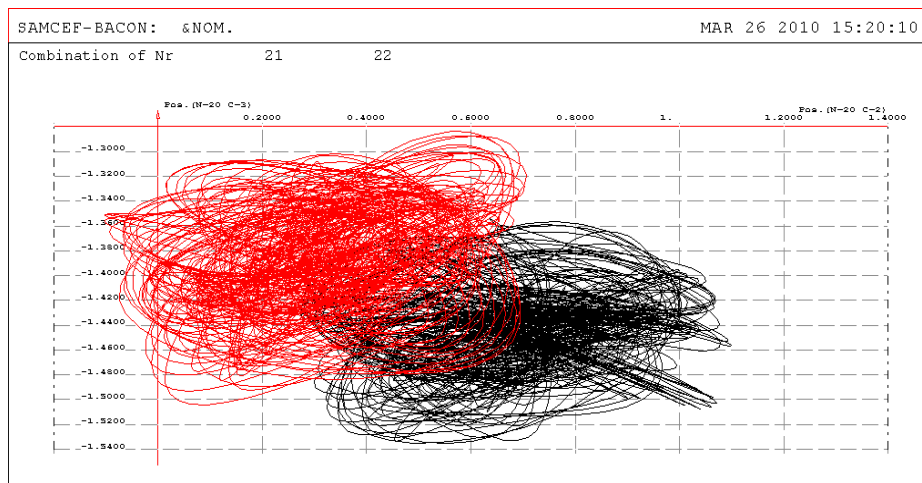


Figure 4-43. Model 1 (staggering) – global subconductor orbits – Subspan 1. Left orbit – windward subconductor, right orbit – leeward

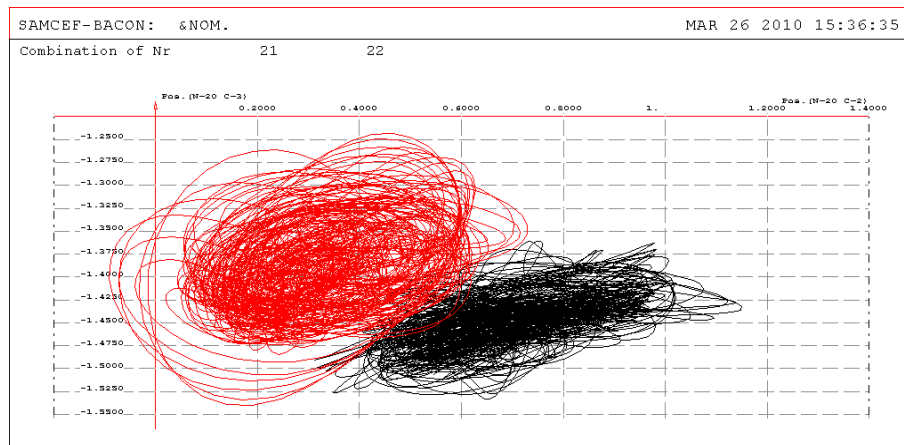


Figure 4-44. Model 2 (staggering + spacer damper) – global subconductor orbits – Subspan 1. Left orbit – windward subconductor, right orbit – leeward

4.4.2.3 Relative orbits

Contrary to above, the relative (subspan) orbit in case of staggered scheme + spacer damper (Figure 4-47) increases as compared to staggered scheme only (Figure 4-46).

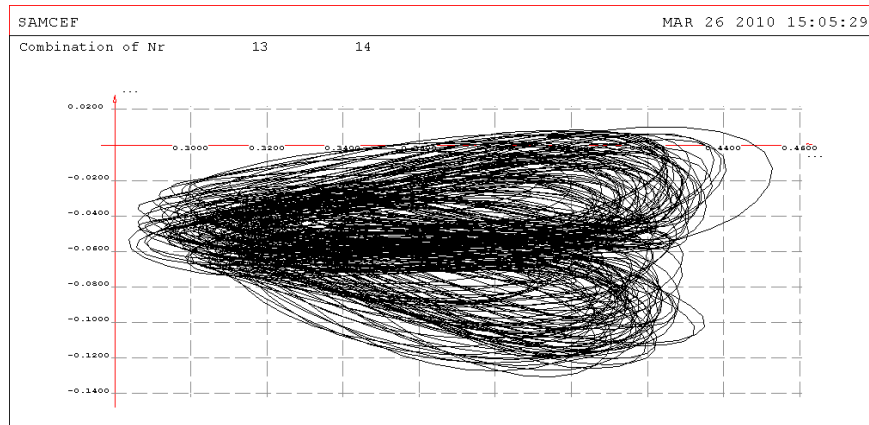


Figure 4-45. Reference model: relative orbit – subspan 1

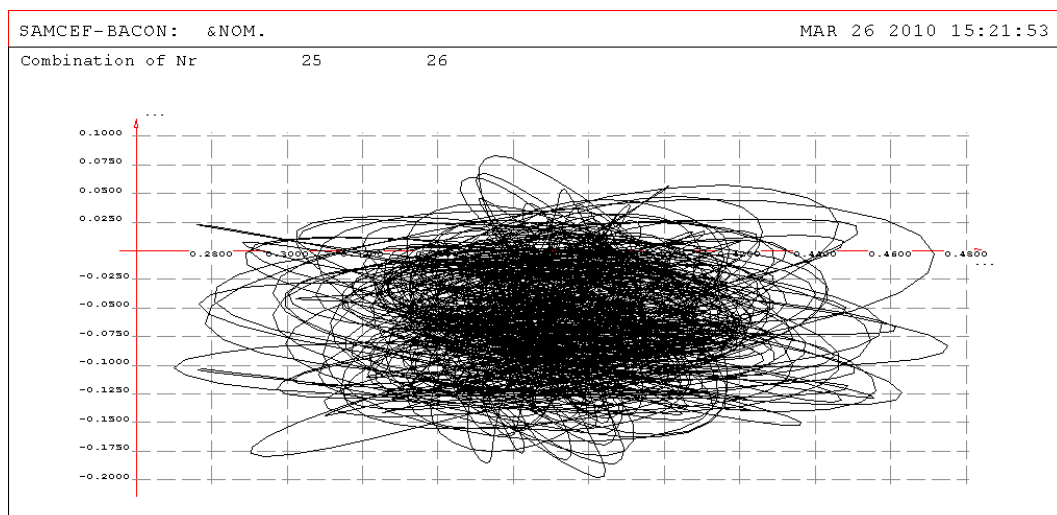


Figure 4-46. Model 1 (staggering): relative orbit – subspan 1

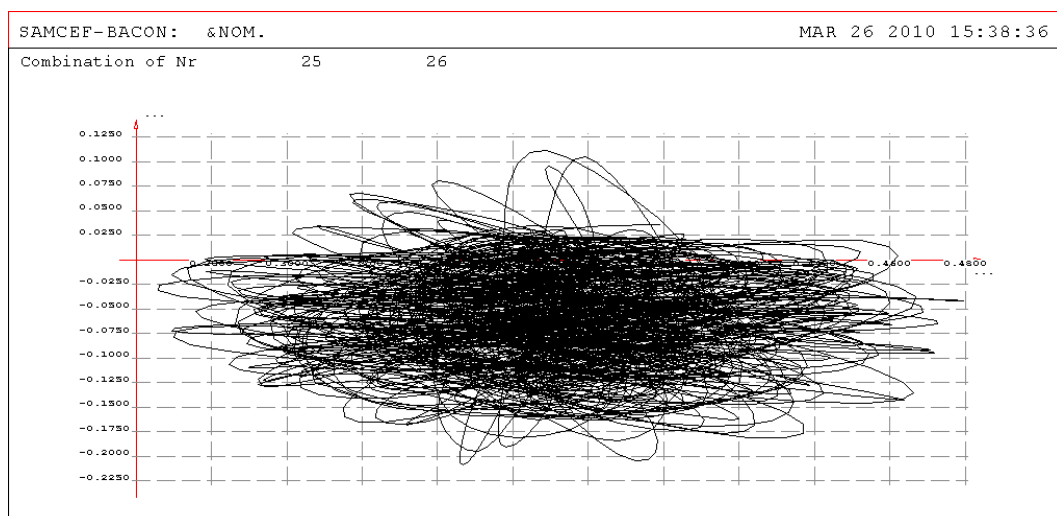


Figure 4-47. Model 2 (staggering + spacer damper): relative orbit – subspan 1

4.4.2.4 Response spectra

The response spectra below are built upon Y-displacements of leeward conductors in each subspan. The Reference model (even rigid spacer placement) spectra are presented in Figure 4-48. Clearly the snaking mode (~ 0.5 Hz) is dominant in all subspans.

Model 1 (staggered rigid spacer placement) spectra are presented in Figure 4-49. At the background of considerably decreased snaking mode, the series of subspan modes are excited; however, their R.M.S. amplitudes are comparable to those of Reference Model (subspans 1 and 4).

Model 2 (staggered spacer damper placement) spectra are presented in Figure 4-50. Comparing to Model 1, the response appears quite comparable to staggered scheme with rigid spacers.

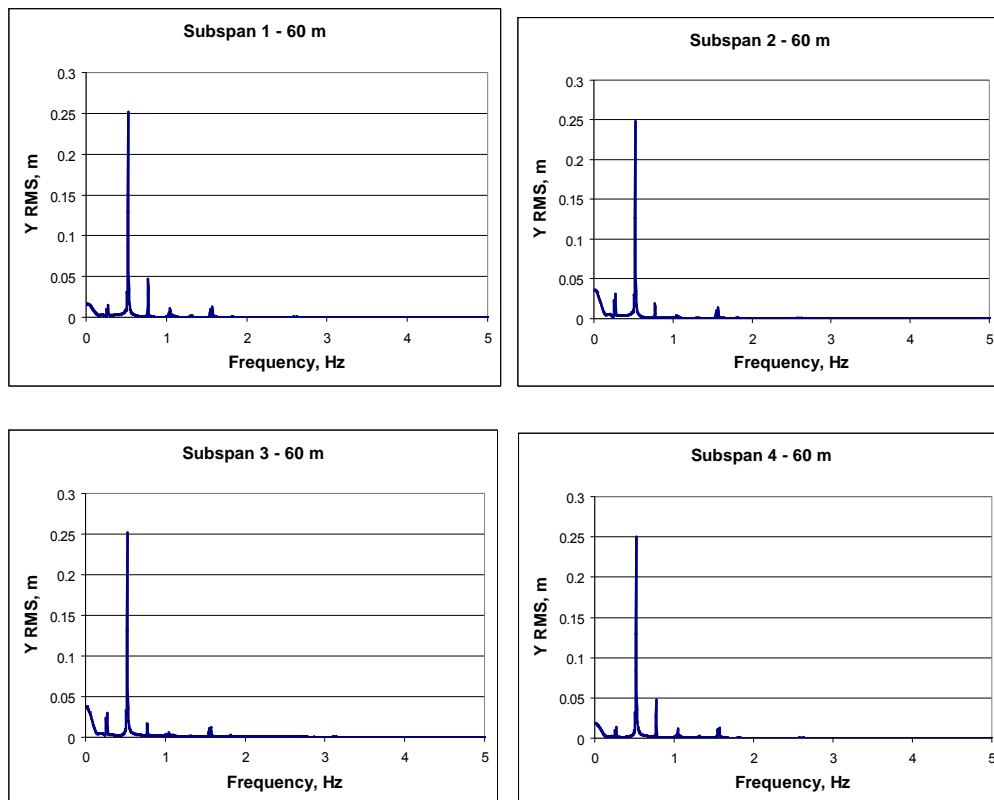


Figure 4-48. Reference Model. Displacement response spectra in the subspans

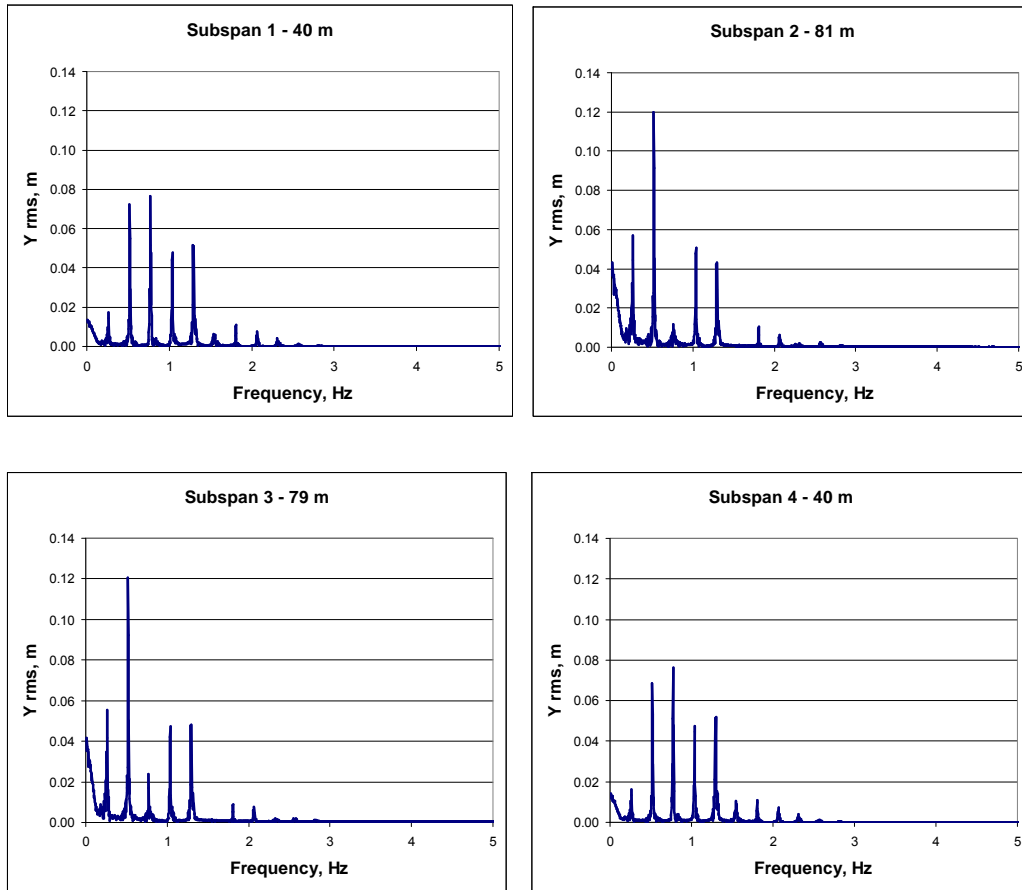


Figure 4-49. Model 1 (staggered). Displacement response spectra in the subspans

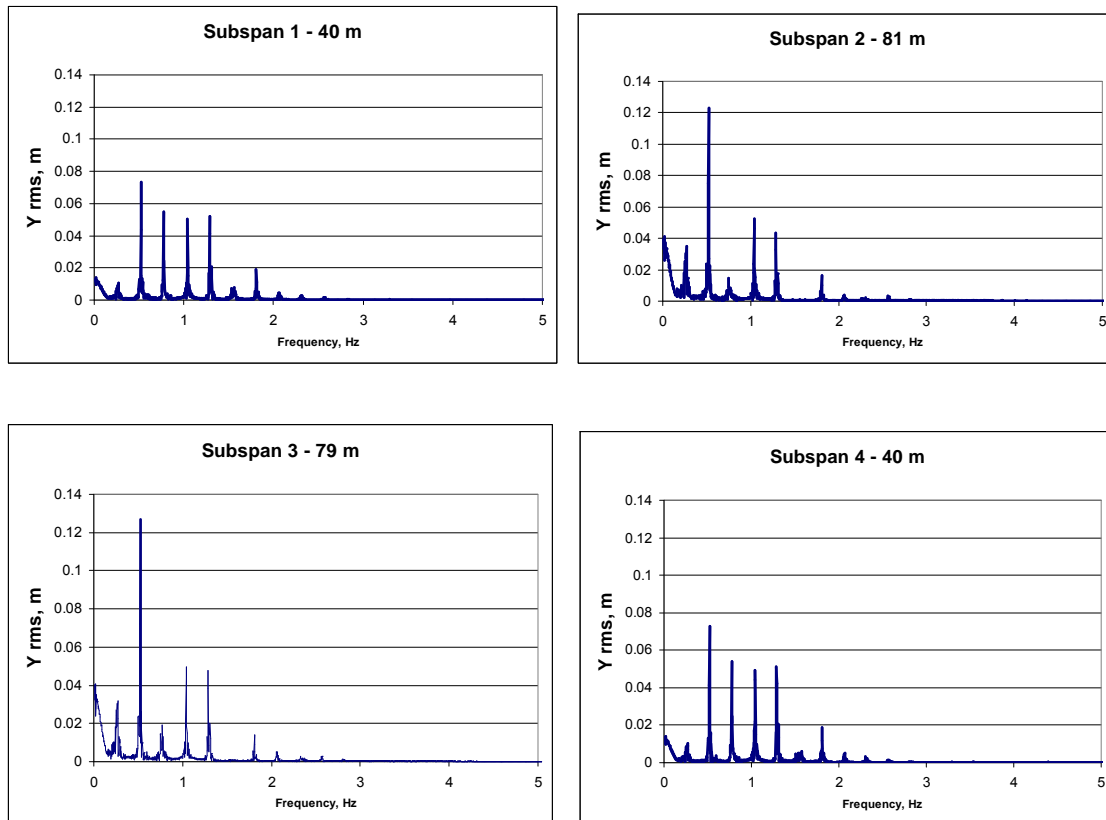


Figure 4-50. Model 2 (staggered + spacer dampers). Displacement response spectra in the subspans

4.4.3 Synthesis – comparison by Global Instability Index

On basis of above spectra, the spectral amplitude values were extracted. Together with respective frequencies, the Instability Indices are computed on basis thereof for three alternative models.

Immediate conclusion follows, that the staggered spacer placement gives a tremendous advantage over the even spacer distribution: the Instability Index falls by 1.6 times. However, the introduction of the spacer damper does not add any benefit – the I.I. is even greater as compared to the staggered span. This conclusion basically supports the results obtained by Hardy and Bourdon [25] regarding effectiveness of spacer dampers, and it fully supports the conclusions done, early in 70s by Mohajery and Rawlins [51] regarding the staggering scheme. The explanation follows from comparison of the response diagrams and spectra. The model demonstrates, and Instability Index reveals clearly the image of spectra, that staggering leads to redistribution of oscillation energy between higher number of modes. Introduction of spacer damper further adds some higher frequency response to the system, and the energy of oscillation is not dissipated but redistributed between greater number of modes.

Reference Model	Subspan No.	1		2		3		4	
	Subspan Length, m	60		60		60		60	
	Mode	Yrms, m	f, hz	Yrms, m	f, hz	Yrms, m	f, hz	Yrms, m	f, hz
	1	2.52E-01	0.523	2.49E-01	0.523	2.52E-01	0.523	2.50E-01	0.523
	2	4.70E-02	0.773	1.93E-02	0.773	1.56E-02	0.777	4.78E-02	0.773
	3	8.44E-03	1.050	3.93E-03	1.050	5.54E-03	1.047	1.01E-02	1.050
	4	7.71E-03	1.577	8.26E-03	1.577	1.19E-02	1.573	1.26E-02	1.573
	Subspan Instability Index	2.956		2.714		2.797		2.963	
Global Instability Index	11.430								
Model 1 (staggering)	Subspan No.	1		2		3		4	
	Subspan Length, m	40		81		79		40	
	Mode	Yrms, m	f, hz	Yrms, m	f, hz	Yrms, m	f, hz	Yrms, m	f, hz
	2	7.22E-02	0.520	1.20E-01	0.520	1.21E-01	0.520	6.85E-02	0.520
	3	7.65E-02	0.773	1.16E-02	0.760	2.38E-02	0.773	7.61E-02	0.773
	4	4.79E-02	1.040	5.07E-02	1.040	4.72E-02	1.040	4.75E-02	1.040
	5	5.13E-02	1.300	4.31E-02	1.300	4.81E-02	1.300	5.20E-02	1.300
	6	4.22E-03	1.560	1.04E-02	1.807	9.00E-03	1.807	8.74E-03	1.553
	7	1.12E-02	1.807	3.40E-03	2.067	7.66E-03	2.067	1.11E-02	1.807
	8	7.65E-03	2.067					7.47E-03	2.067
	9	2.45E-03	2.327					2.20E-03	2.350
	Subspan Instability Index	1.309		2.171		2.290		1.312	
	Global Instability Index	7.083							
Model 2 (staggering + spacer damper)	Subspan No.	1		2		3		4	
	Subspan Length, m	40		81		79		40	
	Mode	Yrms, m	f, hz	Yrms, m	f, hz	Yrms, m	f, hz	Yrms, m	f, hz
	2	7.35E-02	0.523	1.23E-01	0.523	1.27E-01	0.523	7.26E-02	0.523
	3	7.73E-02	0.773	1.48E-02	0.750	1.90E-02	0.773	5.42E-02	0.773
	4	5.05E-02	1.043	5.26E-02	1.043	4.96E-02	1.043	4.93E-02	1.043
	5	5.23E-02	1.287	4.32E-02	1.287	4.76E-02	1.287	5.13E-02	1.287
	6	5.86E-03	1.570	1.66E-02	1.807	1.41E-02	1.807	4.47E-03	1.580
	7	1.88E-02	1.807			3.44E-03	2.073	1.86E-02	1.807
	8	2.15E-03	2.090			1.44E-03	2.577	2.99E-03	2.073
	9	2.68E-03	2.323						
	Subspan Instability Index	1.422		2.376		2.422		1.189	
	Global Instability Index	7.408							

4.5 Overall parametric study synthesis

The above study demonstrates that WIO is quite sensitive in most of introduced parameters. Actual number of factors influencing this oscillation is quite greater (conductor tension, damping / articulated spacer etc.) On basis of the factors considered, a following conclusion can be made:

- a purely modelling issue such as accounting for conductor torsion (and, optionally, bending) stiffness does affect the WIO character, at least at the extent of the considered model with few spacers per span. In particular, the subspan modes become more pronounced (relative to snaking).
- The spacer articulation also does change the accent from snaking mode towards the subspan one, but moreover it adds to reducing the overall oscillation amplitudes.
- The staggered spacer placement reveals to be a quite effective means to attenuate the WIO. Clearly, the oscillation modes become coupled and higher subspan modes become involved into response, as seen in global orbits (Figure 4-32) but also the relative subspan orbit (Figure 4-34). The resulting oscillation amplitudes with staggered placement are reduced.
- Surprisingly, the expected addition of articulated damping + staggering does not seem to add one attenuation effect to another. According to Instability Indices, the combined protection scheme is even slightly less stable than pure staggering. This result confirms the discussion arguments presented in Section 5.1.7, based on CIGRE materials, about effectiveness of spacer dampers within staggered placement against WIO. As it will be shown in Section 6.2, the present analysis confirms the primary value of the damping spacer as a means to protect the line against aeolian vibrations. As for the WIO, only the staggered placement selected according to the spacer's specifics (including its inertial and stiffness properties) appears to be the real instrument to reduce the WIO.

Generally speaking, the above study, despite the line model initially chosen as a worst case regarding its susceptibility to WIO, demonstrates high level of the developed analytical tool for WIO simulation. In this study, there were no cases when the WIO did not occur. This fact characterizes the developed WIO simulation tools as quite a conservative instrument. Perhaps, in similar real line conditions, the WIO would be of less amplitude – at least (see also the experimental validation results, Section 6). Thus, in such kind of simulation, if it results in reduced WIO, this is readily a positive sign indicating the effectiveness of selected means against the oscillation.

5 Overview of protection methods against wake-induced oscillation

5.1 Overview of existing methods

The following techniques of reducing the wake-induced oscillation are adopted in practice:

- Increase of subconductor separation (see Section 5.1.1);
- Reduction of proportion of conductors in the wake (see Section 5.1.2);
- Tilt of bundle to move leeward conductor out of dangerous wake zone (6 – 12) (see Section 5.1.3)
- Reduction of subspan length (see Section 5.1.4);
- Uneven placement of spacers (see Section 5.1.5);
- Installation of spacer dampers (see Section 5.1.6);

Furthermore, a combined technique for line protection against WIO is discussed in the next section.

5.1.1 Increase of subconductor separation

According to observations, the oscillations occur at separations up to 20 diameters. Putting the subconductors apart at distances beyond 30 diameters would weaken the forces in the wake so that the leeward subconductor, even when found in unstable position, would not oscillate.

Application of this method is limited since the increase of subconductor separation introduces considerable modifications in the anchoring and suspension systems. However, the studies in this field are being conducted, since electrical capacity of such bundle also increases. The spacer-free bundles are employed in this case.

5.1.2 Reduction of proportion of conductors in the wake

If there are three or more subconductors in the bundle, it is possible to orient the bundle in a manner that less number of subconductors is submerged in the wake. An exemplary is the diamond orientation of quadruple bundle. Only one pair of subconductors is coupled by the wake. Bigger separation between them (by diagonal) further reduces the wake effects.

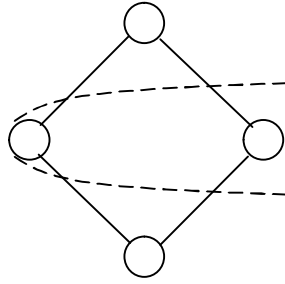


Figure 5-1. Diamond configuration of the quadruple bundle.

5.1.3 Tilt of bundle

In Chapter 2 analyses it has been shown, that wake effect is limited by vertical spacings about 1...2.5 diameters. To ensure the full elimination of wake forces, the bundle shall be tilt by the angle $>20^\circ$. In practice, this angle may reach 90° .

5.1.4 Short subspan lengths

Introducing the shorter spans follows two objectives: (1) increase the threshold velocity and (2) reduce the effects of wake-induced oscillations, would they occur. Basic effect of shorter subspan is pronounced on the relationship between in-plane and out-of-plane frequencies (see Section 2.2.5): it becomes nearly 1, and flutter instability in the wake is virtually eliminated. However, even if the oscillations occur, they will be at reduced amplitude.

This technique is effective in case of articulated spacers and is recommended in the regions prone to wake-induced oscillations. The drawback is economical since it becomes necessary installing a greater number of spacers per line.

5.1.5 Uneven placement of spacers

This technique is currently the most adopted. It allows for significantly reducing the risk of wake-induced oscillations while keeping all existing arrangement of the line; only positions of spacers are varied. According to the studies by Mohadjery at Magdalen Islands test line, staggered subspan scheme was effective regardless the spacers were damping or rigid [19]. The later studies by Hardy and Bourdon [25] confirm this result. Rawlins found, that the span protected with damping spacers with staggered scheme did not oscillate in the subspan or the rolling mode even when several changes in tilt were made. Vertical galloping, however, was observed in this study [19].

The effect in this approach is achieved by making the subspan eigenmodes coupled, so that they involve whole span. Via this coupling the oscillation, even if it arises in a particular subspan, is disharmonized by the waves transferred and received from the other subspans.

Generally, the subspan scheme is a function of specific spacer. There exist some more or less general spacer placement schemes providing subspan lengths depending on the bundle type and span length.

[74] gives some general guidelines to subspan arrangement:

“A sub-span ratio around 0.85 to 0.9 is generally agreed (literature, experimental tests and analytical simulations) to be the optimum solution.

Regarding the end sub-spans, these are generally shorter than the others: a good value for the ratio between the lengths of an end sub-span and the adjacent one is between 0.55 to 0.65.”

Add to here some limitations like end subspan length (same reference):

“...Short sub-spans (20 to 30 m) at the ends do increase the bundle torsional stiffness and, as a result, achieve two goals: a partial contribution to detuning bundle torsional and vertical modes of vibration, and a reduction in the risk of static, torsional collapse.”

Length limitations shall be respected for internal subspans, whose length shall not exceed 60 m.

Examples of spacer placement schemes for 220 kV and 400 kV lines are presented in [76]. Below, a placement chart is shown on basis of earlier CIGRE recommendations [45]:

Span length (m)	Nr of spacers	Relative subspan length / span length
180 - 250	3	0.167; 0.334; 0.333; 0.166
250 - 310	4	0.14; 0.282; 0.162; 0.278; 0.138
310 - 370	5	0.101; 0.227; 0.228; 0.186; 0.163; 0.095
370 - 430	6	0.09; 0.19; 0.172; 0.164; 0.15; 0.159; 0.075
430 - 490	7	0.088; 0.155; 0.149; 0.11; 0.109; 0.147; 0.175; 0.067

When other than a simple rigid spacer is installed, and especially the spacer damper, its effect on span dynamics has to be accounted for calculation of subspan lengths which would be effective to dampen the wake-induced oscillations.

5.1.6 Spacer dampers

Spacer dampers are increasingly used in OHL offering two main functions:

Reduce aeolian vibration level by avoiding its entrapping within subspans, between the spacers, where the end-span dampers are ineffective;

Attenuate or reduce the WIO with two mechanisms:

- spacer arm articulations which let the oscillation waves transfer between subspans to be mutually attenuated
- damping inserts in the articulations thus introducing the distributed damping effect along the span.

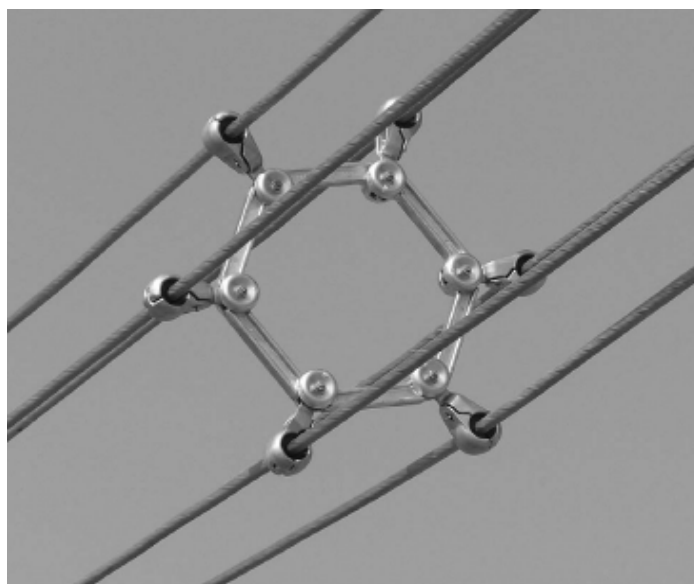


Figure 5-2. Six bundle spacer damper

Discussion about effectiveness of emphasized effects of spacer damper against WIO still continues nowadays. Some illustrative results regarding proper spacer damper contribution into attenuation of WIO are presented in Sections 4.4 and 6.2.

5.1.7 Combined method for protection of line against vibrations and subspan oscillations.

Many years of experience show, that sole reliance to spacer damper does not guarantee good protection of line against WIO. As tests demonstrated [25], with exemplary staggered subspan scheme,

damping spacers may behave even less effectively as compared to non-damping articulated spacers. In this study performed by Hardy and Bourdon, the optimum has been found in low-stiffness articulations enabling both mutual attenuation of subspan modes and damping of aeolian vibrations. However, another important conclusion is that effective use of spacer damper should be combined to their proper distribution along the span.

While analysis results, presented in this work, confirm advantageous effect of uneven placement into attenuation of WIO (see Section 4.3), the uneven spacer placement is ineffective against aeolian vibrations with rigid spacers: as discussed in previous chapters, vibrations are entrapped within a subspan. Therefore, to effectively protect the line against WIO and vibration it is commonly adopted a solution to combine two instruments: spacer damper with uneven placement.

Major line equipment manufacturers offer together with spacer damper, an associated map of their placement in the line spans. Such map is, in general, particular for each span and depends on the wind condition, type of bundle, conductor and spacer damper properties.

5.2 Suggestions to methodology for definition of optimal placement of spacers

The future work within the context highlighted by this thesis may include the development of method to calculate the spacer placement scheme. Its general flow chart is presented in Figure 5-3. The method shall be based on SAMCEF Mecano linked to optimization management toolbox, Boss Quattro by Samtech.

- Step 1. Initial line configuration together with wind loading data and execution parameters is translated into input format of SAMCEF Bacon pre-postprocessor by external routine Linemesh. This routine is readily available.
- Step 2. Bacon executes translation of model into input data file for Mecano analysis.
- Step 3. Mecano calculates the task as follows. After the line is put into equilibrium position, the wind is applied. Under the wind loading, complex eigenvalues and associated mode shapes of the line span are determined. The simulation does not aim at calculating the developed line response to the wind, wake-induced oscillation etc. because of its high time consumption.
- Step 4. The eigenvalues are then analyzed by external routine which sorts the real parts to identify the stability of system. These data are described as output to Boss-Quattro.
- Step 5. Boss Quattro can process as objective function the minimum of several variables, namely:
 - a. maximal value among all real parts of eigenvalue;
 - b. average value of all real parts.

After the analysis of objective function, Boss Quattro modifies the subspan lengths to introduce new data for the line span to the Step 1.

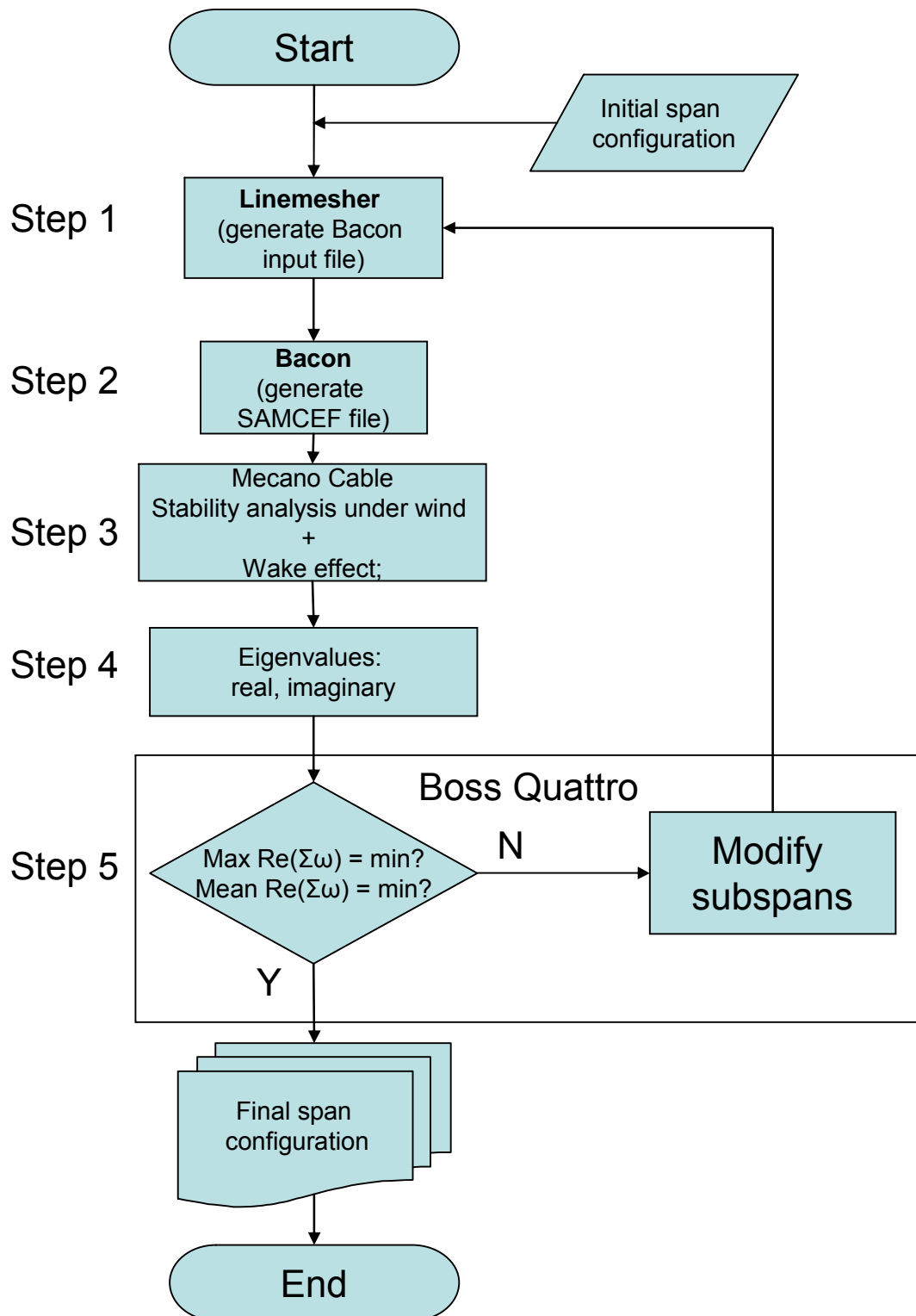


Figure 5-3. Spacer placement optimization flow chart

6 Experimental validation

The test case considered below is relevant to tests conducted at the Magdalen Island by IREQ. The test line is illustrated in Figure 6-1.

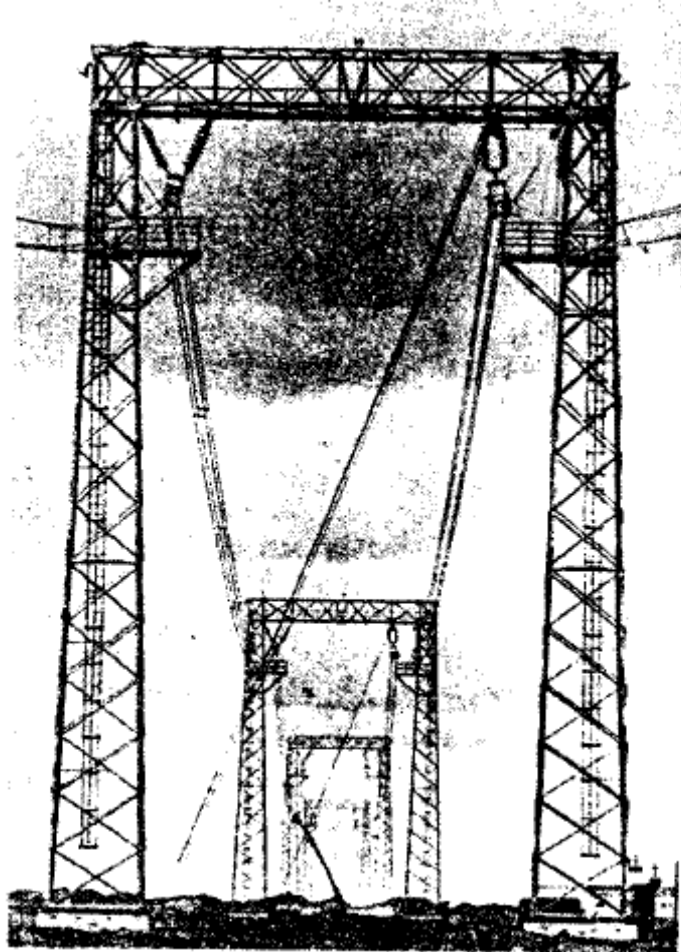


Figure 6-1. Magdalen Island Test Line [25]

The test line comprises three spans. Test data used for the present comparison have been obtained on the middle span.

According to [25], the “I” insulator strings, restricted against blowback, were used at span suspension points. This arrangement facilitates comparison, as it approaches the model of span with subconductors fixed at their ends.

Construction of the line allows for testing different span configurations and arrangements. In particular, the line allows for arbitrary inclination of the bundle vs. direction of wind, within $\pm 20^\circ$.

6.1 Input data

To construct the span model, the following input data were used out of available information about the test span.

6.1.1 Span properties

Tensile load 20% RTS (29.1 kN).

Span: 367 m. (between tower 2 and 3); 7 subspans: 35 - 56 - 64 - 57 - 65 - 55 – 35 m.

Bundle height: Tower N°2: 24.85m

Tower N°3: 26.10m

6.1.2 Conductor properties

The bundle has been equipped with ACAR 1300 conductors (stranding 37 x 4.76). The conductor properties are as follows:

Total cross-section area:	658.39 mm ²
Diameter:	33.325 mm
Mass per unit length:	1.8156 kg/m
Bending stiffness (EI min):	64.29 N.m ²
Density:	2757.64 kg/m ³
The Young Modulus is taken as	56 GPa.

6.1.3 Bundle properties

The quadruple bundle had 450 mm separation between subconductors.

There was no data about bundle inclination. After the published descriptions of the test line as based on the fact that steady WIO have been obtained, the inclination was selected at the angle 9° (leeward conductor below), giving relative vertical separation about -2 conductor diameters.

6.1.4 Spacer damper data

Torsional stiffness of the hinge:	294.3 Nm/rad,
Axial stiffness of the hinge:	820000 N/m,
Torsional damping ratio:	0.32 (*)
Axial damping ratio:	0.32
Arm mass:	0.7 kg
Arm mass moment of inertia with respect to the centre of mass:	1.67E-3 kg m ²
Central body mass:	2.25 kg
Central body mass moment of inertia with respect to the centre of mass:	65.72E-3 kg m ²

(*) NOTE: On basis of above ratio, arm inertia and mass, the calculated physical damping is equal to 1.32 Nm s/rad. See the end of chapter.

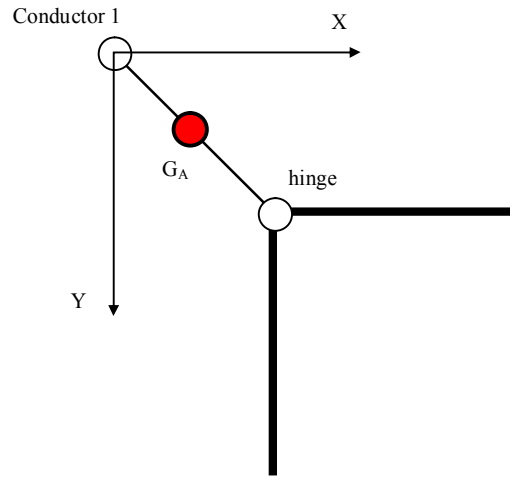


Figure 6-2. Spacer Damper Arm in Reference Coordinate System

Hinge coordinates with respect to conductor 1: $X = + 0.1170$ m; $Y = + 0.0670$ m

Central body centre of mass coordinates with respect to conductor 1:

$X = + 0.225$ m; $Y = + 0.225$ m

Arm centre of mass coordinates with respect to conductor 1:

$X = + 0.048$ m; $Y = + 0.028$ m

The calculation of structural damping value has been done on basis of above data as follows. Given

Arm mass moment of inertia with respect to the centre of mass: $J = 1.67\text{E-}3$ kg m²,

Arm mass $m = 0.7$ kg and

Mass centre offset from the hinge $H = \sqrt{0.117^2 + 0.067^2} = 0.135$ m,

The Arm mass moment of inertia with respect to the hinge is

$$J_H = J + mH^2 = 0.0144 \text{ kg m}^2$$

Then, given torsional stiffness $S_T = 294.3$ Nm/rad and damping factor $\zeta = 0.32$, the torsional damping value is

$$C = 2\zeta \sqrt{S_T \cdot J_H} = 1.32 \text{ Nm s/rad.}$$

6.2 Assessment of spacer damper dynamic properties

As noticed in Section 5.1.7, the spacer damper effectiveness to attenuate the WIO remains questionable. To clarify this issue, consider here two models. The first model represents a “virtual test bench”, where a stand-alone quad spacer damper (illustrated in Figure 3-6) is subject to a sine sweep load at constant amplitude. However, such model does not reflect the contribution of the bundle,

which the spacer damper is, in real service conditions, fully integrated to. Therefore, a second model is built: with the spacer damper installed between two subspans, at full tension (up to some extent, a portion of real line span is thus modelled).

6.2.1 Sine sweep model

6.2.1.1 Input data

The spacer model is illustrated below, in Figure 6-3. Recall, that it is the same spacer as shown in Figure 3-6. The spacer damper properties are identical to those described above in Section 6.1.4.

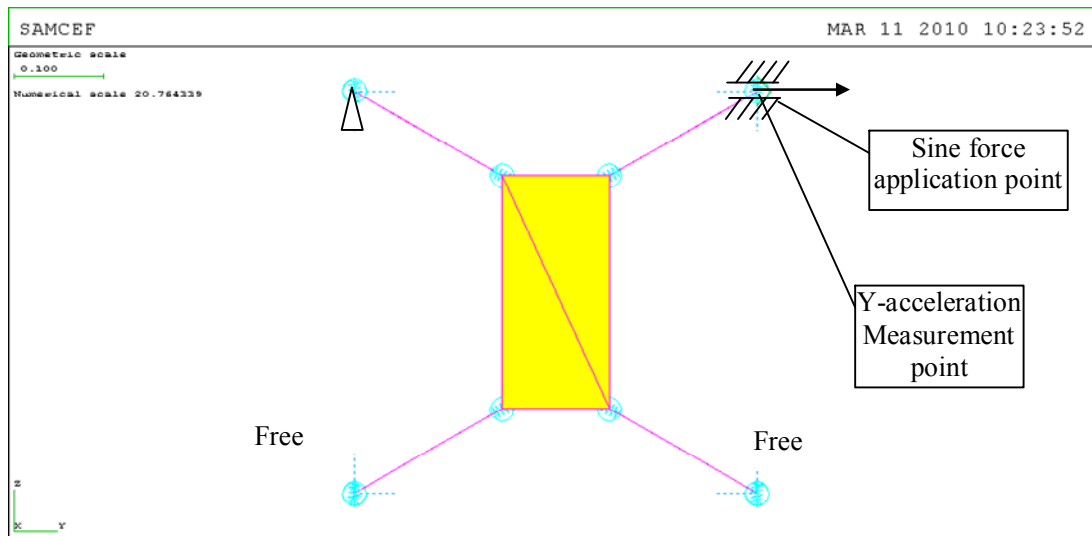


Figure 6-3. Model of spacer damper subject to sine sweep test.

Sine sweep strategy is illustrated in Figure 6-4: the sinusoidal force has been applied at a constant amplitude 40N and frequency increasing from 0 to 60 Hz. The test duration was 120 seconds.

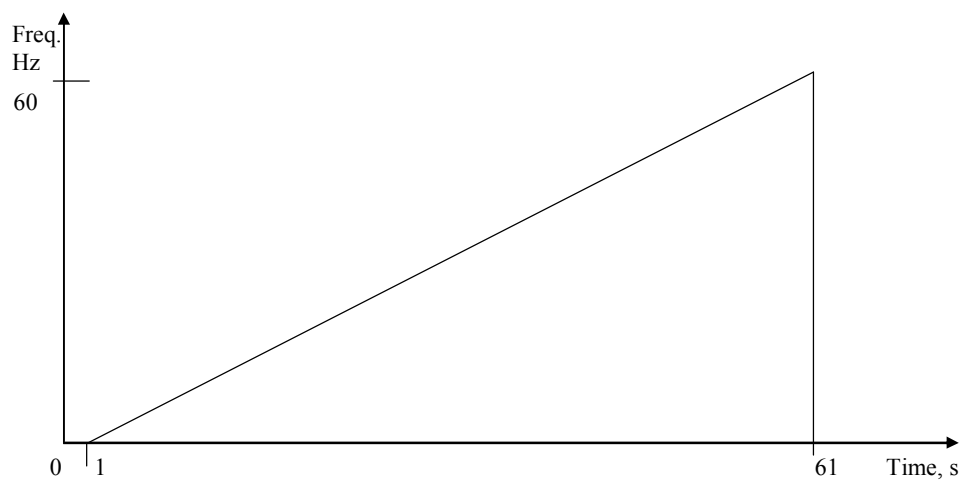


Figure 6-4. Sine sweep sequence

6.2.1.2 Results

The main result output is Y-acceleration (in direction of the loading) at the loaded point (which allows observing the response of the whole structure). Its diagram is shown in Figure 6-5.

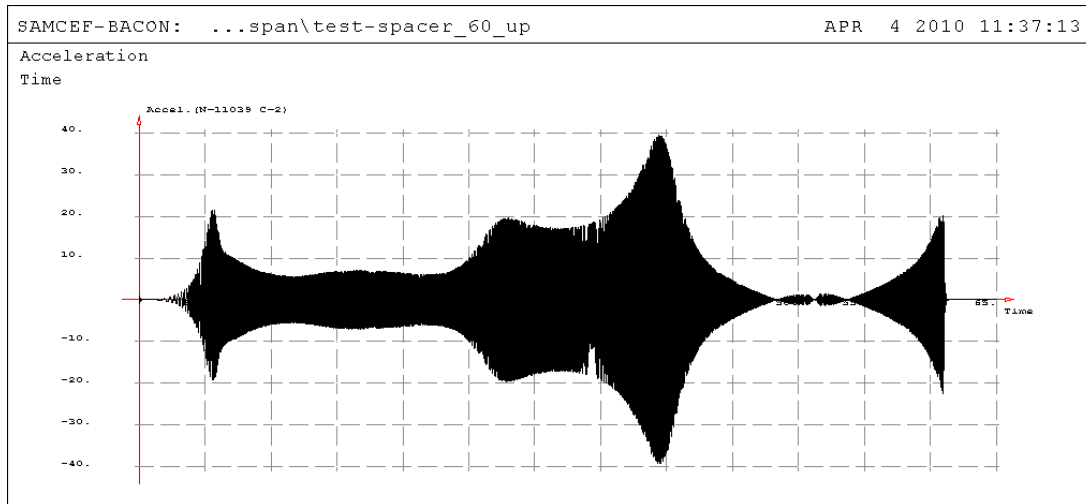


Figure 6-5. Spacer damper response: Y-Acceleration at the loaded point

In Figure 6-6 the response spectrum is shown, which is specific by the fact that first response frequency is at 8.52 Hz. For comparison, in Figure 6-7 the response spectrum is shown with the same spacer damper, but the damping value is set to zero. A number of response frequencies are more pronounced, but also note the amplitude levels (~ 0.25 (damped) against 90 (undamped) m/s^2), giving idea about the amount of energy dissipated by the dampers. In Figure 6-8 the first mode of the spacer damper excited is shown.

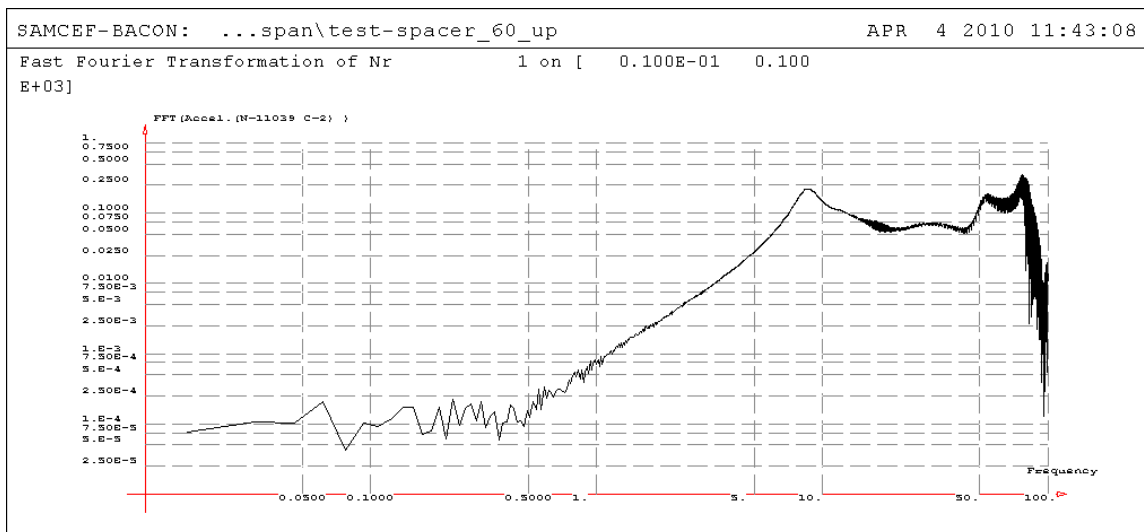


Figure 6-6. Spacer damper response spectrum: Y-Acceleration at the loaded point

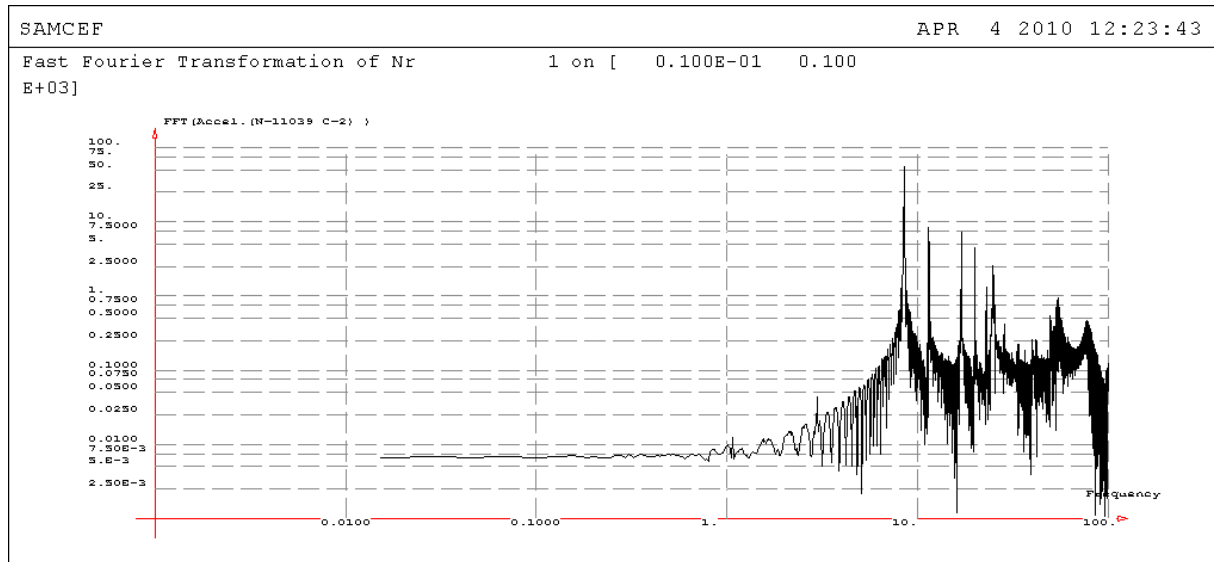


Figure 6-7. No-damping spacer damper response spectrum: Y-Acceleration at the loaded point

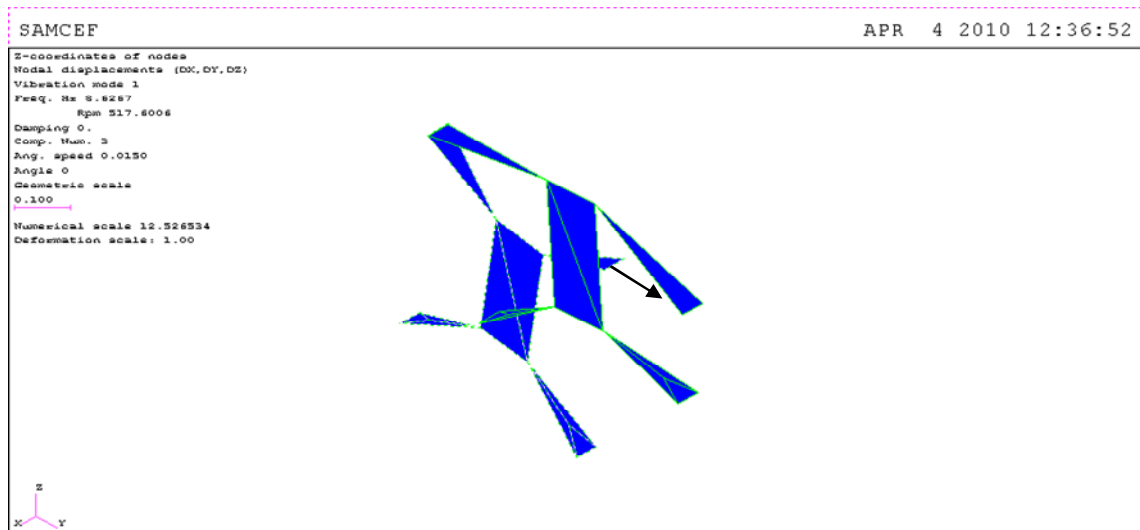


Figure 6-8. Spacer damper: First responded mode (deformed vs. non-deformed configurations)

Clearly, the above test model brings to an idea, that spacer damper is ineffective within WIO frequencies range (0.5...5 Hz) and reacts just starting of the frequency of aeolian vibration (~8 Hz ... 50 Hz). However, such a sine sweep test considers an isolated spacer damper. In reality, unlikely the suspended fittings type Stockbridge, the spacer damper is fully attached to the bundle subconductors; effect of latters' added inertia and stiffness cannot be neglected.

6.2.2 Model of spacer damper integrated with two subspans

To clarify the effect of spacer damper when installed into the bundle span, consider a model of spacer damper integrated into subspans. In general, this is a portion of the benchmarking test span model.

6.2.2.1 Input data

- spacer damper installed between two subspans: 35 m and 56 m.
- each conductor tension is 20% RTS (29.1 kN)
- conductor type: ACAR1300 (see Section 6.1.2 for details)
- bundle properties: idem benchmarking data (see Section 6.1.3 for properties)
- spacer damper: idem previous test (see Section 6.1.4 for properties)

Conductors were modelled with cable elements (no bending and torsional stiffness).

Overall view of the model is shown in Figure 6-9.

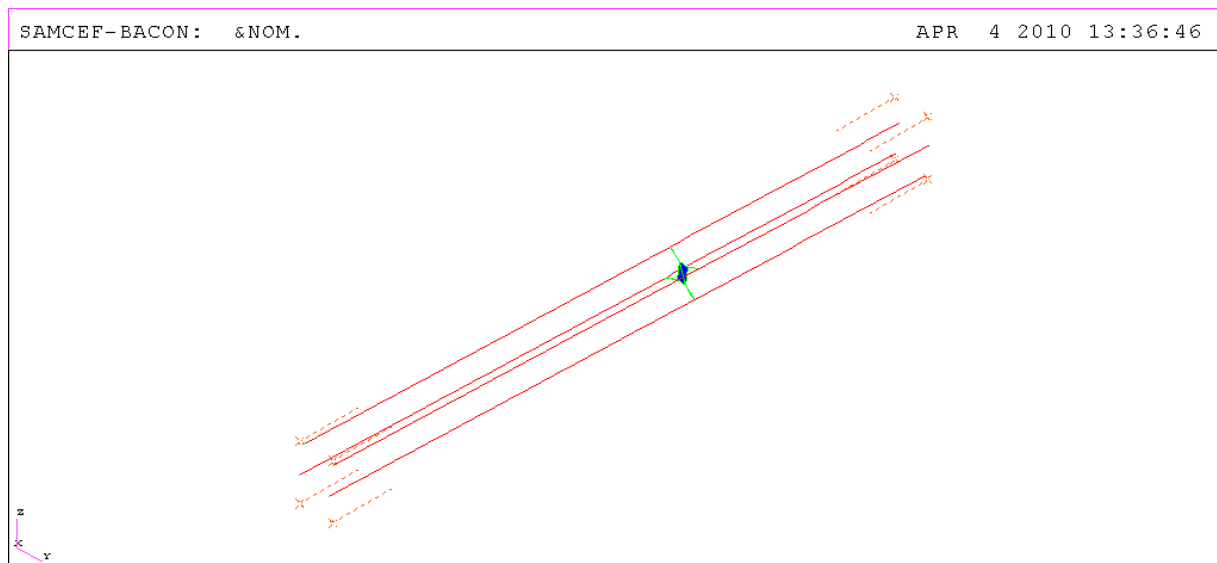


Figure 6-9. Overall view of the Integrated Spacer Damper model

6.2.2.2 Results

The complex modal analysis of the spacer damper integrated into the bundled conductor shows, that even if the spacer deformations do contribute into the coupling of subspan modes, only starting of the frequency around 3.1 Hz (mode 29) its damping capacity becomes effective, still remaining quite low until aeolian vibration level (still around 8.5 Hz – see Figure 6-10). Thus, damping will be of no

help on basic WIO range (typically here 1 Hz). This study explains why such a low difference was observed in parametric study of spacer damper effect in staggered placement (see Section 4.4).

It is interesting to see the first modes relative to the subspans (Figure 6-11 and Figure 6-12). Despite the damping value quite low, a coupling is readily present in this model. However, despite in this model there was no wind taken into account, the issue about damping capacity of neighboring subspan due to aerodynamic damping is questionable, due to its low deformation in the coupled mode. Of course, other modes exist with subspans deformed quite comparatively. However, these are modes at higher frequencies; due to higher input energy needed for their excitation, these modes have less chances to be excited due to the wake.

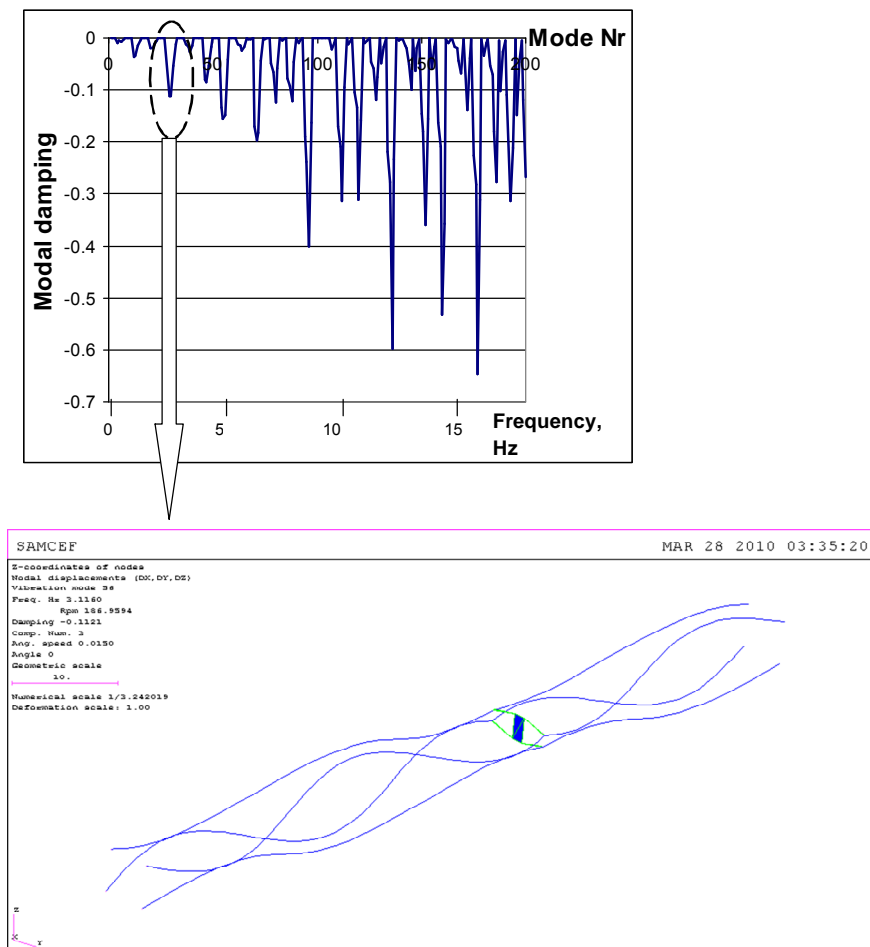


Figure 6-10. Modal damping of the spacer damper + two-subspan bundle vs. eigenfrequency (above) and corresponding mode shape of the first noticeably damped mode (below)

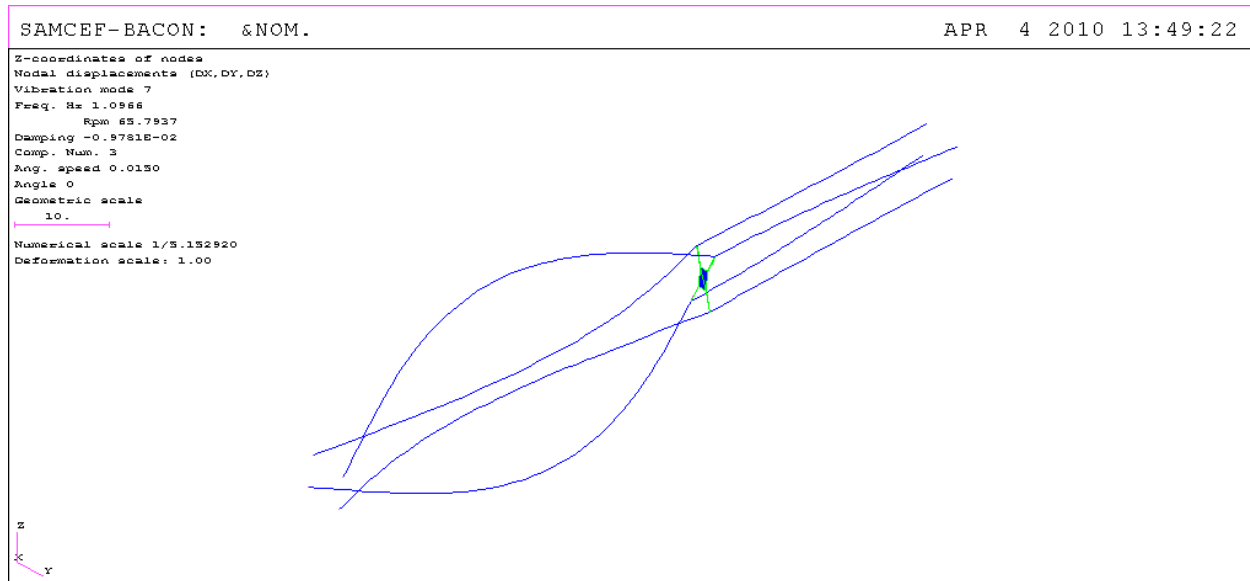


Figure 6-11. First subspan mode: 1.097 Hz

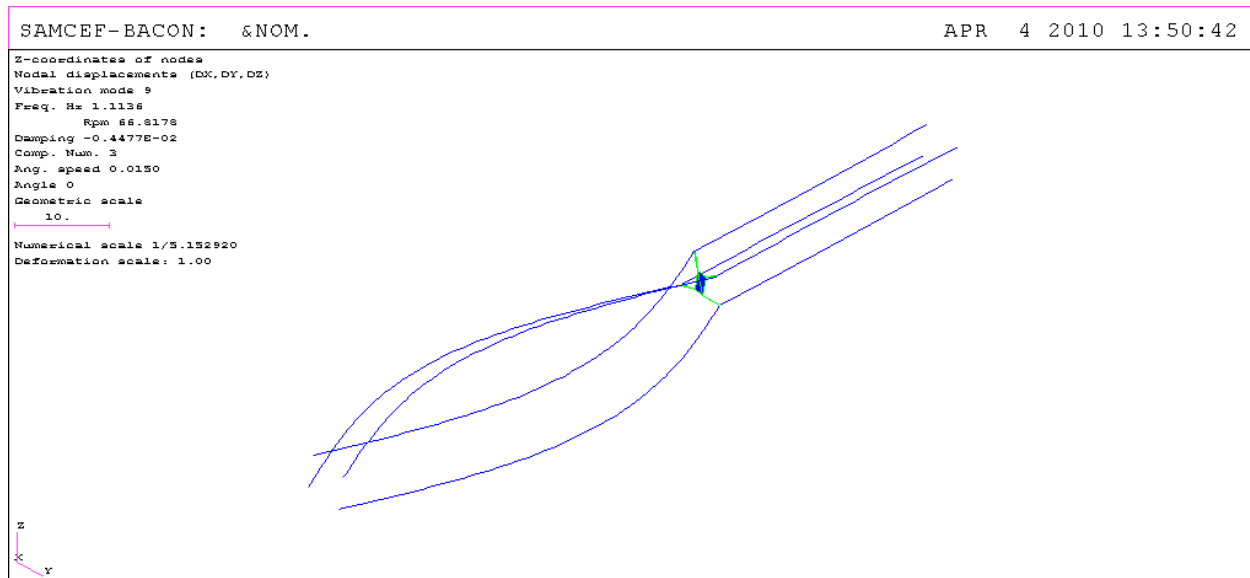


Figure 6-12. Second subspan mode: 1.12 Hz

6.2.3 Synthesis

The model of integrated spacer gives an image of damped coupled subspan modes starting of the frequency around 3 Hz, while the sine sweep model shows resonance of isolated spacer damper at frequency around 8.5 Hz. Where both models coincide, is the amount of effective damping: the former model gives the really effective modal damping starting of the same frequency as shown in an isolated spacer damper (8.5 Hz). Hence, according to above study, damping contribution of the spacer damper is negligible at basic subspan mode frequencies (1...2 Hz).

6.3 Benchmarking calculations results

6.3.1 Reference field test results

The reference results from the field test data give the values of peak-to-peak Y oscillations (out-of-plane of the span) relative to the wind velocities at different subspans:

Subspan no.	Subspan Length m	Wind conditions			Yp-p mm
		velocity m/s	direction degree	velocity normal comp m/s	
1	35	12.2	250	11.4	57.7
		11.4	249	10.7	51.3
2	56	18.2	244	16.3	117.5
		9.9	247	9.1	111
3	64	19.4	243	17.3	145.9
		10.1	246	9.2	64.6
4	57	18.7	243	16.7	95.1
		8.4	107	8.0	51
5	65	19.4	241	17.0	294.1
		11.2	246	10.2	80.6
6	55	19.4	241	17.0	273.5
		10.9	105	10.5	34.8
7	35	19.4	243	17.3	37.9
		11.9	293	11.0	25.6

Table 6-1. Reference Field Test Data: Maximum Y peak-to-peak subspan amplitudes

The wind directions are relative to the span main axis. The data were taken on basis of the distribution of the winds relative to the subspan oscillations over the observation period, shown in Figure 6-13.

The measurements of the oscillations from the calculations were approached to the test line instrumentation, which has been designed specifically to measure subspan oscillation modes. In calculations, the relative subspan oscillations mainly served as source for comparisons, which followed the same approach as described in beginning of Section 4, see item (3). For overview of oscillation character, in each case the oscillations are presented upon five criteria as in Section 4.

For comparison, three wind velocities were selected together with respective subspans as per Table 6-1 – see Table 6-2:

Reference			
Subspan no.	Subspan Length m	Wind velocity normal comp m/s	Yp-p mm
4	57	8.0	51
5	65	17.0	294.1
7	35	11.0	25.6

Table 6-2. Reference test data selected for comparison

EVALUATION DE L'ENTRETOISE-DAM HIVER 87

Du 87/ 3/27 18:46

Au 87/ 5/11 12:25

De 0 A 80 KM/H

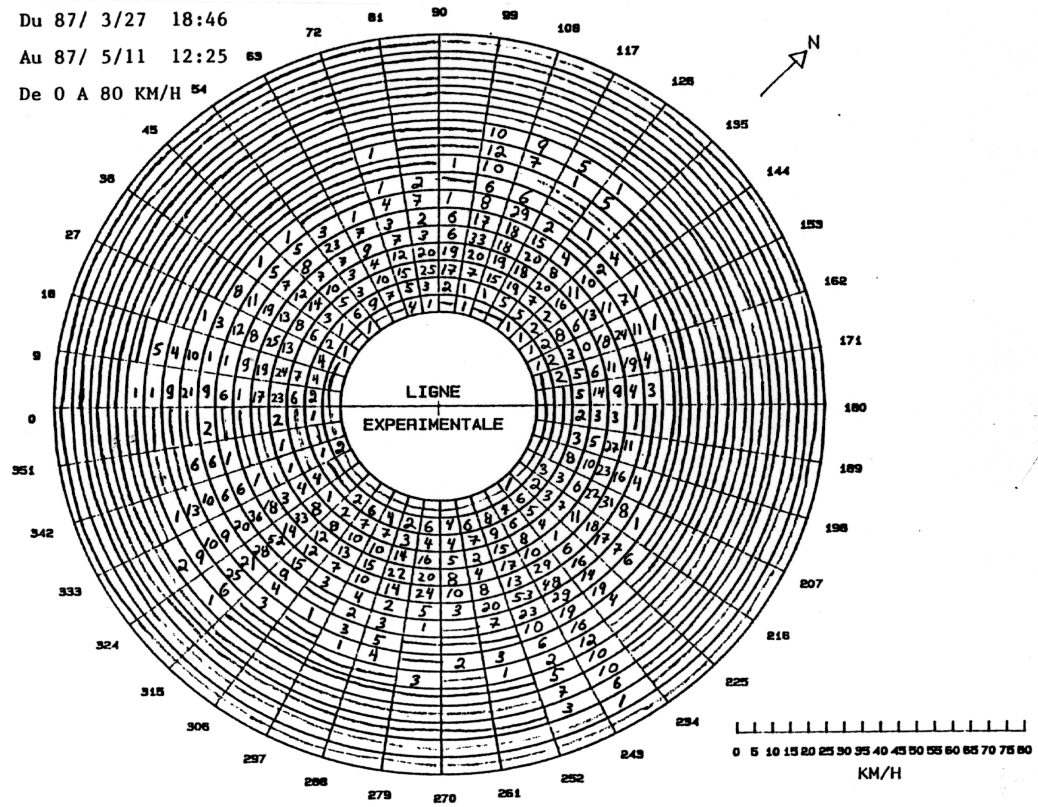


Figure 6-13. Benchmarking field test data: wind exposures relative to the subspan oscillations only.

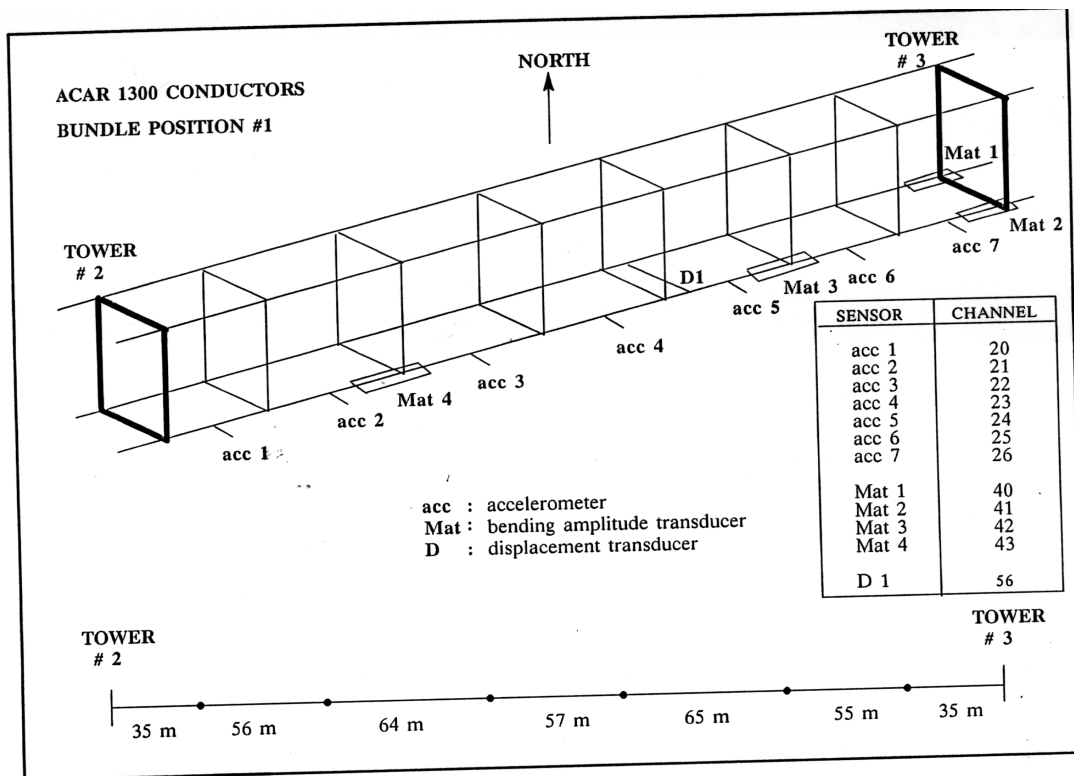


Figure 6-14. Scheme of test line instrumentation

6.3.2 Model of span

The full model of the span is illustrated in Figure 6-15. The calculated sag in the span is 10.5 m. In present calculations, conventional cable element was used (no torsional/bending stiffness).

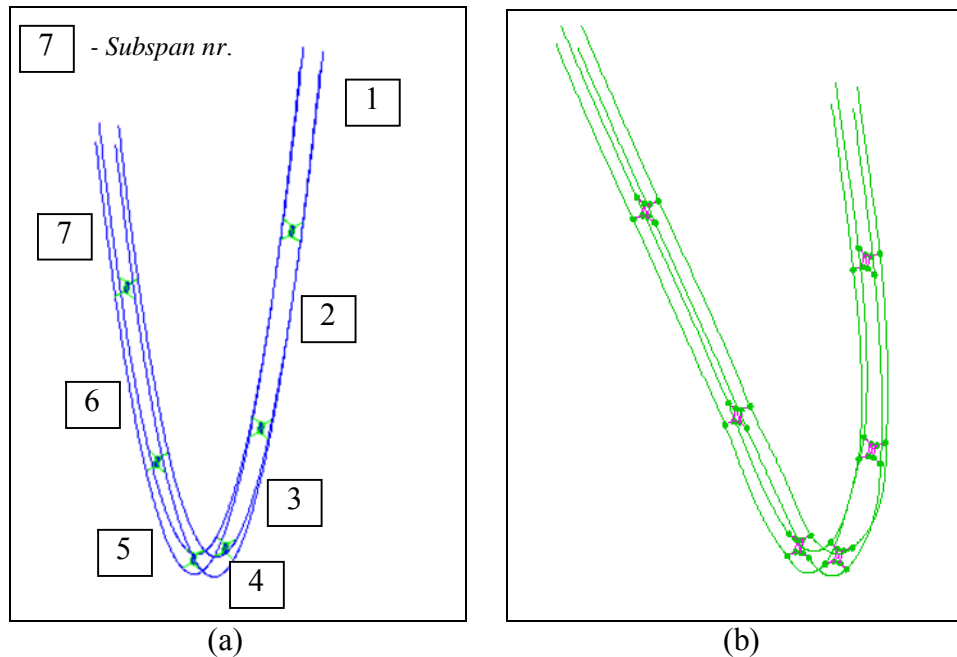


Figure 6-15. Test span FE model: (a) – at zero wind, (b) – during WIO oscillations

6.3.3 Calculation results: Wind 8 m/s, subspan 4

6.3.3.1 Global oscillation

The global Y-oscillation diagram (see Figure 6-16) shows that under such a moderate wind the oscillations set up quite slowly, however, after having built up they remain steady within 5 minute exposure.

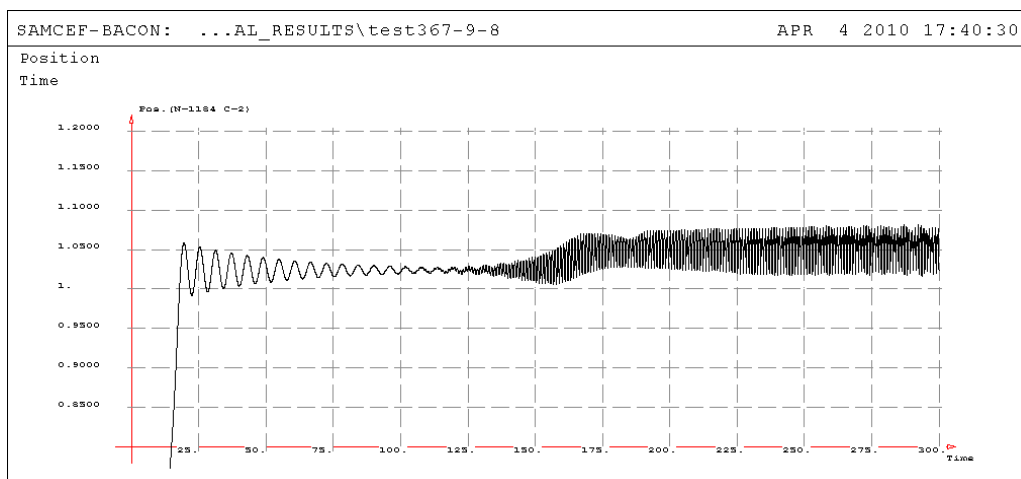


Figure 6-16. Analysis result at 8 m/s: subspan 4 - global Y oscillations

6.3.3.2 Snaking mode

The snaking mode in this case is not pronounced, virtually it does not exist. The oscillations mostly occur at subspan frequency, even in case of subtraction of the subspan before-middle (no.3) and after middle (no. 5) – see Figure 6-18.

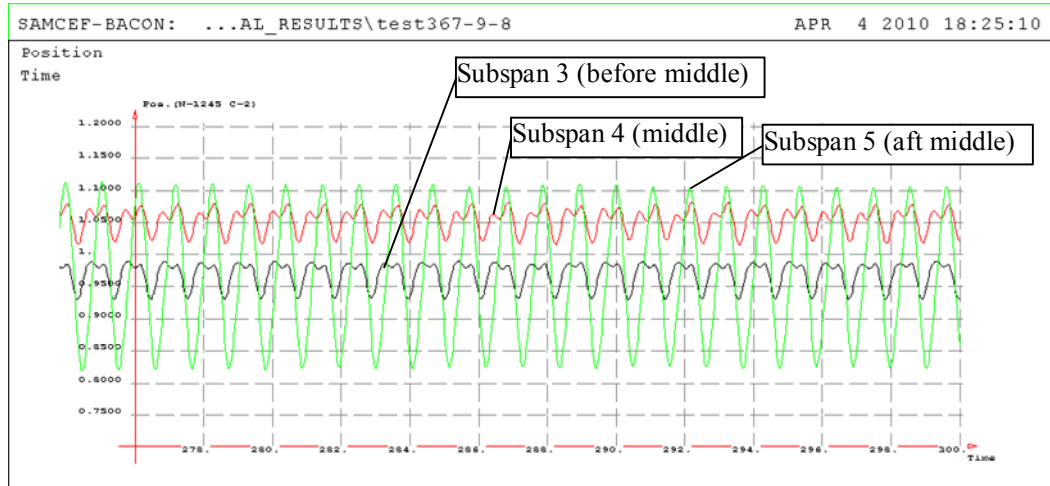


Figure 6-17. Analysis result at 8 m/s: oscillations ensemble at three subspans around middle- zoom at 26 s

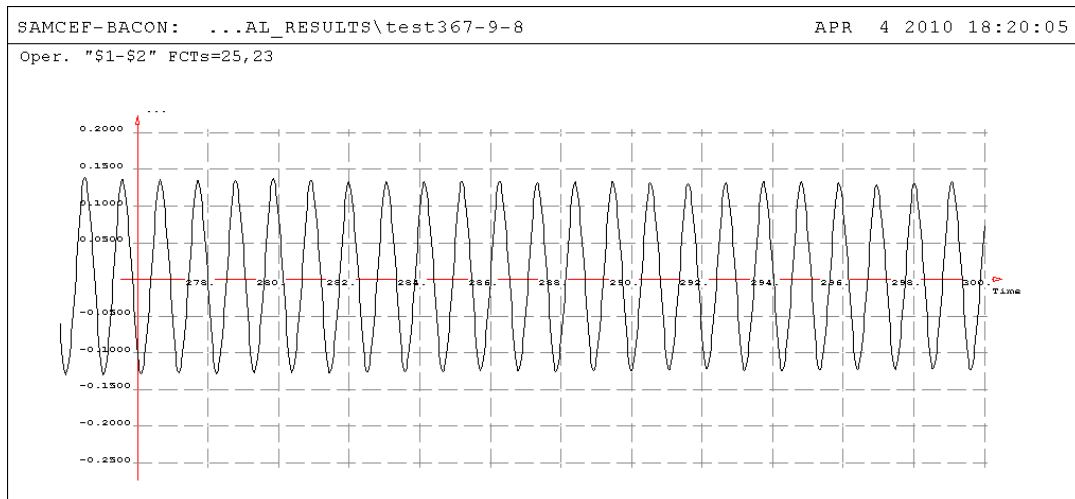


Figure 6-18. Analysis result at 8 m/s: relative Y-oscillation of subspan 3 vs. subspan 5 – no snaking (oscillation frequency is around 1 Hz => subspan)

6.3.3.3 Subspan mode

In Y-oscillation diagram of leeward subconductor relative to the windward one (Figure 6-19), the subspan mode is clearly observable at first subspan frequency (~ 1 Hz), see the zoomed diagram in Figure 6-20.

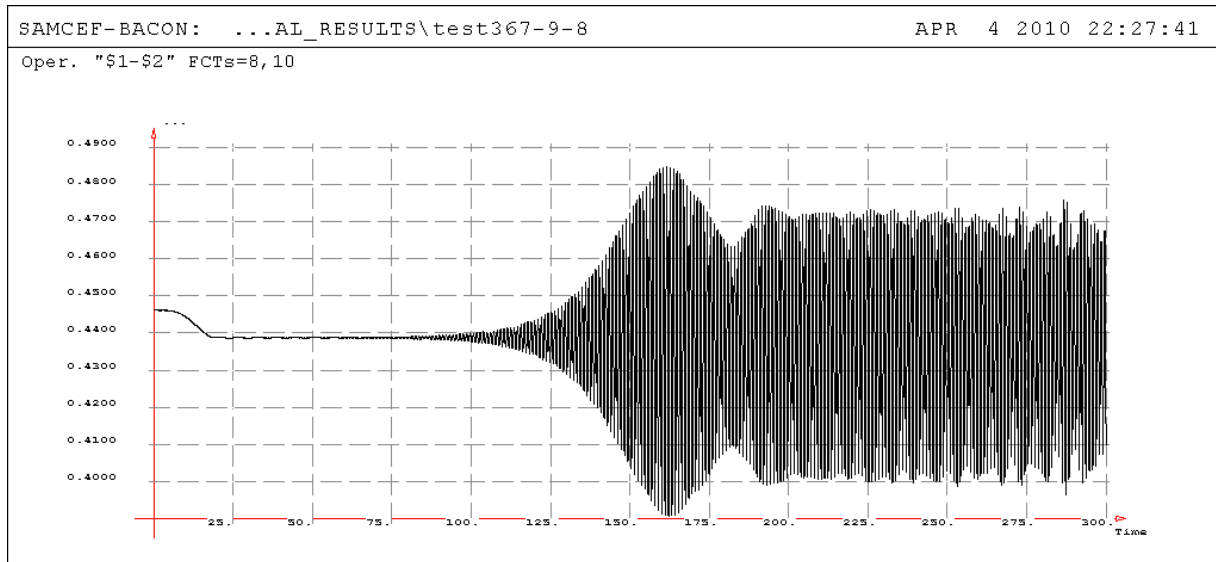


Figure 6-19. Analysis result at 8 m/s: subspan 4 - relative Y oscillation (subspan mode) – global exposure

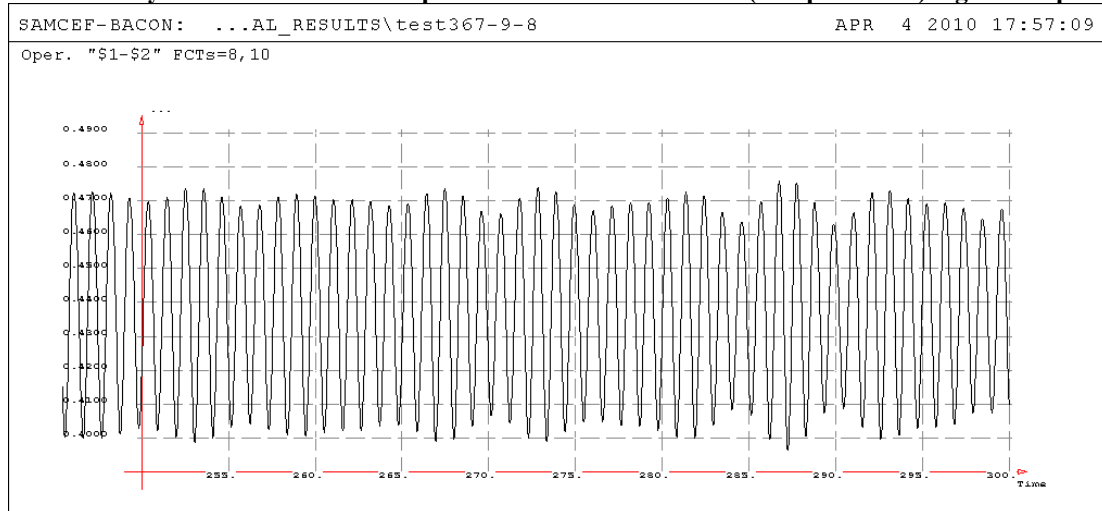


Figure 6-20. Analysis result at 8 m/s: subspan 4 - relative Y oscillation (subspan mode) – zoom at 50 s

6.3.3.4 Global subconductor orbits

The global orbits (see Figure 6-21) show, that despite prevailing subspan mode the oscillation follows quite a complex path. This might be due to contribution of spacer damper arm rotations, due to low amplitude of conductor oscillation.

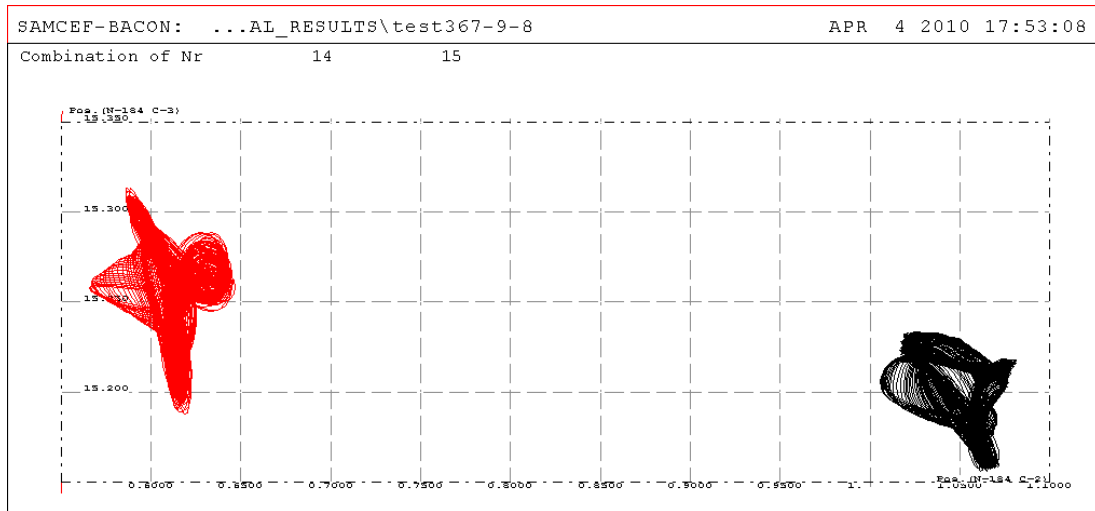


Figure 6-21. Analysis result at 8 m/s: subspan 4 - global orbits

6.3.3.5 Relative subspan orbit

In this orbit (Figure 6-22) showing the leeward subconductor motion vs. windward one within a subspan, the subspan mode is quite clear, which confirms the conclusion out of relative Y-motion (see Section 6.3.3.3).

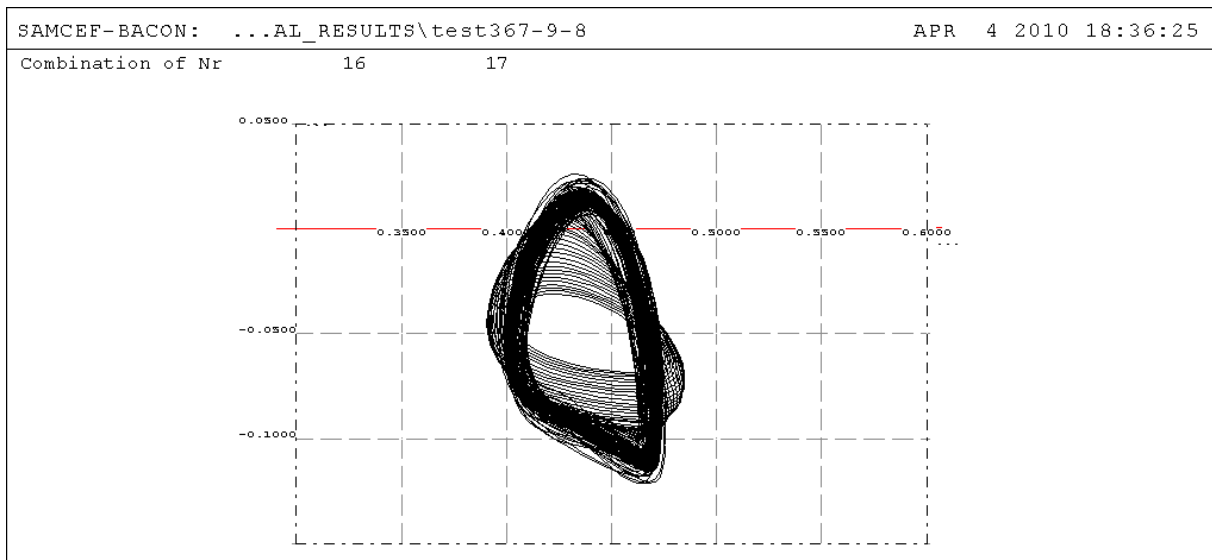


Figure 6-22. Analysis result at 8 m/s: subspan 4 – relative (subspan) orbit

Following above results, the peak-to-peak amplitude of subspan Y-oscillation is 0.075 m.

6.3.4 Calculation results: wind 11 m/s, subspan 7

6.3.4.1 Global oscillation

The global oscillation in this case is transient within calculated time frame (300 s). Nevertheless, it allows making estimation about the whole WIO character in these wind conditions.

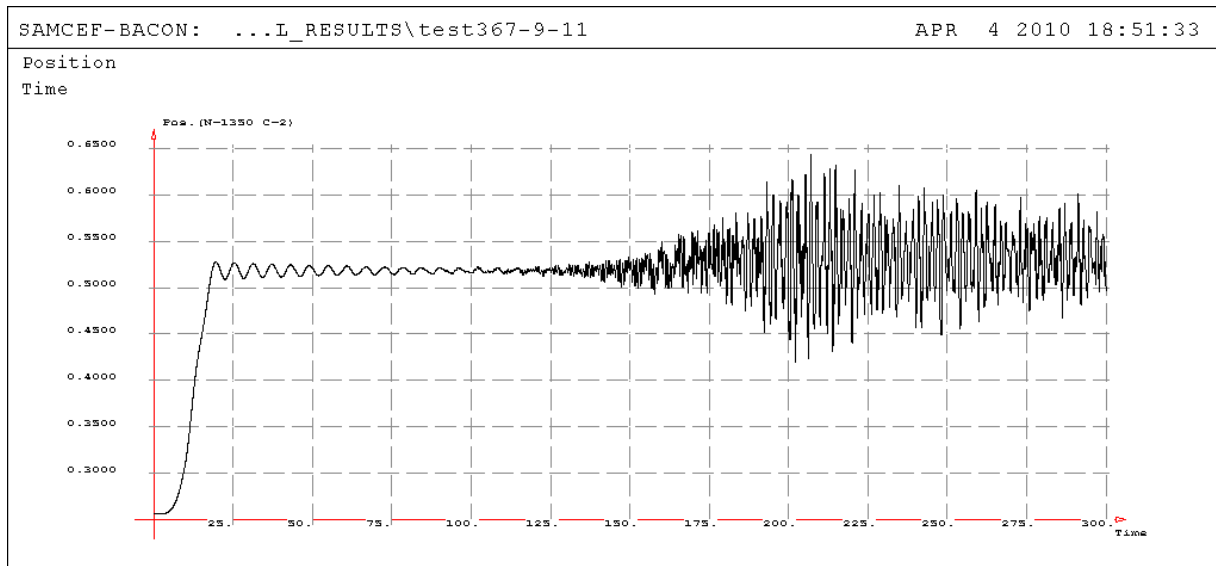


Figure 6-23. Analysis result at 11 m/s: subspan 7 - global Y oscillations

6.3.4.2 Snaking mode

As shown in Figure 6-24, the coupled image of oscillations in the subspans around the mid-span is quite complex, same as the Y-oscillation in the subspan “before-middle” relative to “aft-middle” (see Figure 6-25).

To understand what modes contribute into oscillations along the span, take Fast Fourier Transform of the latter relative Y-oscillation diagram (see Figure 6-26). Clearly, the subspan mode is the main one (~ 1 Hz). However, contribution of the snaking modes at frequencies ~ 0.3 and ~ 0.65 Hz is also noticeable.

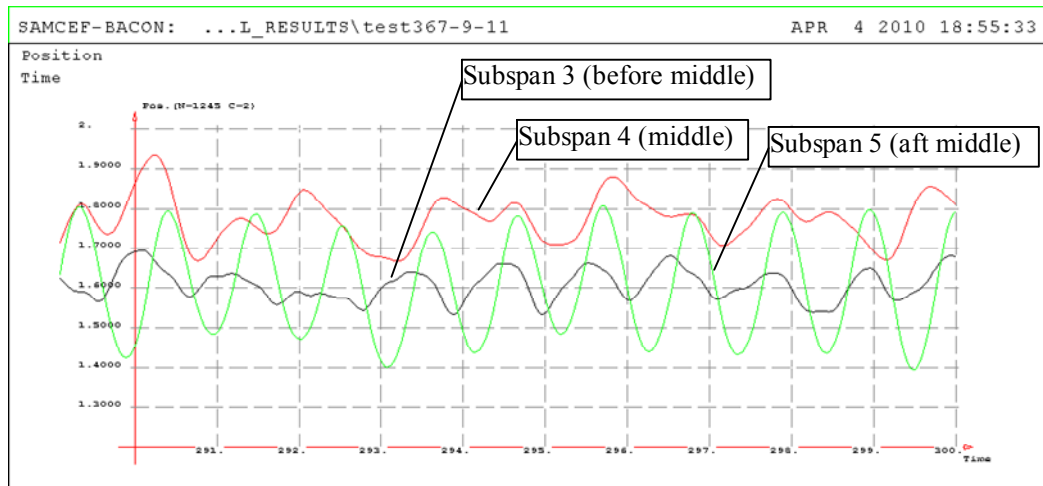


Figure 6-24. Analysis result at 11 m/s: oscillations ensemble at three subspans around middle-zoom at 10 s

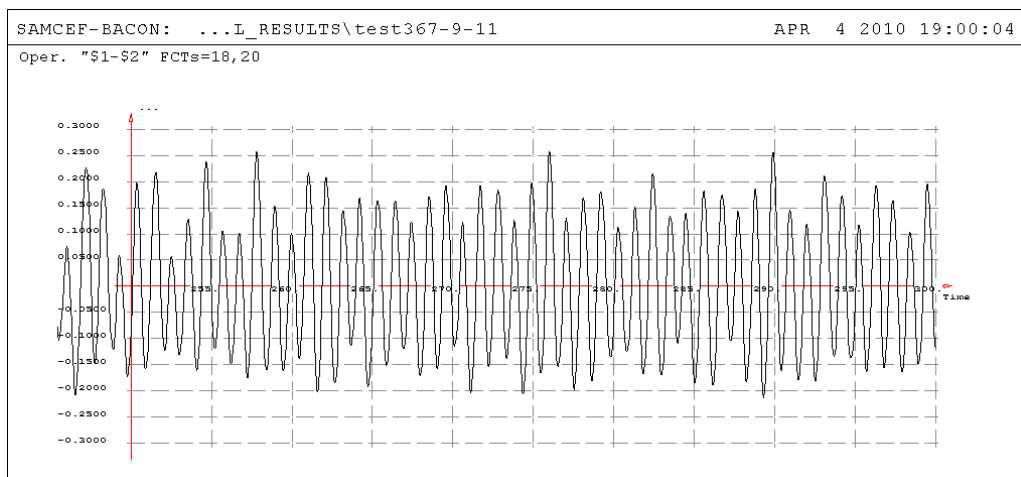


Figure 6-25. Analysis result at 11 m/s: relative Y-oscillation of subspan 3 vs. subspan 5 – zoom at 50 s

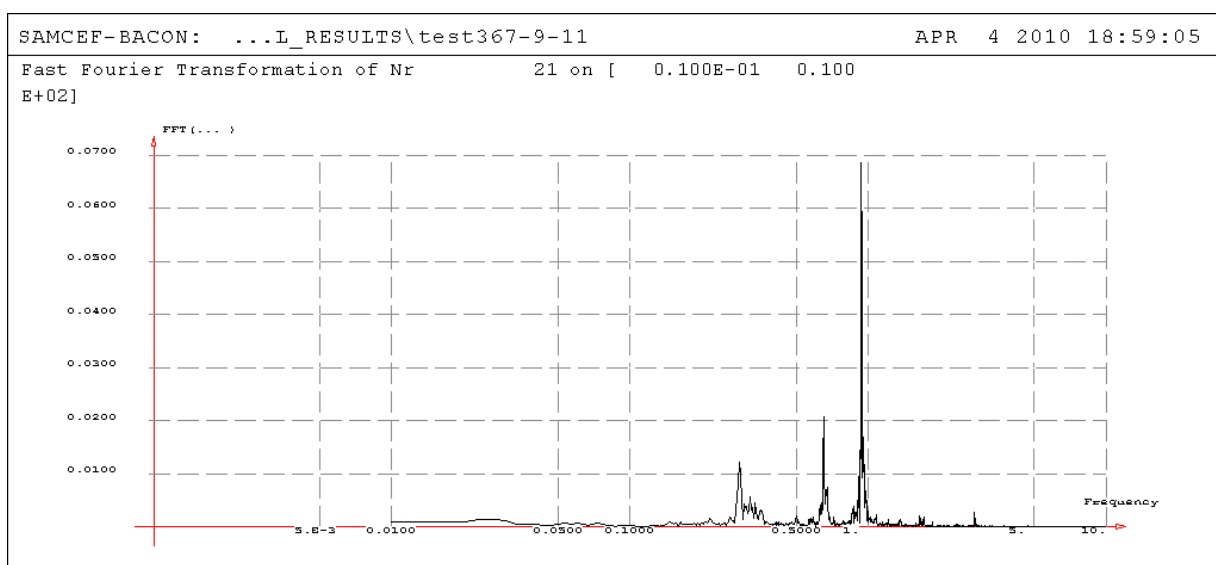


Figure 6-26. Analysis result at 11 m/s: spectrum of relative Y-oscillation of subspan 3 vs. subspan 5 – subspan mode (~1 Hz) combined with snaking modes (~0.3 and ~0.65 Hz)

6.3.4.3 Subspan mode

The overall image of the subspan mode (Y-oscillation of leeward conductor relative to the windward one – see Figure 6-27) shows that, contrary to the wind 8 m/s (see Figure 6-20), the higher harmonics dominate in the subspan oscillation (see the zoom in Figure 6-28). This is clearly observable in the corresponding R.M.S. amplitude spectrum (see Figure 6-29): the dominating is second subspan mode (~ 1.8 Hz).

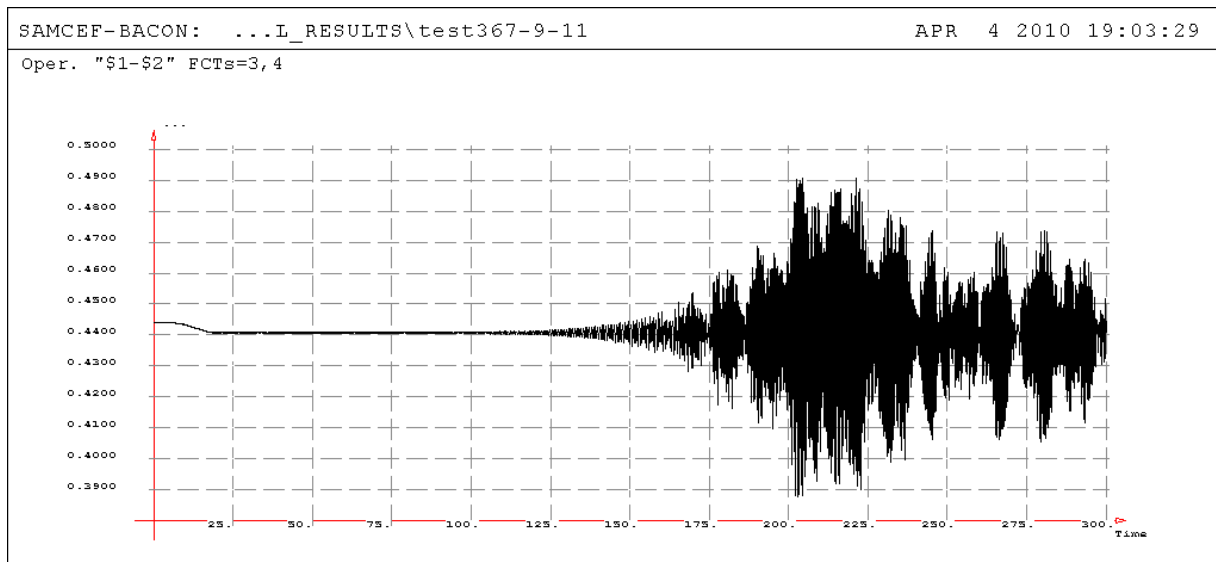


Figure 6-27. Analysis result at 11 m/s: subspan 7 - relative Y oscillation (subspan mode) – global exposure

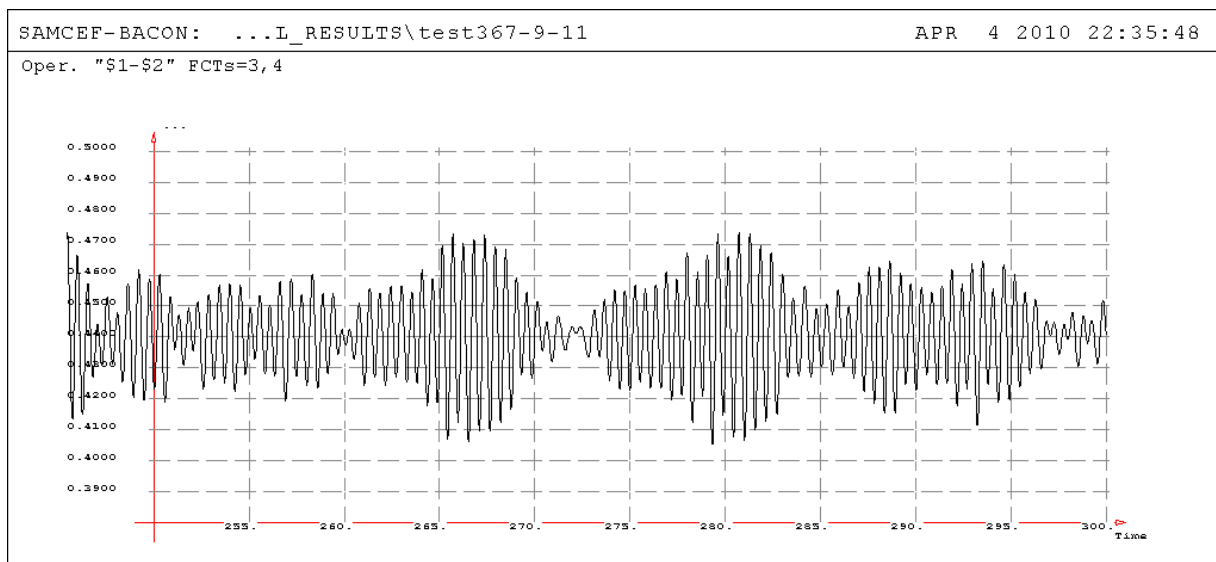


Figure 6-28. Analysis result at 11 m/s: subspan 7 - relative Y oscillation (subspan mode) – zoom at 50 s

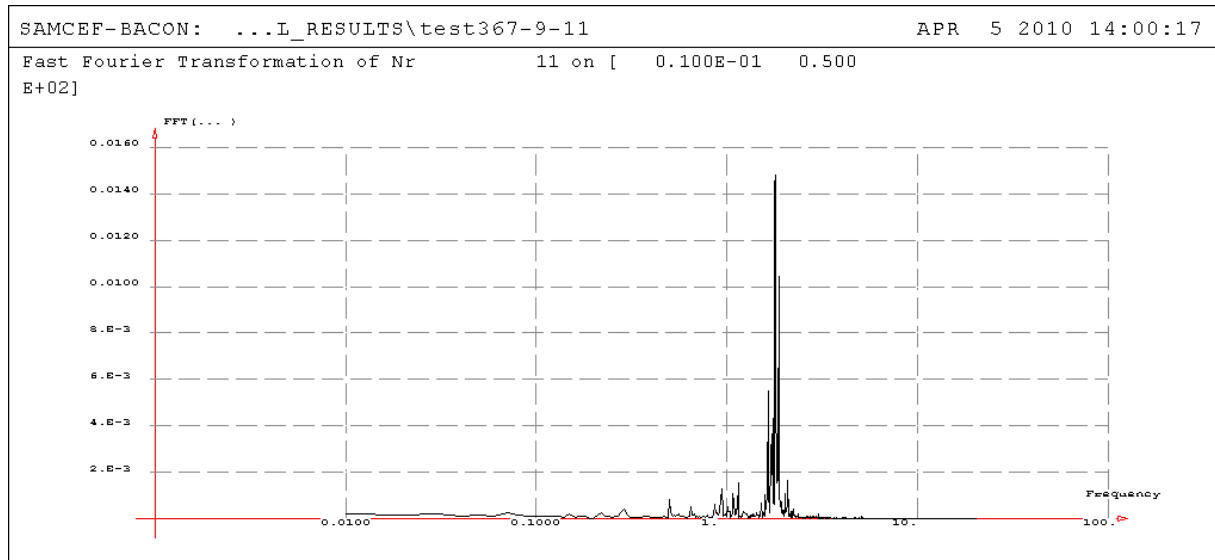


Figure 6-29. Analysis result at 11 m/s: spectrum of relative Y oscillation (subspan mode) at subspan 7: second subspan mode prevails (~1.8 Hz)

6.3.4.4 Global subconductor orbits

The global orbits are clearly concentrated at subspan mode (see Figure 6-30).

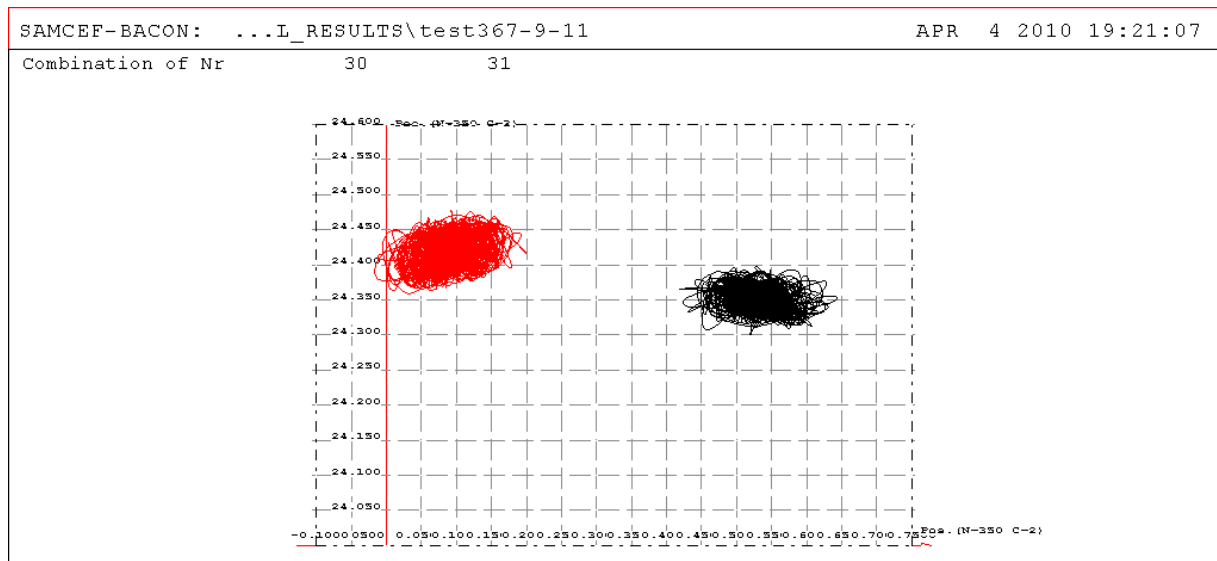


Figure 6-30. Analysis result at 11 m/s: subspan 7 - global orbits

6.3.4.5 Relative subspan orbit

The relative orbit is more complex. Unlikely the case of elliptical orbit under wind 8 m/s (Section 6.3.3.5), in this case it is composed of succession of 8-shape orbits, quite appropriate to the two-loop second subspan mode (see Figure 6-31). The oscillation is transient, making it difficult to estimate the amplitude for comparison to benchmarking. Judging after the core of the ellipse (which indicates the trend for steady oscillation set-up), the Y_p -p amplitude is approximately 0.05 m.

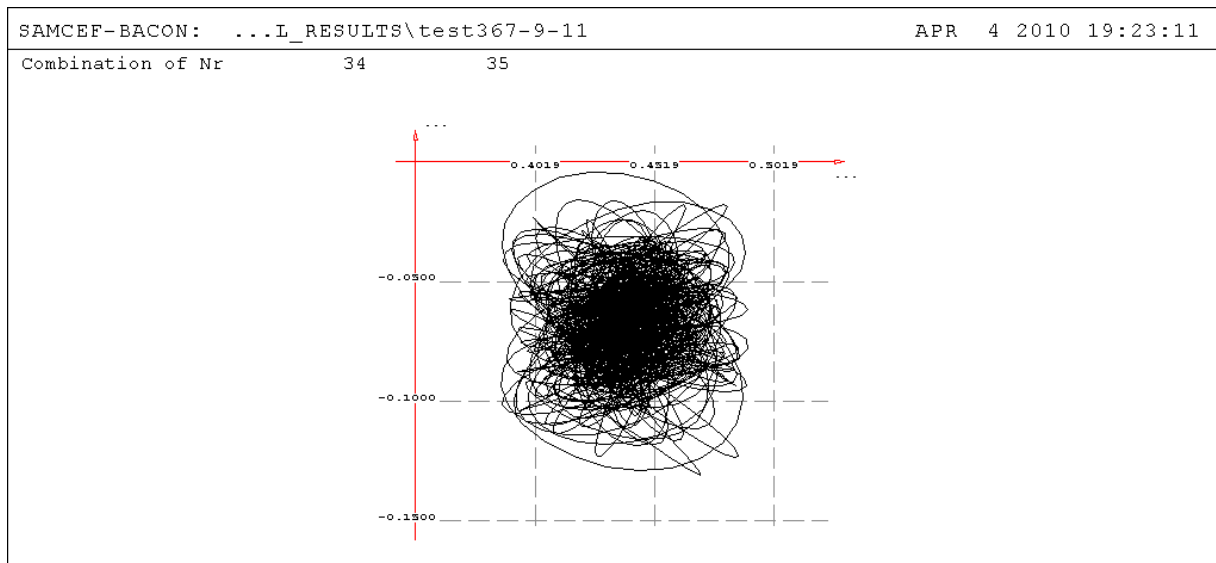


Figure 6-31. Analysis result at 11 m/s: subspan 7 – relative (subspan) orbit

6.3.5 Calculation results: wind 17 m/s, subspan 5

6.3.5.1 Global oscillation

The global oscillation shows fast build-up, after initial transient, of oscillation which frequency, being higher than conventional global mode, remains lower than in cases 8 and 11 m/s. This is a sign that snaking mode is dominant in case of this wind velocity.

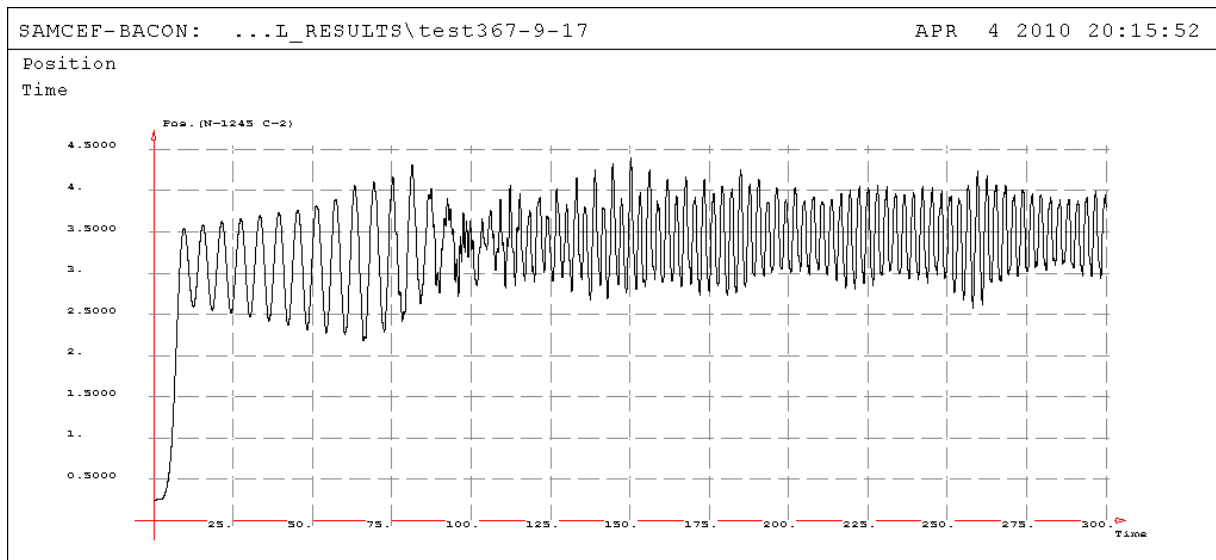


Figure 6-32. Analysis result at 17 m/s: subspan 5 - global Y oscillations

6.3.5.2 Snaking mode

As compared to 11 m/s wind (Section 6.3.4.2), the snaking mode is very well pronounced. Especially the relative snaking motion spectrum shows it clearly, that snaking mode (especially at ~ 0.35 Hz) is dominant.

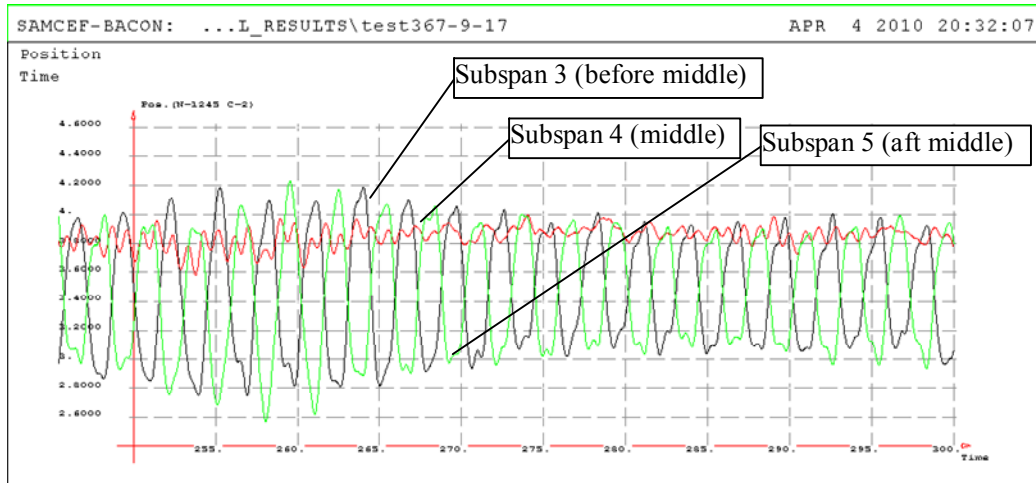


Figure 6-33. Analysis result at 17 m/s: oscillations ensemble at three subspans around middle-zoom at 50 s

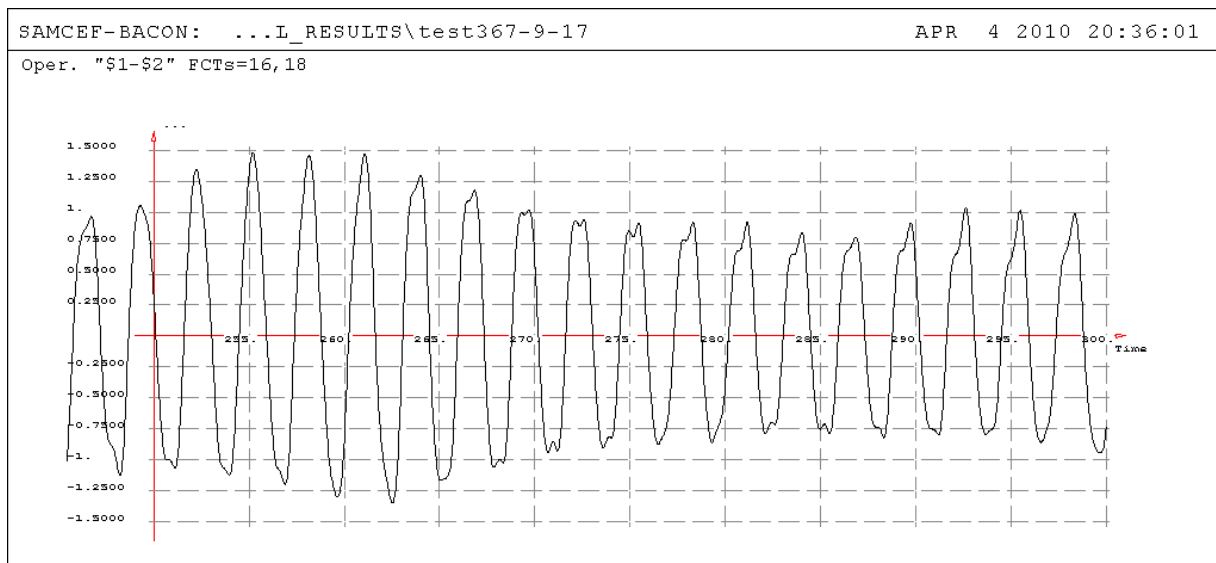


Figure 6-34. Analysis result at 17 m/s: relative Y-oscillation of subspan 3 vs. subspan 5 – zoom at 50 s

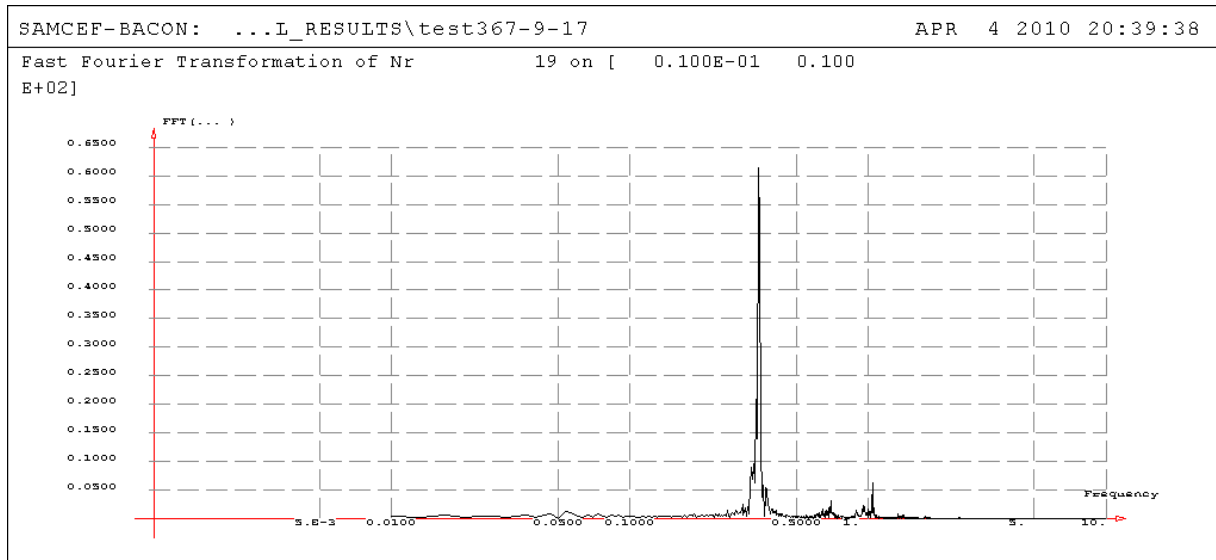


Figure 6-35. Analysis result at 17 m/s: spectrum of relative Y-oscillation of subspan 3 vs. subspan 5 – subspan mode (~1 Hz) combined with snaking modes (~0.35 and ~0.65 Hz, the former being dominant)

6.3.5.3 Subspan mode

Likewise the wind 11 m/s case, here the subspan oscillation is complex and includes higher and lower harmonics (see Figure 6-36 for overall exposure and its zoom in Figure 6-37). Unlikely the previous case, the amplitude spectrum shows, that first subspan mode dominates in its oscillation (see Figure 6-38).

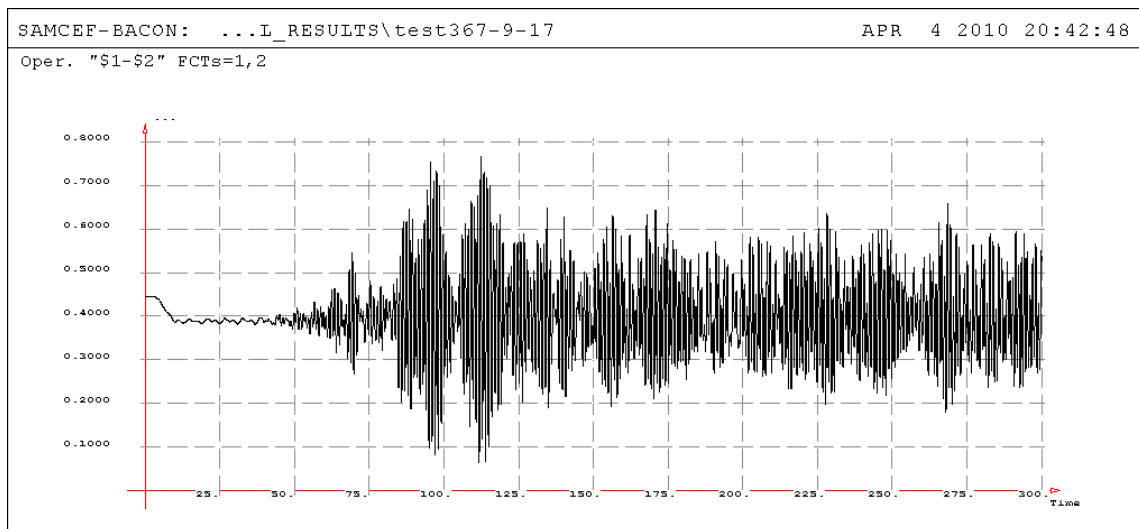


Figure 6-36. Analysis result at 17 m/s: subspan 5 - relative Y oscillation (subspan mode) – global exposure

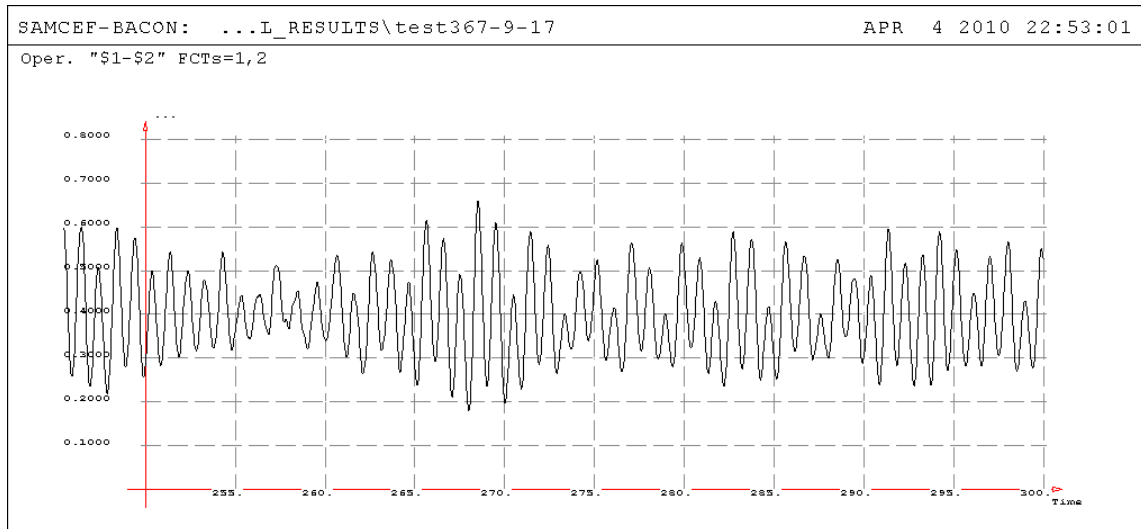


Figure 6-37. Analysis result at 17 m/s: subspan 5 - relative Y oscillation (subspan mode) – zoom at 50 s

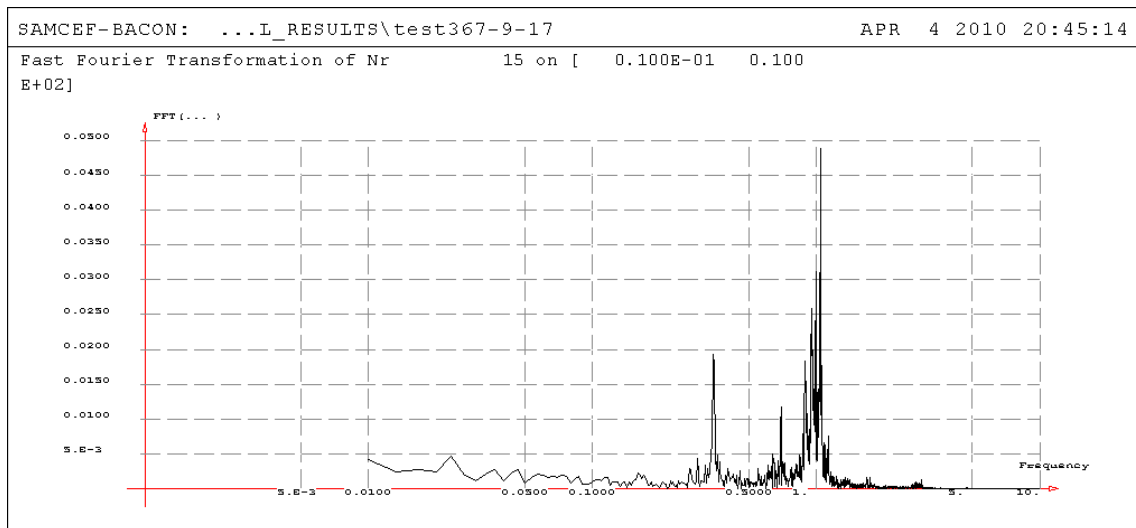


Figure 6-38. Analysis result at 17 m/s: spectrum of relative Y oscillation (subspan mode) at subspan 5: first subspan mode prevails (~1 Hz)

6.3.5.4 Global subconductor orbits

The global orbits (see Figure 6-39) show the interaction of subconductors via the spacer. The windward one seems to oscillate rather in subspan mode, while the leeward one oscillates in a more constrained mode, clearly influenced by snaking.

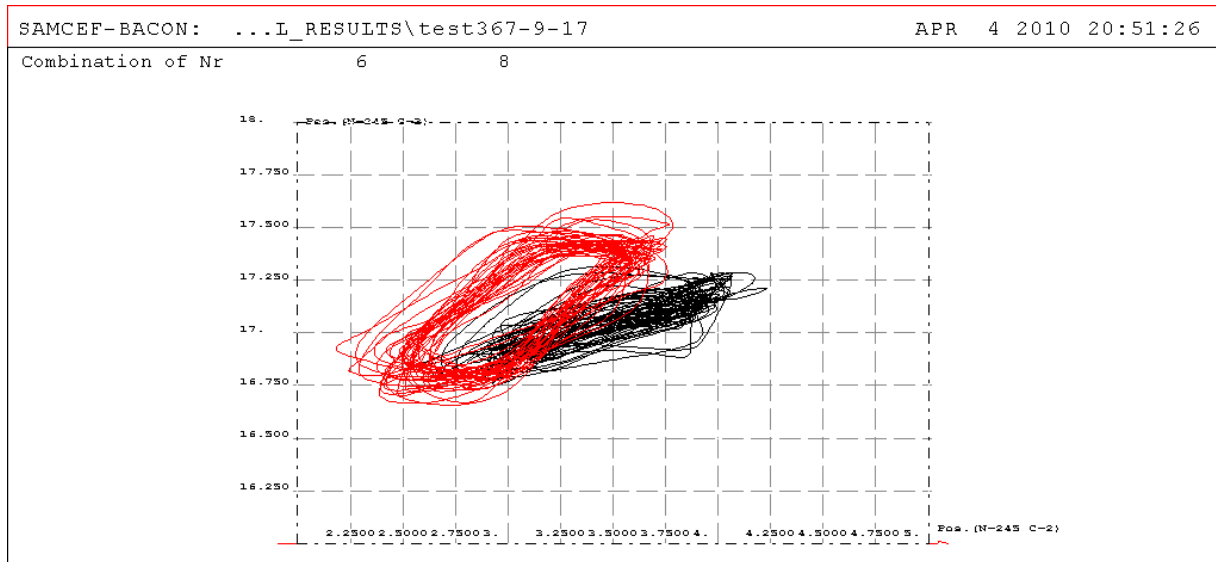


Figure 6-39. Analysis result at 17 m/s: subspan 5 - global orbits

6.3.5.5 Relative subconductor orbit

The relative orbit (see Figure 6-40) recalls the orbit obtained in Parametric Study, case of uniform spacers' placement without torsion (see Section 4.1.2.5). Note, that in this case a calculation including cable torsion/bending stiffness has been done giving nearly the same image of oscillation. One might suggest that such a Z-shaped relative orbit is a signature of snaking present in the WIO. The oscillation is steady-state at last 150 s frame, and maximal Y_{p-p} amplitude is about 350 mm.

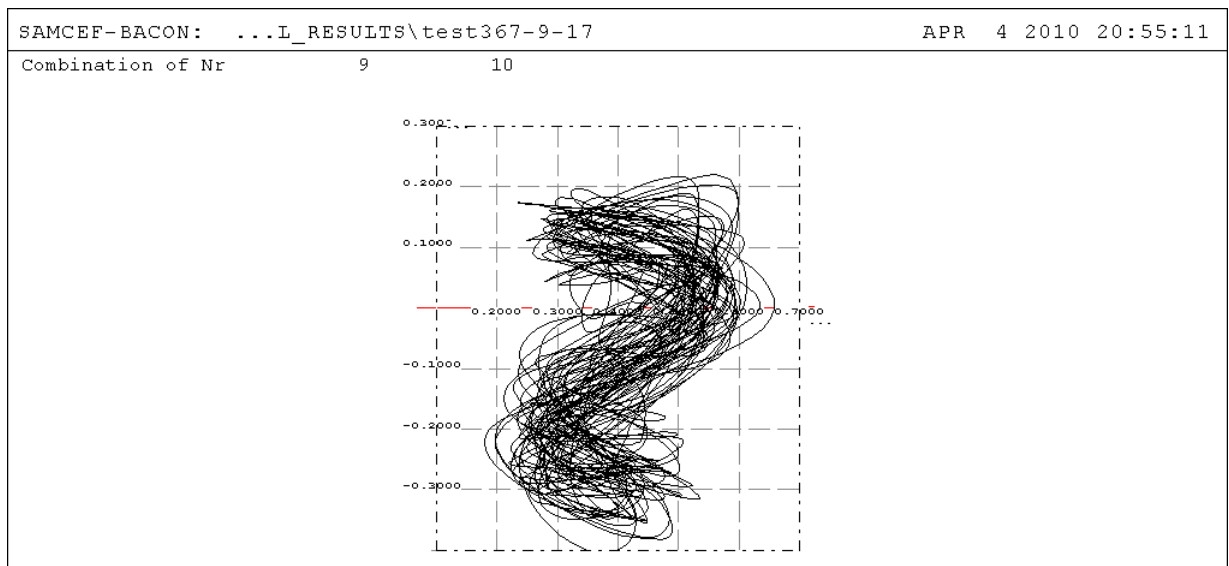


Figure 6-40. Analysis result at 17 m/s: subspan 5 – relative (subspan) orbit

6.4 Summary. Comparison to field test data and other studies

Below is presented a comparison of above results to the field test data. Another comparison is presented for the same calculation results done by Byelorussian researcher, Iosif I. Sergey [66].

Reference				Present analysis		Results by I. Sergey	
Subspan	Subspan Length	Wind velocity normal comp	Yp-p	Yp-p	Relative difference	Yp-p	Relative difference
no.	m	m/s	mm	mm	%	mm	%
4	57	8.0	51	75	32.0	87.5	41.7
5	65	17.0	294.1	350	16.0	368	20.1
7	35	11.0	25.6	50*	48.8	39	34.4

* Note: steady-state oscillation was not reached – result approximate.

Table 6-3. Analysis results compared to the field test data

Except the case 11 m/s (for which the result is approximate) two other analyzed points show fairly good convergence. Note, that in all cases, the calculated amplitude exceeds the measured one, indicating that analytical model provides a “cleaned-up” oscillation which is safe from other effects such as wind turbulence (normally present even if the wind is considered laminar). That might be one of the major reasons for difference against the field test.

Another possible way to improve convergence is that all analyses (same as those by Sergey) are done with smooth cylinder aerodynamic data. As it can be seen from Annex A, the C_D and C_L diagrams in the wake are less pronounced for stranded conductor rather than for the smooth one.

As regards the character of oscillation, the present model provides a whole spectrum of oscillation modes. One could observe the snaking mode, but also the higher subspan modes. These results are believed to be new as compared to the known reported numerical studies of WIO (e.g., [80] and [55]). Below presented is summary of the WIO modes observed in analysis.

Tested wind velocity	Snaking mode	1 st Subspan mode	2 nd subspan mode
8	No	Main	No
11	Weak	Weak	Main
17	Main	Weak	No

Table 6-4. Summary of the WIO modes observed in benchmarking analytical study

7 Conclusions

Summary of the tasks initially put for this thesis:

- Current state-of-the art for analytical calculations of WIO, including the loads in the wake, has been established (see, in particular, Sections 2.1; 2.2.2; 3.1; and Annex A). Overview of protection methods is presented (Section 5)
- Classic theory of wake-induced flutter has been reviewed and evaluated with modern numerical tools for analytical applications (Matlab) – see Section 2.2
- The numerical FE tool has been developed for WIO modelling - a special element implementing classic theory of wake-induced flutter (Section 3.2). A parametric (Section 4) and benchmarking validation of the model upon field experiments (Section 6) have been performed.
- The basic methodology for optimal placement of spacers over the bundle conductor span has been established (Section 5.1.7). The whole results obtained within the framework of this thesis serve as baseline for future development of such methodology.

Main conclusions of the present work are:

1. Application of quasi-steady theory to the wake-induced oscillations may be re-considered: the new criteria, adopted for aircraft aeroelasticity reveal that, when taking into account the fluid dynamics effects, the quasi-steady approach is questionable, at least at higher frequencies of subspan oscillations.
2. Obtaining the lift and drag coefficients distribution in the wake using CFD tools has demonstrated the constraints still existing to use this approach in practice. Such models are, however, useful for theoretical studies, as they can, in particular, emphasize optimal solver parameters which result in satisfactory correlation to the existing wind tunnel test data.
3. Model of flutter of leeward cylinder, when applied to the finite element model, shows good convergence both in the case of a single subspan model and extended model of real transmission line span. Current wake force user element, as is realized in Mecano, allows for loading any line element (cable or beam). At least seldom, if not first ever obtained, result is obtaining with this model the snaking modes, as well as second subspan mode. The well-developed oscillations bring, in some cases, to the clashing of subconductors. The model may be potentially extended to study the wake-induced effects in bundled stay cables and other cable structures. It has been, however, demonstrated the key role of correct structural modelling, as well as importance of good representation of spacer mechanics.
4. The series of simulations done with above model of the wake interaction show, that wake-induced oscillation is sensitive to numerous environmental and structural parameters of the line.

As of now, the ensemble of these parameters are impossible to represent in analytical models at least for predicting the developed amplitudes of oscillations. The finite element approach seems to be the most effective solution giving access to the most adequate estimation of line behaviour, in particular, when equipped with various fittings like spacer dampers.

5. An extension of aerodynamic model of the wake to include close-wake has been done, and close wake interaction occurrences in the simulations performed prove its viability.

Future work may include:

- research to account of non-stationary effects like time delay for a flow to travel between the windward and leeward conductor (flow retardation in the wake)
- account for longitudinal wind component
- account for turbulent wind.

8 List of references

- [1] Anderson, K., Hagedorn, P. (1995) "On the Energy Dissipation in Spacer Dampers in Bundled Conductors of Overhead Transmission Lines", *J. of Sound and Vibration*, 180(4), 539-556
- [2] Blazek, J. (2001) "Computational Fluid Dynamics", Elsevier
- [3] Blevins, R. D. (1990) "Flow-Induced Vibration," Van Nostrand Reinhold, NY
- [4] Bokaian, A., (1989), "Galloping of a Circular Cylinder In the Wake of Another", *J. of Sound and Vibration*, 128(1), 71 – 85
- [5] Bolotin, V. V. (1963) "Nonconservative problems of the theory of elastic stability", Oxford: Oxford University Press, 1963
- [6] Bon, C., Geradin, M. (1974) "On the numerical solution of large eigenvalue problems arising in panel flutter analysis by finite element method", *Computers & Structures*, 4, pp. 1223-1250, 1974
- [7] Chen, S. S. (1987), "Flow-Induced Vibration of Circular Cylindrical Structures", Hemisphere Publishing Corp.
- [8] Chen, S. S. (1987-2) "A General Theory for dynamic instability of tube arrays in the cross-flow", *J. Fluids and Structures*, 1, 1987, pp. 35-53
- [9] Cigada A.; Diana G.; Falco M.; Fossati F.; Manenti A. (1995) "Vortex Shedding and Wake Induced Vibrations in Single and Bundle Cables," *Proceedings of 9ICWE*, New Delhi, India
- [10] Claren, R., Diana, G. (1970) "Riposta di un fascio multiplo di conduttori ad una forzante sinusoidale", *L'Energia Elettrica*, 7, 1970, 435 – 439
- [11] Claren, R., Diana, G., Giordana, F., Massa, E. (1971) "The vibrations of transmission line conductor bundles", *IEEE Trans.-PAS* v. 90, no. 4, 1796-1810
- [12] Cremona, C., Foucriat, J-C, "Comportement au vent des ponts", *Presse de l'Ecole Nationale des Ponts et Chaussées*, 2002
- [13] Davenport, A. (1995) "How can we simplify and generalize wind loads?", *J. Wind Eng. & Ind. Aerodyn.* vol. 54/55, pp. 657-669
- [14] Diana, G., Gasparetto, M. (1972), "Energy method for computing the amplitude of vibration of conductor bundles due to wake effect", *L'Energia Elettrica*, n. 8 - 1972
- [15] Diana, G., Giordana, F. (1972), "Sulle vibrazioni di un cilindro in scia di un altro. Analisi del fenomeno con modello analitico", *L'Energia Elettrica*, n. 7- 1972
- [16] Diana, G., Boccione, M., Cheli, F., Resta, F., Manenti, A. (1999) "The aero-elastic behaviour of the OHTL expanded bundles". *Proc. of the 3rd ISCD (International Symposium on cable dynamics)*, Trondheim. pp 97-102
- [17] Dielen, B., Ruscheweyh, H. (1995) "Mechanism of interference galloping of two identical circular cylinders in cross flow", *J. Wind Engng Indust. Aerodyn.*, 54/55, 289 –300
- [18] H. Dubois, J. L. Lilien, F. Dal Maso (1991) "A New Theory for Frequencies Computation of Overhead Lines with Bundle Conductors", *AIM Review - Liege*, pp. 45 - 62.
- [19] EPRI (1979) "Transmission Line Reference Book: Wind-Induced Conductor Motion", Electric Power Research Institute, Palo Alto, CA, 1979

-
- [20] EPRI (2006) "EPRI Transmission Line Reference Book: Wind-Induced Conductor Motion". EPRI, Palo Alto, CA, 2006
 - [21] FlowVision – a CFD software package (www.flowvision.ru)
 - [22] Gagné, J.-G. (1980) "Spacer-Damper", US Patent 4 188 502
 - [23] Géradin, M., Rixen, D. (1994) «Mechanical Vibrations – Theory and Application to Structural Dynamics », Wiley - Masson, 1994
 - [24] Grigsby, L. L., (2001) "The Electric Power Engineering Handbook", CRC – IEEE. "
 - [25] Hardy, C., Bourdon, P. (1980) "The Influence of Spacer Dynamic Properties in the Control Of Bundle Conductor Motion", *IEEE Trans. PAS*, v. 99 No.2, p. 790 - 799
 - [26] Hardy, C., Van Dyke, P. (1995) "Field Observations on Wind-Induced Conductor Motions", *Journal of Fluids and Structures*, v. 9 p. 43-60
 - [27] Hartlen, R. T., Currie, I. G., "Lift-Oscillator Model of Vortex-Induced Vibration", *ASME Proc. – J. of Eng. Dyn. Div.*, 10, 1970
 - [28] Havard, D. G., (1996) "State of the Art Report on Spacer-Dampers: Mechanisms of Vibration Related to Spacers And Spacer-Dampers", *CIGRE Report* no. 22-96 (WG11-TF1) 24
 - [29] Hawkins, R. G. (1984) "Damping Spacer With Variable Damping Feature", US Patent 4 471 156
 - [30] Hearnshaw, D. (1974) "Spacer dampers performance – a function of in-span positioning", *IEEE Trans. PAS*, v. 93 no.5, 1298-1309
 - [31] Hémon, P. (1999) "An Improvement of the time-delayed quasi-steady model for the oscillations of circular cylinders in the cross-flow", *J. Fluids and Structures*, 13, 1999, 291-307
 - [32] Informenergo (2001) "Fittings and insulators for power transmission overhead lines". Industrial catalogue of the products of batch releases. Moscow (in Russian)
 - [33] Irvine, H.M. (1988) "Cable Structures", Penerbit ITB Bandung, 1988
 - [34] Kashima, S., Yanaka, Y., Suzuki, S., Mori, K., (2001) "Monitoring the Akashi Kaikyo Bridge: First Experiences", *Structural Engineering International*, no. 2, 120 – 123
 - [35] Kern, G., et al., (1995) « Nonlinear Flutter in Flow Induced Subspan Oscillations », *Proc. 1st Int. Symp. on Cable Dynamics*, Liege, 1995, 149 – 156
 - [36] Keutgen, R. (1999) „Galloping Phenomena: Finite Element Approach”, PhD Thesis, *Coll. des Publications de la Faculté des Sciences Appliquées de l’Université de Liège* n° 193, 1999
 - [37] Landau, L. D., and Lifshitz, E. M. (1959) "Fluid Dynamics", Oxford, Pergamon
 - [38] Laneville, A., Brika, D. (2001) «Experimental Simulation of the Fluid and Mechanical Coupling Between Transmission Line Conductors », *Proc. 4th Int. Symp. on Cable Dynamics*, Montreal 2001
 - [39] LAPACK – Linear Algebra Package of Fortran Source Codes (available via Internet: <http://gams.nist.gov/serve.cgi/PackageModules/LAPACK/>)
 - [40] Lilien, J-L. (1983) « Contraintes et conséquences électromécaniques liées au passage d’une intensité de courant dans les structures en câbles », *Coll. des Publications de la Faculté des Sciences Appliquées de l’Université de Liège* n° 87, 1983
-

-
- [41] Lilien, J.L. (1997) "Galloping of Overhead Electrical Lines, mechanisms, wind tunnel experiments – field measurement", *Proc. IInd Symp. on Cable Dynamics*, Tokyo, 1997, pp 37 – 48.
 - [42] Lilien, J.L. (2003) *Tutorial to Vth Cable Dynamics Symposium*, Santa Margherita, Italy, 2003
 - [43] Lilien, J.L., Snegovski, D., (2003) "Hurricane Simulation on Power Transmission Line", *Proc. Vth Cable Dynamics Symp.*, Santa Margherita, 2003, pp. 313-318.
 - [44] Lilien, J.L., Snegovski, D., (2004) "Wake-Induced Vibration of Power Transmission Line: Parametric Study", *Proc. 8th Conf. on Flow-Induced Vibration*, Paris, 2004, 421-425
 - [45] Lilien, J.L., Private Communication
 - [46] Mair, W. A., Maull, D. J., (1971) "Aerodynamic Behaviour Of Bodies In the Wake Of Other Bodies", *Phil. Trans. Roy. Soc. Lond. series A.*, no. 268, 425 –437
 - [47] MATLAB r.12 www.mathworks.com
 - [48] Meneghini, J. R., Saltara, F., Siqueira, C. L. R., Ferrari, J. A. (2001) "Numerical Simulation of Flow Interference Between Two Circular Cylinders in Tandem and Side-By-Side Arrangements", *J. Fluids and Str.*, Vol. 15, No. 2, p. 327-350
 - [49] "Methodology for protection against vibration and subspan oscillations of the electrical conductors and ground wires of 37 – 750 kV aerial overhead lines ", RD 34.20.182-90, SPO ORGRES, Moscow, 1991 (in Russian)
 - [50] Mittal, S., Kumar, V., Raghuvanshi, A. (1997) "Unsteady Incompressible Flows Past Two Cylinders in Tandem and Staggered Arrangements", *Int. J. for Numerical Methods in Fluids*, Vol. 25, p. 1315 -1344
 - [51] Mohajery, M., Rawlins, C. B. (1977) "Transmission Line Having Improved Stability Characteristics From Wake-Induced Subspan Oscillations", US Patent 4 018 980
 - [52] Mohammadi, B., Pironneau, O., "Analysis of the k-epsilon turbulence model", J. Wiley & Sons, 1994
 - [53] Newman, D. J., Karniadakis, G. E. (1997) "A direct Numerical Simulation Study of Flow Past a Freely Vibrating Cable", *J. Fluid Mech.* vol. 344, pp. 95 – 136
 - [54] Numerical Analysis Library of Science & Research Computational Centre, Moscow State University, http://www.srcc.msu.ru/num_anal
 - [55] Oliveira, T. (2007) "Consideration of wind-structure interaction in cable bundles in transmission lines", *Proc. 7th Symp. Cable Dynamics, Vienna, Austria*
 - [56] Price, S.J., (1975) "Wake induced flutter of power transmission conductors", *J. of Sound and Vibration*, 38 (1), 125-147
 - [57] Price, S.J., Maciel, Y. (1990), "Solution of the nonlinear equations for wake-induced flutter via the Krylov and Bogoliubov method of averaging", *Journal of Fluids and Structures*, 4, pp. 519-540
 - [58] Price, S.J., Païdoussis, M.P. (1984/1), "An improved mathematical model for the stability of cylinder rows subject to cross-flow", *J. of Sound and Vibration*, 97(4), 615 – 640
 - [59] Price, S.J., Païdoussis, M.P. (1984/2), "The aerodynamic forces acting on groups of two and three circular cylinders when subject to a cross-flow", *J. of Wind Engineering and Industrial Aerodynamics*, 17, 329-347
 - [60] Rawlins, C. B. (1976) "Fundamental concepts in the analysis of wake-induced oscillation of bundled conductor", *IEEE Trans. PAS*, v. 95 no.4, 1377-1393
-

-
- [61] Rawlins, C. B. (1977) "Extended analysis of wake-induced oscillations of bundled conductors", *IEEE Trans. PAS*, v. 96 no.5, 1681-1689
 - [62] Reynolds, O. (1883) "An experimental investigation of the circumstances which determine whether the motion of water shall be direct or sinuous, and of the law of resistance in parallel channels". *Phil. Trans. of the Royal Society* v. 174, 935–982
 - [63] RIBE (1982) "RIBE Consulting". *RIBE Line Accessories Division Catalog*
 - [64] Roshko, A., "Structure of Turbulent Shear Flows: a New Look", AIAA, 1976 – pp. 1349 – 1357
 - [65] SAMCEF v. 10 – a general-purpose FEA software, by SAMTECH S.A., rue des Chasseurs-Ardennais, 8, B-4031 Angleur-Liege, Belgium
 - [66] Sergey, I. (2010) – private communication
 - [67] Shklyarchuk, F. (1983) "Dynamics and aeroelasticity of flying vehicles", MAI Ed., Moscow
 - [68] Simiu, E., Scanlan, R. H. (1996) "Wind Effects on Structures: Fundamentals and Applications to Design", J. Wiley & Sons, NY, 1996
 - [69] Simpson, A. (1967), "Determination of natural frequencies of multiconductor overhead transmission lines", *Journal of Sound and Vibration*, v. 20(4), 417-449
 - [70] Simpson, A. (1971/1), "On the Flutter of a Smooth Circular Cylinder in a wake", *Aeronautical Quarterly* XXII, 25-41
 - [71] Simpson, A. (1971/2), "Wake induced flutter of circular cylinders: mechanical aspects", *Aeronautical Quarterly* XXII, 101-118
 - [72] Simpson, A., Flower, J.W. (1977), "An improved mathematical model for the aerodynamic forces on tandem cylinders in motion with aero-elastic applications", *J. of Sound and Vibration*, 51(2), 183 – 217
 - [73] Snegovskiy, D., Lilien, J-L. (2010), "Nonlinear Finite Element Approach to Simulate Wake-Induced Oscillation in Transmission Line Span", *Submitted in ASME 2010 Fluids Engineering Summer Meeting (FEDSM2010)*, Montreal, August 1-5
 - [74] State of the art survey on spacers and spacer dampers: Part I - General description, CIGRE Working Group B2.11 of Task Force 5D1.33 – Electra No.209, 2003
 - [75] State of the art survey on spacers and spacer dampers: Part II – Technical aspects CIGRE Working Group B2.11 of Task Force 5D1.33 – Electra No 221, 2005
 - [76] Svenska Kraftnät (2008) Technical Guidelines TR5-08E "Spacers for 220 kV and 400 kV OH lines – version A, 2008
 - [77] Tanaka, H. (2003) "Aerodynamics of Cables", *Proceedings of Vth Cable Dynamics Symposium*, Santa Margherita, Italy, 2003, pp. 11- 25
 - [78] Tsui, Y. T. (1976) Discussion on the article of C. B. Rawlins "Fundamental concepts in the analysis of wake-induced oscillation of bundled conductor", *IEEE Trans. PAS*, v. 95 no.4, 1385-1386
 - [79] Tsui, Y. T., (1977) "On wake-induced flutter of a circular cylinder in the wake of another", *ASME Trans. – J. Appl. Mech.*, June, 1977, 194 – 200
 - [80] Tsui, Y. T., (1986) "On wake-induced vibration of a conductor in the wake of another via a 3-D finite element method", *J. Sound and Vibration*, 107(1), 39 – 58
 - [81] Vanko, V. I. (1997) "On Aerodynamic Instability of Cables in the Bundled Power Transmission Line", trans. Belorussian Acad. Of Sci., series Energy, 1997, No. 1-2, pp. 19-24
-

- [82] Vanko, V. I., Galkin, S. V., Zaitsev, A. A. (1996) "On Optimization of Positioning the Spacer Dampers Within the Span of the Bundled Power Transmission Line", *Trans. Belorussian Acad. Of Sci., series Energetics*, 1996, No. 5, pp. 89-97
- [83] Vanko, V. I., Solovieva, E. V. (1996) "On Conditions of Aerodynamic Instability of the Bluff Body Equilibrium", *Applied Mech. And Techical Physics*, 1996, vol. 37, No. 5 pp.29 – 34 (in Russian)
- [84] Strelyuk, M., Sergey, I., Vinogradov, A., Krasnov, V. (1986) "Dynamic Loads onto the Spacers Under Subspan Oscillations of Super-High Tension Overhead Lines", *Energeticheskoye Stroitel'stvo*, № 1, 68 – 71 (in Russian)
- [85] Vinogradov, A. A. (1988) "Vibrational Spacer Damper", Certificate of Authorship SU 1381636 A1
- [86] Wang, J. (1996) "Large vibrations of overhead electrical lines. A full 3-DOF model for galloping studies", PhD Thesis, *Coll. des Publications de la Faculté des Sciences Appliquées de l'Université de Liège* n° 151, 1996
- [87] Wardlaw, R.L. & Cooper, K.R., (1974) "Mechanisms and alleviation of wind-induced structural vibrations", *Proc. 2nd Symp. on Applications of Solid Mechanics*, Hamilton, Ont., 1974, pp.369-399.
- [88] Wardlaw, R. L., Cooper, K. R., Ko, R. G., Watts, J. A. (1975) "Wind Tunnel And Analytical Investigations Into the Aero-elastic Behaviour Of Bundled Conductors", *IEEE Trans. on PAS*, vol. 94 no. 2 p. 642 - 651
- [89] Williamson, C. H. K., Roshko, A., "Vortex Formation in the Wake Of an Oscillating Cylinder", *J. Fluids and Str.*, vol. 2, pp. 355-381 (1988)
- [90] Zdravkovich, M. M., (1977) , "Review of flow interference between two circular cylinders in various arrangements", *J. Fluids Engng. Trans ASME*, 99, 618 – 633
- [91] Zdravkovich, M. M. (1985), "Flow Induced Oscillations Of Two Interfering Circular Cylinders", *J. of Sound and Vibration*, 101(4), 511-521
- [92] Zdravkovich, M. M., (1987), "The effects of interference between circular cylinders in cross flow", *J. Fluids and Structures*, 1, 239-261
- [93] Zdravkovich, M. M., "Flow Around Circular Cylinders", vol. I, Oxford University Press, 1997

Acknowledgments

It's been a long way, this thesis. This page will fit my gratitude to its completion just very briefly...

I would like to express my deepest gratitude to Professor Jean-Louis Lilien, who granted me the opportunity to make this study and guided my work throughout these years.

I bring my deepest thanks to the University of Liege and its Montefiore Institute, which has been a homeland for my research throughout all these years, the research in science, in engineering, and in myself.

I am very indebted to Dr. Helmut Wenzel, General Manager of European project IMAC G1RD-CT2000-00460 who sponsored my thesis, and all participants of IMAC project.

Many thanks to all members of CIGRE group B2.11, especially Dr. Chuck Rawlins, Dr. Giorgio Diana, Pr. André Laneville and Pr. Peter Hagedorn for fruitful discussions.

Many thanks to my Russian colleagues who acquainted me with the world of electricity, Dr. Alexander Vinogradov and Dr. Alexander Daniline. I would like to make note of extremely positive role in this thesis of all team at Russian enterprise Elektrossetstroyproekt (ESSP), including those who are not among us anymore, Mr. Yuri Tsvetkov and Dr. Vassily Kravchenko.

My special thanks go to:

- Samtech S.A. for their support which was genius especially at the concluding stage allowing me to bring this study to the final;
- JSC ECAR (Engineering Centre of Airbus in Russia), my current and brilliant employer, for their support by all means, you gave me so much of inspiration to finalize this work.

At the top of all, I am deeply grateful to all my family, especially my parents Pobeda and Valery, my wife Tatiana, our children Dasha and Vladimir, my sister Anna. This thesis would not be possible without their encouragement and support.

Whatever is our success in the life, we acknowledge to many of our supporters, our friends, our beloved, but there are always much more people whom our progress is due to. I thank all of you.

Dmitry Snegovskiy

05/04/2010

Annex A. Aerodynamic coefficients of a leeward cylinder

A-1. Polynomial approximation by Simpson [70]

This is probably one of the first approximations which is effected in

$\kappa\Delta$ = distance between cylinders; α - incidence angle

$$C_D = \begin{cases} 0.797 + 0.00958\kappa\Delta - (0.4 - 0.00958\kappa\Delta)\cos(3 + 0.561\kappa\Delta)\alpha; & \alpha \leq \pi / (3 + 0.561\kappa\Delta) \\ 1.197; & \alpha > \pi / (3 + 0.561\kappa\Delta) \end{cases} \quad (7.1)$$

$$C_L = \begin{cases} (0.42 - 0.01684\kappa\Delta)\sin(2 + 0.561\kappa\Delta)\alpha; & \alpha \leq \pi / (3 + 0.561\kappa\Delta) \\ 0; & \alpha > \pi / (3 + 0.561\kappa\Delta) \end{cases}$$

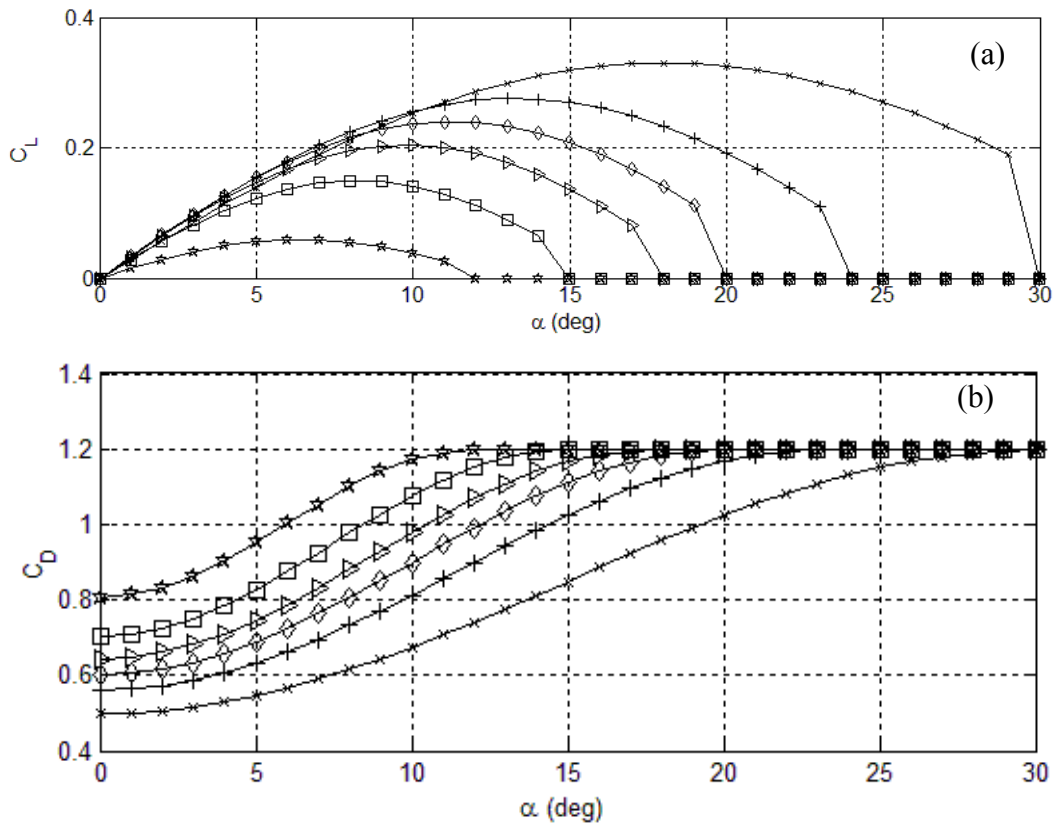


Figure A - 1. (a) Lift coefficient, (b) Drag coefficient. Curves correspond to the spacings $\kappa\Delta$: x = 5.5, + = 7, ◇ = 11, Δ = 13, □ = 15, * = 21

In the following plots the early distributions of the aerodynamic derivatives have been done. Note the high levels of derivatives C_{Dz} and C_{Lz} due to the scale of inclination angle, α .

Cylinders' spacing $Y/D = 10$, $Re \sim 40k$

alfa	y	z	C_D	C_L
0	0,0	10	0,54	0
2	0,3	10,0	0,57	0,13
4	0,7	10,0	0,67	0,22
6	1,0	9,9	0,77	0,24
8	1,4	9,9	0,9	0,23
10	1,7	9,8	1,03	0,2
12	2,1	9,8	1,13	0,15
14	2,4	9,7	1,21	0,09
16	2,8	9,6	1,26	0,03
18	3,1	9,5	1,26	0,01
20	3,4	9,4	1,24	0

alfa	C_{Dy}	C_{Dz}	C_{Ly}	C_{Lz}
0	-0,27	0	0	5,37
2	-0,275	0,73	0,22	3,437
4	-0,132	3,275	0,31	1,415
6	-0,138	3,29	0,328	-0,035
8	-0,022	3,287	0,256	-0,762
10	0,213	3,273	0,168	-1,116
12	0,368	2,89	-0,026	-1,89
14	0,376	1,5	-0,218	-1,86
16	0,19	-0,02	-0,146	-0,945
18	-0,006	-0,096	0,019	-0,333
20	-0,025	-0,104	0,056	-0,186

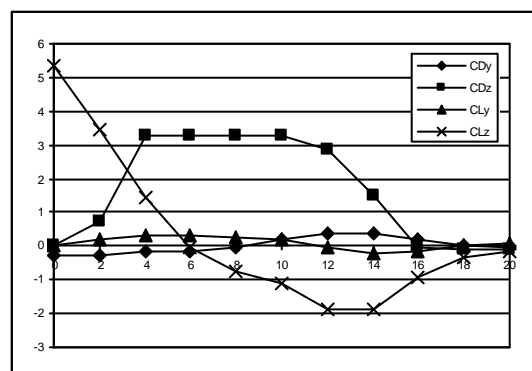
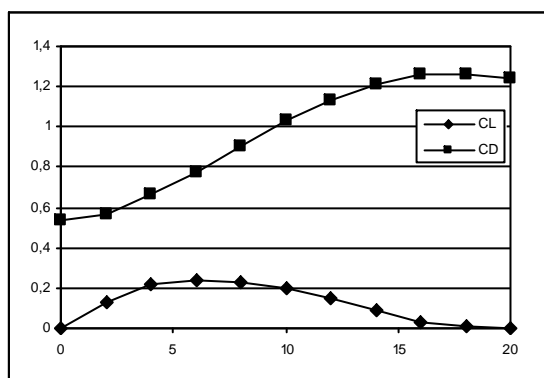


Figure A - 2. Test Data by Simpson [71]

2. Wardlaw et al. [88]

The present measures by Wardlaw and Cooper demonstrate the effect of drag crisis. It is the leeward conductor which is subject to the post-critical regime first, its incipience being forwarded by the turbulence in the wake. The overall drag coefficient decreases with slight increase of minimum value at the wake axis. The maximum of lift coefficient approaches to the wake axis because the wake in post-critical and is getting narrower.

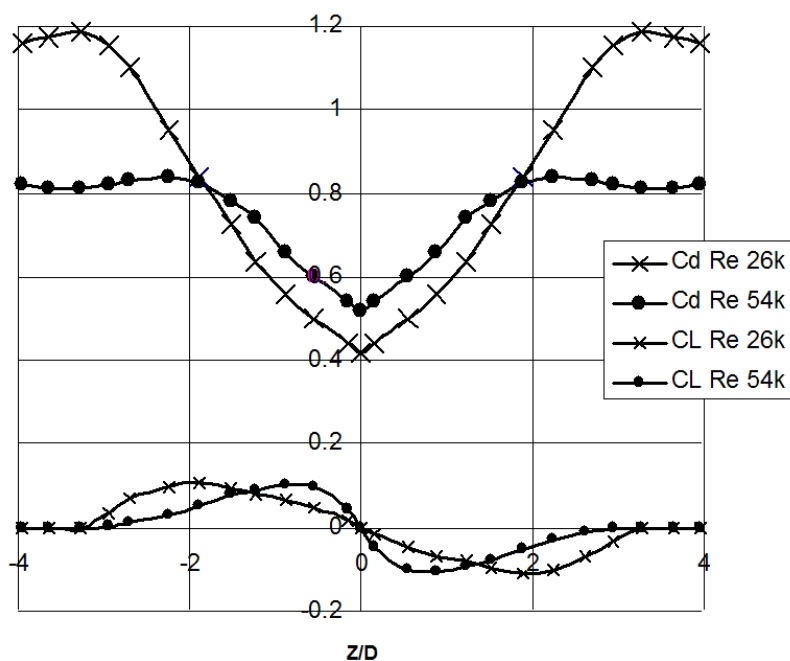


Figure A - 3. Variation of lift and drag forces on stranded conductor (diameter: 4.06 cm, horizontal spacing $Y/D = 10$) [87]

Diana [15]

Polynomial approximation of the test data on smooth cylinder ($Re \sim 40k$)

Drag coefficient

$$0 < |Z/D| < 3, \quad Y/D < 25:$$

$$C_D = 1.2 - 1.6 \left[1.215 - 7.2 \cdot 10^{-2} \xi + 1.44 \cdot 10^{-3} \xi^2 \right] \cdot \left[74 - 0.712 \eta^2 - 10.5 \eta^3 + 2.66 \eta^4 \right] \cdot 10^{-2}$$

$$0 < |Z/D| < 3, \quad Y/D > 25:$$

$$C_D = 1.2 - 0.5056 \cdot \left[74 - 0.712 \eta^2 - 10.5 \eta^3 + 2.66 \eta^4 \right] \cdot 10^{-2} \quad (7.2)$$

$$|Z/D| > 3$$

$$C_D = 1.2$$

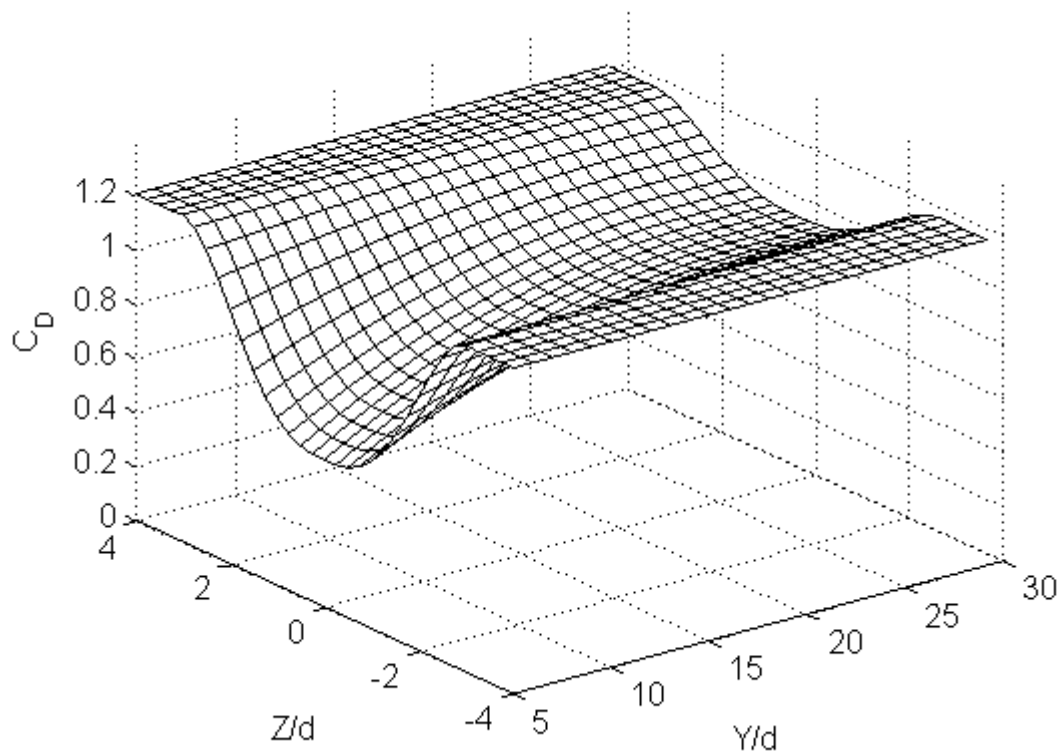


Figure A - 4. Drag coefficient after polynomial approximation (7.2)

Lift coefficient

$0 < |Z/D| < 3.66, \quad Y/D < 26.6:$

$$C_L = \left[-1.78 + 0.127\xi - 2.38 \cdot 10^{-3} \xi^2 \right] \cdot \left[0.928\eta^2 - 0.827\eta^3 + 0.244\eta^4 - 0.0239\eta^5 \right] \cdot \text{sign}(\eta)$$

$0 < |Z/D| < 3.66, \quad Y/D > 26.6:$

$$C_L = -0.08 \cdot \left[0.928\eta^2 - 0.827\eta^3 + 0.244\eta^4 - 0.0239\eta^5 \right] \cdot \text{sign}(\eta) \quad (7.3)$$

$|Z/D| > 3.66$

$$C_L = 0$$

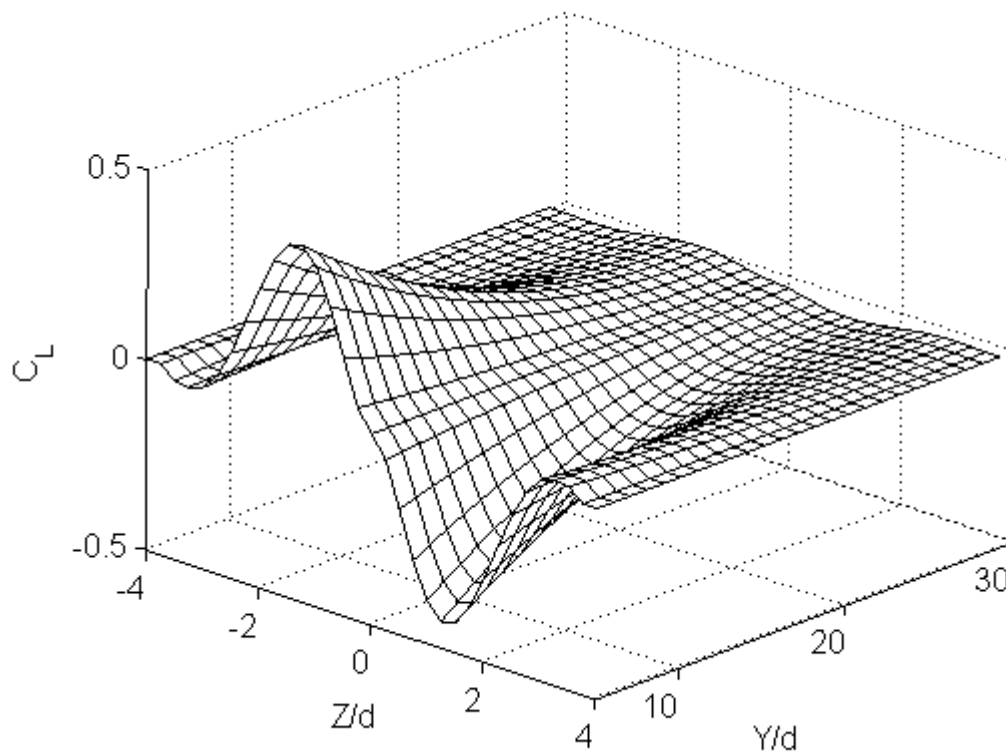
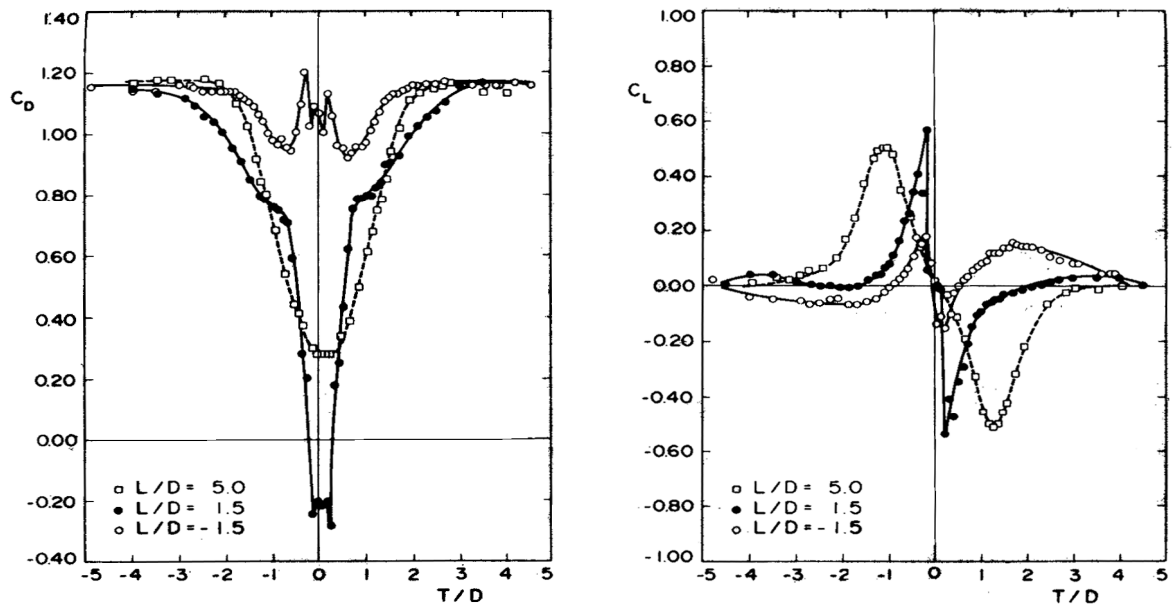


Figure A - 5. Lift coefficient after polynomial approximation (7.3)

Price & Païdoussis [59]

Figure A - 6. Smooth cylinder ($Re = 5.3 \times 10^4$) (Price, Païdoussis, 1984)

Price [56]

The polynomial approximation adopted here is similar to the polynomials of Bokaian [4] except that here the precision is higher and permits the coverage of the larger wake region.

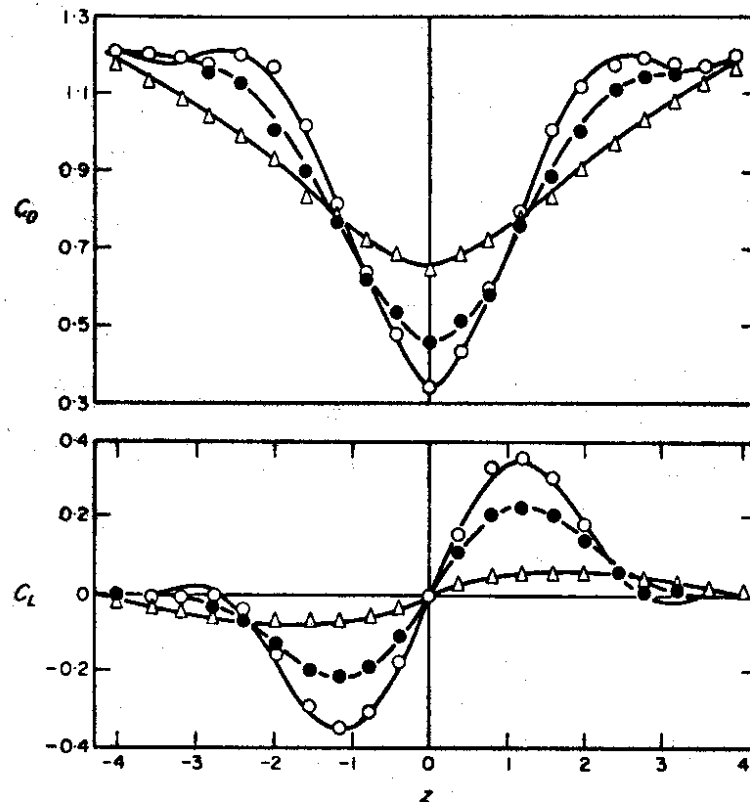


Figure A - 7. Smooth cylinder ($Re\ 3.58 \times 10^4$, turbulence intensity 1.5%. \circ $X/D\ 5.0$, \bullet $X/D\ 9.0$, \triangle $X/D\ 20.3$) (Price, 1975)

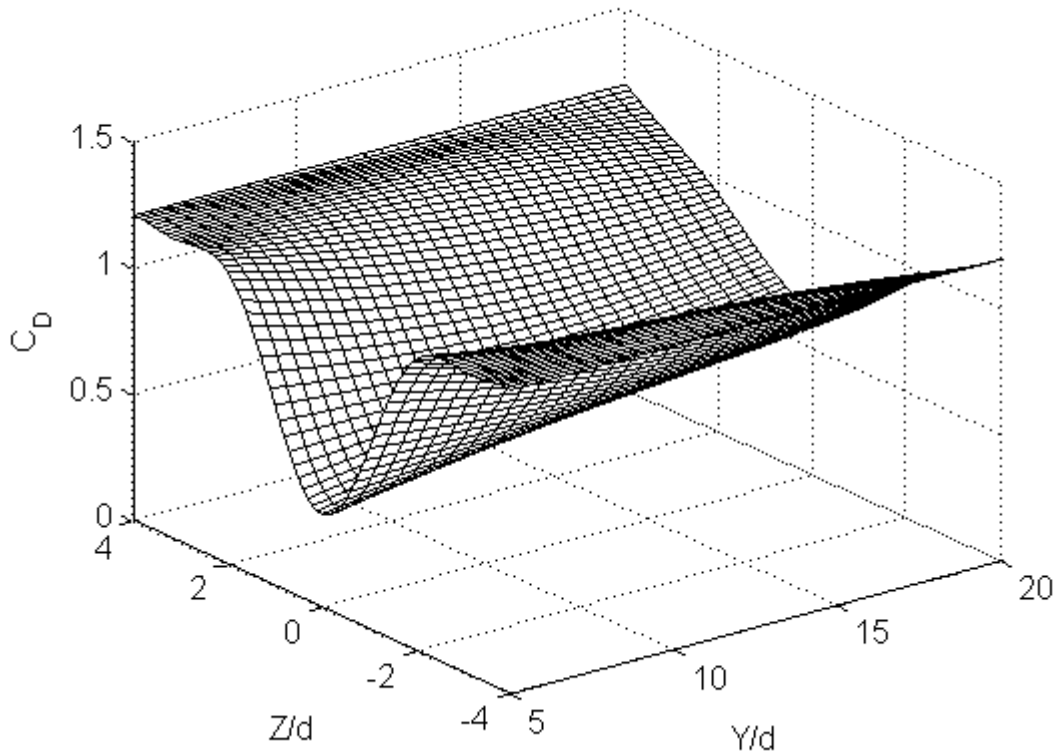


Figure A - 8. Data by Price [56]. Fitted surface of drag coefficient for smooth cylinder (Re 35.8k, turbulence intensity 1.5%)

Fitting polynomial:

For $|z| \leq 4$ and $5 \leq y \leq 20.3$

$$C_D(y, z) = a_{10}z^{10} + a_8z^8 + a_6z^6 + a_4z^4 + a_2z^2 + a_0$$

$$a_i = \sum_{j=1}^3 b_{ij} y^{j-1}, \quad i = 0; 2; \dots; 10$$

$$b_{01} = 2.323294982163092\text{e-}001 \quad b_{21} = 7.264297381642306\text{e-}001$$

$$b_{02} = 2.844681316572165\text{e-}002 \quad ; b_{22} = -7.129965014332403\text{e-}002$$

$$b_{03} = -3.831362667418982\text{e-}004 \quad b_{23} = 2.002378704380350\text{e-}003$$

$$b_{41} = -1.628227576498350\text{e-}001 \quad b_{61} = 1.536080273957189\text{e-}002$$

$$b_{42} = 1.950084905957192\text{e-}002 \quad ; b_{62} = -1.930079534172798\text{e-}003 ;$$

$$b_{43} = -5.952414931982878\text{e-}004 \quad b_{63} = 5.979023476687854\text{e-}005$$

$$b_{81} = -6.428424055644690\text{e-}004 \quad b_{101} = 9.761759132226317\text{e-}006$$

$$b_{82} = 7.929895962013830\text{e-}005 \quad ; b_{102} = -1.116095087816932\text{e-}006$$

$$b_{83} = -2.403369109975760\text{e-}006 \quad b_{103} = 3.173009934540457\text{e-}008$$

For $|z| > 4$, $C_D(y, z) = 1.2$

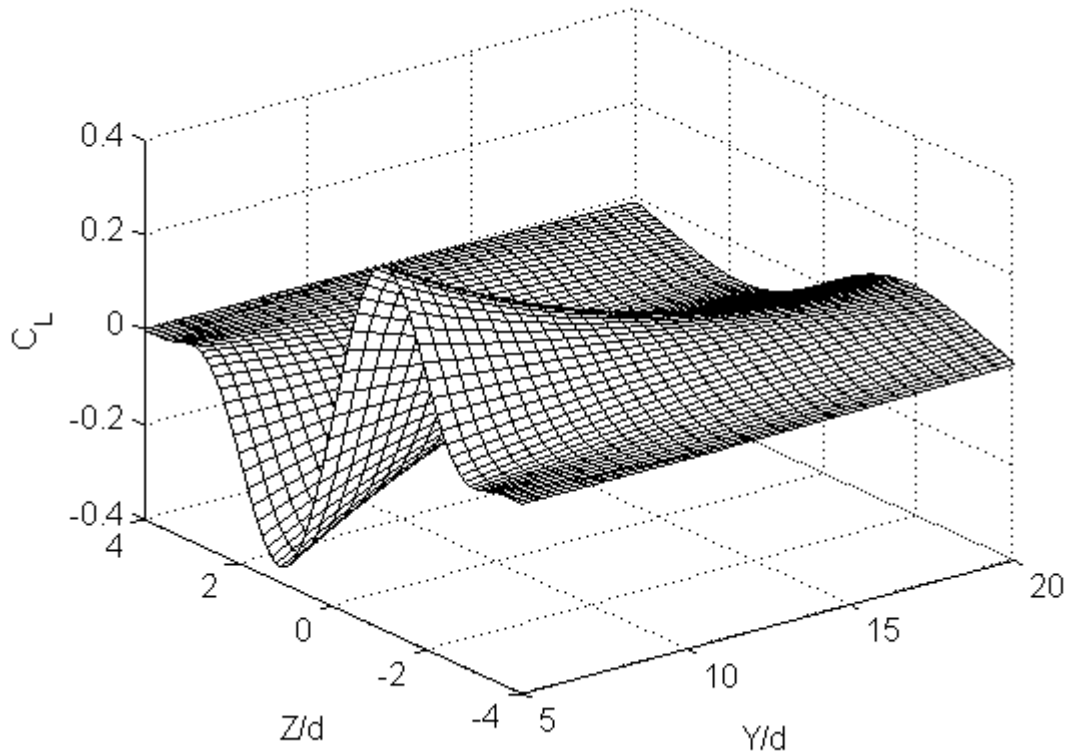


Figure A - 9. data by Price [56]. Fitted surface of lift coefficient for smooth cylinder (Re 35.8k, turbulence intensity 1.5%)

Fitting polynomial:

For $|z| < 4$ and $5 \leq y \leq 20.3$:

$$C_L(y, z) = \sum_{i=1, 3, \dots}^9 \left(\sum_{j=0}^2 q_{i,j} y^{(2-j)} \right) z^{(9-i)}$$

$$\begin{aligned} q_{11} &= -9.366116523539152\text{e-}001 & q_{31} &= 3.622073725080496\text{e-}001 \\ q_{12} &= 9.453571110216909\text{e-}002 & q_{32} &= -4.049373525837849\text{e-}002; \\ q_{13} &= -2.571093910023341\text{e-}003 & q_{33} &= 1.147815561818735\text{e-}003 \\ q_{51} &= -4.904551885931337\text{e-}002 & q_{71} &= 2.815451239687794\text{e-}003 \\ q_{52} &= 5.781434477530589\text{e-}003 & q_{72} &= -3.411751082960935\text{e-}004; \\ q_{53} &= -1.684462803797870\text{e-}004 & q_{73} &= 1.009254549253525\text{e-}005 \\ q_{91} &= -5.853126807000320\text{e-}005 \\ q_{92} &= 7.187070581552582\text{e-}006 \\ q_{93} &= -2.140673043868416\text{e-}007 \end{aligned}$$

For $|z|$ outside boundaries, $C_L(y, z) = C_{Lz}(y, z) = 0$.

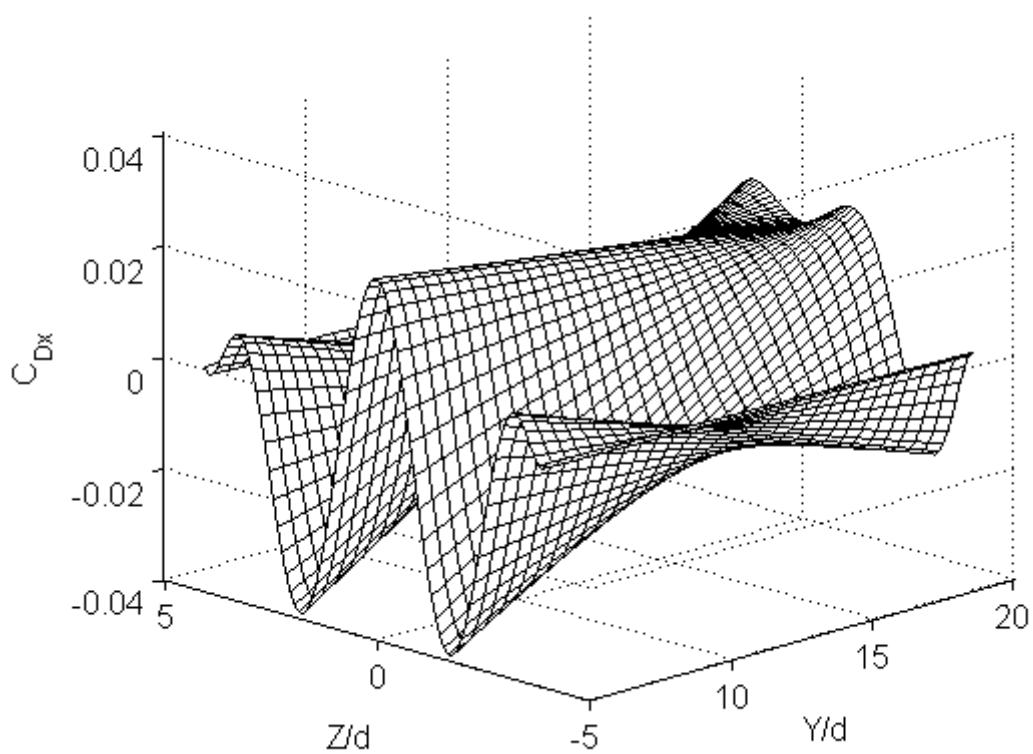


Figure A - 10. Derivative C_{Dy} from polynomial fit, see Figure A - 8

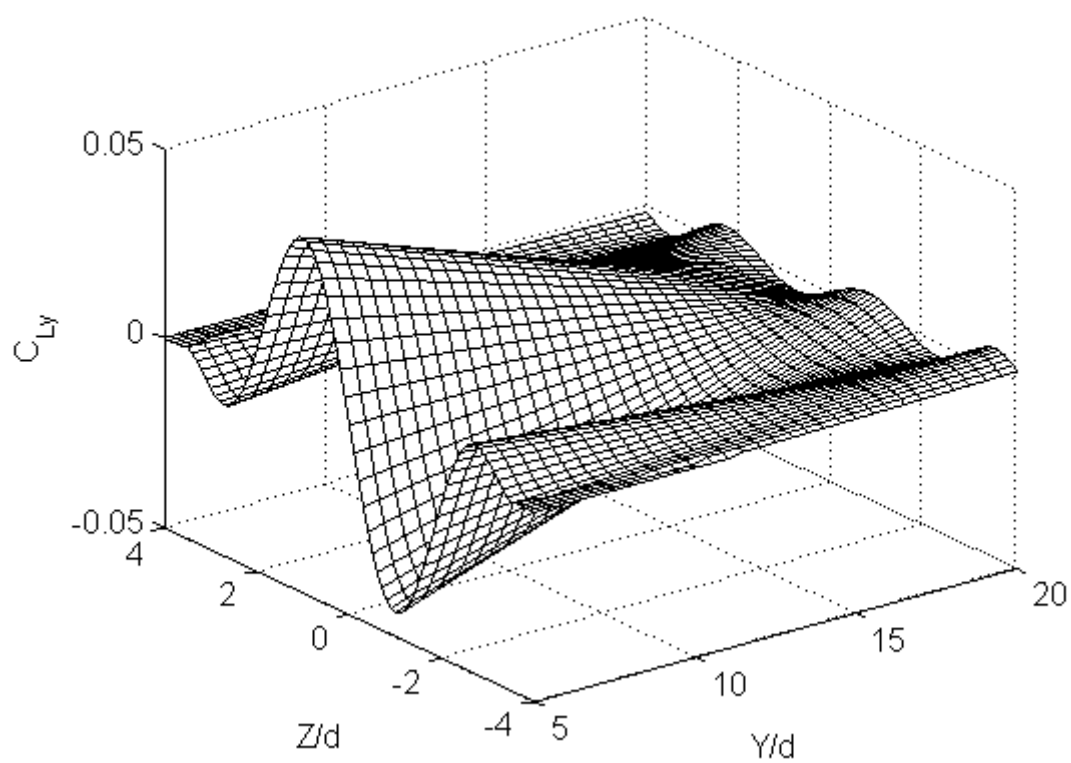


Figure A - 11. Derivative C_{Ly} from polynomial fit, see Figure A - 9

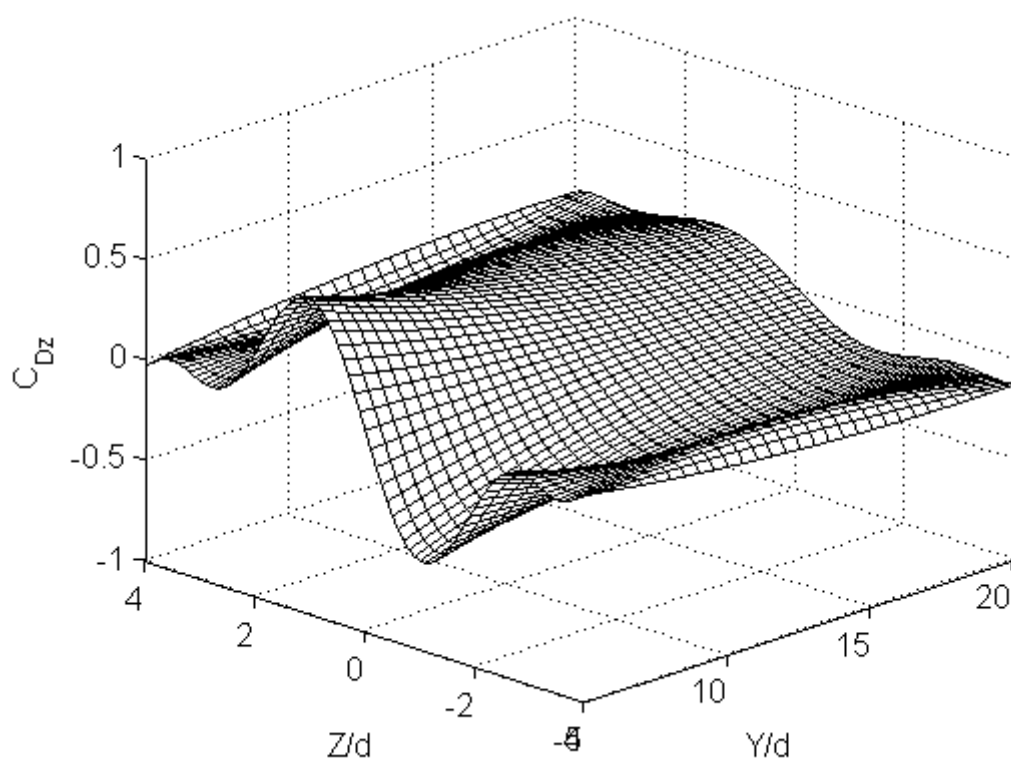


Figure A - 12. Derivative C_{Dz} . From polynomial fit, see Figure A - 8

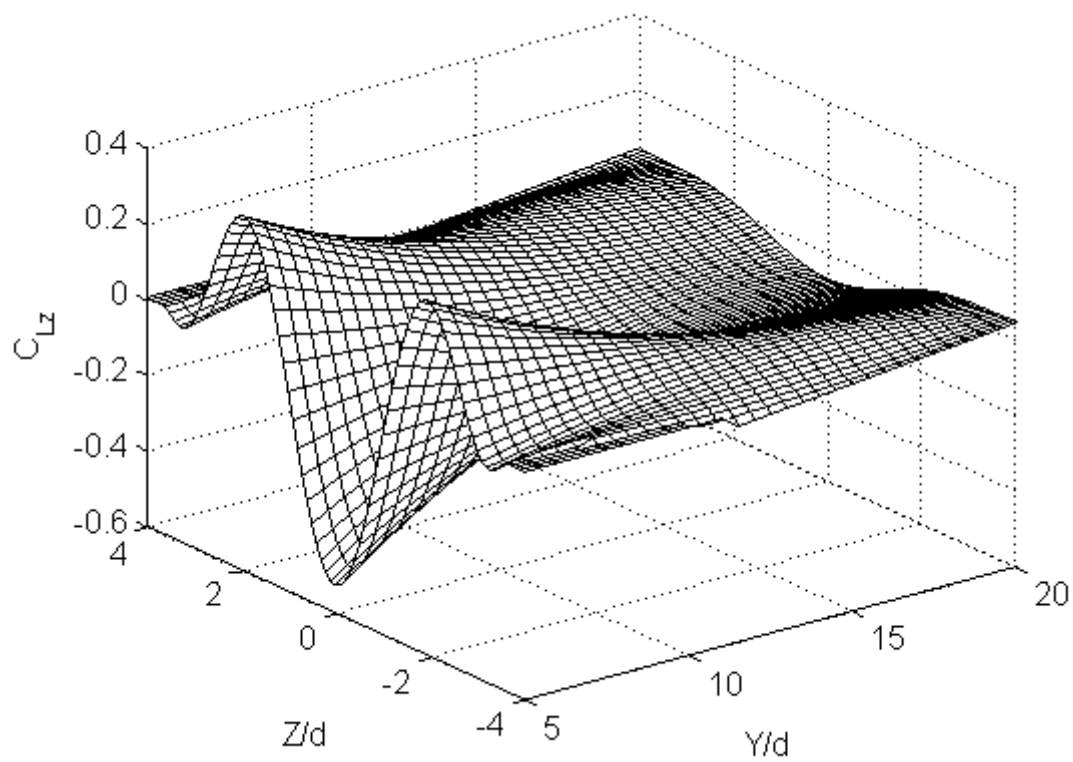


Figure A - 13. Derivative C_{Lz} . From polynomial fit, see Figure A - 9

Annex B. On numerical resolution of wake loads on a leeward cylinder

The wake-induced oscillations of power transmission lines occur at mean wind speeds ranging from 7 to 18 m/s. Given the standard value of kinematic viscosity $\nu = 1.5e-5 \text{ m}^2/\text{s}^2$, the characteristic size $D \sim 0.03 \text{ m}$ for conductor, we obtain that WIO occurs at Reynolds number range $Re = 14...36 \times 10^3$.

To evaluate the wake-induced effects, we need either to measure or calculate the aerodynamic forces on the cylinder in the wake. Numerical analysis of the flow around the bundled conductors is an extremely hard problem. In the range of Re where bundle conductors or stay cables are subject to WIO, it is important to properly account the flow viscosity defining the rate of the energy dissipation near the boundary layer of cylinder. As established by Kolmogorov [37], dissipation in the flow energy is directly related to the small-scale flow turbulence. The small-scale turbulences have characteristic sizes of the flow *structures* emanating in the free shear layers (at subcritical regime) and boundary layer (critical and transcritical regime) around cylinder. Narrowness of the spectrum of fluctuations in the near-wake demonstrates that the small-scale fluctuations which occupy the narrow range around central fluctuation frequency (i.e. Strouhal frequency), are very important in the signature of the wake.

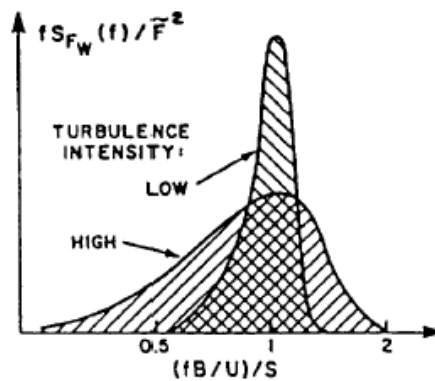


Figure B - 1. General image of the force spectrum in the wake depending on the turbulence of incident flow [13]

Thus, in order to obtain the adequate values and distribution of the wake-induced loads it is important to resolve these small, low-fluctuation flow scales.

The estimate for the size of these scales follows from the Kolmogorov-Obukhov's law which relates the velocity fluctuation, v_λ , along the distance of the order of λ , and the viscous dissipation of the energy, ε , as

$$v_\lambda \sim (\varepsilon \lambda)^{\frac{1}{3}}$$

The value v_λ may be considered as the velocity of turbulent structures having the scale λ . Consider now the viscous flow scales λ_0 which simultaneously define the values of the scales of the smallest pulsations in the turbulent flow (the value λ_0 is called the *internal* turbulence scale, contrary to the *external* scale, l . For that purpose compose the “local Reynolds number”

$$Re_\lambda \sim \frac{v_\lambda \lambda}{\mu} \sim \frac{\Delta u \cdot \lambda^{\frac{4}{3}}}{\mu l^{\frac{1}{3}}} \sim Re \left(\frac{\lambda}{l} \right)^{\frac{4}{3}}$$

here, $Re \sim \Delta u \cdot l / \mu$ is the global Reynolds number characterising the fluid motion as a whole. The order of value λ_0 is defined by that it should be $Re_{\lambda_0} \sim 1$. From there, obtain the one-dimensional relationship:

$$\frac{l}{\lambda_0} = Re^{\frac{3}{4}}$$

For the volume scales, the above estimate becomes

$$\frac{v}{V_0} = Re^{\frac{9}{4}}.$$

Thus, for discretization of the volume $Re = 20\,000$, the number of grid points is $\sim 5e9$.

In the Navier-Stokes based CFD algorithms⁵ the spatial discretization of the flow domain near cylinder's wall is determined by characteristic size of these scales.

The time discretization needs to be fine enough to ensure the computation converging to the steady process. For explicit resolution algorithms, time discretization is very small.

In order to reduce the computational cost, industrial CFD applications include some models of the fluid energy dissipation on the walls of the cylinder. For subcritical flows the most common are $k - \varepsilon$ and $k - \omega$ model, and for supercritical flows the Spalart-Allmaras model is recommended [1].

A series of benchmarking computations of the flow around a pair of cylinders was performed using commercial fluid package [21]. This package implements 3D finite-volume method and, up to date of model testing, $k - \varepsilon$ model for modelling the viscous turbulent flows. It has a very fast mesher with automatic mesh adaptation following various properties of the flow (e.g., pressure variation, velocity gradient etc.) and conditions on the boundaries across time computation steps.

The velocity of incident flow was selected 10 m/s, and cylinders' diameter 30 mm; the corresponding Reynolds number being 20k.

⁵ An alternative to Navier-Stokes is Discrete Vortex method, described namely in [1]

presents the general view on the computational domain. It was discretized in a manner that allows flow resolution on the cylinder walls and tuned to follow the turbulence inhibition in the wake.

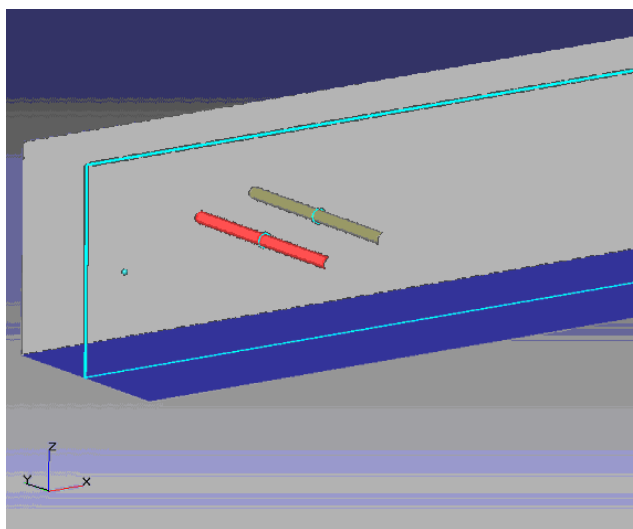


Figure B - 2. Computational domain (cylinders' aspect ratio $l/D = 16$)

In Figure B - 3 to Figure B - 5 some modelling results are presented. For instance, in Figure B - 3 velocity streamlines indicate eddies deployment in the wake. Two eddies behind a windward cylinder are superimposed due to spanwise variation of the vortices' detachment.

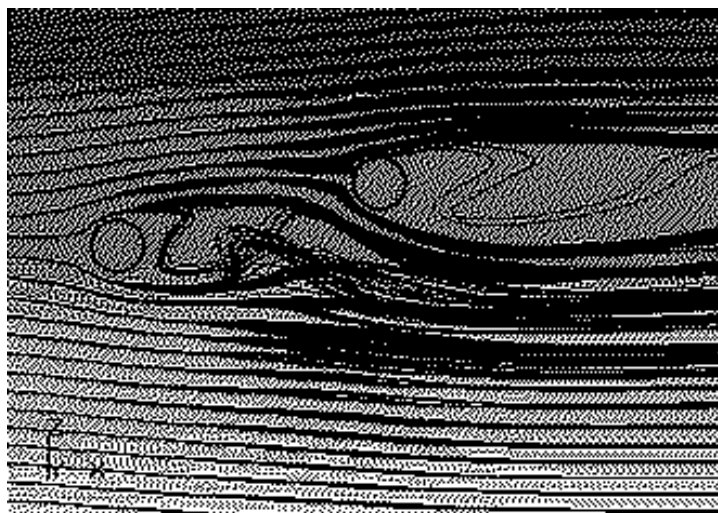


Figure B - 3. Pair of cylinders under flow at Re 20k. Velocity streamlines

Figure B - 4 and Figure B - 5 show time histories of drag and lift coefficient on a windward cylinder. Obtaining good C_D and C_L was a primary task of this computation. It was achieved after some tune up of the model with time variations recalling test data. However, amplitude of C_L variation was about two times lower in all computation runs.

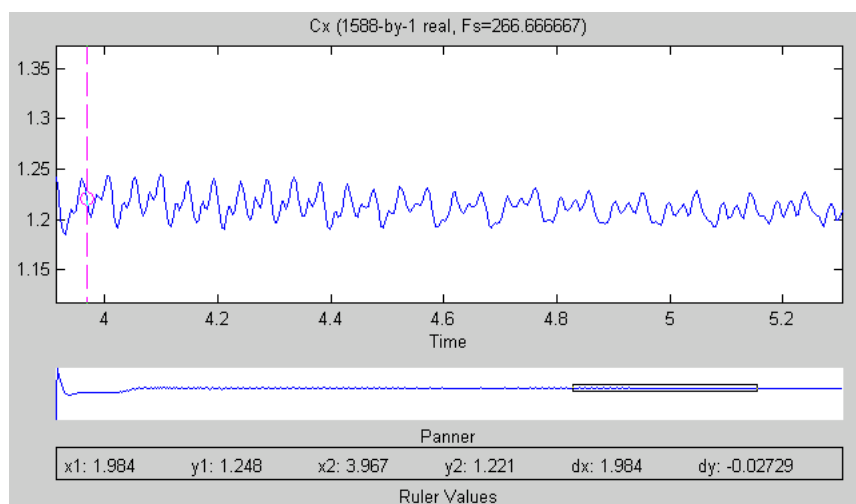


Figure B - 4. Drag coefficient time history on a windward cylinder

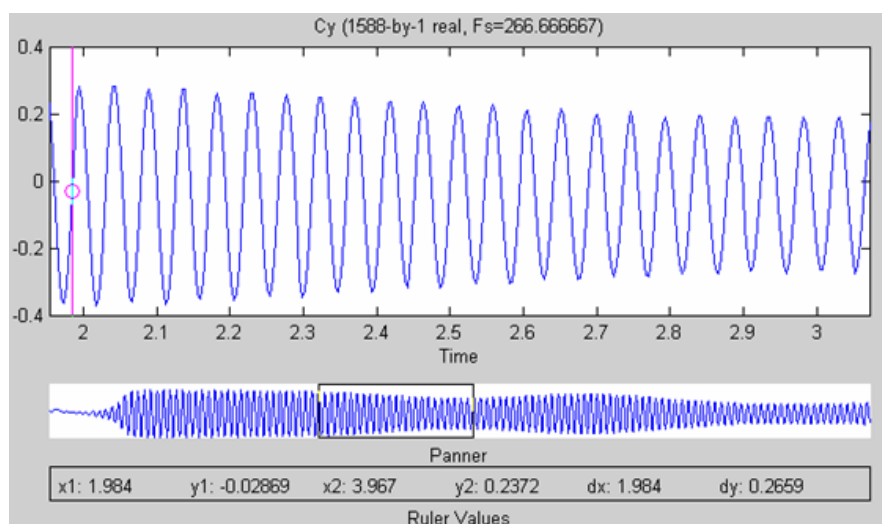


Figure B - 5. Lift coefficient time history on a windward cylinder

As shown in the spectrum in Figure B - 6, for this arrangement the frequency of vortex shedding which should be around 66 Hz (for Strouhal number $Sh \sim 0.18$), is present with the peak at 64.32 Hz.

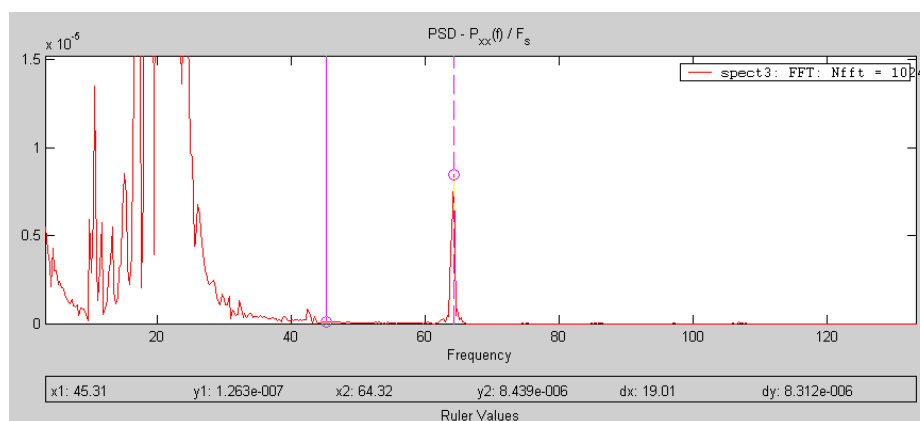


Figure B - 6. Power spectrum of lift coefficient on a windward cylinder

Several positions of leeward cylinder in the wake were computed, however due to time limitations of benchmarking license only a few results are available, see Table B - 1. In the course of this benchmarking, some advantages of the package saved the time (like fast mesher), but other common drawbacks of CFD method as a whole were put to evidence. Time cost for tuning model variables and running preliminary computations was high. Secondly, it was impossible to extrapolate the model parameters onto different Reynolds number and cylinders' separation. Only computation posteriori to the test data known in advance was possible at given time.

		DIANA				CFD			
		Upwind		Downwind		Upwind		Downwind	
x/D	y/D	Cd	Cl	Cd	Cl	Cd	Cl	Cd	Cl
5	0,5	1,2	0	0,16	-0,17	1,1	-0,0	0,25	-0,17

Table B - 1. Commercial CFD benchmarking results

Annex C. Close-wake interference

When the conductors approach each other, the leeward conductor enters the near-wake of the windward one, i.e. the zone of eddy formation. The image of the wake interaction between them may look close to the patterns forwarded by Zdravkovich [90], [91] for smooth cylinder. Depending on the spacing between cylinders, the mode of interaction varies strongly .

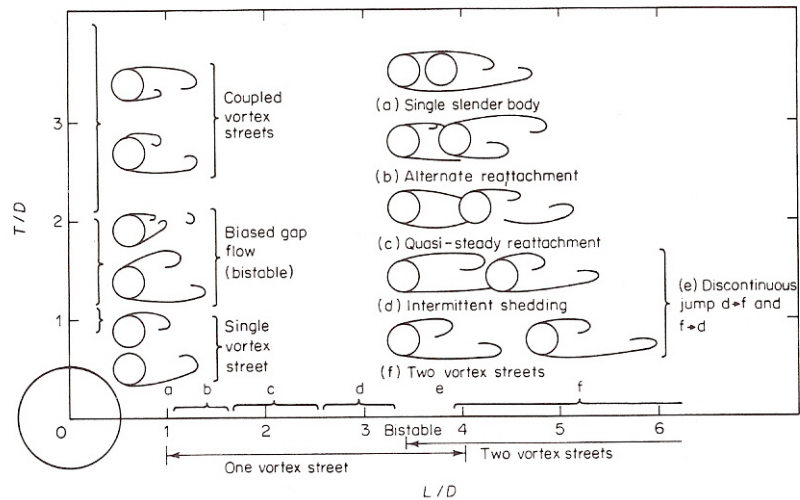


Figure C - 1. Flow patterns for different close separations of a pair of smooth cylinders [92]

In the close wake (up to separation 5 diameters), drag and lift coefficients on a leeward cylinder are distributed extremely non-homogeneously (see Figure C - 2 and Figure C - 4). In separations less than 1.5 diameters (Figure C - 1, (a) and (b)) the windward cylinder has space-dependent drag and non-zero lift coefficients as found in tests by Price and Païdoussis [59].

A reconstruction of literal data was done using spreadsheets, followed by spline interpolation in Matlab (see Figure C - 3 and Figure C - 5). The models obtained are available for future studies.

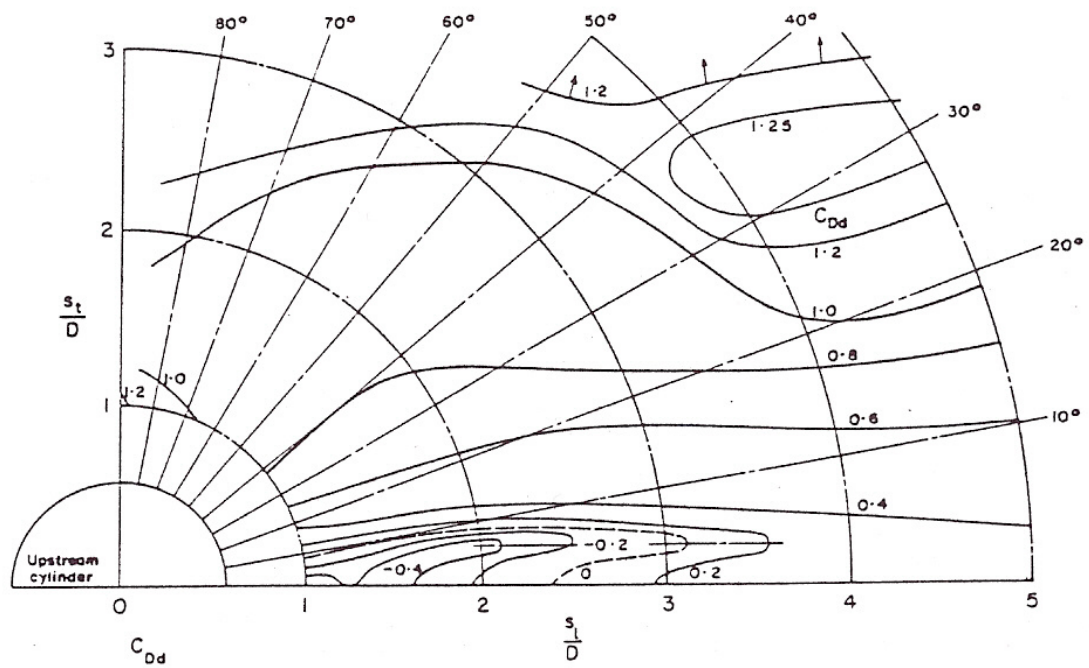


Figure C - 2. Distribution of drag coefficient in the near-wake by Zdravkovich [92]

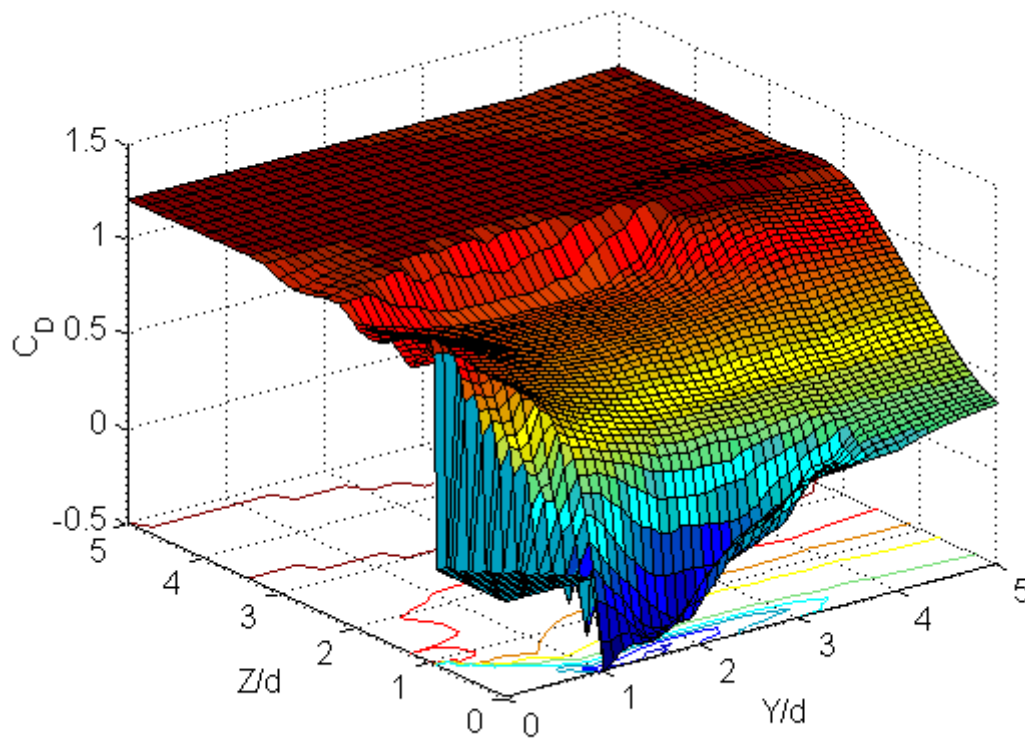


Figure C - 3. Reconstruction of drag coefficient using spline interpolation

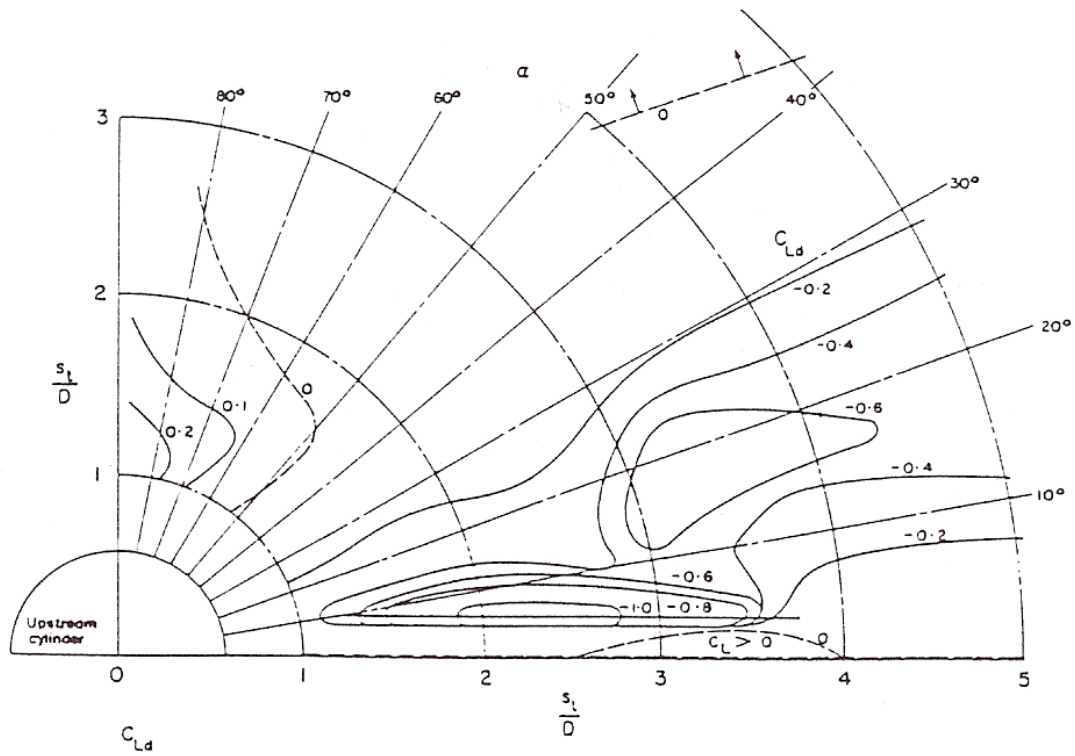


Figure C - 4. Lift coefficient distribution in the near-wake [92]

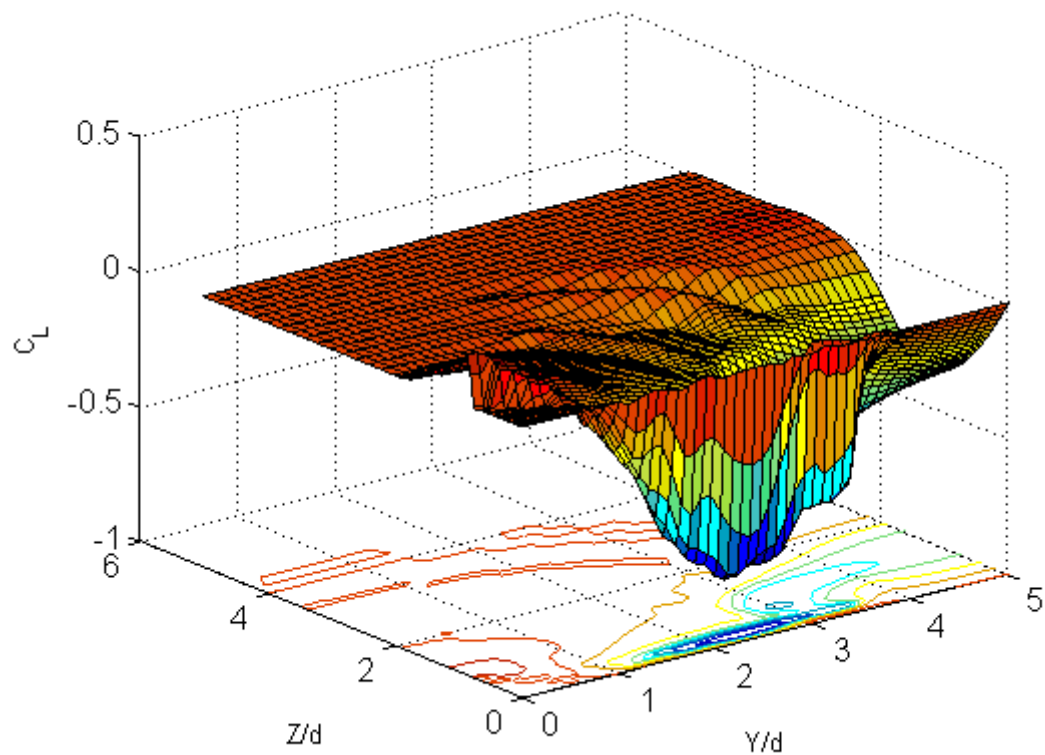


Figure C - 5. Reconstruction of lift coefficient using spline interpolation

Annex D. Summary of bundle oscillation theory by Transfer Matrix Method

The baseline description of Rawlins theory has been presented in 1976 in his work [60], this theory has been further extended in [61]. The analysis of subconductors oscillation in this theory is based upon the vibration power transfer and, finally, establishes the relationship for power balance between the part of received by leeward conductor due to the motion in the wake, and the power lost due to aerodynamic damping. The latter accounts, for analysis of the whole bundle, the aerodynamic damping by windward conductor.

The power transfer in the bundle is ensured by the travelling waves characterized by equations such as

$$x(s, t) = X e^{j(\omega t - \gamma_0 s)}$$

Where

s is distance along the conductor, m

t is time, s

ω is circular frequency, rad/s

$$\gamma_0 = \omega \sqrt{m/T}$$

m is mass per unit length of conductor, kg/m

T is conductor tension

The power transported by such a wave is

$$P = \frac{1}{2} \omega^2 X^2 \sqrt{Tm}$$

The conductor motions describing wake-induced oscillation must include such waves delivering power to spacers from leeward conductors and from spacers to windward conductors, since spacers provide the only paths along which power can be transferred from leeward to windward. As the travelling waves (looking as in Figure D - 1) may grow or decay, the formulation of waves may be modified by replacing a real constant γ_0 with a complex constant $\gamma_0 = \alpha + i\beta$.

For the twin bundle, the oscillation in one subspan may be described by the system of four uncoupled equations of motion with respect to transversal coordinates x, y of the subconductor 1 and 2:

$$-m\ddot{x}_1 + Tx_1'' = 0$$

$$-m\ddot{y}_1 + Ty_1'' = 0$$

$$-m\ddot{x}_2 + Tx_2'' = 0$$

$$-m\ddot{y}_2 + Ty_2'' = 0$$

After differentiation, these equations become coupled by aerodynamic stiffness and damping terms. However, by similarity transformation, their uncoupling may be effected.

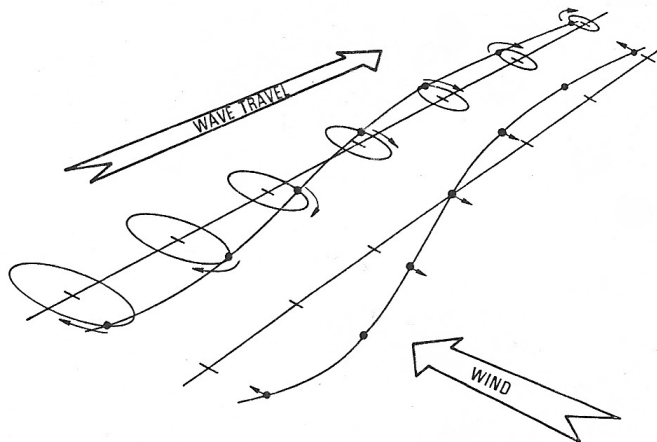


Figure D - 1. Travelling waves in the bundle

Solving this system of equations results in obtaining the propagation modes which read as

$$w(s, t) = W_A e^{j(\omega t - \underline{\gamma} s)} + W_B e^{j(\omega t + \underline{\gamma} s)}$$

where $w(s, t)$ is the vector of modal displacements at position s along the bundle and time t , and W_A and W_B are vectors of the complex amplitudes of the positive – and negative – travelling modes respectively at $s = 0$. The exponentials are diagonal matrices over γ_i , $i = 1 \dots 4$.

This information may be then used to relate the oscillation at one end of a subspan to that at the other. This is done via transfer matrix approach relating the displacements and slopes at the ends of subconductors at each subspan:

$$\begin{bmatrix} z(s) \\ z'(s) \end{bmatrix} = \begin{bmatrix} M \\ M \end{bmatrix} \begin{bmatrix} \cosh \underline{\gamma} s & \frac{j}{\underline{\gamma}} \sinh \underline{\gamma} s \\ j \underline{\gamma} \sinh \underline{\gamma} s & \cosh \underline{\gamma} s \end{bmatrix} \begin{bmatrix} M^{-1} \\ M^{-1} \end{bmatrix} \begin{bmatrix} z(0) \\ z'(0) \end{bmatrix}$$

Here, displacement vector $z = (x_1 \ y_1 \ x_2 \ y_2)'$, $z' = (x'_1 \ y'_1 \ x'_2 \ y'_2)'$

The hyperbolic functions matrix is denoted as Field Matrix **F**. To relate the motions between adjacent subspans, another kind of transfer matrix is used, representing the function of power transfer by the spacer, a Point Transfer Matrix **P**:

$$\mathbf{P} = \begin{bmatrix} I_4 & \\ & I_4 \end{bmatrix} = \begin{bmatrix} I_4 & \\ G & I_4 \end{bmatrix}$$

Where

J is a spacer stiffness matrix divided by the scalar T , the conductor tension, $J = \frac{1}{T} K$

R is a coordinate transformation matrix which brings the local spacer axes to the wind vector via inclination angle α .

The equation relating the displacement – slope vector on side b of a spacer to that on opposite side a is

$$\begin{bmatrix} z(b) \\ z'(b) \end{bmatrix} = \begin{bmatrix} I_4 & \\ G & I_4 \end{bmatrix} \begin{bmatrix} z(a) \\ z'(a) \end{bmatrix}$$

The equation relating the vector at one end of the span to that at the other thus has the form

$$\begin{bmatrix} z(n) \\ z'(n) \end{bmatrix} = \mathbf{N} \mathbf{F} \mathbf{N}^{-1} \mathbf{P} \mathbf{N} \mathbf{F} \mathbf{N}^{-1} \dots \mathbf{F} \mathbf{N}^{-1} \begin{bmatrix} z(0) \\ z'(0) \end{bmatrix}$$

Here, $\mathbf{N} = \begin{bmatrix} M & \\ & M \end{bmatrix}$ - a matrix composed of modal submatrices.

The product of Modal, Field and Point matrices may be expressed as single matrix, the above equation being expressed as

$$\begin{bmatrix} z(n) \\ z'(n) \end{bmatrix} = \begin{bmatrix} Q_1 & Q_2 \\ Q_3 & Q_4 \end{bmatrix} \begin{bmatrix} z(0) \\ z'(0) \end{bmatrix}$$

Each Q is a fourth order submatrix.

If the conductors are fixed at the span ends, then $z(0) = z(n) = \bar{0}_4$, where $\bar{0}_4$ is the fourth-order zero vector. Then, by partitioning and multiplying, obtain

$$\begin{aligned} Q_2 z'(0) &= \bar{0}_4 \\ z'(n) &= Q_4 z'(0) \end{aligned}$$

If the determinant of Q_2 is zero, then there is a vector $z'(0)$ that satisfies above equation and can be found by standard methods. The other vectors z and z' can be found from $z'(0)$.

Annex E. Short glossary

E-1. Strouhal number

In dimensional analysis, the **Strouhal number** is a dimensionless number describing oscillating flow mechanisms. The parameter is named after Vincenc Strouhal, a Czech physicist who experimented in 1878 with wires experiencing vortex shedding and singing in the wind. The Strouhal number is often given as:

$$Sh = \frac{fL}{V}$$

where Sh is the dimensionless Strouhal number, f is the frequency of vortex shedding, L is the characteristic length (for example cylinder diameter) and V is the velocity of the fluid.

For electric conductors under moderate to strong wind, the Strouhal number is around 0.18 – 0.2 and characterizes alternate vortices shedding from the conductor at the given wind velocity.

E-2. Reynolds number

In fluid mechanics and heat transfer, the **Reynolds number** Re is a dimensionless number that gives a measure of the ratio of inertial forces ($V\rho$ with V - fluid velocity, m/s; ρ - fluid density, kg / m³) to viscous forces (characterized by dynamic viscosity of fluid μ , N·s/m²) and, consequently, it quantifies the relative importance of these two types of forces for given flow conditions with a relationship:

$$Re = \frac{VD}{\mu}$$

Reynolds numbers frequently arise when performing dimensional analysis of fluid dynamics and heat transfer problems, and as such can be used to determine dynamic similitude between different experimental cases. They are also used to characterize different flow regimes, such as laminar or turbulent flow: laminar flow occurs at low Reynolds numbers, where viscous forces are dominant, and is characterized by smooth, constant fluid motion, while turbulent flow occurs at high Reynolds numbers and is dominated by inertial forces, which tend to produce random eddies, vortices and other flow fluctuations.

Reynolds number is named after *Osborne Reynolds* (1842–1912), who proposed it in 1883 [62].

Typical values of Reynolds number

(Note: these values are meaningless without a definition of the characteristic length in each case)

- Spermatozoa $\sim 1 \times 10^{-4}$
- Blood flow in brain $\sim 1 \times 10^2$
- Blood flow in aorta $\sim 1 \times 10^3$

- Onset of turbulent flow $\sim 2.3 \times 10^3 - 5.0 \times 10^4$ for pipe flow to 10^6 for boundary layers
- Typical pitch in Major League Baseball $\sim 2 \times 10^5$
- Person swimming $\sim 4 \times 10^6$
- Blue Whale $\sim 3 \times 10^8$
- A large ship (RMS Queen Elizabeth 2) $\sim 5 \times 10^9$

E-3. Scruton number

In its application to the cable vibration, a dimensionless Scruton number is the aerodynamic stability parameter which introduces a relationship between dimensionless cable damping ζ and its mass per unit length m (kg/m) to the air density ρ (kg / m³) and cable diameter D (m):

$$Sc = \frac{m\zeta}{\rho D^2}$$

The oscillation amplitude of vortex shedding vibrations varies in inverse proportion to the Scruton number. Since vortex oscillations become smaller as the Scruton number is increased, the more dense and highly damped the cable, the less it will oscillate. Typical value for electrical conductor is 0.02 to 0.04.

E-4. Wake

(Possibly from Middle Low German, hole in the ice, of Scandinavian origin; akin to Old Norse vök.) Originally used for the visible track of turbulence left by something moving through water: the wake of a ship. Relatively to the flow around cylindrical body, the wake may be defined as a region of disturbed but structured flow past the cylinder. One distinguishes the near-wake, - a region at the relative distance $0 < X/D < 3.5$, followed by the far-wake. It is the latter representing the most interest in studies of the wake-induced vibrations, but understanding its character implies the study of the near-wake as well.

Note that the meaning *wake up* belongs to the Middle English *wakien*, *waken*, from Old English *wacan*, to wake up and *wacian*, to be awake, keep watch. Original root is Indo-European *weg* - to be strong, be lively. See <http://www.bartleby.com/61/roots/IE553.html>. Such relationship can be found phonetically and semantically in the Russian roots “vek” (the time of human life, century), “vet” (to blow, cast upon – derivative “veter” – the wind) and to the French root “veil” (one of derivative words: “réveil” – wake up).